creative commons
COMMONS DEED

저작자표시-비영리-동일조건변경허락 2.0 대한민국

이용자는 아래의 조건을 따르는 경우에 한하여 자유롭게

- 이 저작물을 복제, 배포, 전송, 전시, 공연 및 방송할 수 있습니다.
- 이차적 저작물을 작성할 수 있습니다.

다음과 같은 조건을 따라야 합니다:



저작자표시. 귀하는 원저작자를 표시하여야 합니다.



비영리. 귀하는 이 저작물을 영리 목적으로 이용할 수 없습니다.



동일조건변경허락. 귀하가 이 저작물을 개작, 변형 또는 가공했을 경우에는, 이 저작물과 동일한 이용허락조건하에서만 배포할 수 있습니다.

- 귀하는, 이 저작물의 재이용이나 배포의 경우, 이 저작물에 적용된 이용허락조건을 명확하게 나타내어야 합니다.
- 저작권자로부터 별도의 허가를 받으면 이러한 조건들은 적용되지 않습니다.

저작권법에 따른 이용자의 권리는 위의 내용에 의하여 영향을 받지 않습니다.

이것은 이용허락규약(Legal Code)을 이해하기 쉽게 요약한 것입니다.

Disclaimer

dCollection

Ph.D. DISSERTATION

Novel material and device for ferroelectric memory: thin $Hf_{1-x}Zr_xO_2$ film and tri-states memory

by

Min Hyuk Park

February 2014

Department of Materials Science and Engineering
College of Engineering
Seoul National University

Ph.D. DISSERTATION

Novel material and device for ferroelectric memory: thin $Hf_{1-x}Zr_xO_2$ film and tri-states memory

by

Min Hyuk Park

February 2014

Department of Materials Science and Engineering
College of Engineering
Seoul National University

Novel material and device for ferroelectric memory: thin $Hf_{1-x}Zr_xO_2$ film and tri-states memory

Advisor : Prof. Cheol Seong Hwang

By

Min Hyuk Park

A thesis submitted to the Graduate Faculty of Seoul National University in partial fulfillment of the requirements for the Degree of Doctor of Philosophy

Department of Materials Science and Engineering

February 2014

Approved

by

Chairman of Advisory Committee : Hyeong Joon Kim

Vice-chairman of Advisory Committee : Cheol Seong Hwang

Advisory Committee : Seungwu Han

Advisory Committee : Sung-Min Yoon

Advisory Committee : Seong Keun Kim

Abstract

Ferroelectric random access memory (FeRAM) has been considered as one of the best candidates for universal memory. On the other hand, difficult scaling of the memory cell size has hindered the realization of high density FeRAM. Given that size scaling is inherently limited by the complicated crystal structure and difficult processing of ferroelectric materials, exploring new material or new device might be the best solution for that. In this dissertation, $Hf_{1-x}Zr_xO_2$ thin films and tri-state memory is studied as new material and device for next-generation high-density ferroelectric memory.

As the first step, the origin of the ferroelectricity in $Hf_{1-x}Zr_xO_2$ thin films is examined based on their crystallographic structure, micro-structures and resulting in-plane stress. Although it seems evident that the formation of the non-centrosymmetric $Pbc2_1$ orthorhombic phase causes ferroelectricity in the doped and alloyed HfO_2-based films, the origin of such evolution has not yet been elucidated. From the electrical and physical characterization on $Hf_{1-x}Zr_xO$ films with various film thickness (t_f) and composition, ferroelectric orthorhombic phase is formed with the composition of ~0.4 - 0.6 and t_f of < 25 nm. Even though these conditions are appropriate for the formation of tetragonal phase due to the size effect, the unexpected ferroelectric orthorhombic phase is formed. To elucidate the origin of the phenomenon, the film stress calculated from the change of substrate curvature and that of

interplanar distance calculated from the change of diffraction peaks of X-ray diffraction spectra were analyzed, and it could be noticed that the unexpected orthorhombic phase is formed with the tensile strain of >1.5% and the grain size of < 25 nm. The large tensile strain is formed due to the huge tensile stress during the stage of island coalescence of Volmer-Weber type growth. In addition to that, the $Hf_{0.5}Zr0.5O_2$ (HZO) films on Pt bottom electrode (BE) were deposited with tetragonal phase with (111)-prefered orientation, and they hardly showed ferroelectric behavior. On the other hand, the in-plane strain of HZO films on Pt BE was almost equivalent with that on TiN BE, which is large enough for the formation of orthorhombic phase. However, the stress along a-, b-, and c-axis are almost equivalent for the case of (111)-oriented films, so it does not meet the condition of asymmetric stress for orthorhombic phase formation.

In addition to that, the effects of annealing temperature (T_{anneal}) and film t_f on the crystal structure and ferroelectric properties of HZO films were examined. The HZO films consist of tetragonal, orthorhombic, and monoclinic phases. The orthorhombic phase content, which is responsible for the ferroelectricity in this material, is almost independent of T_{anneal}, but decreases with increasing t_f. In contrast, increasing T_{anneal} and t_f monotonically increases (decreases) the amount of monoclinic (tetragonal) phase, which coincides with the variations in the dielectric constant. The remanant polarization was determined by the content of orthorhombic phase

as well as the spatial distribution of other phases.

As the next step, the effects of forming gas annealing (FGA) on the ferroelectric properties of HZO films were examined. Although the H-incorporation during FGA degrades the ferroelectric properties of HZO films, the degree of degradation was much lower compared with other ferroelectrics, such as $Pb(Zr,Ti)O_3$. Pt worked as a catalyst for H-incorporation, and maximum $2P_r$ loss of ~40% occurred. However, the insertion of a ~20-nm-thick TiN layer between Pt and HZO decreased the degradation to ~12%. HZO is more resistant to degradation by FGA compared with the conventional ferroelectrics, which is a highly promising result for next-generation ferroelectric memory.

In addition to that, the effect of the top electrode (TE) on the ferroelectric properties and switching endurance of thin HZO films was examined. The TiN/HZO/TiN capacitor can endure up to 10^9 times the electric cycling, which is promising for the next-generation memory. RuO_2 TE was reduced during annealing due to the reactive TiN BE, resulting in the degradation of the ferroelectric properties and endurance. In addition, the endurance of the TiN/HZO/TiN capacitors was optimized by changing the film thickness and the post-annealing temperature.

Finally, this thesis presents a feasible structure and actual operation of a tri-state memory function for high density FeRAM using stacked ferroelectric $Pb(Zr,Ti)O_3$/insulating Al_2O_3/semiconducting ZnO layers with

Pt top and BEs. The complicated electrical responses of the stacked structure to external stimuli were well understood based on the separated trapping of the compensating charges at the $Pb(Zr,Ti)O_3/Al_2O_3$ and Al_2O_3/ZnO interfaces and the discrete dissipation of the trapped charges during polarization switching in one direction. This unique function of the structure induced three discrete charge states that can be used to increase the memory density by 50% compared to conventional FeRAM at a given cell size.

It is believed that this thesis presents new pathways for the next-generation ferroelectric memory by exploring the new material system of $Hf_{1-x}Zr_xO_2$ films and by suggesting the new structure and operation of ferroelectric capacitor with novel ferroelectric-insulator-semiconductor heterojunction. Even though the ferroelectric memory is still far from the adoption as a universal memory, the results in this thesis could shed light on this field by suggesting new pathways different from the conventional approach.

Keywords : Ferroelectric, HfO_2, $(Hf,Zr)O_2$, ZrO_2, $Pb(Zr,Ti)O_3$, $Pbc2_1$, In-plane stress, microstructure, Tri-state memory, FeRAM, Capacitor, Nonvolatile memory, Atomic Layer Deposition

Student ID : 2008-22846

Min Hyuk Park

Table of Contents

Abstract.....i

Table of Contents.....v

List of Figures.....x

List of Tables.....xxiv

List of Abbreviations.....xxv

1. Introduction.....1

1.1. Overview and issues on ferroelectrics.....1

1.2. Objective and chapter overview.....5

1.3. References.....7

2. Literature.....9

2.1. Ferroelectric materials for memory applications.....9

2.1.1. Conventional ferroelectric materials for memory applications 9

2.1.2. Ferroelectricity in thin HfO_2-based films.....13

2.2. Ferroelectric devices for memory applications.....23

2.2.1. Conventional ferroelectric random access memory 23

2.2.2. Ferroelectric field effect transistor.....25

2.2.3. Ferroresistive storage.....34

2.3. References.....43

3. The origin of the ferroelectricity in thin $Hf_{1-x}Zr_xO_2$ films: microstructure and resulting in-plane stress [1].....50

3.1. Introduction.....50

3.2. Experimental.....53

3.3. Results and discussions.....55

3.3.1. Electrical characteristics on TiN bottom electrode.....55

3.3.2. Structural analysis.....60

3.3.3. Stress and microstructures.....65

3.3.4. Effects of bottom electrode.....75

3.3.4.1. Effect of film orientation: comparative study on $Hf_{0.5}Zr_{0.5}O_2$ films on TiN and Pt bottom electrode [2].....75

3.3.4.2. Effect of microstructure: comparative study on $Hf_{0.5}Zr_{0.5}O_2$ films on TiN and Ir bottom electrode [3].....98

3.3.5. Schematic phase diagram.....111

3.4. Conclusions.....113

3.5. References.....115

4. Evolution of phases and ferroelectric properties of thin $Hf_{0.5}Zr_{0.5}O_2$ films according to the thickness and

annealing temperature [4].....120

4.1. Introduction.....120

4.2. Experimental.....124

4.3. Results and discussions.....125

4.4. Conclusions.....144

4.5. References.....145

5. Effect of forming gas annealing on the ferroelectric properties of $Hf_{0.5}Zr_{0.5}O_2$ thin films with and without Pt electrodes [5].....148

5.1. Introduction.....148

5.2. Experimental.....150

5.3. Results and discussions.....152

5.4. Conclusions.....164

5.5. References.....165

6. The ferroelectric properties and switching endurance of $Hf_{0.5}Zr_{0.5}O_2$ films on TiN bottom and TiN or RuO_2 top electrodes [6]

6.1. Introduction.....167

6.2. Experimental.....170

6.3. Results and discussions.....172

6.4. Conclusions.....184

6.5. References.....185

7. Novel ferroelectric device: tri-states memory using ferroelectric-insulator-semiconductor hetero-junction [7].....187

7.1. Introduction.....187

7.2. Experimental.....192

7.3. Results and discussions.....195

7.4. Conclusions.....234

7.5. References.....235

8. Conclusions.....238

Curriculum Vitae.....242

List of publications.....246

Abstract (in Korean).....256

Acknowledgement.....260

[1] Park et al., Submission preparation

[2] Park et al., Submission preparation

[3] Park et al., Submission preparation

[4] Park et al., *Appl. Phys. Lett.* **102**, 242905 (2013).

[5] Park et al., *Appl. Phys. Lett.* **102**, 112914 (2013).

[6] Park et al., Submission preparation

[7] Park et al., *Adv. Funct. Mater.* **21**, 4305 (2011).

List of Figures

Figure 2.1 The crystal structure of $Pb(Zr,Ti)O_3$ with cubic structure (Left panel, $T>T_c$) and that with tetragonal structure (Right panel, $T>T_c$), respectively

Figure 2.2 Polarization hystereses (black) and AC C-V characteristics (thick red) of a set of "capped" MIM capacitors with 8.5 nm insulator thickness. [12]

Figure 2.3 (a) GAXRD diffractograms for PMA samples having different aluminium concentrations. (b) Enlarged 2θ scans from 80 ° to 90 ° for paraelectric HfO_2 containing no aluminium, ferroelectric HfO_2 containing 4.8 mol% aluminium, and, again, paraelectric HfO_2 containing 11.8 mol% aluminium. [13]

Figure 2.4 (a) Polarization hysteresis for PMA samples annealed at 1000 °C for 20s. (b) Polarization hysteresis for PDA samples annealed at 1000 °C for 20 s. (c) Polarization hysteresis of a HfO_2 MIM capacitor with 7.1 mol% of incorporated aluminium for different annealing temperatures. (d) Remanent polarization and relative permittivity versus amount of incorporated aluminium for PMA capacitors annealed at 1000 °C for 20 s. [13]

Figure 2.5 (A) PV hysteresis at 1 kHz and small signal CV hysteresis at 10 kHz (50 mV level) of 9 nm thin HfO_2–ZrO_2 based metal−insulator−metal capacitors at room temperature. (B) Current response to a triangular voltage excitation reveals polarization switching to be clearly separable from leakage current contributions at high fields. (C) Remanent polarization, dielectric

constant, and monoclinic phase fraction in the HfO_2–ZrO_2 solid solution with respect to the mixing ratio of the oxides. [14]

Figure 2.6 Dependence of ferroelectric hysteresis properties on the concentration of yttrium dopant. [15]

Figure 2.7 (a) Polarization and (b) corresponding current-voltage measurements for Gd: HfO_2 thin films. (c) PUND measurements for field-cycled films show increased current responses when ferroelectric switching occurs (1st and 3rd pulse). [16]

Figure 2.8 Retention characteristics of (a) Pt/SBT/Hf-Al-O/Si FeFETs developed in 2002 and (b) a self-aligned gate FeFET with equivalent gate stack. [26,27]

Figure 2.9 Concept of chain FeRAM. [55]

Figure 2.10 (a) Schematic illustration and (b) top view of a composite oxide memory cell composed of a FeTFT and a TFT (FeNOR) [29]

Figure 2.11 Fe-NAND flash memory cell array including NAND strings, word lines, bit lines, pages and blocks. [57]

Figure 2.12 Retention of a Si : HfO_2-based FeFET. Despite an initially fast retention loss, extrapolation yields an MW of 620 mV after ten years. [60]

Figure 2.13 DC current-voltage (I-V) characteristics (a) and slope of the log(l)-log(V) curve (b), indicating the conduction mechanism through the 0.2 p,m $PbTiO_3$ film for a voltage sweep from 0 → 4 → -4 → 0 V. The inset (a) shows the I-V characteristics on a logarithmic scale. [62]

Figure 2.14 Schematic diagram of a tunnel junction, which consists of two electrodes separated by a nanometer-thick ferroelectric barrier layer.

(E gap is the energy gap. EF is the Fermi energy, V is the applied voltage, V_c is the coercive voltage, t is the barrier thickness, and Δt is the thickness variation under an applied field. [64]

Figure 2.15 Direct evidence for ferroelectricity-related giant TER with ultrathin strained BTO films. **a–f**, Parallel PFM phase image (**a–c**) and CTAFM resistance mapping (**d–f**) of four written ferroelectric stripes (134 mm^2) for BTO films 1, 2 and 3nm thick. **g–i**, Corresponding resistance profiles of the poled area. **j**, Thickness dependence of the resistance (R) of unpoled (red squares), and positively (black triangles) and negatively (blue circles) poled, regions. An exponential increase with t_{BTO} is found, as expected for direct tunnelling. **k**, The TER also increases exponentially with t_{BTO}, reaching ~75,000% for the 3-nm film. In **j** and **k**, vertical error bars correspond to the standard deviation of the resistance distribution over selected areas (and corresponding TER variations), and the horizontal error bars to the thickness uncertainty from growth calibrations. [65]

Figure 2.16 Reproducible, fast and reversible switching. (a) ON and OFF resistance states measured after applying 100 ms voltage pulses to 50 different junctions. Average OFF/ON ratio is 64 (range, 15–220). (b) Reversible resistance switching between ON and OFF resistance states of a typical junction for more than 900 cycles (five resistance measurements are carried out at V_{read} = 100 mV between each 100 ms voltage pulse of +2.9 V and -3.4 V). (c) OFF/ON resistance switching of a typical device measured at V_{read} = 100 mV after applying 10 ns voltage pulses. [67]

Figure 2.17 (A) Sketch of the setup for the simultaneous PFM and J(E) measurements on Ag/BFO/Ag. One hundred electric pulses with ±150 V (E = 17 kV/cm) and a duration of 0.01 s were used to flip electric polarization. J(E) was measured up to E = 2.5 kV/cm, and ac voltage of 1 V_{rms} and 17 kHz was used for PFM. (B) Topography image and out-of-plane PFM images after ±150-V pulses. The PFM signal is color-scaled. These images show that +150-V pulses induce a homogeneous state with downward out-of-plane polarization, and –150-V pulses induce a homogeneous state with upward polarization. (C) J(E) curves of BFO3 after +150-V, –150-V. and +150-V pulses, in sequence. The diode forward and reverse directions switch when the direction of out-of-plane polarization (P) is reversed by ±150-V pulses. The diode forward direction turns out to be the same as the direction of electric pulses used for polarization flipping. [71]

Figure 2.18 Local polarization and diode current for BFO capacitor. (a) AFM image of the fi lm topography. (b) Piezoelectric phase image of original preferred polarization patterns (downward) switched upward through PFM tip scanning of the fi lm surface at –8 V within a square area of 3 × 3 μm^2. After that, the polarization in the center 1 × 1 μm^2 area is scanned downward at + 8 V. (c) The diode current mapping at –3 V acquired in the same region as in (b). (d) The forward and backward voltage sweeping of the diode current within the positively and negatively polarized regions in (b). [72]

Figure 3.1. The P-E curves of HZO films with various composition (Zr/[Zr+Hf]=0.00, 0.19, 0.43, 0.70, 1.00) and thickness (~9.2, 14.2, 19.2, 24.2, and 29.2 nm).

Figure 3.2. (a) Polarization-electric field hysteresis and (b) grazing-angle incidence X-ray diffraction spectra of as-deposited, post-deposition annealed, and post-metallization annealed 9.2-nm-thick $Hf_{0.49}Zr_{0.51}O_2$ film, respectively.

Figure 3.3. (a) The dielectric constant-electric field curves of HZO films with various composition (Zr/[Zr+Hf]=0.00, 0.19, 0.43, 0.70, 1.00) and thickness (~9.2, 14.2, 19.2, 24.2, and 29.2 nm).

Figure 3.4. The horizontal view (upper panel) and the vertical view (bottom panel) of the schematic of modified GIXRD using 6-circle X-ray diffractometer with synchrotron X-ray source in 3A beam line in PAL.

Figure 3.5. (a) The modified GIXRD spectra with full range (10 - 90°) and (b) the enlarged 30 - 40° (left panel) and 50 - 60° region (right panel) of ~9.2-nm-thick HfO_2, $Hf_{0.57}Zr_{0.43}O_2$, ZrO_2 films with ~15-nm-thick upper TiN capping layer after PMA using synchrotron X-ray source (3A beam line in PLS). The enlarged 30 - 40° (left panel) and 50 - 60° region (right panel) of the GIXRD spectra of (c) ~9.2-nm-thick $Hf_{0.57}Zr_{0.43}O_2$ with and without upper TiN capping layer and (d) those of ~9.2-, ~19.2-, and ~29.2-nm-thick $Hf_{0.57}Zr_{0.43}O_2$ without upper TiN layer.

Figure 3.6. The modified GIXRD spectra with full range (10 - 90°) of (a) ~9.2-nm-thick $Hf_{0.57}Zr_{0.43}O_2$ with upper TiN capping layer and that without capping layer. (b) Those of ~9.2-, ~19.2-, and ~29.2-nm-

thick $Hf_{0.57}Zr_{0.43}O_2$ without upper TiN capping layer using synchrotron X-ray source (3A beam line in PLS).

Figure 3.7. The schematics of difficulties in polycrystalline films with randomly oriented grains (left panel), estimation of in-plane strain from (111) diffraction peaks (cetral panel), and Mohr's circle of strain for thin films (right panel), respectively.

Figure 3.8. The GAXRD spectra of (a) HfO_2, (b) $Hf_{0.5}Zr_{0.5}O_2$, and (c) ZrO_2 films with various thickness in as-deposited and annealed at 500°C, respectively.

Figure 3.9. The polarization-electric field and (b) dielectric constant-electric field curves of HZO films with various thickness, respectively.

Figure 3.10. The change of (a) d_{111}, (b) ε_{111}, and (c) ε_{in} of HZO and ZrO_2 films as a function of film thickness, respectively.

Figure 3.11. The change of ε_{in} of ZrO_2 films in as-deposited and annealed state (PMA @ 500°C) (left panel) and the schematic for the growth of low-strained ZrO_2 films (right panel), respectively.

Figure 3.12. (a) Growth behaviour of the $Hf_{0.5}Zr_{0.5}O_2$ films on the TiN and Pt BEs as a function of the number of cycles of atomic layer deposition. (b) Cross-sectional scanning electron microscopy image of the 40-nm-thick $Hf_{0.5}Zr_{0.5}O_2$/TiN/Ti/SiO_2/Si-stacked sample. (c) Change in the average grain size of the $Hf_{0.5}Zr_{0.5}O_2$ films on the TiN and Pt BEs as a function of film thickness, respectively.

Figure 3.13. Scanning electron microscopy images of the HZO films on the TiN and Pt electrodes with various film thickness, which were used to analyze the average grain size included in figure 3.12c.

Figure 3.14. (a) Grazing-angle incidence angle X-ray diffraction spectra of the 9.8-, 19.6-, and 24.5-nm-thick $Hf_{0.5}Zr_{0.5}O_2$ films on the TiN BE. (b) Normal X-ray diffraction spectra of the 13.0-, 18.1-, and 24.9-nm-thick $Hf_{0.5}Zr_{0.5}O_2$ films on the Pt BE. (c) Change in the in-plane strain calculated from the shift of the t(111) diffraction peaks as a function of film thickness, respectively.

Figure 3.15. (a) Schematic diagram for the grain from which the t(111) diffraction peak in GAXRD originated in the $Hf_{0.5}Zr_{0.5}O_2$ films on the TiN electrode. (b) Mohr's circle for stress and (c) that for strain in the $f_{0.5}Zr_{0.5}O_2$ films.

Figure 3.16. (a) Grazing-angle incidence angle X-ray diffraction spectra of the $Hf_{0.5}Zr_{0.5}O_2$ films on the TiN electrode and (b) X-ray diffraction spectra using normal θ-2θ scan of the $Hf_{0.5}Zr_{0.5}O_2$ films on the Pt electrode. (c) Change in the inter-planar distance of the (111) planes of the $Hf_{0.5}Zr_{0.5}O_2$ films on the TiN and Pt electrodes as a function of film thickness.

Figure 3.17. (a) P-E characteristics of the $Hf_{0.5}Zr_{0.5}O_2$ capacitors with various film thicknesses on TiN, and (b) those on Pt, respectively. The TE was Pt(60nm)/TiN(20nm) for both cases. (c) P-E characteristics of the 8.4-nm-thick $Hf_{0.5}Zr_{0.5}O_2$ capacitor on TiN with Pt(60nm)/TiN(20nm) and Pt(80nm).

Figure 3.18. (a) The change of thickness of $Hf_{0.5}Zr_{0.5}O_2$ films on TiN and Ir bottom electrode as a function of number of cycles, and cross-sectional scanning electron microscope images of ~40-nm-thick $Hf_{0.5}Zr_{0.5}O_2$ films on (b) TiN and (c) Ir bottom electrode, respectively.

Figure 3.19. The polarization-electric field hysteresis curves of $Hf_{0.5}Zr_{0.5}O_2$ films with various film thickness on (a) TiN and (b) Ir bottom electrode, and (c) the change of double remanent polarization of $Hf_{0.5}Zr_{0.5}O_2$ films on TiN and Ir bottom electrode as a function of film thickness, respectively.

Figure 3.20. The grazing-angle incidence X-ray diffraction spectra of $Hf_{0.5}Zr_{0.5}O_2$ films with various film thickness on (a) TiN and (b) Ir bottom electrode, respectively.

Figure 3.21. (a) The change of the ratio of the intensity of o(111)/{o(111)+m(-111)+m(111)} and (b) that of grain size as functions of film thickness, respectively.

Figure 3.22. The result of peak analysis of grazing-angle incidence X-ray diffraction spectra of $Hf_{0.5}Zr_{0.5}O_2$ films on Ir bottom electrode with film thickness of (a)12.2, (b) 15.3, (c) 18.3, (d) 21.4, and (e) 24.4 nm, respectively.

Figure 3.23. The result of peak analysis of grazing-angle incidence X-ray diffraction spectra of $Hf_{0.5}Zr_{0.5}O_2$ films on TiN bottom electrode with film thickness of (a) 9.2, (b) 14.2, (c) 19.2, (d) 24.2, and (e) 29.2 nm, respectively.

Figure 3.24. The plan-view sccaning electron microscope images of $Hf_{0.5}Zr_{0.5}O_2$ films with various film thickness on Ir and TiN bottom electrode.

Figure 3.25. Schematic phase diagram of $Hf_{1-x}Zr_xO_2$ films annealed at 500 ^oC with various composition and thickness, where m, t, FE, and AFE correspond to monoclinic, tetragonal, ferroelectric, and antiferroelectric phase, respectively.

Figure 4.1. Grazing-angle incidence X-ray diffraction spectra with 2θ range of 27-33° of (a) 10-nm-thick, (b) 17-nm-thick, and (c) 25-nm-thick HZO films with annealing temperature of 400-800 °C, respectively. (d) The peak position of superimposed o(111) and t(011) peaks as a function of annealing temperature.

Figure 4.2. Grazing-angle incidence X-ray diffraction spectra of (a) 10-, (b) 17-, and (c) 25-nm-thick HZO films with annealing temperature of 400-800 °C.

Figure 4.3. Gaussian fitting results of GIXRD spectra with 2θ range of 27.5-33° of 10-, 17-, and 25-nm-thick HZO films with annealing temperature of 400-800°C.

Figure 4.4. SEM images of 10-, 17-, and 25-nm-thick HZO films with annealing temperature of 400-800°C.

Figure 4.5. The change of $2P_r$ and ε_r (upper panel) and that of the relative ratio of o-, t-, and m-phases (lower panel) as a function of annealing temperature of (a) 5.5-nm-thick, (b) 10-nm-thick, (c) 17-nm-thick, and (d) 25-nm-thick HZO films.

Figure 4.6. Polarization-voltage characteristics of (a) 5.5-nm-thick, (b) 10-nm-thick, (c) 17-nm-thick, and (d) 25-nm-thick HZO films with annealing temperature of 400-800 °C.

Figure 4.7. Dielectric constant-voltage characteristics of (a) 5.5-, (b) 10-, (c) 17-, and (d) 25-nm-thick HZO films with annealing temperature of 400-800 °C, respectively.

Figure 4.8. Current-voltage characteristics of (a) 5.5-, (b) 10-, (c) 17-, and (d) 25-nm-thick HZO films with annealing temperature of 400-800 °C, respectively.

Figure 4.9. The change of $2P_r$ as a function of number of electric field cycling of (a) 5.5-, (b) 10-, (c) 17-, and (d) 25-nm-thick HZO films with annealing temperature of 400-600 °C, respectively.

Figure 5.1. Polarization-voltage characteristics of ~10-nm-thick $Hf_{0.5}Zr_{0.5}O_2$ films after (a) FGA with Pt TE, (b) FGA with Pt/TiN TE, and (c) NA with Pt TE. (d) Summary of the changes in $2P_r$ as a function of annealing temperature. (FGA: forming gas annealing, NA: N_2 annealing)

Figure 5.2. (a) X-ray diffraction spectra, and (b) current-voltage characteristics of ~10-nm-thick $Hf_{0.5}Zr_{0.5}O_2$ films with Pt TE before and after the FGA at 300, 400, 500, and 600 °C, respectively. Subscripts m and o in (a) mean monoclinic and orthorhombic phases, respectively.

Figure 5.3. (a) Zr 3d and (c) Hf 4f XPS spectra of HZO films before and after the FGA with 2-nm-thick Pt TE at 300 and 600 °C, and after the FGA without the TE at 300 °C. (b) and (d) show the same XPS spectra for the NA samples with the 2-nm-thick Pt TE.

Figure 5.4. SEM images of 2-nm-thick Pt/10-nm-thick HZO film after FGA at (a) 300 and (b) 600 °C, and those after NA at (c) 300 and (d) 600 °C. The inset figure in figure (a) shows the SEM images of 2-nm-thick Pt/HZO film before FGA.

Figure 6.1. (a) P-E hysteresis of 10.5-nm-thick $Hf_{0.5}Zr_{0.5}O_2$ capacitors with a TiN and RuO_2 top electrode with various annealing conditions. (b) Grazing-angle incidence angle X-ray diffraction spectra of the $Hf_{0.5}Zr_{0.5}O_2$ and SiO_2 films with an RuO_2 top layer with various annealing conditions.

Figure 6.2. The polarization-electric field characteristics of (a) TiN/PMA, (b) RuO/PMA, (c) RuO/PDA, and (d) RuO/curing with various film thickness, respectively.

Figure 6.3. Auger electron spectroscopy spectra of (a) TiN/PMA, (b) RuO/PMA, and (c) PDA/curing. (d) The change of the equivalent oxide thickness from the C-E characteristics of various capacitors as a function of film thickness.

Figure 6.4. The capacitance-electric field characteristics of (a) TiN/PMA, (b) RuO/PMA, (c) RuO/PDA, and (d) RuO/curing with various film thickness, respectively.

Figure 6.5. Endurance properties of (a) TiN/PMA and (b) RuO/PMA with 2.5, 3, and 3.5 MV/cm electric field cycling, respectively.

Figure 6.6. Endurance properties of (a) TiN/PMA with a 10 nm film thickness and annealed at 400, 500, and 600^{o}C, and (b) TiN/PMA with 5.5, 10, and 17 nm film thicknesses and a 500^{o}C annealing temperature, respectively.

Figure 7.1. Schematic diagram of the measurement system using a pulse generator and digital oscilloscope (left panel), shape of the input pulse by the pulse generator (right upper panel), and switching current density as a function of time read by a digital oscilloscope (right lower panel).

Figure 7.2. (a) Structure of the fabricated MFISM capacitor with a ZnO semiconducting layer between the Al_2O_3 and top electrode, (b) schematic diagram of the ferroelectric capacitor with two interfaces with charge trap states

Figure 7.3. The SEM image of (a) 150-nm-thick PZT film on Pt electrode,

(b) 5.5-nm-thick Al_2O_3 film on 150-nm-thick PZT film, (c) 5-nm-thick ZnO film on 5.5-nm-thick Al_2O_3/150-nm-thick PZT film, (d) 10-nm-thick ZnO film on 5.5-nm-thick Al_2O_3/150-nm-thick PZT film, and (e) 20-nm-thick ZnO film on 5.5-nm-thick Al_2O_3/150-nm-thick PZT film.

Figure 7.4. The X-ray diffraction patterns of a 150-nm-thick PZT film on Pt electrode, 5.5-nm-thick Al_2O_3 film on 150-nm-thick PZT film, 5-nm-thick ZnO film on 5.5-nm-thick Al_2O_3/150-nm-thick PZT film, 10-nm-thick ZnO film on 5.5-nm-thick Al_2O_3/150-nm-thick PZT film, and 20-nm-thick ZnO film on 5.5-nm-thick Al_2O_3/150-nm-thick PZT film, respectively. P: Perovskite, Z: ZnO

Figure 7.5. (a) low magnification and (b) high resolution transmission electron microscopy of the Pt/20-nm ZnO/5.5-nm Al_2O_3/150-nm PZT/Pt stack capacitor.

Figure 7.6. P-V hysteresis (upper panel) and current response (lower panel) curves measured using a TF analyzer 2000 with a 1000Hz triangular pulse with an amplitude of 4, 8, 12, 16, 20, 24 V of MFISM capacitors using Pt top electrode with (a) 5-nm-thick ZnO, (b) 10-nm-thick ZnO, and (c) 20-nm-thick ZnO. Al_2O_3 thickness was 5.5 nm.

Figure 7.7. Switching current as a function of time (Upper panel) and switching charge integrated from the measurement as a function of Vpulse (Bottom panel) for the case of the samples (Al_2O_3 thickness =4.0 nm) with (a) 5-nm-thick ZnO film, (b) 10-nm-thick ZnO film and (c) 20-nm-thick ZnO film, respectively.

Figure 7.8. the P-V hysteresis(Upper panel) and the switching current

density-time curve(Bottom panel) of the MFISM capacitors(d_i = 4nm) with (a) 5-nm, (b) 10-nm, (c) 20-nm thick, which were used for the pulse measurement.

Figure 7.9. Retention properties of the three memory states of the MFISM capacitor with 4-nm Al_2O_3 and 10-nm ZnO (a) at room temperature and (b) at 80°C.

Figure 7.10. Measured C-V characteristics using a 100kHz AC voltage input with an amplitude of 0.05V combined with the DC voltage sweep of MFISM capacitors using a Pt top electrode with (a)5-nm-thick ZnO, (b)10-nm-thick ZnO, (c)20-nm-thick ZnO, of (d)MFM capacitor, and of (e)MFIM capacitor, respectively. Al_2O_3 thickness was 5.5 nm.

Figure 7.11. P-V hysteresis using a triangular voltage pulse with a height of 4V for the MFISM capacitors with (a) 5-nm-thick ZnO, (b) 10-nm-thick ZnO, and (c) 20-nm-thick ZnO

Figure 7.12. Calculated voltage across each layer (a) for the case of a negative-to-positive sweep, (b) for the case of a positive-to-negative sweep, respectively.

Figure 7.13. Electrical band structure calculated based on the model of the MFISM capacitors under certain bias conditions: (a) -17.5V with positive polarization, (b) -5V before depletion of the ZnO layer, (c) -5V after depletion of the ZnO layer, (d) +9V with partial polarization switching due to the flow of Q_{is}, (e) +9V with the recombination of electrons at the FI interface and holes at IS interface due to tunneling, (f) -9V after partial polarization, (g)+17.5V tunneling of carriers at PZT/Al_2O_3 interface , (h) +17.5V

after the polarization switching due to Q_{fi}, (i) +5V before the transition of ZnO from the depleted state to the non-depleted state, (j) +5V after the transition of ZnO from the depleted state to the non-depleted state, (k) -7.5V with the polarization switching, (l) -15V with the positive polarization; (m) The switching current density-voltage curve, and (n) small signal C-V curve of the MFISM capacitor with d_s=10nm. Al_2O_3 thickness was 5.5 nm.

List of tables

Table 3.1. The strain on the (100), (010), and (001) directions for various substrate-normal film orientations as a function of in-plane stress (σ_0) and elastic modulus (Y). The last line shows the relative ratio of substrate-normal remanent polarization ($P_{r,\perp}$) to the maximum remanent polarization along the c-axis of the o-phase ($P_{r,max}$).

Table 4.1 Experimental and theoretical structural parameters and 2c/(a+b) ratio for the HfO_2, ZrO_2, and HZO polymorphs.

Table 4.2 The average grain size of 10-, 17-, and 25-nm-thick HZO films with annealing temperature of 400-800 ^oC calculated from SEM images in figure 4.5.

Table 7.1 Band gap, relative permittivity, electron affinity, and Schottky barrier with Pt for PZT, Al_2O_3, and ZnO, respectively.

List of Abbreviations

AC	Alternating Current
AES	Auger Electron Spectroscopy
AFM	Atomic Force Microscope
ALD	Aromic Layer deposition
BE	Bottom Electrode
BFO	$BiFeO_3$
BL	Bit Line
BTO	$BaTiO_3$
CMOS	Complementary Metal Oxide Semiconductor
C-E	Capacitance-Electric field
C-V	Capacitance-Voltage
D_{avg}	Average grain size
d_{hkl}	Inter-planar distance of (hkl) planes
DRAM	Dynamic Random Access Mermory
DC	Direct Current
E_c	Coercive field
E_g	Bandgap
FeFET	Ferroelectric Field Effect Transistor
FeRAM	Ferroelectric Random Access Mermory
FGA	Forming Gas Annealing
FRRAM	Ferro-Resistive Random Access Mermory
FTJ	Ferroelectric Tunnel Junction
GAXRD	Grazing Angle incidence X-ray Diffraction

HRTEM	High Resolution Transmission Electron Microsopy
HZO	$Hf_{0.5}Zr_{0.5}O_2$
I-V	Current-Voltage
MFM	Metal-Ferroelectric-Metal
MFS	Metal-Ferroelectric-Semiconductor
MIM	Metal-Insulator-Metal
m-phase	$P2_1/c$ m-phase
MOSFET	Metal-Oxide-Semiconductor Field-Effect-Transistor
o-phase	$Pbc2_1$ orthorhombic phase
P-E	Polarization-Electric field
P-V	Polarization-Voltage
RcRAM	Phase-change Random Access Mermory
PDA	Post-Deposition Annealing
PMA	Post-Metallization Annealing
PZT	$Pb(Zr,Ti)O_3$
RAM	Random Access Memory
P_r	Remanent Polarization
PUND	Positive Up Negative Down
P(VDF-TrFE)	Poly(vinylidene fluoride-trifluoroethylene)
ReRAM	Resistive Random Access Mermory
R_{on}	On-state Resistance
R_{off}	Off-state Resistance
RTA	Rapid Thermal Annealing
SBT	$SrBi_2Ta_2O_9$
SEM	Scanning Electron Microscope
TE	Top Electrode

TEMA-Hf	Tetrakis-Ethyl-Methyl-Amino-Hafnium
TEMA-Zr	Tetrakis-Ethyl-Methyl-Amino-Zirconium
TER	Tunneling Electroresistance
T_c	Curie Temperature
t_{ox}	Equivalent oxide thickness
t_f	Film thickness
t-phase	$P4_2/nmc$ tetragonal phase
V_c	Coercive voltage
WL	Word Line
XPS	X-ray photoelectron spectroscopy
XRD	X-ray Diffraction
Y	Elastic modulus
ε_r	Dielectric constant
ε_r-E	Dielectric constant-Electric field
γ_{gb}	Grain boundary energy
γ_{sv}	Surface energy
ν	Poisson's ratio
ε_{in}	In-plane strain
ε_{hkl}	Strain along <hkl> direction
σ_{in}	In-plane stress

Chapter 1. Introduction

1.1. Overview and issues on ferroelectrics

Ferroelectricity has been considered as a promising property for memory applications due to their bistable polarizations. Among the various ferroelectric memories, charge based ferroelectric random access memory (FeRAM) has the longest history of being the most promising candidate for nonvolatile memory due to its potential for high speed, low power consumption, complementary metal-oxide-semiconductor (CMOS) compatibility, and nonvolatility of the stored data. On the other hand, its future as a mass-productive memory appears elusive and studies on it tend to be retarded, particularly due to the difficulties in scaling down its feature size. Because of its inappropriate reliability originating from the depolarization field and leakage current, there has been no great success in reducing the feature size of the ferroelectric memory compared to other nonvolatile memories, such as phase-change random access memory (PcRAM). [1-3] Despite some impressive reports on overcoming the size effect, improving the low retention property of nano-scale ferroelectric devices still remains a tough challenge. [4-6]

One critical problem of conventional FeRAM is intrinsic properties of conventional ferroelectric materials. Most of the ferroelectic memories have

been based on the perovskite structured materials, such as $Pb(Zr,Ti)O_3$ (PZT), $BaTiO_3$ (BTO), and $SrBi_2Ta_2O_9$ (SBT), which show large remanent polarization (P_r) to make the two memory states distinguishable more clearly. However, the crystal structure of perovskite-structured materials is far different from that of Si, which is the fundamental material of contemporary memory technology, so the interface of ferroelectric layer and Si substrate shows poor electric properties resulted from the difference of crystal structure. [7] Generally, interfacial SiO_2 layer is formed at the interface, and resulting depolarization field weaken the stability of the bistable polarization states. In addition to that, the electrical bandgap (E_g) of the conventional ferroelectric materials are generally in the range of 3-4 eV, and it forms schottky barrier with height of only ~1 eV. The E_g of conventional ferroelectric materials are relatively smaller compared with the dielectric materials used in the contemporary memory technology, such as SiO_2, Al_2O_3, HfO_2, and ZrO_2. Therefore, relatively large thickness is required for the applications of capacitive layer of charge-based FeRAM, and it might be a barrier to be applied to the capacitive layer of 3-dimensional capacitor structure with technology node of a few tens of nanometers level. [8] Therefore, the new ferroelectric materials which are compatible with Si technology with large E_g is one important topic in ferroelectric memories.

If scaling down of the feature size of the conventional ferroelectric memory is difficult, on the other hand, the increase in the number of memory

states per ferroelectric memory cell could be a viable solution for the scaling problem. There have been many reports on the design and fabrication of multi-level or even analog type ferroelectric memories but no breakthrough has been reported yet. [9-11] Most efforts were concentrated on using a depolarized state as the third memory state in addition to the two spontaneously polarized states with opposite signs. Raiter reported the possibility of using three data signal levels to increase the array storage density from 1 bit per cell to 1.5 bits per cell using three-level FeRAM. [11] As a result, 50% increase in data can be memorized in the same area compared to conventional FeRAM with binary memory states. They suggested that three levels are possible if the depolarized state as well as two polarization states of the ferroelectric material can be used. On the other hand, this approach has a fundamental problem of low reliability and narrow sensing margin for the general charge (or voltage) sense circuitry. Depolarizing a polarized ferroelectric state in FeRAM circuit is not a trivial task. The use of unsaturated ferroelectric polarization can be a possible solution but this also has several problems; the ferroelectric layer with unsaturated polarization is not in a thermodynamically stable state. As a result, the memory state using unsaturated polarization may not be reliable. In addition, the unsaturated polarization state can be achieved more readily from the non-square-like polarization – voltage (P-V) hysteresis loop, but this P-V loop actually decreases the signal margin for the two basic

(saturation) polarization states. The other approach was focused on the circuitry or programming sequence, which can result in a highly improved reliability. [11] Such a radical change in the circuit structure is quite burdensome to the design and may not be compatible with the conventional CMOS technology. Therefore, a novel approach is needed to realize a ferroelectric memory cell with three or even more memory states.

1.2. Objective and chapter overview

The present thesis has two important objectives ferroelectric memories: (1) One is to elucidate the origin of the ferroelectricity in HfO_2-based thin films and to optimize it, and (2) the other is to fabricate a tri-stable memory by a novel mechanism of dividing compensating charges of ferroelectric layer into two interfaces.

Chapter 3 covers the origin and the optimization of ferroelectricity in $Hf_{1-x}Zr_xO_2$ films. The ferroelectricity of HfO_2-based films is believed to result from the formation of non-centrosymmetric $Pbc2_1$ orthorhombic phase (o-phase).[12-16] However, the formation of the o-phase in thin HZO film is not trivial, since it is stable only under certain high-pressure (or anisotropic-strain) circumstances, [17-20] In this dissertation, the origin of the unexpected formation of non-centrosymmetric $Pbc2_1$ o-phase would be explored.

Chapter 4 presents the optimization of ferroelectric properties of HZO by examining the effect of phase evolution by changing film thickness and annealing temperature on the ferroelectric properties of thin films. Even though it is already known that HZO can be ferroelectric when it is in non-centrosymmetric o-phase, the effect of phase evolution on the ferroelectric properties has not yet been reported before.

Chapter 5 reports the effect of forming gas annealing (FGA), which is

inevitable for Si devices to achiece an appropriate performance of transistor, on the ferroelectric properties of HZO films. The effect of FGA was compared with the previous reports on conventional ferroelectrics such as PZT, and the differences between them and the origin of the differences were discussed.

Chapter 6 covers the effect of top electrode (TE) on the ferroelectric properties and endurance of HZO capacitors. HZO films were deposited on TiN bottom electrode (BE), and TiN or RuO_2 TE was used for the electrical characterization. The chemical reaction between reactive top and BE was examined, and the endurance of HZO capacitors was optimized by changing the thickness and annealing temperature of the films.

Chapter 7 deals with the fabrication and characterization of the novel tri-states memory based on ferroelectric-insulator-semiconductor heterojunction. It is different from the previous trial for tri-states memory with an additional depolarized state, and its basic principle is to divide the compensating charges of ferroelectric polarization into two different interfacial layers. The novel tri-states memory was successfully fabricated based on the ferroelectric-insulator-semiconductor structure, and it was also characterized electrically and physically. Its operation principles were also successfully explained based on its electrical and physical properties.

Finally, in chapter 8, the conclusion of the thesis is made.

1.3. References

[1] J. F. Scott, C. A. Araujo, *Science* **246**, 1400 (1989).

[2] J. F. Scott, L. Kammerdiner, M. Parris, S. Traynor, V. Ottenbacher, A. Shawabkeh, and W. F. Oliver, *J. Appl. Phys.* **64**, 787 (1988).

[3] J. F. Scott, H. M. Duiker, P. D. Beale, B. Pouligny, K. Dimmler, M. Parris, D. Butler and S. Eaton, *PhysicaB/C* **150**, 160 (1988).

[4] D. D. Fong, G. B. Stephenson, S. K. Streiffer, J. A. Eastman, O. Auciello, P. H. Fuoss, and C. Thompson, *Science* **304**, 1650 (2004).

[5] M. Stengel, D. Vanderbilt and N. A. Spaldin, *Nat. Mater.* ***8***, 2429 (2009).

[6] C. Lichtensteiger, and J. –M. Triscone, *Phys. Rev. Lett.* **94**, 047603 (2005).

[7] T. P. Ma, *Electr. Dev. Lett.* **23**, 386 (2012)

[8] D. S. Jeong, , R. Thomas, R. S. Katiyar, J. F. Scott, H. Kohlsted, A. Petraru, C. S. Hwang, *Rep. Prog. Phys.* **75**, 076502 (2012).

[9] T. C. MacLeod, T. A. Phillips, and F. D. Ho, *Integr. Ferroelectr.* **89**, 12 (2007).

[10] Y. –H. Xie, Y. –Y. Lin, T. -A. Tang, *Integr. Ferroelectr.* **67**, 263 (2010).

[11] D. Ricinschi, and M. Okuyama, *J. Phys. D: Appl. Phys.* **42**, 085410 (2009).

[12] T. S. Böscke, J. Müller, D. Bräuhaus, U. Schröder, and U. Böttger, *Appl. Phys. Lett.* **99**, 102903 (2011).

[13] J. Müller, U. Schröder, T. S. Böscke, I. Müller, U. Böttger, L. Wilde, J. Sundqvist, M. Lemberger, P. Kücher, T. Mikolajick, and L. Frey, *J. Appl. Phys.* **110**, 114113 (2011).

[14] S. Mueller, J. Mueller, A. Singh, S. Riedel, J. Sundqvist, U. Schroeder, T. Mikolajick, *Adv. Funct. Mater.* **22**, 2412 (2012).

[15] J. Müller, T. S. Böscke, U. Schröder, S. Mueller, D. Bräuhaus, U. Böttger, L. Frey, and T. Mikolajick, *Nano Lett.* **12**, 4318 (2012).

[16] M. H. Park, H. J. Kim, Y. J. Kim, W. Lee, H. K. Kim, and C. S. Hwang, *Appl. Phys. Lett.* 102, 112914 (2013).

[17] J. E. Lowther, J. K. Dewhurst, J. M. Leger, and J. Haines, *Phys. Rev. B* **60**, 14485 (1999).

[18] E. H. Kisi, *J. Am. Ceram. Soc.* 81, 741 (1998).

[19] E. H. Kisi and C. J. Howard, *J. Am. Ceram. Soc.* **72**, 1757 (1989).

[20] C. J. Howard and E. H. Kisi, *J. Am. Ceram. Soc.* **73**, 2828 (1990).

Chapter 2. Literature

2.1. Ferroelectric materials for memory applications

2.1.1. Conventional ferroelectric materials for memory applications

Most of the ferroelectric materials for memory application are based on the perovskite or layered perovskite structure, of which chemical formula has the form of ABO_3. Generally, A-site cation is monovalent or divalent and B-site one is a tetra- or pentavalent. Perovskite structure is based on cubic structure, with A ions at the cube corners, B ions at the body center, and the oxygen ions at the face center when its temperature (T) is higher than curie temperature (T_c), and it is distorted to lower-symmetric structure such as tetragonal, orthorhombic and rhombohedral in some cases when T decreases lower than T_c. Figure 2.1 shows the crystal structure of PZT with cubic structure (Left panel, $T > T_c$) and that with tetragonal structure (Right panel, $T > T_c$), respectively. It should be noted that the cubic perovskite structure cannot be ferroelectric due to its center of symmetry. Among the various ferroelectric materials based on perovskite structure, BTO was the first ferroelectric perovskite to be discovered, and only complex hydrogen-bonded crystals had been known to exhibit ferroelectricity before its discovery. The simple physics of the ferroelectricity in perovskite structured

materials gave physicists an opportunity to study the onset of ferroelectricity from a simple high-symmetric prototype phase for the first time. BTO shows ferroelectric properties below 120 ^{o}C, and it can exist in three ferroelectric phase, such as 4mm tetragonal (5 - 120 ^{o}C), mm orthorhombic (-90 – 5 ^{o}C), and 3m trigonal phase (below -90 ^{o}C). The polar axis of the three phases are [001], [011], and [111], respectively.[1] PZT might be the material that is widely being used by industry today. It has the huge P_r of ~80 μC/cm^2, which is also a strong point for the ferroelectric memory applications. Even in the thin film form, the P_r of PZT is generally 30 – 50 μC/cm^2 with the thickness of a few hundred nanometers. Scott et al. reviewed the researches on ferroelectric memory in United States and western Europe during mid-1970s in their paper entitled “Ferroelectric Memories”, and it can be noted that PZT has been the most important material in ferroelectric memory since the initiating state.[2] However, PZT was suffered from many problems, such as poor endurance, degradation due to hydrogen annealing, poor interface with Si, and environmental issue of Pb, and SBT was suggested for the replacement of PZT, due to its more reliable and lead-free characteristics. Araujo et al. reported that SBT can be fatigue-free even after the electric cycling of 10^{12} times which is larger than that of PZT several order of the magnitude. [3] $BiFeO_3$ (BFO) is another important material with its multiferroic properties which means the coexsistence of ferroelectricity, ferromagnetism, and ferroelecsticity. [4,5] Even though multiferroelectric

phenomena can be found in other materials, but they were far from the real applications due to their temperature limit. [6] The P_r (~50 - 60 μC/cm^2) of thin BFO film was larger than that of bulk BFO almost an order of magnitude, because it exsists in P4mm tetragonal phase in thin film, different from R3c rhombohedral in bulk form. [7] Its antiferromagnetic property also can be found from the magnetic characterizations. [7] Another important application of BFO in memory field is the ferroresistive storage. Choi et al. firstly reported that optical E_g of BFO is only ~2.2 eV, which is smaller compared to that of PZT (~3.5 eV), and it can work as a switchable diode.[8] It means that forward/reverse bias polarity can be controlled by switching ferroelectric polarizations. After the first report by Choi et al., Jiang et al. reported that the bistable diode current can be as large as 5.4 A/cm^2, which is the largest current reported in resistive memory based on the ferroelectricity from the author's knowledge. [9] The detailed operation principles of the switchable diode would be dealed with in section 2.2.3. Poly(vinylidene fluoride-trifluoroehylene) might be the most important organic ferroelectric material. [10] Its P_r is large enough for memory applications, but its operation voltage and speed is not so good as that of inorganic ferroelectrics. Therefore, the research on this attractive organic ferroelectric material is generally focused on its flexible and transparent characteristics. [11]

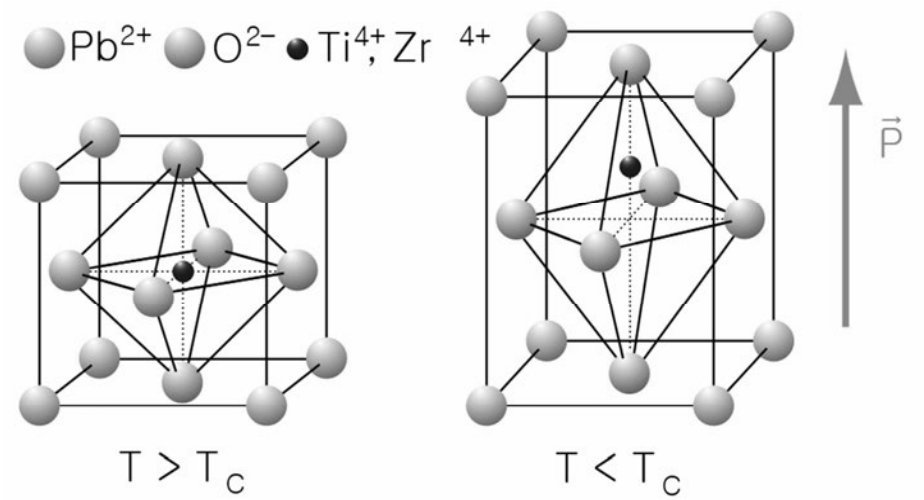


Figure 2.1. The crystal structure of $Pb(Zr,Ti)O_3$ with cubic structure (Left panel, $T>T_c$) and that with tetragonal structure (Right panel, $T>T_c$), respectively

2.1.2. Ferroelectricity in thin HfO_2-based films

HfO_2 is well-known material especially in memory field due to its compatibility with Si and relatively high dielectric constant ($\varepsilon_{r,}$ ~17-20 for monoclinic phase (m-phase) and ~35-40 for tetragonal phase (t-phase)) with large E_g (~5 eV). Pure HfO_2 exists in m-phase with a space group of $P2_1/c$ at room temperature and 1 atm, and transform into t- and cubic phase at the transition temperature of 2050 K and 2803 K, respectively. However, it was reported that doping with appropriate dopants such as Si, Al, Zr, Y, and Gd can result in the stabilization of meta-stable t- or cubic phase even at room temperature.[12-16] Lee et al. reported that doping of appropriate dopants can lower the free energy of the metastable phases than stable m-phase by their first-principle work.[17] In 2011, it was firstly reported by Böscke et al. that ferroelectric properties can be found in Si-doped HfO_2 with a doping concentration of ~3%. Figure 2.2 shows the polarization-electric field curves of 8.5-nm-thick Si-doped HfO_2 films with various doping concentration. It seems that the P_r of Si-doped HfO_2 was smaller than that of PZT, it was even larger compared with PZT films with equivalent thickness. The coercive field (E_c) of Si-doped HfO_2 was ~1MV/cm, and it is larger than PZT thin films about one order of magnitude. The ferroelectric properties of Si-doped were strongly influenced by the doping concentration of Si dopant, and it changes to antiferroelectrics with the concentration of ~4.3%. The doping

concentration of ~3% is smaller than that for the stabilization of t-phase of HfO_2. [12] Therefore, it seems that the ferroelectric phase occurs at the morphotropic phase boundary of m- and t- phase of HfO_2. However, the ferroelectricity can be hardly expected based on the above-mentioned polymorphs of HfO_2, because m-, tt-, and cubic phase are all centrosymmetric which prevents occurrence of ferroelectricity. Therefore, they argued that the formation of the non-centrosymmetric o-phase with a space group of $Pbc2_1$ is the origin of the unexpected ferroelectricity. [12] $Pbc2_1$ phase is reported for the case of the Mg-stabilized ZrO_2 by Kisi and Howard, even though they did not report the ferroelectricity in the structure.[18-20] Because HfO_2 has a structure almost identical with that of ZrO_2, it is reasonable that the the $Pbc2_1$ phase can be formed with certain condition. However, it is very challenging to distinguish o-phase from other polymorphs, expecially for the case of t-phase. Even worse, the ferroelectricity occurs for the case of ~10-nm-thick or thinner films, which is too thin for the structural analysis using X-ray diffraction (XRD). However, Mueller et al. successed in the phase identification of the o-phase using the diffraction spectra with 2θ range of 80-90° for their 16-nm-thick Al-doped HfO_2 films. [13] Figure 2.3 shows the GI-XRD spectra of Al-doped HfO_2 films with various doping concentration. As seen in the figure, diffraction spectra of 80 – 90° changes dramatically with increasing doping concentration. The ferroelectric properties were also well-matched with the

structural analysis, and figure 2.4 shows the P-E curves with various doping and annealing conditions. P_r of Al-doped HfO_2 was ~6 $\mu C/cm^2$ at best, which is smaller compared to that of Si-doped HfO_2.[13] Effect of doping concentration agrees with the previous results of Si-doped HfO_2 qualitatively, and doping concentration of ~7% resulted in the largest polarization. Müller et al. reported the ferroelectricity in simple binary ZrO_2 and HfO_2.[14] This system can be more beneficial compared to other dopants, because Zr is almost chemically-equivalent with Hf. Therefore, ZrO_2 and HfO_2 have same crystal structure and can form solid-solution for the whole range of the composition. Figure 2.5 (a) shows P-E (upper panel) and ε_r-E curves (lower panel) of $Hf_{1-x}Zr_xO_2$ films with various doping concentrations. The P_r of HZO film can be as large as 17 $\mu C/cm^2$ with the doping concentration of 50 %, and it also shows the antiferroelectricity with increasing doping concentration of Zr, even for the case of pure ZrO_2. Compared to other dopants, $Hf_{1-x}Zr_xO_2$ can have robust ferroelectricity in a much mider region of concentration, which can be beneficial for the mass production. In addition to that, its ALD process using the TEMA-Hf and TEMA-Zr as precursors for HfO_2 and ZrO_2 is easy to be controlled. Their growth rate is also almost equivalent, and the composition can be easily controlled simply by changing the ALD cycle ratio of HfO_2 and ZrO_2. Crystallization temperature of HZO is also the lowest (~450 ^oC) among the HfO_2 films with various dopants, so it can be relatively free from the electrical degradation

resulted from the thermal budget during annealing process. Therefore, Zr might be one of the most promising dopants for the future applications of the ferroelectric HfO_2 films. Dopants larger than Hf also can result in the ferroelectric phase of HfO_2. Olsen et al. reported that the ferroelectricity of Y-doped HfO_2, whose P_r is as large as ~10 $\mu C/cm^2$, can be seen with doping concentration of 2 %.[15] Different from the previous results, Y-doped HfO_2 was deposited using RF magnetron sputtering, not by ALD. Figure 2.6 shows P-V curves of Y-doped HfO_2 with various doping concentration. Mueller et al. reported the ferroelectricity with the P_r of 12 $\mu C/cm^2$ in Gd-doped HfO_2 thin films.[16] Figure 2.7 shows P-V characteristics of the as-grown and field-cycled Gd-doped HfO_2 films.

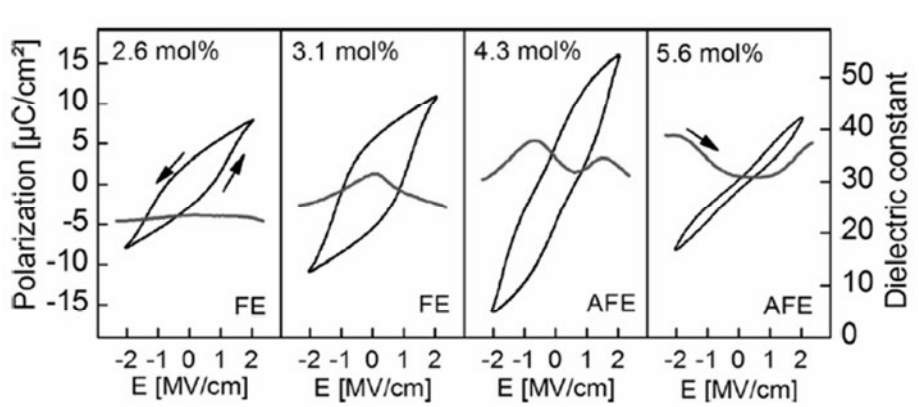


Figure 2.2. Polarization hystereses (black) and AC C-V characteristics (thick red) of a set of "capped" MIM capacitors with 8.5 nm insulator thickness. The shape of the polarization loops changes from ferroelectricto antiferroelectric with increased SiO_2 admixture. This is reflected in one or two peaks in the AC C-V sweeps, respectively.[12]

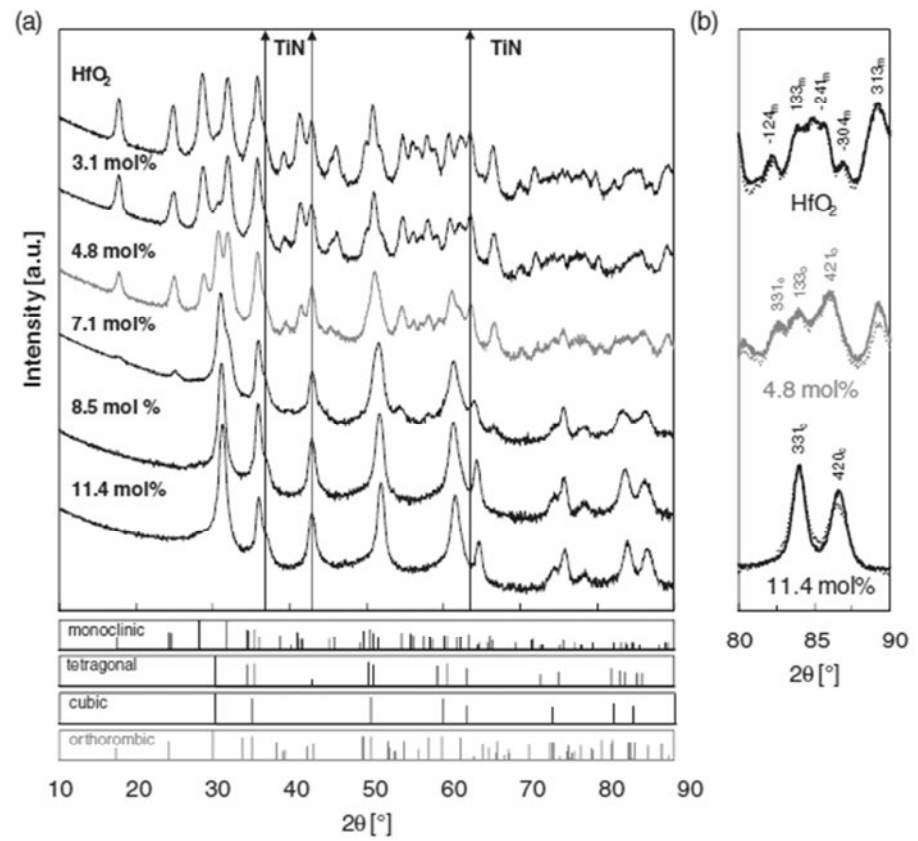


Figure 2.3. (a) GAXRD diffractograms for PMA samples having different aluminium concentrations. A monoclinic-to-cubic phase transition is clearly visible for increasing aluminium content. The powder diffraction patterns as well as the calculated orthorhombic $Pbc2_1$ reference pattern are shown below the diffractograms. The composition which possesses the purest ferroelectric properties is highlighted in blue. (b) Enlarged 2θ scans from 80 ° to 90 ° for paraelectric HfO_2 containing no aluminium, ferroelectric HfO_2 containing 4.8 mol% aluminium, and, again, paraelectric HfO_2 containing 11.8 mol% aluminium. The diffractogram of the ferroelectric composition shows a triplet which would not be expected for monoclinic, tetragonal, or cubic phases. The dotted lines show results for PDA samples of the same composition. [13]

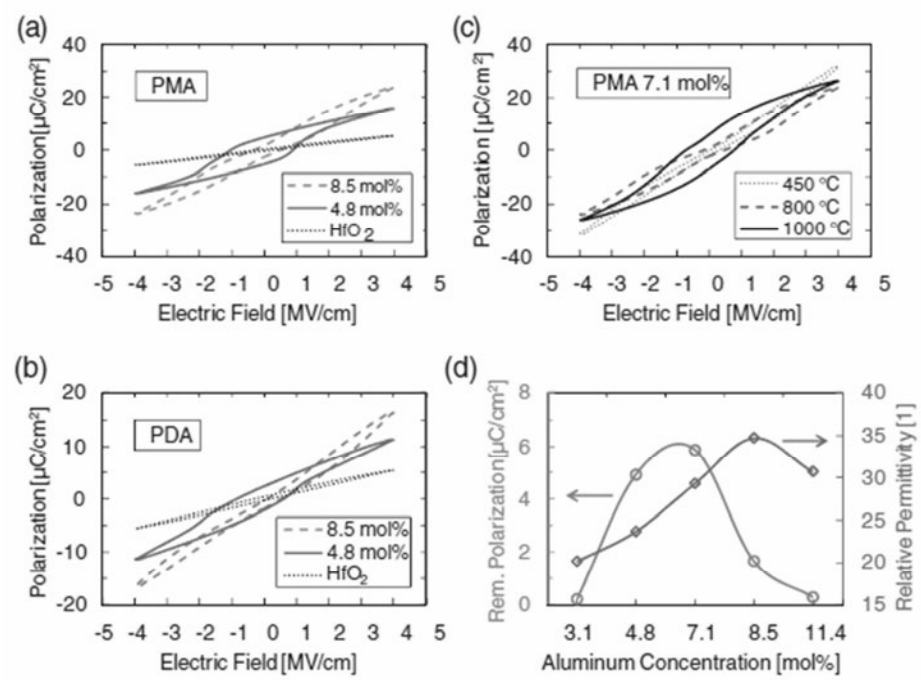


Figure 2.4. (a) Polarization hysteresis for PMA samples annealed at 1000 °C for 20s. Decreasing aluminium concentration yields an antiferroelectric-toferroelectric transition whereas the pure hafnium oxide is paraelectric, as expected. (b) Polarization hysteresis for PDA samples annealed at 1000 °C for 20 s. The same antiferroelectric-to-ferroelectric transition as for the PMA samples can be observed but the remanent polarization is signifi cantly lower. (c) Polarization hysteresis of a HfO_2 MIM capacitor with 7.1 mol% of incorporated aluminium for different annealing temperatures. A transition towards ferroelectric behavior can be observed if higher temperatures are used for the PMA. (d) Remanent polarization and relative permittivity versus amount of incorporated aluminium for PMA capacitors annealed at 1000 °C for 20 s. [13]

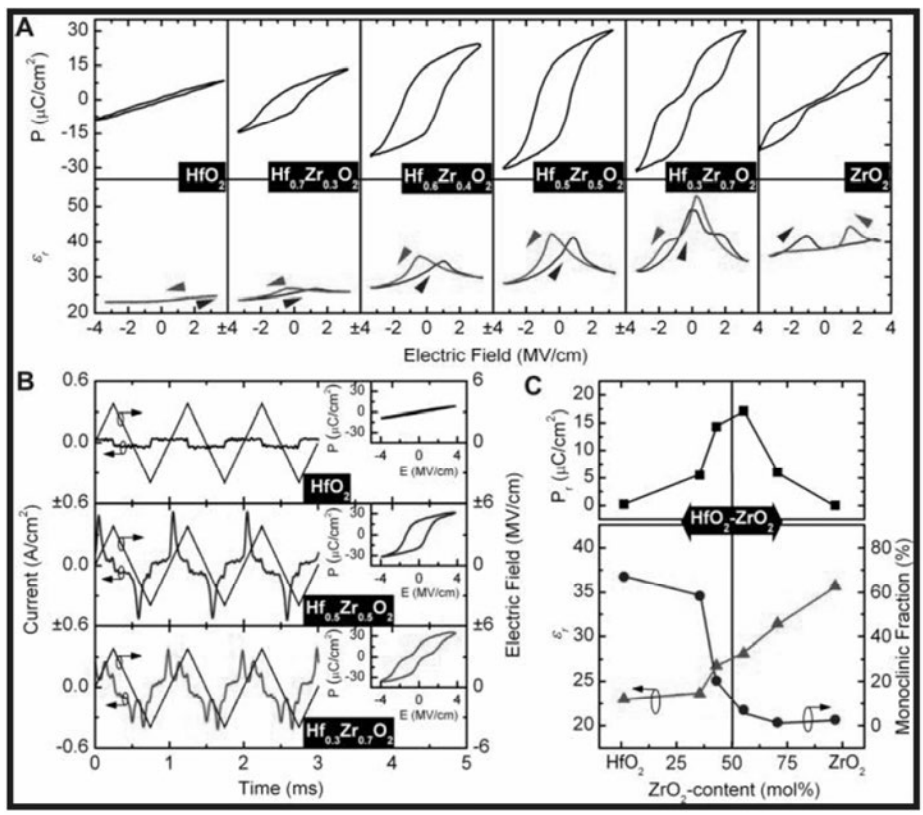


Figure 2.5. (A) P-V curve at 1 kHz and small signal CV hysteresis at 10 kHz (50 mV level) of 9 nm thin HfO_2–ZrO_2 based metal–insulator–metal capacitors at room temperature. An evolution from paraelectric HfO_2 to ferroelectric HfO_2–ZrO_2 to an antiferroelectric-like behavior in ZrO_2 can be observed in PV as well as in C-V characteristics. (B) Current response to a triangular voltage excitation reveals polarization switching to be clearly separable from leakage current contributions at high fields. (C) Remanent polarization, dielectric constant, and monoclinic phase fraction in the HfO_2–ZrO_2 solid solution with respect to the mixing ratio of the oxides. With increasing ZrO_2 content the dielectric constant increases due to a reduction in monoclinic phase fraction, whereas the remanent polarization is maximized in the transition region. [14]

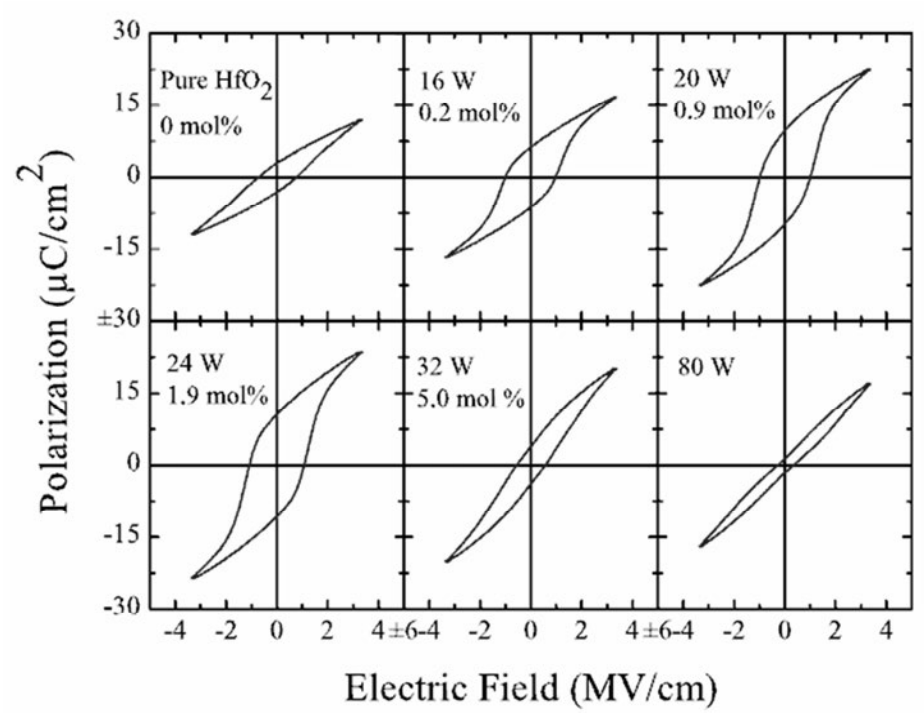


Figure 2.6. Dependence of ferroelectric hysteresis properties on the concentration of yttrium dopant. For sputtering powers in the range of 20 W, clear ferroelectric hysteresis is visible. For lower and higher doping concentrations, a transition to paraelectric behaviour occurs. [15]

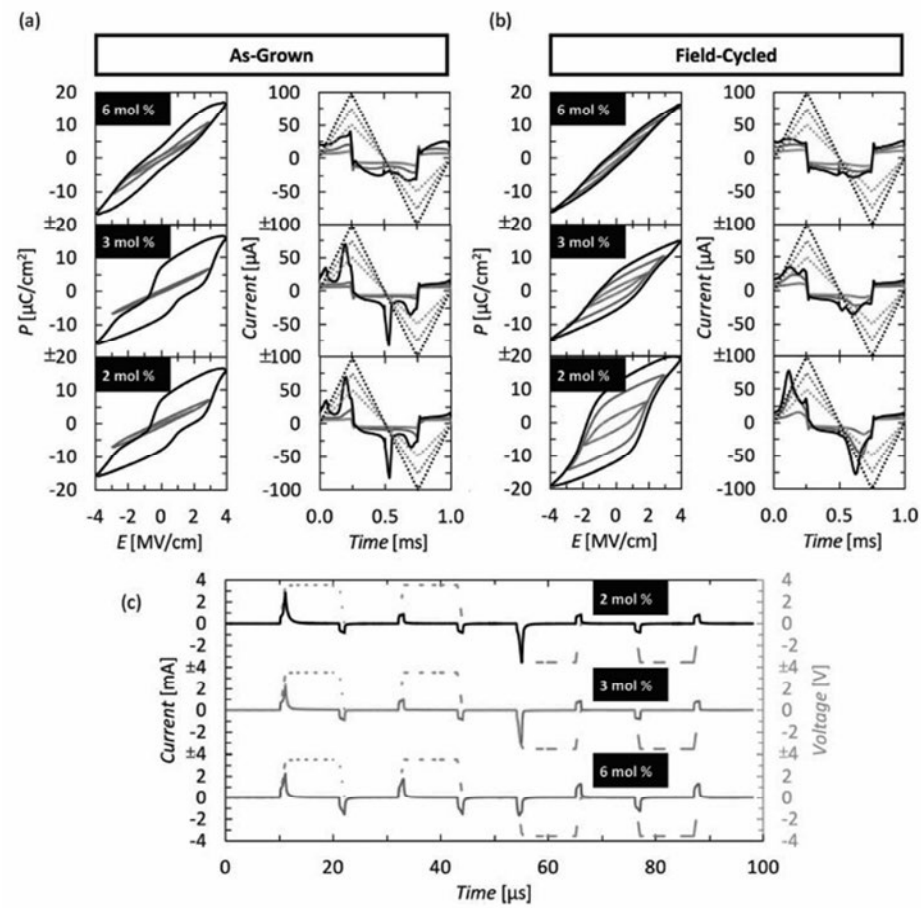


Figure 2.7. (a) Polarization and (b) corresponding current-voltage measurements for Gd: HfO_2 thin films. Significant effects of field cycling are visible, especially for 3 mol% and 2 mol% of Gd. Initially, two coercive voltages coexist, which are merged into one after 5000 field cycles at 3 MV/cm. (c) PUND measurements for field-cycled films show increased current responses when ferroelectric switching occurs (1st and 3rd pulse). Almost purely dielectric responses are visible for the sample doped with 6 mol% Gd. [16]

2.2. Ferroelectric devices for memory applications

2.2.1. Conventional ferroelectric random access memory

Since ferroelecticity was first discovered in 1921,[1,21,22] it has been regarded as a promising candidate for the memory application due to the bistable polarization. There have been many devices based on the ferroelecticity such as FeRAM, ferroelectric field effect transistor (FeFET), and ferroresistive storage. Among them, FeRAM has the longest history of research. The idea of ferroelectric memories was firstly presented by the researchers in Bell Laboratory in 1955. [2] Its device operation and structure are based on the principle of dynamic random access memory (DRAM) basically. FeRAM show attractive features such as high operation speed, low power consumption, nonvolatility, clear physical mechanism, and good reliability.[2] However, FeRAM suffer from the large size of its memory unit as large as $32F^2$, in which F is the state-of-the-art feature size of memory node. FeRAM consists of at least one transistor and one capacitor, and the dielectric layer of the capacitor is a ferroelectric film. In addition to that, FeRAM needs a plate line due to its operation principle which cannot be found for the case of DRAM. The possible smallest cell size without 3-D integration is $4F^2$, and that of DRAM is 6 - 8 F^2. Therefore, FeRAM seems to be not appropriate for the high-density memory compared to the other

memories such as resistive random access memory (ReRAM), phase change memory (PcRAM), and spin-transfer-torque magnetic random access memory (STT-MRAM). Therefore, researches on FeRAM are moving to FeFET effect transistor or ferroresistive storage, which would be dealed with in section 2.2.2 and 2.2.3, respectively.

2.2.2. Ferroelectric field effect transistor

FeFET was fabricated firstly by Wu in 1974, and has the history of research only for 40 years.[23] The structure of FeFET is very simple; the oxide layer of metal-oxide-semiconductor field effect transistor (MOSFET) is replaced by ferroelectric layer. In addition to that, its operation principle is also simple; the inversion/depletion or accumulation/depletion of carriers in semiconducting channel is controlled by the polarity of ferroelectric polarization. Physics of FeFET is successfully reported by Miller and McWhorter. [24] Different from the conventional FeRAM, a unit cell of FeFET consists of only one transistor in principle, so the cell size can be reduced to $4F^2$. It means that FeFET can be relatively free from the scaling issue compared to FeRAM. However, the most serious problem of FeFET is the poor retention properties. When ferroelectric polarization is compensated by sufficient electrons or holes in metal electrode, ferroelectrics can have good retention properties. However, for the case of FeFET, one side of ferroelectric polarization should be compensated by semiconducting layer, so there should exist the depolarization field resulted from imperfect compensation.[25] Even worse, perovskite-structured materials form poor interface with Si in many cases, and the interfacial dead layer is formed at the ferroelectric/Si interface. To overcome the problem, insertion of the dielectric layer such as HfO_2 and HfAlO between ferroelectric and Si, and it

improved the retention properties.[26,27] The best retention property of FeFET is only a few month level, which needs to be improved to meet the required retention of 10 years for nonvolatile memory. Another approach is to change the semiconducting channel material from Si to others, such as oxide semiconductor [11,28-33], pentacene[34-36], graphene[37-42], carbon nanotube[43,44], and semiconducting polymer[45-49]. Kato et al. reported the FeFET using ZnO as a channel layer, and the relatively better interface between PZT and ZnO result in the improvement retention properties, whose I_{on}/I_{off} ratio is expected to be as large as ~10^4 after 10 years from the extrapolation. [28] Even with the channel width of 60 nm, the FeFET with ferroelectric PZT and ZnO channel shows robust reliability. [30] Liao et al. reported the fabrication and characterization of FeFET with ZnO nanowire whose retention property was a few hundreds seconds level. [32] Sohn et al. reported a room temperature processed FeFET with ZnO nanowire, where the nanowire channel is coated with ferroelectric nanoparticles. [33] The retention properties in the report by Sohn et al. improved to ~10^4 s level, but it is still far from the requirement of 10 years. Yoon et al. reported a fully transparent non-volatile memory thin-film transistor, whose gate stack is composed of organic ferroelectric P(VDF-TrFE) and oxide semiconducting Al-Zn-Sn-O layers, in which thin Al_2O_3 is introduced between two layers. [11] However, its retention properties were only ~10^2 s level, and yet to be improved. Carbon-based materials such as CNT, pentacene, and graphene

are also condidered as a promising candidate for the channel material of FeFET. Son et al. reported field-effect nonvolatile memory device made of a ferroelectric copolymer gate nanodot and a single-walled carbon nanotube with the robust retention properties up to ~10^6 s.[34] Raghavan et al. reported a FeFET with a ferroelectric P(VDF-TrFE) and a graphene channel, and its retention property was ~10^5 s level. In fact, the role of graphene as a semiconducting material is controversial, because its E_g is zero in principal when it exists in a single-layer structure. [38] Even worse, an ideal graphene is very hard to form chemical bonds with other materials. The FeFET with pentacene channel reported by Kang et al. was also ~10^4 s level. [35] Semiconducting polymers, such as bisalkoxy-substituted poly(p-phenylene vinylene) and poly(methylmethacrylate) are also candidate for the new channel materials, and their reported retention properties were all 10^4 s level. [45,47]

Researches on FeFET are still going on not only in universities and laboratories but also in industry, especially in Japan. The most industry-friendly researches on FeFET might be chain FeRAM,[50-55] oxide memory transistor (OxiM) [29-31], FeNAND[56-59], and HfO_2-based FeFET.[60,61] The chain FeRAM architecture has been proposed firstly in 1997 by Takahima et al., and the concept of chain FeRAM is depicted in figure 2.9. [50] Applications of chain FeRAM to solid-state drive (SSD) and hard-disk drive (HDD) and their system performance improvements has been

demonstrated up to 128Mb size. [55] Unit cell of FeNAND firstly suggested in 2008 with SBT/HfAlO stacked gate, and is thought to be a candidate for the replacement of flash memory.[56] Takashima et al. reported that the hard disk drive (HDD) performance could be improved by nonvolatile FeRAM cache.[59] An unit cell of OxiM has a NOR or NAND-type memory cell which consists of a FeTFT and a switch TFT, and its cell size is $6F^2$.(See figure 2.10) The OxiM exhibited a high ON/OFF ratio in drain current of more than 10^5, and data retention measurements of the memory cell showed no significant change in binary states up to the retention time of 10^4 s. [30] The operation principle of the FeNAND is similar to that of a NAND flash memory composed of floating-gatetype FETs (See figure 2.11), but the FeNAND has such advantages that the "write" voltage is lower (7.5 V) and the "rewrite" endurance is higher (10^8 cycles) than those in the NAND flash. Operation of a 64 kbit cell array has been reported.[59] FeFET with Si-doped HfO_2 was firtly reported in 2012 by Müller et al. with poly-Si/TiN/Si:HfO_2/SiO_2/Si gate stack.[60,61] Its switching speeds, limited only by the measurement setup, down to 20 ns were observed with a memory window of 1.2 V. The stable memory window was demonstrated after 17 days, and a simple linear extrapolation of retention data predicts a residual memory window of 620 mV after ten years as seen in figure 2.12.

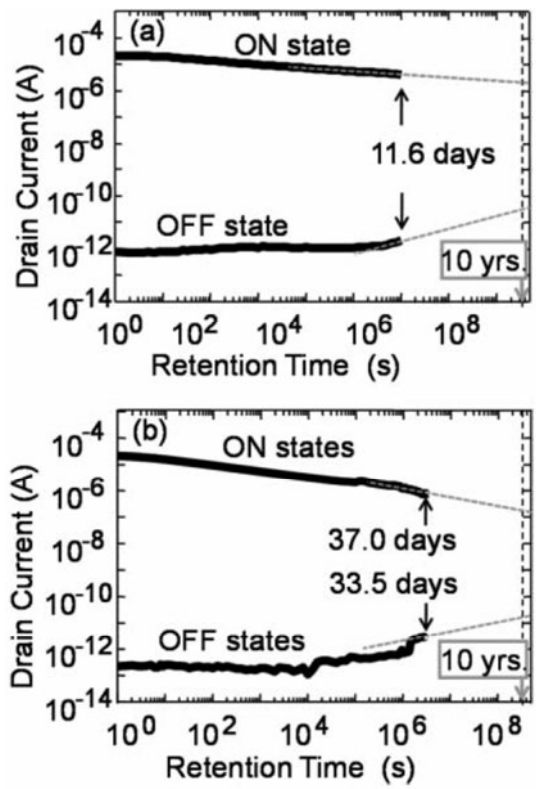


Figure 2.8. Retention characteristics of (a) Pt/SBT/Hf-Al-O/Si FeFETs developed in 2002 and (b) a self-aligned gate FeFET with equivalent gate stack. [26,27]

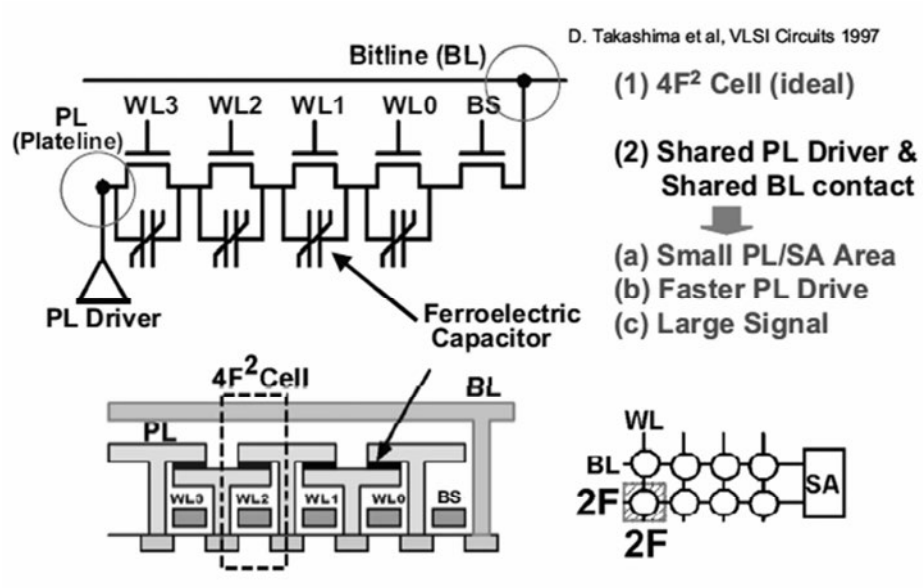


Figure 2.9. Concept of chain FeRAM. [55]

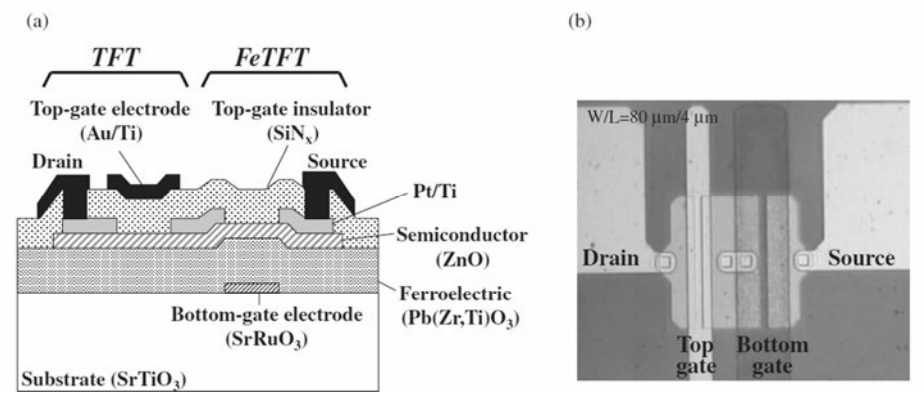


Figure 2.10. (a) Schematic illustration and (b) top view of a composite oxide memory cell composed of a FeTFT and a TFT (FeNOR) [29]

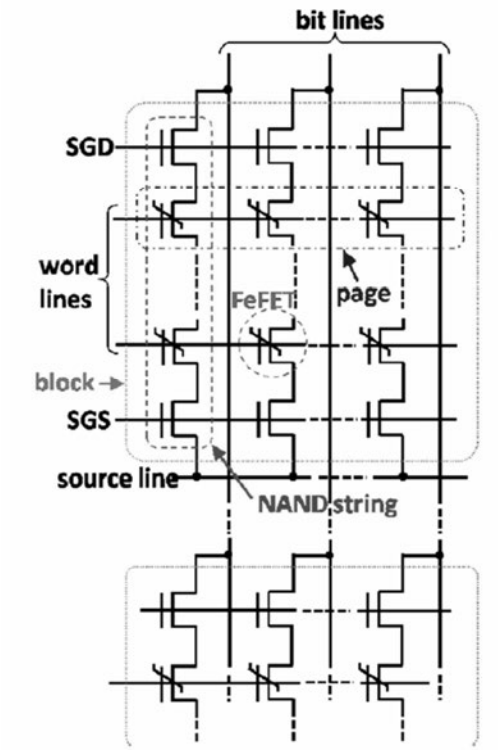


Figure 2.11. Fe-NAND flash memory cell array including NAND strings, word lines, bit lines, pages and blocks. [57]

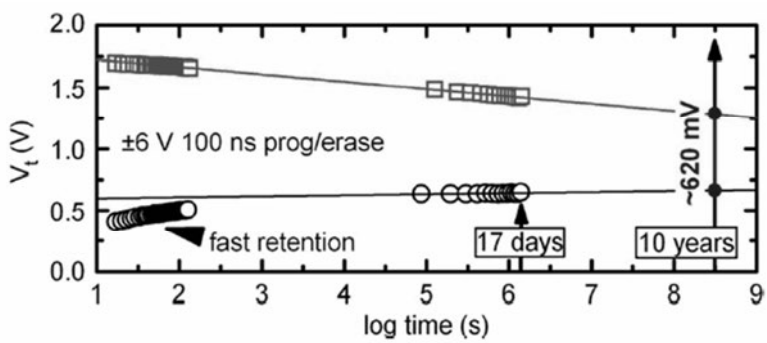


Figure 2.12. Retention of a Si : HfO_2-based FeFET. Despite an initially fast retention loss, extrapolation yields an MW of 620 mV after ten years. [60]

2.2.3. Ferroresistive storage

Ferroresistive storage is a relatively new device compared to other ferroelectric memories such as FeRAM and FeFET, and is a resistance-based memory which can be appropriate for the scaling of the memory. The basic concept of the ferroresistive storage is very simple; the resistance through ferroelectrc single layer or stacked structure with ferroelectric layer is controlled by the P_r of the ferroelectric layer. From the author's lnowledge, the first experimental work on the current hysteresis controlled by the ferroelectric polarization was reported by Blom et al. in 1994. [62] They first report the current hysteresis of their Au/$PbTiO_3$/$LaSrCoO_3$ capacitor, and figure 2.13 shows the resistive hysteresis by them. The resistive hysteresis could be explained successfully by the effecr of P_r. The conduction mechanism through the ferroelectric layer can be categorized into two groups according to the conduction mechanism; the tunneling current and the band conduction. The former concept is well-known as ferroelectric tunnel junction (FTJ), and it was formulated in 1971 by Esaki et al..[63] Figure 2.14 shows the schematic diagram of a FTJ, and there are three mechanisms under debate for the origin of the current hysteresis: (1) electrostatic effect, (2) interface effect, and (3) strain effect.[64] Because the tunneling conduction large enough for sensing is essential for FTJ, it needs a ultra-thin ferroelectric layer with a thickness of a few nanometers. However,

it is very challenging to fabricate such a thin ferroelectric film with robust P_r, sufficient uniformity, and low defect level. Therefore, FTJ is still far from the real application in the memory industry, and most of the academic research is based on the scanning probe microscope. From the author's knowledge, the highest ratio of off-state resistance to on-state one (R_{off}/R_{on}) is ~10^3. [65,66] Figure 2.15 shows the direct evidence for ferroelectricity-related giant TER with ultrathin strained BTO films and corresponding resistance profiles of the poled area reported by Garcia et al..[65] Chanthbouala et al. firstly reported the solid-state memory based on FTJ without scanning probe miscoscope. [67] R_{off}/R_{on} at room temperature was slightly less than 10^2, it can be electrically-cycled more than 900 times. (See figure 2.16)

General ferroelectric materials, such as PZT, SBT, and BTO, have a electric E_g of 3.3 – 3.7 eV, and are considered as wide E_g semiconductors. Therefore, increasing the on-current is one of the challenges in the ferroresistive storage based on the band conduction. Meyer and Waser suggested the mechanism of the ferroresistive storage based on band conduction in 2005. [68] They dealed with metal-ferroelectric-metal (MFM) and metal-ferroelectric-semiconductor (MFS) structure. For the case of MFM structure, nonferroelectric interfacial layer can be an origin of the current hysteresis. [69] Blom et al. attributed the resistance change to a polarization and field-dependent ε_r. [62] The latter leads to different screening lengths in the

ferroelectric. As a result, different profiles of the inner electric potential and different local conductivities across the film give rise to a polarization dependent conductivity. For the case of MFS capacitor, the screening of the polarization charge at the ferroelectric/semiconductor interface is less efficient as compared to a metal electrode. An electric field penetrates into the semiconductor causing a band bending at the near-interface region. The electric field can be also influenced by the ferroelectric polarization, and can be the origin of the current hysteresis. Voora et al. reported the current hysteresis of their Pt/ZnO/BTO/Pt stacked capacitor, and it can be explained by the change of the depletion width of semiconducting ZnO layer. [70]. Use of the semiconducting ferroelectric, such as BFO, is also a good candidate for the ferroresistive hysteresis with increased on-current. The switchable ferroelectric diode using BFO was firstly suggested by Choi et al. in 2009. [71] Figure 2.17 shows the switching diode behavior of BFO films with switching polarization and its mechanism. Jiang et al. increased the on-current of BFO switchable diode as large as 5.4 A/cm^2 as seen in figure 2.18. [72]

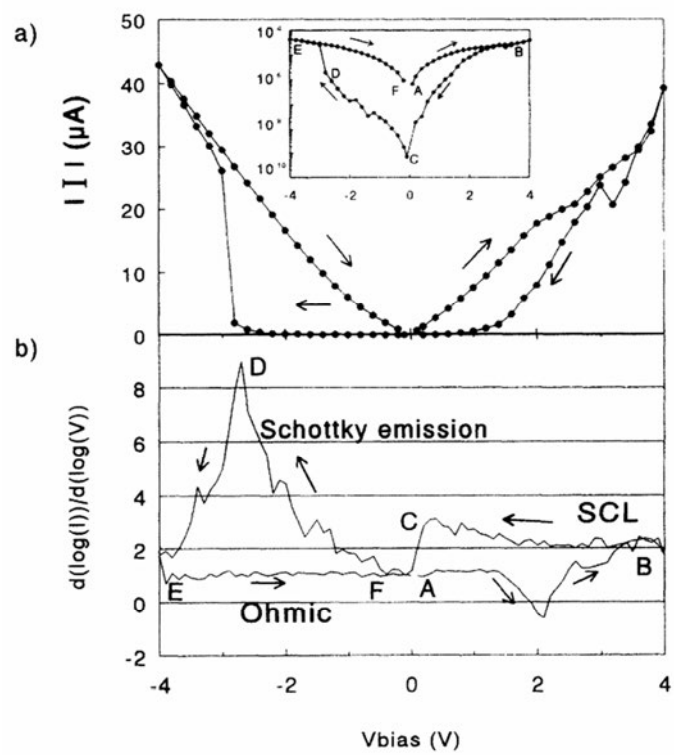


Figure 2.13. dc current-voltage (I-V) characteristics (a) and slope of the log(l)-log(V) curve (b), indicating the conduction mechanism through the 0.2 p,m PbTi03 film for a voltage sweep from 0 → 4 → -4 → 0 V. The inset (a) shows the I-V characteristics on a logarithmic scale. Before the measurement was started the polarization was set to $-P_r$ by applying a dc bias of -10 V and the structure was switched into the open state, characterized by Ohmic conduction. With increasing positive bias (AB) the conductivity decreases and the structure exhibits an asymmetric Schottky-like I-V behavior (BCD) In the closed sta.te (BC) the current for positive bias is dominated by space-chargelimited conduction, due to the increased depletion of the film. For negative bias (CD) the large reverse-biased barrier of the Au contact gives rise to Schottky barrier controlled conduction. After exceeding the switching voltage (D) the conduction increases with 2 orders of magnitude and the I-V characteristic of this open state (FF) is symmetric and again Ohmic. [62]

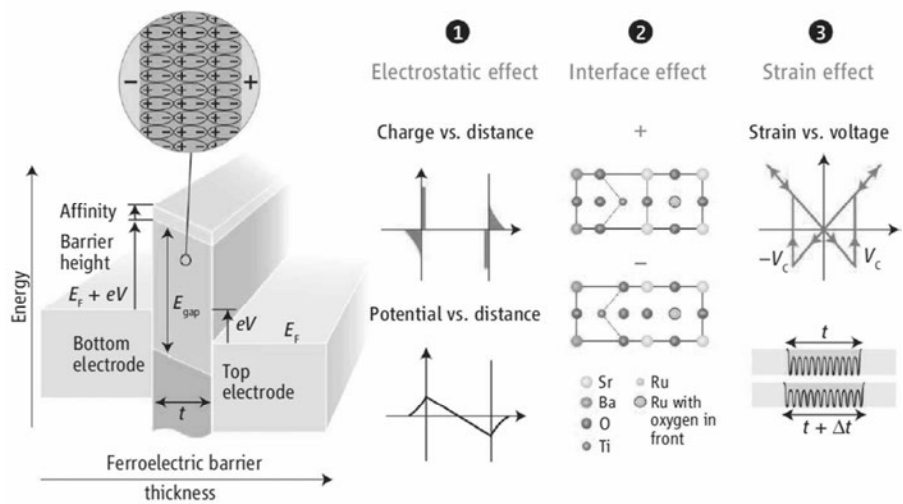


Figure 2.14. Schematic diagram of a tunnel junction, which consists of two electrodes separated by a nanometer-thick ferroelectric barrier layer. (E gap is the energy gap. E_F is the Fermi energy, V is the applied voltage, V_c is the coercive voltage, t is the barrier thickness, and Δt is the thickness variation under an applied field. [64]

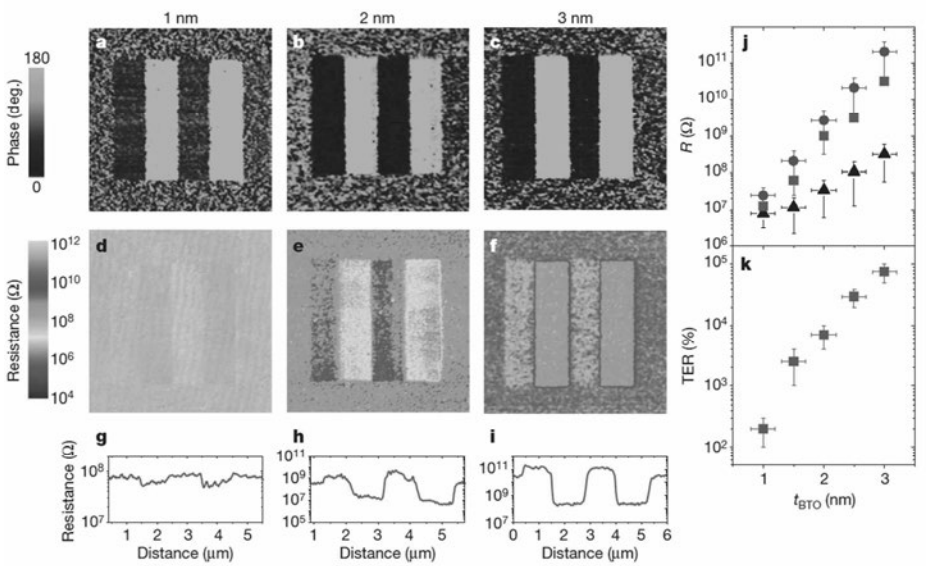


Figure 2.15. Direct evidence for ferroelectricity-related giant TER with ultrathin strained BTO films. **a–f**, Parallel PFM phase image (**a–c**) and CTAFM resistance mapping (**d–f**) of four written ferroelectric stripes (134 mm^2) for BTO films 1, 2 and 3nm thick. **g–i**, Corresponding resistance profiles of the poled area. **j**, Thickness dependence of the resistance (R) of unpoled (red squares), and positively (black triangles) and negatively (blue circles) poled, regions. An exponential increase with t_{BTO} is found, as expected for direct tunnelling. **k**, The TER also increases exponentially with t_{BTO}, reaching ~75,000% for the 3-nm film. In **j** and **k**, vertical error bars correspond to the standard deviation of the resistance distribution over selected areas (and corresponding TER variations), and the horizontal error bars to the thickness uncertainty from growth calibrations. [65]

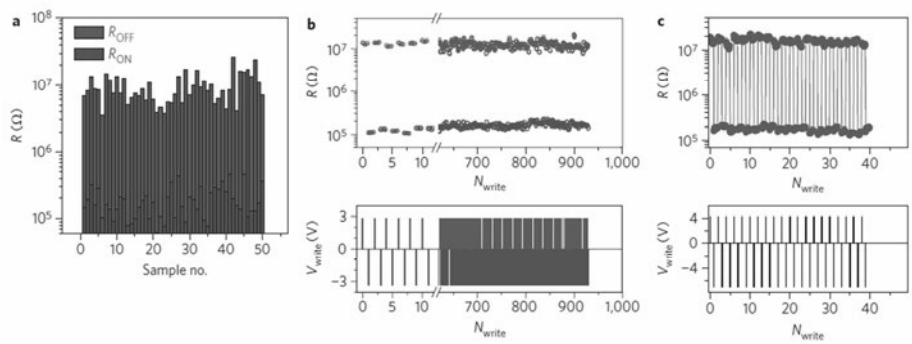


Figure 2.16. Reproducible, fast and reversible switching. (a) ON and OFF resistance states measured after applying 100 ms voltage pulses to 50 different junctions. Average OFF/ON ratio is 64 (range, 15–220). (b) Reversible resistance switching between ON and OFF resistance states of a typical junction for more than 900 cycles (five resistance measurements are carried out at V_{read} = 100 mV between each 100 ms voltage pulse of +2.9 V and -3.4 V). (c) OFF/ON resistance switching of a typical device measured at V_{read} = 100 mV after applying 10 ns voltage pulses. [67]

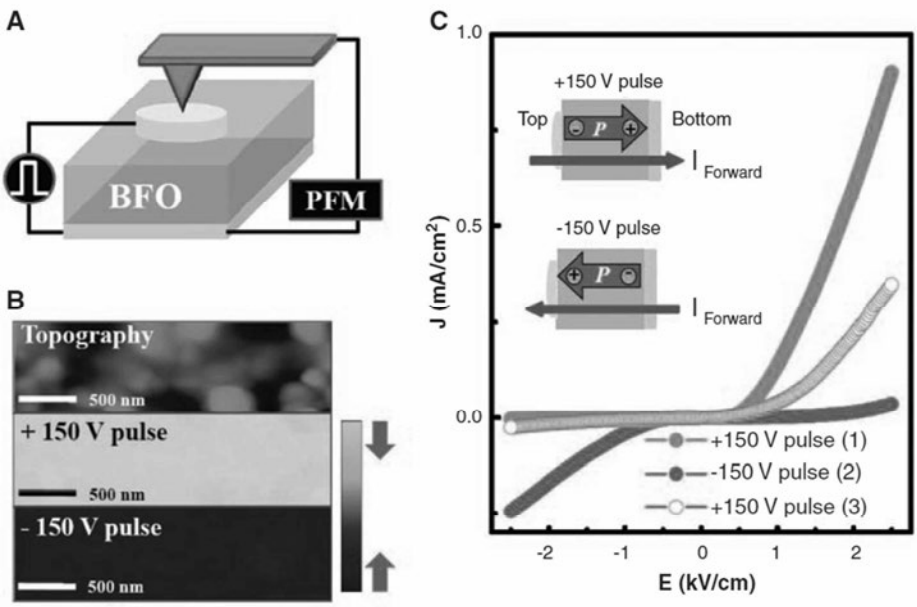


Figure 2.17. (A) Sketch of the setup for the simultaneous PFM and J(E) measurements on Ag/BFO/Ag. One hundred electric pulses with ±150 V (E = 17 kV/cm) and a duration of 0.01 s were used to flip electric polarization. J(E) was measured up to E = 2.5 kV/cm, and ac voltage of 1 V_{rms} and 17 kHz was used for PFM. (B) Topography image and out-of-plane PFM images after ±150-V pulses. The PFM signal is color-scaled. These images show that +150-V pulses induce a homogeneous state with downward out-of-plane polarization, and –150-V pulses induce a homogeneous state with upward polarization. (C) J(E) curves of BFO3 after +150-V, –150-V. and +150-V pulses, in sequence. The diode forward and reverse directions switch when the direction of out-of-plane polarization (P) is reversed by ±150-V pulses. The diode forward direction turns out to be the same as the direction of electric pulses used for polarization flipping. [71]

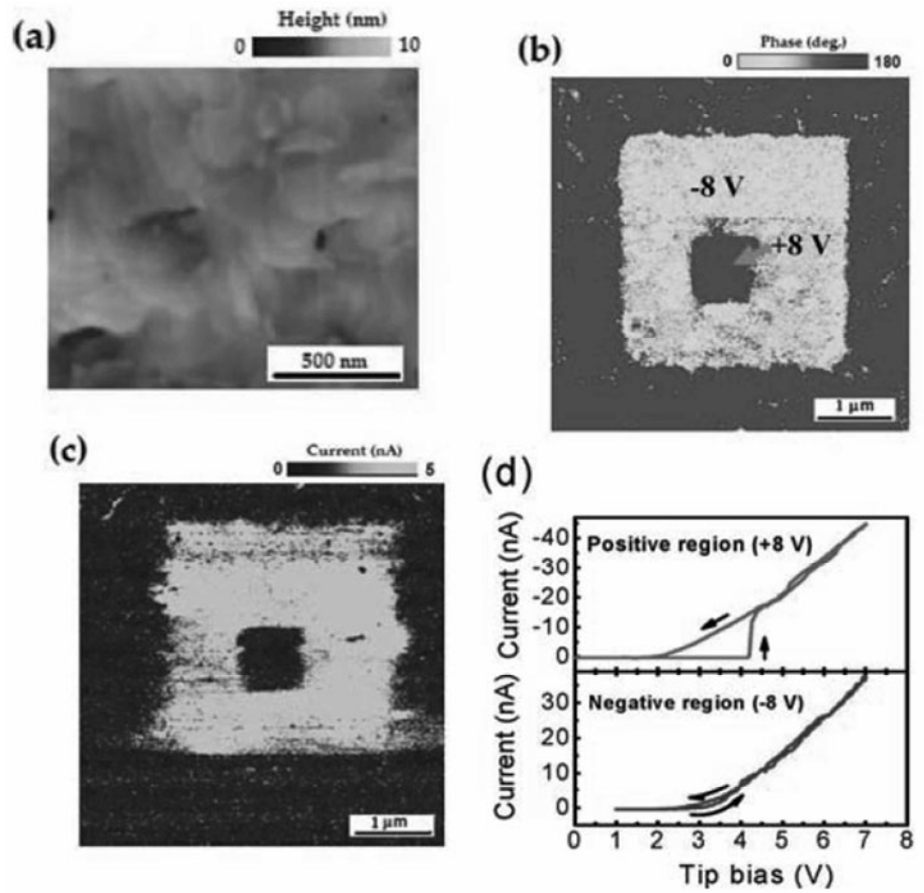


Figure 2.18. Local polarization and diode current for BFO capacitor. (a) AFM image of the fi lm topography. (b) Piezoelectric phase image of original preferred polarization patterns (downward) switched upward through PFM tip scanning of the fi lm surface at –8 V within a square area of $3 \times 3\ \mu m^2$. After that, the polarization in the center $1 \times 1\ \mu m^2$ area is scanned downward at + 8 V. (c) The diode current mapping at –3 V acquired in the same region as in (b). (d) The forward and backward voltage sweeping of the diode current within the positively and negatively polarized regions in (b). [72]

2.3. References

[1] M. E. Lines and A. M. Glass, "Principles and applications of ferroelectrics and related materials", Oxford, New York, USA (1977).

[2] J. F. Scott and C. A. P. de Araujo, *Science* **246**, 1400 (1989).

[3] C. A. P. de Araujo, J. D. Cuchiaro, L. D. McMillan, M. C. Scott, and J. F. Scott, *Nature* **374**, 627 (1995).

[4] E. K. H. Salje, Phase Transitions in Ferroelastic and Co-elastic Crystals (Cambridge Univ. Press, Cambridge, 1990).

[5] G. A. Smolenskii, I. Chupis, *Sov. Phys. Usp.* **25**, 475 (1982).

[6] G. Catalan and J. F. Scott, *Adv. Mater.* **21**, 2463 (2009).

[7] J. Wang, J. B. Neaton, H. Zheng, V. Nagarajan, S. B. Ogale, B. Liu, D. Viehland, V. Vaithyanathan, D. G. Schlom, U. V. Waghmare, N. A. Spaldin, K. M. Rabe, M. Wuttig, and R. Ramesh, *Science* **299**, 1719 (2003).

[8] T. Choi, S. Lee, Y. J. Choi, V. Kiryukhin, S.-W. Cheong, *Science* **324**, 63 (2009).

[9] A. Q. Jiang, C. Wang, K. J. Jin, X. B. Liu, J. F. Scott, C. S. Hwang, T. A. Tang, H. B. Lu, and G. Z. Yang, *Adv. Mater.* **23**, 1277 (2011).

[10] Q. M. Zhang, V. Bharti, and X. Zhao, *Science* **26**, 2101 (1998).

[11] S.-M. Yoon, S. Yang, C. Byun, S.-H. K. Park, D.-H. Cho, S.-W. Jung, O-S. Kwon, and C.-S. Hwang, *Adv. Funct. Mater.* **20**, 921 (2010).

[12] T. S. Böscke, J. Müller, D. Bräuhaus, U. Schröder, and U. Böttger, *Appl.*

Phys. Lett. **99**, 102903 (2011).

[13] S. Mueller, J. Mueller, A. Singh, S. Riedel, J. Sundqvist, U. Schroeder, T. Mikolajick, *Adv. Funct. Mater.* **22**, 2412 (2012).

[14] J. Müller, T. S. Böscke, U. Schröder, S. Mueller, D. Bräuhaus, U. Böttger, L. Frey, and T. Mikolajick, *Nano Lett.* **12**, 4318 (2012).

[15] J. Müller, U. Schröder, T. S. Böscke, I. Müller, U. Böttger, L. Wilde, J. Sundqvist, M. Lemberger, P. Kücher, T. Mikolajick, and L. Frey, *J. Appl. Phys.* **110**, 114113 (2011).

[16] S. Mueller, C. Adelmann, A. Singh, S. Van Elshocht, U. Schroeder, and T. Mikolajicka, *ECS J. Solid St. Sci. and Technol.***1**, N123 (2012).

[17] C. -K Lee, E. Cho, H. –S. Lee, C. S. Hwang, and S. Han, *Phys. Rev. B* **78**, 012102 (2008).

[18] E. H. Kisi, *J. Am. Ceram. Soc.* **81**, 741 (1998).

[19] E. H. Kisi and C. J. Howard, *J. Am. Ceram. Soc.* **72**, 1757 (1989).

[20] C. J. Howard and E. H. Kisi, *J. Am. Ceram. Soc.* **73**, 2828 (1990).

[21] J. Valasek, *Phys. Rev.* **15**, 537 (1920).

[22] J. Valasek, *Phys. Rev.* **17**, 475 (1921).

[23] S. Y. Wu, *IEEE Trans. Electron. Devices* **ED-21**, 499 (1974).

[24] S. L. Miller and P. J. McWhorter, *J. Appl. Phys.* **72**, 5999 (2012).

[25] Y. Watanabe, *J. Appl. Phys.* **83**, 2179 (1998).

[26] K. Takahashi, K. Aizawa1, B. –E. Park, and H. Ishiwara, *Jpn. J. Appl. Phys.* **44**, 6218 (2005).

[27] M. Takahashi and S. Sakai, *Jpn. J. Appl. Phys.* **44**, L800 (2005).

[28] Y. Kato, Y. Kaneko, H, Tanaka, and Y. Shimada, *Jpn. J. Appl. Phys.* **47**, 2719 (2008).

[29] Y. Kaneko, H. Tanaka, and Y. Kato, *Jpn. J. Appl. Phys.* **48**, 09K19 (2009).

[30] Y. Kaneko, Y. Nishitani, M. Ueda, E. Tokumitsu, and E. Fujii, *Appl. Phys. Lett.* **99**, 182902 (2011).

[31] Y. Kaneko, H. Tanaka, M. Ueda, Y. Kato, and E. Fujii, *IEEE Trans. Electron. Dev.* **58**, 1311 (2011).

[32] L. Liao, H. J. Fan, B. Yan, Z. Zhang, L. L. Chen, B. S. Li, G. Z. Xing, Z. X. Shen, T. Uw, X. W. Sun, J. Wang, and T. Yu, *ACS Nano* **3**, 700 (2009).

[33] J. I. Sohn, S. S. Choi, S. M. Morris, J. S. Bendall, H. J. Coles, W. –K. Hong, G. Jo, T. Lee, and M. E. Welland, *Nano Lett.* **10**, 4316 (2010).

[34] K. H. Lee, G. Lee, K. Lee, M. S. Oh, and S. Im, *Appl. Phys. Lett.* **94**, 093304 (2009).

[35] S. J. Kang, I. Bae, Y. J. Park, T. H. Park, J. Sung, S. C. Yoon, K. H. Kim, D. H. Choi, and C. Park, *Adv. Funct. Mater.* **19**, 1609 (2009).

[36] T. Kanashima, K. Yabe, and M. Okuyama, *Jpn. J. Appl. Phys.* **51**, 02BK06 (2012).

[37] E. B. Song, B. Lian, S. M. Kim, S. Lee, T. –K. Ching, M. Wang, C. Zeng, G. Xu, K. Wong, Y. Zhou, H. I. Rasool, D. H. Seo, H. –J. Chung, J. Heo, S. Seo, and K. L. Wang, *Appl. Phys. Lett.* **99**, 042109 (2011).

[38] S. Raghavan, I. Stolichnov, N. Setter, J. –S. Heron, M. Tosun, and A. Kis, *Appl. Phys. Lett.* **100**, 023507 (2012).

[39] C. Baeumer, S. P. Rogers, R. Xu, L. W. Martin, and M. Shim, *Nano Lett.* **13**, 1693 (2012).

[40] X. Hong, A. Posadas, K. Zou, C. H. Ahn, and J. Zhu, *Phys. Rev. Lett.* **102**, 136808 (2009).

[41] Y. Zheng, G. –X. Ni, C. –T. Toh, M. –G. Zeng, S. –T. Chen, K. Yao, and B. Özyilmaz, *Appl. Phys. Lett.* **94**, 163505 (2009).

[42] Y. Zheng, G. –X. Ni, C. –T. Toh, C. –Y. Tan, K. Yao, and B. Özyilmaz, *Phys. Rev. Lett.* **105**, 166602 (2010).

[43] W. Fu, Z. Xu, C. Gu, and E. Wang, *Nano Lett.* **9**, 921 (2009).

[44] J. Y. Son, S. Ryu, Y. –C. Park, Y. –T. Lim, Y. –S. Shin, Y. –H. Shin, and H. M. Jang, *ACS Nano* **4**, 7315 (2010).

[45] R. C. G. Naber, C. Tanase, P. W. M. Blom, G. H. Gelinck, A. W. Marsman, F. J. Touwslager, S. Setayeshi, and D. M. de Leeuw, *Nat. Mater.* **4**, 243 (2005).

[46] K. Asadi, D. M. de Leeuw, B. D. Boer, and P. W. M. Blom, *Nat. Mater.* **7**, 547 (2008).

[47] S. J. Kang, Y. J. Park, I. Bae, K. J. Kim, H. –C. Kim, S. Bauer, E. L. Thomas, and C. Park, *Adv. Funct. Mater.* **19**, 2812 (2009).

[48] R. C. G. Naber, K. Asadi, P. W. M. Blom, D. M. de Leeuw, and B. de Boer, *Adv. Mater.* **22**, 933 (2010).

[49] S. K. Hwang, I. Bae, R. H. Kim, and C. Park, *Adv. Mater.* **24**, 5910 (2012).

[50] D. Takashima and I. Kunishima, *IEEE J. Solid-st. Circ.* **33**, 787 (1998).

[51] D. Takashima, S. Shuto, I. Kunishima, H. Takenaka, Y. Oowaku, and S. Tanaka, *IEEE Solid-st. Circ.* **34**, 1557 (1999).

[52] D. Takashima, Y. Takeuchi, T. Miyakawa, Y. Itoh, R. Ogiwara, M. Kamoshida, K. Hoya, S. M. Doumae, T. Ozaki, H. Kanaya, K. Yamakawa, I. Kunishima, and Y. Oowaki, , *IEEE Solid-st. Circ.* **36**, 1713 (2001).

[53] S. Shiratake, T. Miyakawa, Y. Takeuchi, R. Ogiwara, M. Kamoshida, K. Hoya, K. Oikawa, T. Ozaki, I. Kunishima, K. Yamakawa, S. Sugimoto, D. Takashima, H. –O. Joachim, N. Rehm, J. Wohlfahrt, N. Nagel, G. Beitel, M. Jacob, and T. Roehr, *IEEE Solid-st. Circ.* **38**, 1911 (2003).

[54] Hi. Shiga, D. Takashima, S. Shiratake, K. Hoya, T. Miyakawa, R. Ogiwara, R. Fukuda, R. Takizawa, K. Hatsuda, F. Matsuoka, Y. Nagadomi, D. Hashimoto, H. Nishimura, T. Hioka, S. Doumae, S. Shimizu, M. Kawano, T. Taguchi, Y. Watanabe, S. Fujii, T. Ozaki, H. Kanaya, Y. Kumura, Y. Shimojo, Y. Yamada, Y. Minami, S. Shuto, K. Yamakawa, S. Yamazaki, I. Kunishima, T. Hamamoto, A. Nitayama, and T. Furuyama, *IEEE Solid-st. Circ.* **45**, 142 (2010).

[55] D. Takashima, *Mater. Res. Soc. Symp. Proc.* **1250**, G11-01 (2010).

[56] S. Sakai, M. Takahashi, K. Takeuchi, Q. –H. Li, T. Horiuchi, S. Wang, K. -Y. Yun, M. Takamiya, and T. Sakurai, *IEEE Non-Volatile Semiconductor*

Memory Workshop and 3rd International Conf. on Memory Technology and Design, 103 (2008).

[57] S. Wang, M. Takahashi, Q. –H. Li, K. Takeuchi, and S. Sakai, *Semicond. Sci. Technol.* **24**, 105029 (2009).

[58] T. Hatanaka, R. Yajima, T. Horiuchi, S. Wang, X. Zhang, M. Takahashi, S. Sakai, and K. Takeuchi, *IEEE Solid-st. Circ.* **45**, 2156 (2010).

[59] X. Zhang, M. Takahashi, and S. Sakai, *Integr. Ferroelec.* **132**, 114 (2011).

[60] J. Müller, T. S. Böscke, U. Schröder, R. Hoffmann, T. Mikolajick, and L. Frey, *IEEE Electr. Divece L.* **33**, 185 (2012).

[61] S. Mueller, S. R. Summerfelt, J. Müller, U. Schroeder, and T. Mikolajick, *IEEE Electr. Divece L.* **33**, 1300 (2012).

[62] P. W. M. Blom, R. M. Wolf, J. F. M. Cillessen, and M. P. C. M. Krijin, *Phys. Rev. Lett.* **73**, 2107 (1994).

[63] L. Esaki, R. B. Laibowitz, P. J. Stiles, *IBM Tech. Discl. Bull.* **13**, 2161 (1971).

[64] E. Y. Tsymbal and H. Kohlstedt, *Science* **313**, 181 (2006).

[65] V. Garcia, S. Fusil, K. Bouzehouane, S. Enouz-Vedrenne, N. D. Mathur, A. Barthélémy, and M. Bibes, *Nature* **460** (2009).

[66] D. J. Kim, H. Lu, S. Ryu, C. –W. Bark, C. –B. Eom, E. Y. Tsymbal, and A. Gruverman, *Nano Lett.* **12**, 5697 (2012).

[67] A. Chanthbouala, A. Crassous, V. Garcia, K. Bouzehouane, S. Fusil, X.

Moya, J. Allibe, B. Dlubak, J. Grollier, S. Xavier, C. Deranlot, A. Moshar, R. Proksch, N. D. Mathur, M. Bibes, and A. Barthélémy, *Nat. Nanotechnol.* **7**, 101 (2011).

[68] R. Meyer and R. Waser, *J. Appl. Phys.* **100**, 051611 (2006).

[69] R. Meyer, J. R. Contreras, A. Petraru, and H. Kohlstedt, *Integr. Ferroelectr.* **64**, 77 (2004).

[70] V. M. Voora, T. Hofmann, M. Brandt, M. Lorenz, M. Grundmann, N. Ashkenov, and M. Schubert, *Appl. Phys. Lett.* **94**, 142904 (2009).

[71] T. Choi, S. Lee, Y. J. Choi, V. Kiryukhin, and S. W. Cheng, *Science* **324**, 63 (2009).

[72] A. Q. Jiang, C. Wang, K. J. Jin, X. B. Liu, J. F. Scott, C. S. Hwang, T. A. Tang, H. B. Liu, G. Z. Yang, *Adv. Mater.* **23**, 1277 (2011).

Chapter 3. The origin of the ferroelectricity in thin $Hf_{1-x}Zr_xO_2$ films: microstructure and resulting in-plane stress

3.1. Introduction

Ferroelectric memories, such as FeRAM and FeFET, have been considered as the most promising universal non-volatile memories, because of their reversibly bi-stable polarization states.[1] Most of the previous research in these fields have focused on material systems based on the perovskite structure.[1] However, integrating them into conventional Si-based memory technology has proven very challenging, and as a result, the development of very high-density FeRAM has been hindered. Other emerging memories, such as PcRAM, ReRAM, and STT-RAM, are attracting greater attention at the moment.[2] However, it was recently reported that HfO_2 thin films can show ferroelectric properties when doped or alloyed with various elements, such as Si, Y, Al, Zr, and Gd.[3-9] This could revolutionize the field of ferroelectric memories, because this technology is compatible with conventional Si technology. The technology is also appropriate for three-dimensional capacitor fabrication -- which is inevitable for ultra-high density devices -- thanks to the small thickness (~10 nm, perovskite materials require thickness ~100 nm) and matured atomic layer deposition (ALD) technique. It is evident that robust ferroelectricity in such materials can be achieved by forming non-centrosymmetric o-phase

(space group $Pbc2_1$), which is generally an uncommon (or even unstable) phase in the ALD temperature and pressure window. However, the origin of the evolution of such uncommon phase has not yet been understood. Müller et al., who are pioneers in this research field, have reported that film stress due to several intrinsic and extrinsic factors is the origin of the emergence of the o-phase.[3] This appears to be related to the fact that the o-phases are stable at high pressure (3-4 GPa) in both HfO_2 and ZrO_2 near the ALD temperatures.[10,11] Even though o-phase cannot be found in the phase digram of HfO_2 or ZrO_2, its free energy is very similar with that of orthorhombic I phase.[12] However, the thin films are under biaxial stress, and there must be no stress along the direction normal to the surface, while the thermodynamic data corresponds to the situation under the hydrostatic pressure. In fact, there have been only theoretical reports on the formation of o-phase due to hydrostatic pressure.[12] Kisi et al., who observed $Pbc2_1$ o-phase first time, suggested different mechanism, in which the large tensile stress along the c-axis of t-phase (space group: $P4_2/nmc$) of ZrO_2 is the origin of the formation of unexpected non-centrosymmetric phase.[13] In their report, the required tensile stress was ~4 GPa, which is still large value, but the stress of a few GPa level can be observed in thin films. Park et al. reported the 2c/(a+b) ratio of HfO_2, ZrO_2, and HZO, and 2c/(a+b) ratio of HfO_2 is much smaller than that of ZrO_2.[9] (It should be noted that the longest axis of o-phase was considered as c-axis for the sake of convenience.)

They predicted that the large difference of 2c/(a+b) ratio of o- and t-phase of ZrO_2 prevents the formation of o-phase in pure ZrO_2. For the case of HfO_2, on the other hand, the stable m-phase (space group: $P2_1/c$) is formed with very small grain size based on the surface energy argument.[14,15] Therefore, they concluded that m-phase of HZO can be prevented with relatively large film thickness and the difference of 2c/(a+b) ratio of o- and t-phase is small enough to be overcome by in-plane film stress. In this study, the origin of the ferroelectricity in $Hf_{1-x}Zr_xO_2$ material system is examined based on the stress and microstructure of thin films.

3.2. Experimental

HZO films were deposited on Si substrate coated with various metal layers using thermal ALD at a wafer temperature of 280 °C. $Hf[N(C_2H_5)CH_3]_4$, $Zr[N(C_2H_5)CH_3]_4$, and ozone were used as the Hf precursor, Zr precursor, and oxygen source, respectively. 100-nm-thick Ir, 50-nm-thick TiN, 100-nm-thick Ru, or 100-nm-thick Pt films were coated onto the Si substrate and used as the BE. The HZO films with various Hf/(Hf+Zr) ratios were prepared by controlling the ALD cycle ratios of HfO_2 and ZrO_2, with almost identical growth rates of HfO_2 and ZrO_2 (0.125 nm/cycle on TiN substrate).

For electrical characterization, Pt (60 nm)/TiN (20nm) TEs were deposited using a shadow mask and RF magnetron sputtering. For the samples on Pt and Ru substrates, the TiN layer was omitted from the TEs to decrease the leakage current. After TE deposition, post-metallization annealing (PMA) was performed at 500°C in N_2 atmosphere using a rapid thermal annealing (RTA). To examine the effect of the upper TiN capping layer during annealing, post-deposition annealing (PDA) under identical conditions before the deposition of TE was also attempted. The composition and the thickness of HZO films were examined using X-ray fluorescence (Quant'X, Thermo SCIENTIFIC) and ellipsometry (L-116d, Gaetner), respectively. P-V and C-V characteristics were measured using a

ferroelectric tester (TF analyzer 2000, Aixacct Systems) and impedance analyser (4194A, HP) at a frequency of 10 kHz, respectively. The microstructure of the films was analysed using field emission scanning electron microscopy (SEM, SU70, Hitachi), and the topography of the films were analysed using atomic force microscopy in contact mode (JSPM-5200, JEOL). TEM was performed using high-resolution TEM (JEM-3000F, JEOL). For the measurement of in-plane stress in thin films, the change of the curvature of the substrate was analysed using multi-beam optical system (K-space Associates) at room temperature.

3.3. Results and discussions

3.3.1. Electrical characteristics on TiN bottom electrode

Figure 3.1 shows the polarization-electric field (P-E) curves of HfO_2, $Hf_{0.81}Zr_{0.19}O_2$, $Hf_{0.57}Zr_{0.43}O_2$, $Hf_{0.30}Zr_{0.70}O_2$, and ZrO_2 films, with various thicknesses (9.2, 14.2, 19.2, 24.2, and 29.2 nm) sandwiched between a Pt/TiN TE (where the TiN layer contacts the dielectric layer), and a TiN BE. All the samples used for the electrical characterization were annealed at 500°C in N_2 atmosphere for 30 s after the formation of the TE. It has been reported that the TiN capping on the top of the HZO film before the annealing improves the ferroelectric performance.[3-5] Therefore, two types of 9.2-nm-thick $Hf_{0.57}Zr_{0.43}O_2$ films with and without the TiN capping layer were tested, and the electrical results are included in figure 3.2. From the results, it can be concluded that the upper TiN capping layer does not play an important role during annealing for HZO film in the present work. The variation in the P-E curves along with the cation composition of 9.2-nm-thick HZO films were almost identical to the previous report by Müller et al.[6]; 9.2-nm-thick $Hf_{0.57}Zr_{0.43}O_2$ film shows a robust ferroelectricity with $2P_r$ of ~33 $\mu C/cm^2$, and the $2P_r$ value decreases with increasing Zr or Hf contents. For the side richer in Hf, $2P_r$ monotonically decreases, while the films richer in Zr show anti-ferroelectric properties before they become

linear dielectric with ZrO_2 composition. For the $Hf_{0.57}Zr_{0.43}O_2$ films, $2P_r$ remains almost constant when the thickness of the film is ≤19.2 nm, but it decreases rapidly when the thickness is >19.2nm. Other films with slightly higher or lower Zr-contents show similar variations with thickness. This is in stark contrast to the general degradation of ferroelectricity of the perovskite structured films with decreasing thickness, which can be understood by the effects of the depolarizing field effect due to the inevitable involvement of the so-called dead-layer formed at the metal/ferroelectric interface.[16] The variation of the ε_r with thickness and composition was also examined by capacitance - voltage (C - V) analysis, the results of which are included in figure 3.3. The variations of ε_r with composition and thickness corroborate the variation of P-E curves shown in figure 3.1. From the estimated P-E and ε_r characteristics, and necessary O-phase formation for ferroelectricity, it is believed that the crystal structures of the HZO films change (or at least partly change) between the o- and m-phases or o- and t-phases at a certain critical thickness, depending on the x value. For example, the critical film thickness is ~20 nm for x = 0.43.

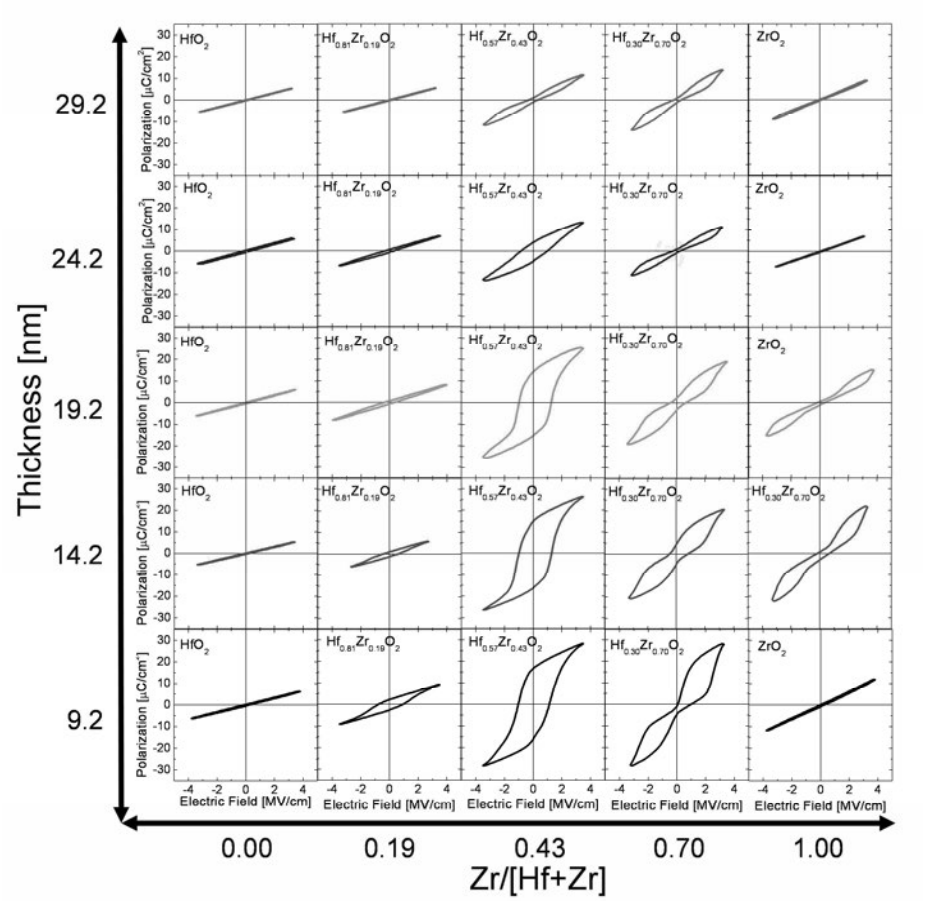


Figure 3.1. The P-E curves of HZO films with various composition (Zr/[Zr+Hf]=0.00, 0.19, 0.43, 0.70, 1.00) and thickness (~9.2, 14.2, 19.2, 24.2, and 29.2 nm).

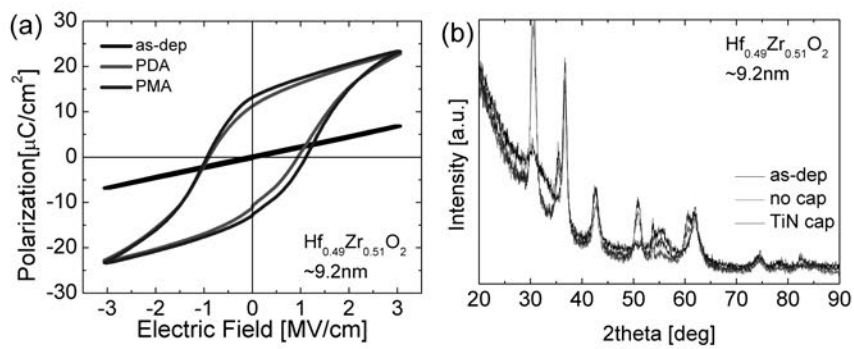


Figure 3.2. (a) Polarization-electric field hysteresis and (b) grazing-angle incidence X-ray diffraction spectra of as-deposited, post-deposition annealed, and post-metallization annealed 9.2-nm-thick $Hf_{0.49}Zr_{0.51}O_2$ film, respectively.

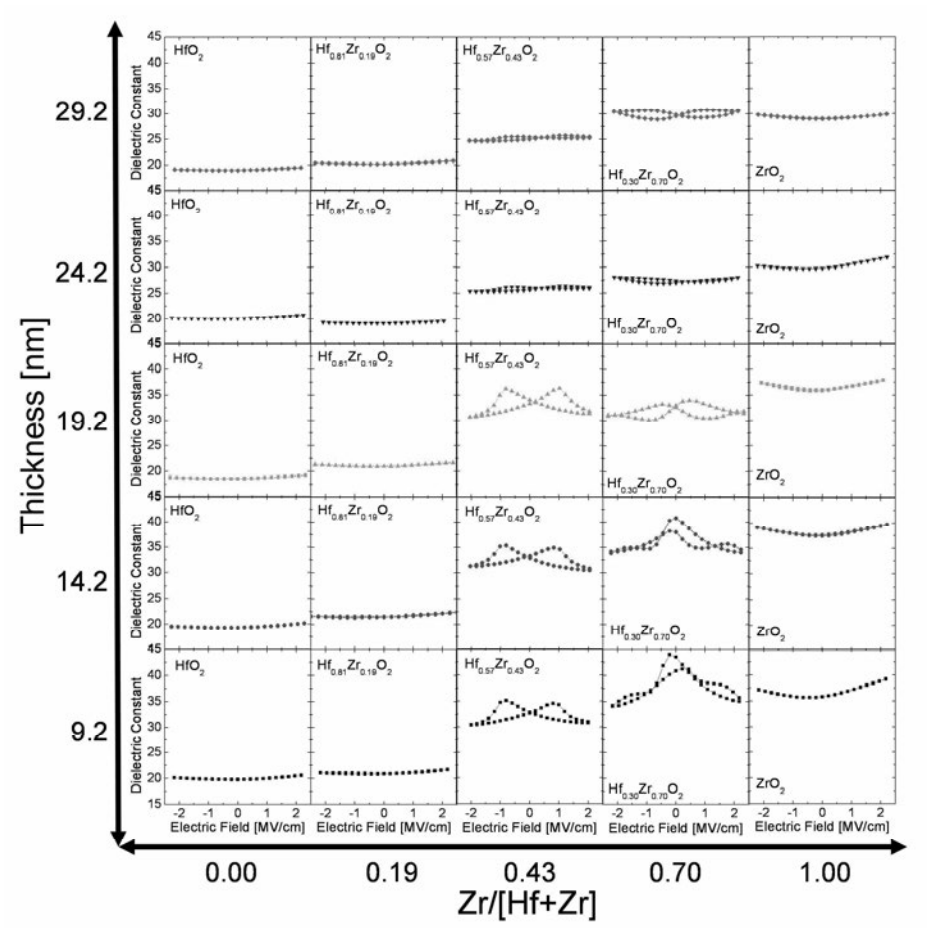


Figure 3.3. (a) The dielectric constant-electric field curves of HZO films with various composition (Zr/[Zr+Hf]=0.00, 0.19, 0.43, 0.70, 1.00) and thickness (~9.2, 14.2, 19.2, 24.2, and 29.2 nm).

3.3.2. Structural analysis

As the next step, the crystal structure of HZO films was analysed using XRD. However, the thickness of the ferroelectric HZO film is too small, and the crystal structures are too complicated to clearly distinguish the M-, T-, and o-phases using a laboratory X-ray source. Therefore, a synchrotron X-ray source and 6-circle X-ray scattering equipment installed at the 3A beam line at the Pohang Light Source were used. The details of this XRD setting are described in detail in figure 3.4, and the details of the 6-circle X-ray scattering are described in Ref. 17. Even though the wavelength of the synchrotron X-ray source was 1.11899 Å, the diffraction angle data were transformed to the values corresponding to the case with characteristic XRD with Cu Kα radiation (1.5481 Å) for easy comparison with previous reports. Figure 3.5a shows the XRD spectra of 9.2-nm-thick HfO_2, $Hf_{0.57}Zr_{0.43}O_2$, and ZrO_2 films with a ~15-nm-thick TiN capping layer. The XRD spectra for the HfO_2 and ZrO_2 were coincided well with the m- and t-phases, except for the TiN peaks which are indicated by vertical arrows. However, the spectra for the $Hf_{0.57}Zr_{0.43}O_2$ film show several peaks that cannot be attributed to the m- and t-phases. Although all the peaks in that spectrum were assigned to the o-phases, many of the peaks are overlapped with the peaks from m- and t-phases, such as 111 and 220 peaks. Therefore, it is not unequivocally stated that the film is solely composed of o-phase, but it is highly probable that the

material is composed of m-, t-, and o-phases. Nevertheless, the most characteristic peaks that must be assigned to the O-phase can be found near the two-theta region of 34 – 36° and 53 – 54°, which are enlarged in figure 3.5b. Therefore, it is quite clear that the $Hf_{0.57}Zr_{0.43}O_2$ film at least partly contains O-phase. Figure 3.5c shows the XRD spectra (30 – 40° and 50 – 60°) of the 9.2-nm-thick $Hf_{0.57}Zr_{0.43}O_2$ film with and without the TiN capping. It can be understood that the TiN capping certainly improves the splitting of 020 and 200 peaks, and the emergence of the 221 peak of the o-phase. The comparable peak intensity near a two-theta of 34 – 35° with that of TiN at ~37°, which has an intensity distribution clearly distinguishable from those of HfO_2 (m-phase) and ZrO_2 (t-phase), suggests that the material is still O-phase with slightly degraded crystalline quality, or less perfect transition to the o-phase. Figure 3.5d shows the variation of the same peaks from the $Hf_{0.57}Zr_{0.43}O_2$ film with three different thicknesses of 9.2, 19.2 and 29.2 nm without the TiN capping. The spectrum near 34 – 35° indicates that the film structure becomes more m-phase-like as the film thickness increases, while the peak near 53 – 54° shows that the o-phase is most evident at 19.2 nm. This corroborates the variation of $2P_r$ with film thickness shown in Figs. 3.2. XRD spectra in the full scan range (10 – 90°) are included in figure 3.6. Therefore, it can be concluded that the crystalline structure of HZO film varies according to the film thickness and that ferroelectric properties of HZO film originate from non-centrosymmetric o-phase.

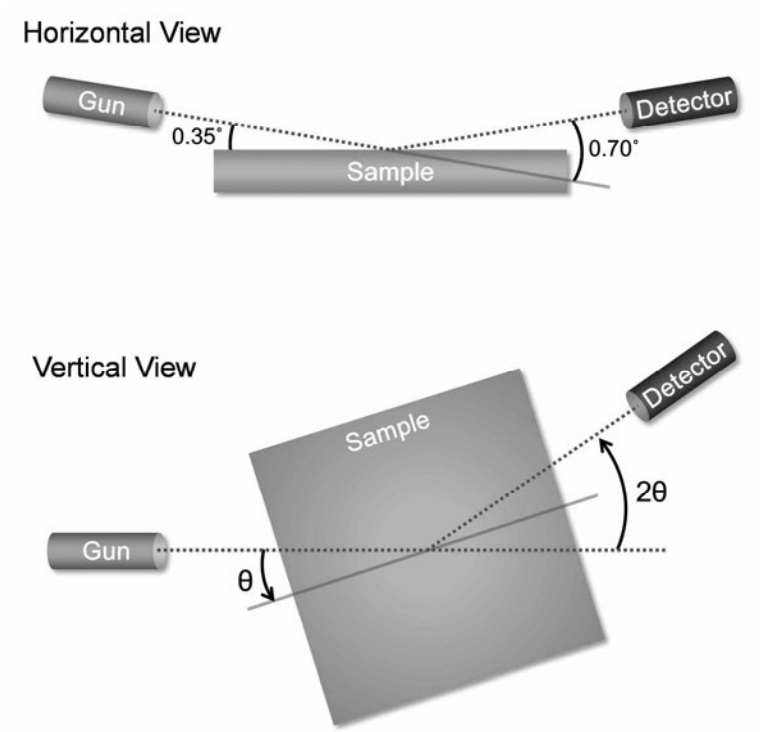


Figure 3.4. The horizontal view (upper panel) and the vertical view (bottom panel) of the schematic of modified GIXRD using 6-circle X-ray diffractometer with synchrotron X-ray source in 3A beam line in PAL.

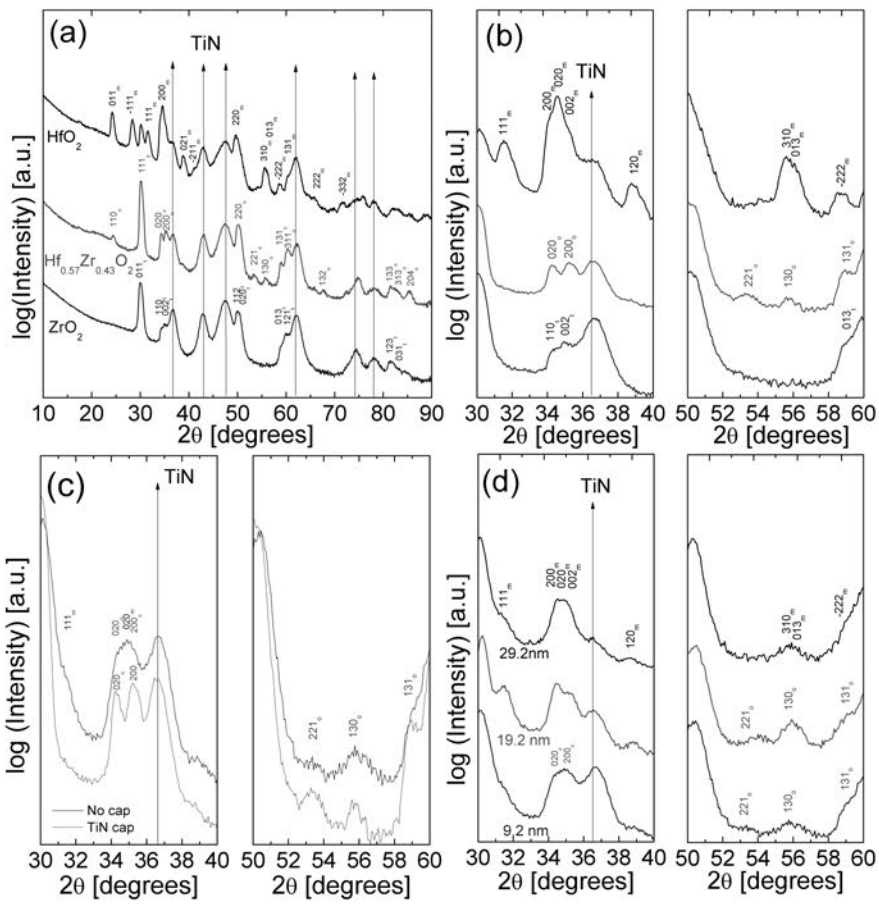


Figure 3.5. (a) The modified GIXRD spectra with full range (10 - 90°) and (b) the enlarged 30 - 40° (left panel) and 50 - 60° region (right panel) of ~9.2-nm-thick HfO_2, $Hf_{0.57}Zr_{0.43}O_2$, ZrO_2 films with ~15-nm-thick upper TiN capping layer after PMA using synchrotron X-ray source (3A beam line in PLS). The enlarged 30 - 40° (left panel) and 50 - 60° region (right panel) of the GIXRD spectra of (c) ~9.2-nm-thick $Hf_{0.57}Zr_{0.43}O_2$ with and without upper TiN capping layer and (d) those of ~9.2-, ~19.2-, and ~29.2-nm-thick $Hf_{0.57}Zr_{0.43}O_2$ without upper TiN layer.

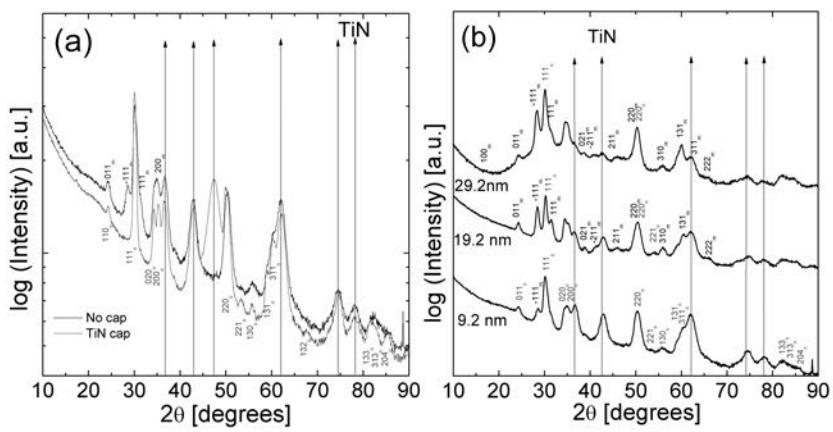


Figure 3.6. The modified GIXRD spectra with full range (10 - 90°) of (a) ~9.2-nm-thick $Hf_{0.57}Zr_{0.43}O_2$ with upper TiN capping layer and that without capping layer. (b) Those of ~9.2-, ~19.2-, and ~29.2-nm-thick $Hf_{0.57}Zr_{0.43}O_2$ without upper TiN capping layer using synchrotron X-ray source (3A beam line in PLS).

3.3.3. Strain and microstructure of HZO films on TiN

Park et al. pointed out that 2c/(a+b) ratio of o- and t-phase of ZrO_2 is much larger than that of HfO_2, and they predeicted that it might be reason that ferroelectricity could not be seen in ZrO_2.[9] Therefore, the strain of HZO films need to be examined to elucidate the role of tensile strain. Figure 3.7 shows the schematics of the estimation of in-plane strain of HZO films from GAXRD spectra. The best method to analyze the stress in thin film is the well-known $Sin^2\Psi$ method, but it is impossible for the polycrystalline films with randomly oriented grains which cannot show any diffraction peaks using normal θ-2θ scan as seen in the left panel of figure 3.7. Therefore, the strain should be estimated from the limited information can be measured by experiment, and only the GAXRD spectra could be measured for the purpose. Among the various diffraction peaks in the GAXRD spectra, the t(111) or o(111) peak which located at ~30.5^o was chosen due to the largest intensity and the absence of the superposition from the different orientations as seen in the central panel of figure 3.7. From the change of the 2θ of the t(111) diffraction peak, the change of interplanar distance of (111) planes (d_{111}) and strain along (111) direction (ε_{111}) can be calculated. As the next step, the Mohr's circle for strains in thin films can be constructed as seen in the right panel of figure 3.7.

As the next step, the crystal structure of the films was examined using

GAXRD to check the strain of them. Figure 3.8 shows the GAXRD spectra of HfO_2, $Hf_{0.5}Zr_{0.5}O_2$ (HZO), and ZrO_2 films with various thickness before and after annealing at 500°C, respectively. For the case of HfO_2 films, as seen in figure 3.8a, the stable m-phase is easily formed after annealing even with the thickness of ~5nm. It can be explained successfully by well-known size effect.[14] On the other hand, Olsen et al. reported that ferroelectricity could be found for the case of pure HfO_2 deposited using sputtering.[18] It means that o-phase can be formed for the case of pure HfO_2, if the deposition process is well-controlled. However, for the case of the ALD process in the present chapter, ferroelectricity could not be found in pure HfO_2. For the case of HZO, the stress required for the strain of 1.5% for t→o. However, the loss of ferroelectricity with antiferroelectric double loop with decreasing thickness was hard to be understood from the stress calculated from the change of substrate curvature. Figure 3.9 shows P-E and ε_r-E curves of HZO films thinner than 9.3 nm. The ferroelectric-to-antiferroelectric transition can be clearly seen in P-E loops, and the increase of ε_r supports that orthorhombic-to-tetragonal transition might be the reason of it. Interestingly, the location of o(111) or t(111) peak of HZO film shifts to the high angle with increasing thickness, as seen in figure 3.8b. It means that the interplanar distance of (111) planes (d_{111}) decreases with increasing thickness. From the comparison with the lattice parameters of tetragonal HfO_2 and ZrO_2 in literature, the strain in (111) derection (ε_{111}) can be

calculated.(d_{111} for HfO_2 and ZrO_2 are 2.947 and 2.977 Å, respectively. [19]) Finally from the directional relation of (111) direction and material properties, such as Y=210 GPa [20] and ν=1/3, in-plane strain (ε_{in}) can be calculated. Figure 3.10a-c show the change of d_{111}, ε_{111}, and ε_{in} of HZO and ZrO_2 as a function of t_f, respectively. For the case of HZO films, ε_{in} becomes larger than 1.5 % between t_f of 5 and 9 nm, and it is consistent with the electrical characteristics in figure 3.8. For the case of ZrO_2 films, on the other hand, ε_{in} is smaller than 2 %, which is required for t→o transition from lattice parameter, and it is also consistent with the electrical characteristics. Therefore, the electrical characteristics and the change of strain are well-matched consistentsly.

From the large value of tensile stress and its change with increasing thickness, the origin of the stress is thought to originate from the island coalescence during the growth of the polycrystalline films. Nix and Clemens suggested a model for the large tensile stress formed inintial growth of polycrystalline films with Volmer-Weber type growth.[21] In the model, the tensile stress is formed at the point of crystallite coalescence to lower the total free energy by reducing the surface area. Even though the elastic strain energy is formed by the large tensile stress, the decrease of the surface energy is larger than the increase of it. They also suggested the equations for the maximum stress based on the energy argument similar with the Griffith criteria of the theory for crack generation in materials. Equation 3.1

formulates the maximum stress which can be formed during crystallite coalescence suggested by Nix and Clemens.[21]

$$<\sigma>=[(\frac{1+\nu}{1-\nu})Y\frac{(2\gamma_{sv}-\gamma_{gb})}{a}]^{1/2} \quad (3.1)$$

, where $<\sigma>$, γ_{sv}, γ_{gb}, Y, ν, and a are average stress, surface energy, grain boundary energy, elastic modulus, poisson's ratio, and the radius of crystallite of the film. On the other hand, the initial nuclei size at the coalescence of the crystallite of HfO_2 and ZrO_2 using ALD were reported experimentally as 1-2 nm.[22-24] If we take characteristic values for t-phase as Y = 200 GPa [25], γ_{sv} = 2.15 J/m^2 [26], γ_{gb} =1.075 J/m^2, ν =1/3, then for a grain size of 1 – 2 nm, the upper bound estimates for this model is $<\sigma>$ = 36 - 51 GPa. For the case of amorphous phase, which corresponds to HZO or HfO_2, the upper bound is estimated as 25 - 36 GPa, where γ_{sv} and γ_{gb} are assumed to be a half of t-phase, and they are large enough for the large tensile strain of a few % level.

Remaining question is why ZrO_2 film has tensile strain smaller compared to that of HZO films. The left panel of figure 3.11 shows the in-plane strain of ZrO_2 film in as-deposited and annealed state (at 500 °C), respectively. Interestingly, the tensile strain in as-deposited state is smaller than that in as-deposited state for all the cases. Therefore, it can be deduced that the ZrO_2 films crystallized with small thickness at ALD temperature shows relatively

small tensile strain, and they affect the films deposited on the low-strained bottom layer as seen in the right panel of figure 3.11. After annealing process at 500 ^{o}C, the tensile strain increases, but they are still smaller than the critical strain needed for the tetragonal to orthorhombic transition. In fact, the strain along out-of-plane direction is generally increasing with decreasing thickness. It is generally due to the large empty spaces near grain boundary, and the equivalent phenomena were reported in various metal and metal oxide films. [27-37]

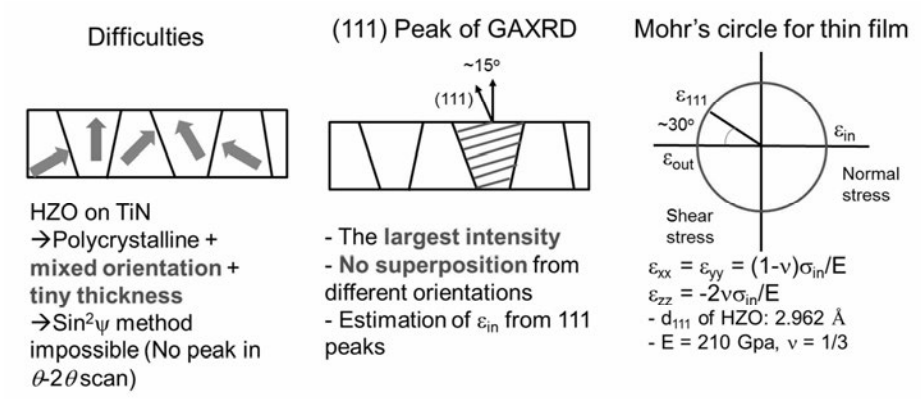


Figure 3.7. The schematics of difficulties in polycrystalline films with randomly oriented grains (left panel), estimation of in-plane strain from (111) diffraction peaks (cetral panel), and Mohr's circle of strain for thin films (right panel), respectively.

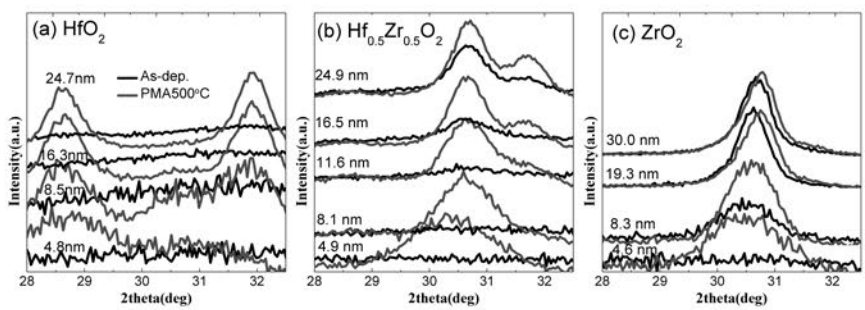


Figure 3.8. The GAXRD spectra of (a) HfO_2, (b) $Hf_{0.5}Zr_{0.5}O_2$, and (c) ZrO_2 films with various thickness in as-deposited and annealed at 500°C, respectively.

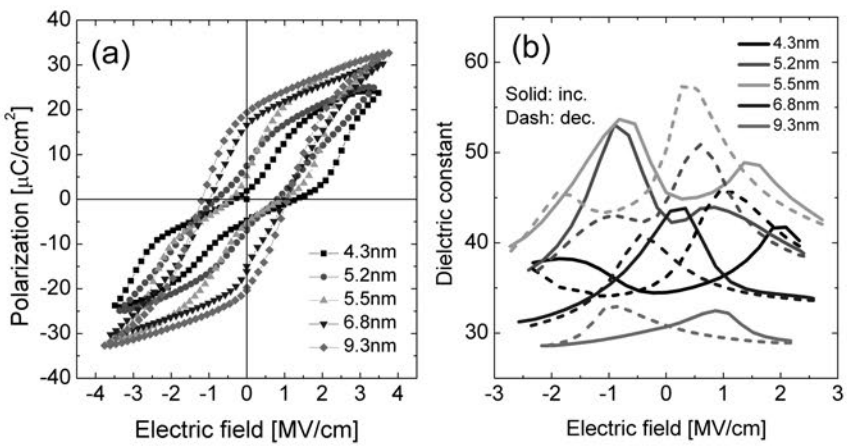


Figure 3.9. (a) The polarization-electric field and (b) dielectric constant-electric field curves of HZO films with various thickness, respectively.

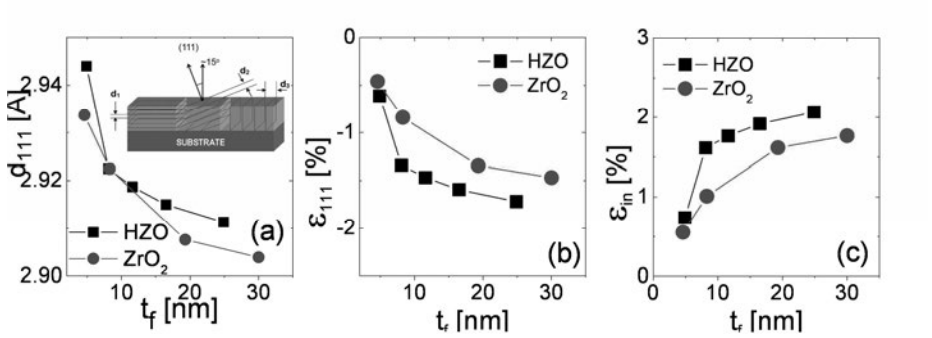


Figure 3.10. The change of (a) d_{111}, (b) ε_{111}, and (c) ε_{in} of HZO and ZrO_2 films as a function of film thickness, respectively.

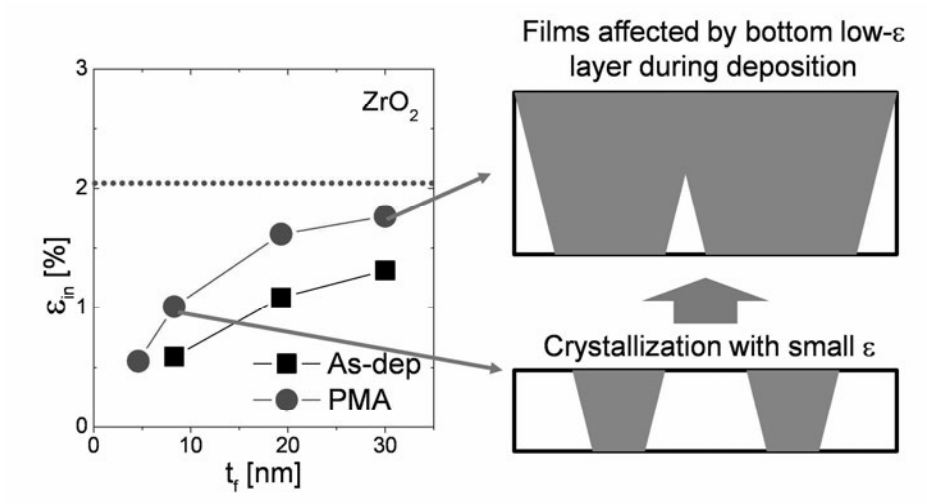


Figure 3.11. The change of ε_{in} of ZrO_2 films in as-deposited and annealed state (PMA @ 500°C) (left panel) and the schematic for the growth of low-strained ZrO_2 films (right panel), respectively.

3.3.4. Effect of bottom electrode

3.3.4.1. Effect of film orientation: comparative study on the $Hf_{0.5}Zr_{0.5}O_2$ films on TiN and Pt bottom electrode

As seen in the previous sections, HfO_2-based ferroelectric materials work well with the TiN electrode, which is another great merit for mass production. On the other hand, the type of BE is also a key factor that affects the growth behaviour and resulting microstructure of oxide films.[38-40] The origin of the unexpected ferroelectricity of the HfO_2-based films is reported to be the formation of the non-centrosymmetric o-phase as already discussed in the previous sections and literature. The origin of the formation of the o-phase in thin HfO_2-based films, however, has not yet been clearly unveiled. According to the theoretical calculation by Lowther et al., the o-phase is one of the high-hydrostatic-pressure (3-4 GPa) polymorphs of HfO_2 and ZrO_2 while the m-phase (space group: $P2_1/c$) is the stable phase under the usual thin-film processing conditions.[12] Hydrostatic pressure can hardly be achieved in thin films, however, because the stress along the substrate-normal direction cannot exist in thin films. The o-phase was first experimentally observed by Kisi et al. in Mg-doped cubic ZrO_2.[13,41] In their experiments, the lenticular-shaped t-phase (space group: $P4_2/nmc$) grains were embedded in the cubic phase matrix of the Mg-doped ZrO_2. A

large tensile stress was induced along the c-axis, and a small compressive stress was developed along the a- and b-axis directions of the t-phase due to the difference in the anisotropic coefficient of thermal expansion (CTE) of the two phases upon cooling from room temperature to 80 K. The CTE of the c-axis of the t-phase ($1.43\times10^{-5}\ ^{o}C^{-1}$) was larger than that of the cubic phase ($1.11\times10^{-5}\ ^{o}C^{-1}$) whereas those of the a- and b-axis ($1.01\times10^{-5}\ ^{o}C^{-1}$) were smaller than that of the cubic phase.[13] The magnitude of the tensile stress on the c-axis needed for the phase transition was calculated to be ~3.6 GPa. Meanwhile, the 2a/(b+c) ratios of the o-phase were 1.036 and 1.038 for ZrO_2 and HfO_2,[12] respectively, whereas the c/a ratios of the t-phase were 1.015-1.016 [42,19] and 1.028-1.029 [19,43,44] for ZrO_2 and HfO_2. (The longest axis of the o-phase was the a-axis while it was the c-axis in the t-phase, and P_r in the o-phase is mainly presented along the c-axis.) Therefore, the longest axis of the t-phase should become longer, and the shorter axes should become shorter to transform it to the o-phase. Therefore, the anisotropic stress condition imposed on the t-phase grains in the cubic-structured Mg-doped ZrO_2 must be a highly favourable condition for the grains to be transformed into the unusual o-phase. In fact, this o-phase cannot be found in the phase diagrams of ZrO_2 and HfO_2, which means that its thermodynamic stability range must be quite limited.[10,11]

The t-phase formation, however, when the grain or crystallite size is very small due the surface energy effects is well known. [14,15,26,45,46] As

the stable m-phase cannot be transformed into o-phase, the o-phase formation must be induced from the t-phase grains.[47] It was indeed reported that the ferroelectricity of HZO and Si-doped HfO_2 films is degraded with the increasing portion of m-phase in the film due to the increasing t_f and annealing temperature.[9,48] Therefore, the remaining question is how the unusual o-phase can be formed even under the conditions suitable for t-phase formation. In this chapter, it is reported that the origin of o-phase formation is the large tensile stress on the c-axis of the t-phase by controlling the in-plane strain and the texture of the HZO films using TiN and Pt BEs.

HZO films were deposited on a TiN- or Pt-electroded SiO_2/Si substrate via thermal ALD at a 280°C substrate temperature, using $Hf[N(C_2H_5)CH_3]_4$, $Zr[N(C_2H_5)CH_3]_4$, and ozone as the Hf precursor, Zr precursor, and oxygen source, respectively. Here, the 50-nm- thick TiN and 100-nm-thick Pt electrodes were deposited on Si and SiO_2/Si substrates via DC reactive stuttering and sputtering, respectively. The growth per cycle of HfO_2 and ZrO_2 were almost identical (~0.12 and ~0.18 nm/cycle on TiN and Pt, respectively); as such, HZO films with a 0.5:0.5 Hf:Zr ratio can be deposited using a 1:1 HfO_2:ZrO_2 ALD cycle ratio. For electrical characterization, a Pt(60nm)/TiN(20nm) TE was deposited via DC sputtering through a shadow mask with a 300 μm hole diameter (TiN contacted the HZO film). After the TE deposition, post-metallization-annealing was performed for 30 s at 500°C

in an N_2 atmosphere using RTA, for the crystallization of the films. The composition and t_f of the HZO films were examined via X-ray fluorescence (Quant'X, Thermo SCIENTIFIC) and ellipsometry (L-116d, Gaetner), respectively. For electrical characterization, the polarization-electric field (P-E) characteristics were measured using a ferroelectric tester (TF Analyzer 2000, Aixacct Systems) at a 1 kHz frequency. The crystal structure of the HZO films was analysed using an X-ray diffractometer (X'pert Pro, Panalytical), via grazing-angle incidence X-ray diffraction (GAXRD, incidence angle=0.5°) or normal θ-2θ scan.

Before describing the experimental results, the effects of the film orientation on the strain along the a-, b-, and c-axis of the t-phase film when a strain is induced in the film for any reason were examined. For these considerations, the starting thin films were assumed to be t-phase polycrystalline material, mostly due to the grain size effect, with various crystallographic orientations with respect to the direction normal to the substrate surface. Table 3.1 shows the calculated strains along the a-, b-, and c-axis of t-HZO as a function of in-plane stress (σ_0) and Y when the Poisson's ratio was 1/3. For the sake of convenience, the double-sized unit cell of the t-phase was used for the direct comparison with the o-phase. The last row of Table 3.1 shows the relative ratio of the P_r along the normal direction to the film surface ($P_{r,\perp}$) to the maximum P_r along the c-axis of the

o-phase ($P_{r,max}$). The ferroelectric distortion occurred along the c-axis in the o-phase. The relative ratio of $P_{r,\perp} / P_{r,max}$ would therefore be 100 % if the film is composed of (001)-textured o-phase. To understand the ferroelectric properties of the grains with other directions, the structural relations between the t- and o-phase need to be considered. The t-phase has the longest c-axis and equivalent a- and b-axis whereas the o-phase has the longest a-axis and shorter b- and c-axis (the c-axis is slightly longer than the b-axis). Therefore, for the fluent transition from t-phase to o-phase, the c-axis of the t-phase should be transformed into the a-axis of the o-phase whereas the a- and b-axis of the t-phase should be transformed into the b- or c-axis of the o-phase. Therefore, the large in-plane tensile strain must be the best condition for o-phase formation with a large $P_{r,\perp}$ when the c-axis of the t-phase lies along the film surface direction. The strain needed for o-phase formation is estimated to be ~1.5% from the c- (t-phase) and a-axis (o-phase) lattice parameters.[9] The t-phase grains with several specific orientations ((100)- and (010)-oriented t-phase grains) under the in-plane tensile stress conditions, however, might not be transformed into o-phase grains with a (001)-oriented direction along the normal direction to the film surface even if the c-axis of the t-phase is along the surface direction. The reason for this is that the lattice parameter of the c-axis of the o-phase is slightly larger than that of the b-axis, and as such, the (010) orientation of the o-phase might be favoured

compared to the (001) orientation, even when the c-axis of the t-phase lies along the film surface direction. From Table 3.1, therefore, it can be understood that the best orientation for o-phase formation is the (110) direction (t-phase), which can induce the largest tensile strain along its c-axis and negligible strains on the a- and b-axis. In this orientation of the grain, the a- and b-axis of the t-phase is located along the direction 45° inclined from the direction normal to the surface so that it could not have any strain in principle (Mohr's circle consideration). When the c-axis parameter is increased by the in-plane tensile strain, however, the o-phase could be stabilized over the t-phase by the strain effect, and this could be accompanied with the contraction of the a- and b-axis lattice parameters.

In the case of the t-phase grains with a (111) orientation, on the other hand, this direction is believed to be inappropriate for o-phase formation because the tensile strains along the a-, b-, and c-axis are almost equivalent, making the involvement of the anisotropic strain highly unlikely. This is a peculiar aspect of the (111)-oriented grains, making it highly useful in identifying the factors that induced o-phase formation in the HZO films.

It is well known that the orientation of the thin film is sensitively affected by the bottom layer for the deposition,[39,40] and it was reported that a (111)-textured tetragonal ZrO_2 film can be grown epitaxially on a (111)-textured Pt layer to lower the interfacial energy.[49-51] Considering the structural similarities between ZrO_2 and HfO_2, a (111)-textured HZO

film is expected to be grown on a (111)-textured Pt BE. According to the above discussion, the (111)-textured HZO film would not show any ferroelectricity, which was indeed the case, as shown below, suggesting that the in-plane tensile strain is the main driving force for o-phase formation.

Figure 3.12a shows the thickness variations of the HZO films as a function of the ALD cycles on the TiN and Pt BEs. The growth rate of the HZO films on Pt (~0.18 nm/cyc) was ~50% larger than that on TiN (~0.12 nm/cyc). This result is contradictory to the recent report on NiO by Song et al., in which the growth rate of the local epitaxial film with a (111) orientation on the (111)-oriented Pt was the smallest among the W, Ru, and Pt substrates.[40] This contradiction is thought to have originated from the difference in relative energy of the (111)-textured surface and interface of the HZO and NiO films on the (111)-textured Pt BE, which originated from the different crystal structure. The crystal structure of HZO and NiO are based on the fluorite and rock salt structure, respectively. The origin of the local epitaxial growth for both materials was the lowering of the interfacial energy of Pt and each film. Another important factor that can influence the growth behaviour, however, is the energy of the (111)-oriented surface. In fact, the (111)-textured surface of ZrO_2 had the lowest energy whereas that of NiO had the largest energy among the low-index surfaces, such as the (100)-, (110)-, and (111)-textured surfaces.[52,53] Therefore, the nucleation of the (111)-textured NiO films can be hindered by the competition between the

high surface energy and the low interfacial energy, and the successive growth of NiO films will also be hindered by the large density of adsorption sites, which can be estimated from the high surface energy. In the case of the (111)-textured HZO, in contrast, both the surface and interfacial energy of the (111) orientation are the smallest, and the nucleation and growth rate of the films will be larger than those of the films with random orientations.

Figure 3.12b shows the cross-sectional SEM image of the ~40-nm-thick HZO film on the TiN BE showing the uniform microstructure of the HZO films. Figure 3.12c shows the change in the average grain size (D_{avg}) calculated from SEM images as a function of t_f. Figure 3.13 shows the SEM images of the HZO films on the TiN and Pt electrodes with various film thicknesses (t_f), which were used to analyse the average grain size included in Figure 3.12c.

The D_{avg} of the HZO films on the TiN BE increased linearly with increasing t_f whereas that on the Pt BE seems to have been saturated at ~17 nm. It was reported that the critical D_{avg} values at which the t-phase is transformed into m-phase are known to be ~30 and ~5 nm for ZrO_2 and HfO_2, respectively.[45,14] Therefore, that of the HZO film is estimated to be ~18 nm, well matching the present results. From the change of the D_{avg} value in Figure 3.12c, it is expected that some parts of the HZO films that are thicker than ~15 and ~25 nm on the TiN and Pt BEs could be m-phase. Figures 3.14a and b show the GAXRD spectra of the HZO films on the TiN

BE and the XRD spectra of the HZO films on the Pt BE using the θ-2θ scan mode, respectively. On the TiN BE, the HZO films showed a polycrystalline nature with random crystallographic orientations; thus, the diffraction peaks of the HZO films could hardly be found in the θ-2θ scan mode, but could be clearly observed in the GAXRD spectra. With increasing t_f, the intensity of the diffraction peaks from the m-phase grew larger, which is consistent with the previous report.[9] In contrast, the diffraction peaks of the HZO films on the Pt BE could hardly be found using GAXRD but could be clearly observed in the θ-2θ scan results. The (111)-preferred texture of the t-phase HZO films could be clearly seen in the case of the 13-nm-thick films whereas the intensity of the m(111) and m(200) peaks increased as the t_f increased over that value (the m(200) peaks might be the superposition of the peaks from various planes, such as m(200), m(020), and m(002)). From these XRD analyses, it can be noted that the (111)-textured HZO films were deposited on the Pt BE whereas the films with random orientations were grown on the TiN BE.

As the next step, the in-plane strain (ε_{in}) of the HZO films on the TiN and Pt BEs was calculated from the variations in the inter-planar distance of the (111) planes (d_{111}), which could be estimated from the shift of the t(111) diffraction peaks. In fact, the best method for measuring the in-plane tensile strain (ε_{in}) in thin films is the $\sin^2\Psi$ method, in which the inter-planar distance of specific planes in various orientations are measured via XRD, by

tilting the sample according to each major orientation of the grains. This method, however, can hardly be applied to polycrystalline films with random crystallographic orientations, whose thickness is only a few nm. Therefore, it was impossible to apply this method to the HZO films on the TiN BE in the present experiment. On the other hand, ε_{in} can also be estimated from the GAXRD spectra from the shift of the diffraction peak of the specific plane. In the present study, the diffraction peak from the (111) planes was chosen for the analysis due to the following two reasons: the intensity of the diffraction peak from t-phase (111) was the strongest among the diffraction peaks, and the t-phase (111) peak was free from superposition with the other diffraction peaks. Figure 3.15a shows the schematic diagram that shows the grain that is the origin of the t-phase (111) diffraction in the GAXRD spectra. The (111) direction was ~15° tilted from the substrate-normal direction. (It should be noted that the incidence angle was 0.5°, and the 2θ value of the t-phase (111) diffraction peak was ~30.5°.) The next question is how ε_{in} can be calculated from the diffraction peaks from the (111) planes with a specific direction. Figures 3.15b and c show the Mohr's circle for the stress and strain in the thin films, respectively. The three-dimensional Mohr's circle generally consists of three circles, which shows the stress state in the xy-, yz-, and zx-plane, respectively. The Mohr's circle for thin films, however, is relatively simpler due to the absence of the stress along the substrate-normal direction. In addition, if the in-plane stress is independent of the in-plane

directions, which must be the case here, it becomes even simpler. In this case, the three-dimensional Mohr's circle for the stress in a thin film consists of only one circle, with the condition that $\sigma_{in}=\sigma_0$ and $\sigma_{out}=0$, where σ_{in} and σ_{out} are the in-plane and out-of-plane stresses, respectively. Therefore, its x-intercepts are 0 and σ_0, as can be seen in Figure 3.15b. The Mohr's circle for the strain in a thin film can also be constructed from that for the stress, in which $\varepsilon_{in}=(1-\nu)\sigma_0/Y$ and $\varepsilon_{out}=-2\nu\sigma_0/Y$. If ν is assumed to be 1/3, ε_{in} and ε_{out} will be ~0.67 σ_0/Y and ~-0.67 σ_0/Y, respectively, as can be seen in Figure 3.15c. As mentioned above, the t-phase (111) diffraction peak in the GAXRD spectra is 15° tilted from the substrate-normal direction and corresponds to the 30° rotation in the Mohr's circle. Therefore, ε_{in} can be calculated from this relation. Figures 3.16a and b show the GAXRD spectra of the HZO films on the TiN BE and the XRD spectra of the HZO films using normal θ-2θ scan on the Pt BE, respectively. As can be seen in the figures, the t-phase (111) peaks shifted to the high 2θ angle region with increasing t_f, which means that the inter-planar distance of the (111) planes (d_{111}) decreased with increasing t_f. Figure 3.16c shows the change in d_{111} as a function of t_f. The ε_{in} values of the HZO films can be calculated from the method mentioned above. The final result of the change in ε_{in} is included in figure 3.14c. For the calculation, the Poisson's ratio was assumed to be 1/3, and the d_{111} of the t-phase HZO was taken as 2.96 Å, which was calculated from the lattice constants of the tetragonal ZrO_2 and HfO_2 in the

literature.[19] From the calculated strain along the <111> direction, the in-plane strain can be calculated with the stress conditions in the thin films ($\sigma_x=\sigma_y=\sigma_0$, $\sigma_z=0$; the z-axis is along the substrate-normal direction whereas the x- and y-axis are along the in-plane directions) and the relation of the <111> direction in the GAXRD spectra and in-plane direction. Figure 3.14c shows the change of the ε_{in} of the HZO films on the TiN and Pt BEs as a function of t_f. The HZO film on the TiN BE showed an in-plane tensile strain of >1.5% when t_f >10 nm, which means that the t-phase HZO film in this case can be transformed into o-phase if the crystallographic orientation is favourable. It can be noted that the HZO film on Pt also shows similar or even higher tensile strain values when t_f>10 nm. The ε_{in} of the ~5-nm-thick HZO film on the TiN BE, however, was lower than the critical ε_{in} of 1.5 % for its transition from t-phase to o-phase. Figures 3a and b show the P-E hysteresis curves of the HZO capacitors with various t_f values on the TiN and Pt BEs. In the case of the HZO capacitors on TiN, the P_r values of the films were >15 $\mu C/cm^2$ when 9 nm$\leq t_f \leq$20 nm, whereas P_r decreased rapidly with increasing t_f when t_f>20 nm. This was due to the m-phase formation with increasing t_f, which can be understood from Figure 3.14a. The antiferroelectric-like double loop can be observed in the case of the ~5-nm-thick HZO film. The double hysteresis loop implies that there exists phase transition between the ferroelectric and non-ferroelectric phases, induced by the applied electric field.[21] This suggests that the ~1.5% tensile ε_{in}

corresponds to the boundary between the t- and o-phase. In the case of the HZO capacitors on the Pt BE, in contrast, their P_r values were almost ~0 for all t_f values despite the fact that the ε_{in} was as high as that on the TiN TE and the grain size was small enough not to totally induce the m-phase. This well coincides with the expectation on the evolution of the o-phase based on the calculations of the strains along each axis discussed above and summarized in Table I.

To further confirm that such a large difference in the ferroelectric properties between the capacitors with Pt/TiN(TE)/HZO/TiN(BE) and TiN(TE)/HZO/Pt(BE) stacking sequences was not induced by the contact properties between the metallic electrode and oxide films, a structure with a Pt(TE)/HZO/TiN(BE) configuration was also fabricated. This can be achieved, in fact, by omitting the TiN (TE) layer when fabricating the Pt/TiN (TE)/HZO/TiN (BE) structure. Figure 3.17c shows the P-E loop of the Pt(TE)/HZO/TiN(BE) and Pt/TiN(TE)/HZO/TiN(BE) samples, where the HZO film thickness was commonly 8.4 nm. While there was a slight degradation in the P_r value when the TiN (TE) layer was omitted, the two samples showed similar ferroelectric properties, suggesting that the large degradation in the ferroelectric properties from the HZO film on Pt (BE) was really due to the different crystallographic structures rather than the electrical contact properties.

For the HZO films on the TiN BE, which have random grain

orientations, some grains could have appropriate orientations for o-phase formation, which are expected to be the (110)-oriented or near-(110)-oriented grains in this case, and they can be transformed into o-phase with a ε_{in} large enough for o-phase formation. It should be noted that this does not mean that the whole film exists in the o-phase. From the first-order approximation considering the degree of ferroelectric distortion of the lattice and the effective charges of the anions and cations, the theoretical P_r of the (001)-textured o-HfO_2 and o-ZrO_2 could be as large as ~51-53 $\mu C/cm^2$, and that of the fully (110)-textured film is estimated to be as large as ~36-37 $\mu C/cm^2$. Therefore, the experimentally determined P_r value of 16 $\mu C/cm^2$ for the 9.2-nm-thick HZO film implies that only ~44% of the grains were transformed into o-phase under the tensile ε_{in}, even when the o-phase grains are assumed to be (110)-oriented. This suggests that there is plenty of room for further improving the ferroelectric performance by controlling the grain size and orientations.

One remaining question is what the possible origins of the large in-plane tensile strain are. A ~1.5% ε_{in} coincides with the ~4.7 GPa σ_{in} in HZO. Even though there are many possible origins of σ_{in} in thin films, such as surface stress, thermal stress, and coalescence stress, the only origin of such a large σ_{in} is believed to be the stress formed during the island coalescence, which is usually observed in the Volmer-Weber-type growth.[21] From the simple calculations, the surface and thermal stresses were determined to be

as small as ~0.1 and <2 GPa, respectively, which are not high enough for achieving the high ε_{in} in the present experiment. In contrast, the coalescence stress can be as large as ~30 GPa based on the theoretical equations suggested by Thompson and Clemens, with the island size just before the coalescence of HfO_2 and ZrO_2 during ALD.[21] A short discussion on the magnitude of the coalescence stress is included in section 3.3.3. The experimental values, in fact, are generally much smaller than the theoretical ones because such a large stress could be relaxed due to the other mechanisms, such as the diffusion of atoms.[21]

In conclusion, to elucidate the origin of the occurrence of ferroelectricity in HZO films, the effect of their ε_{in} and texture on the ferroelectric properties was examined. From the considerations of the structural difference and the possible transformation route by the mechanical strain effect in the thin-film growth between the t- and o-phase, it was noted that the (111) orientation of the HZO film was inappropriate for o-phase formation due to the almost equivalent tensile strain along the a-, b-, and c-axis. Using highly (111)-textured Pt BE films, highly (111)-textured t-phase HZO films were deposited. Even though the HZO films on the Pt BE showed an almost equivalent ε_{in} value compared to those on the TiN BE, and a small enough average grain size to induce the t-phase (and subsequently, the o-phase, if the strain condition was appropriate), they did not show ferroelectricity at all. In addition, it was noted that the electrical contact

properties of the Pt/HZO interface had an insignificant influence on the ferroelectric properties of the HZO films. Based on the results, it was concluded that the origin of the formation of the unstable o-phase under the ALD and the annealing conditions in this experiment was the large tensile strain along the c-axis of the t-phase, which could have been induced by the coalescence of the nucleating grains. This insight provides a way to further enhance the ferroelectric performance of the HfO_2-based thin films if their grain size and crystallographic orientations could be further optimized.

Table 3.1. The strain on the (100), (010), and (001) directions for various substrate-normal film orientations as a function of in-plane stress (σ_0) and elastic modulus (Y). The last line shows the relative ratio of substrate-normal remanent polarization ($P_{r,\perp}$) to the maximum remanent polarization along the c-axis of the o-phase ($P_{r,max}$).

	(100)	(001)	(110)	(101)	(111)
ε_{100}	$-0.67\sigma_0/Y$	$0.67\sigma_0/Y$	~0	~0	$0.33\sigma_0/Y$
ε_{010}	$0.67\sigma_0/Y$	$0.67\sigma_0/Y$	~0	$0.67\sigma_0/Y$	$0.33\sigma_0/Y$
ε_{001}	$0.67\sigma_0/Y$	$-0.67\sigma_0/Y$	$0.67\sigma_0/Y$	~0	$0.33\sigma_0/Y$
$P_{r,\perp} / P_{r,max}$	0 %	0 %	70.7 %	70.7 %	57.7 %

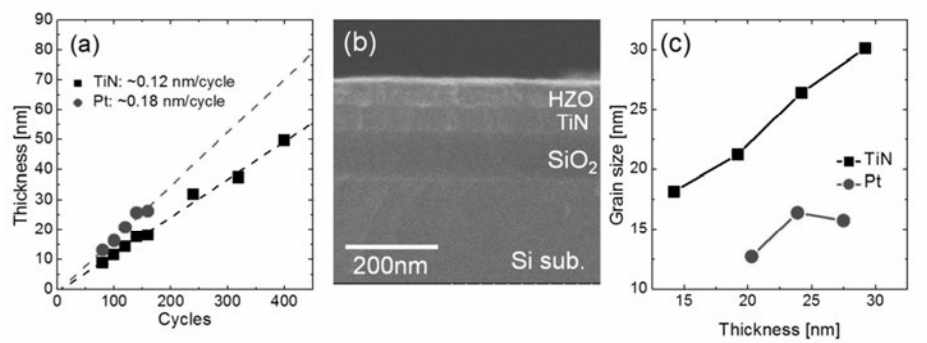


Figure 3.12. (a) Growth behaviour of the $Hf_{0.5}Zr_{0.5}O_2$ films on the TiN and Pt BEs as a function of the number of cycles of atomic layer deposition. (b) Cross-sectional scanning electron microscopy image of the 40-nm-thick $Hf_{0.5}Zr_{0.5}O_2$/TiN/Ti/SiO_2/Si-stacked sample. (c) Change in the average grain size of the $Hf_{0.5}Zr_{0.5}O_2$ films on the TiN and Pt BEs as a function of film thickness, respectively.

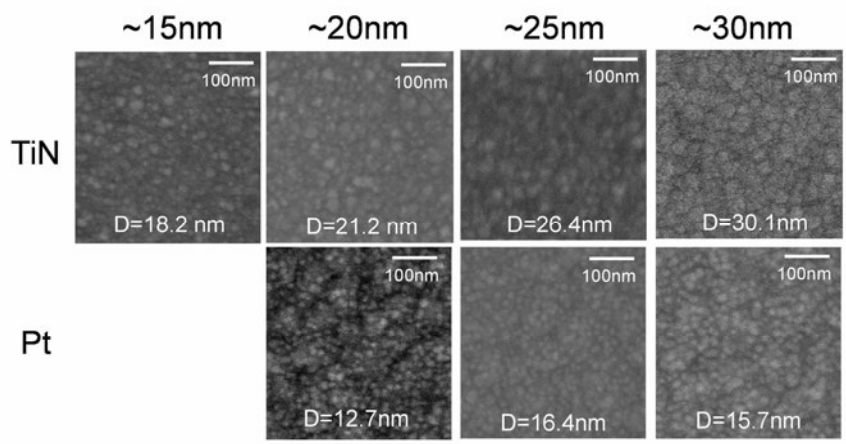


Figure 3.13. Scanning electron microscopy images of the HZO films on the TiN and Pt electrodes with various film thickness, which were used to analyze the average grain size included in Figure 3.12c.

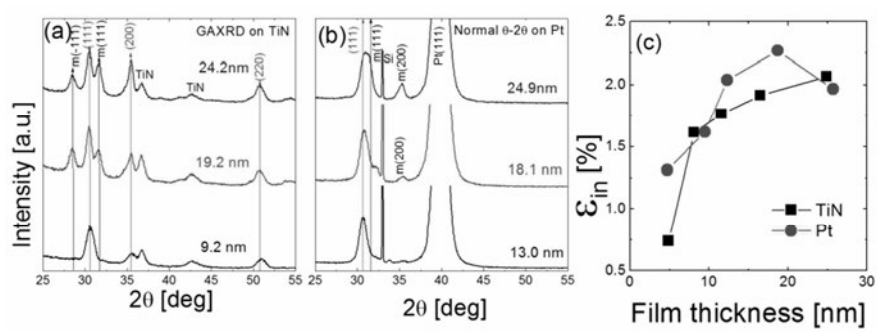


Figure 3.14. (a) Grazing-angle incidence angle X-ray diffraction spectra of the 9.8-, 19.6-, and 24.5-nm-thick $Hf_{0.5}Zr_{0.5}O_2$ films on the TiN BE. (b) Normal X-ray diffraction spectra of the 13.0-, 18.1-, and 24.9-nm-thick $Hf_{0.5}Zr_{0.5}O_2$ films on the Pt BE. (c) Change in the in-plane strain calculated from the shift of the t(111) diffraction peaks as a function of film thickness, respectively.

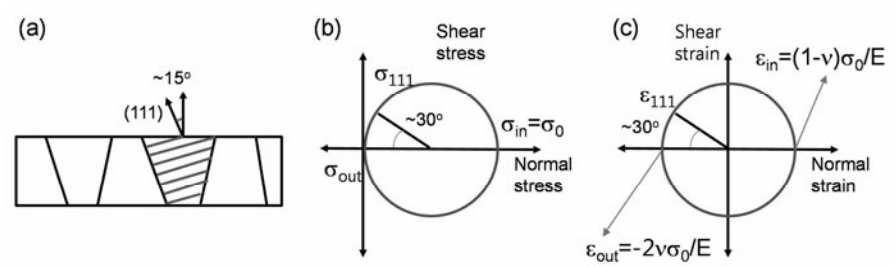


Figure 3.15. (a) Schematic diagram for the grain from which the t(111) diffraction peak in GAXRD originated in the $Hf_{0.5}Zr_{0.5}O_2$ films on the TiN electrode. (b) Mohr's circle for stress and (c) that for strain in the $f_{0.5}Zr_{0.5}O_2$ films.

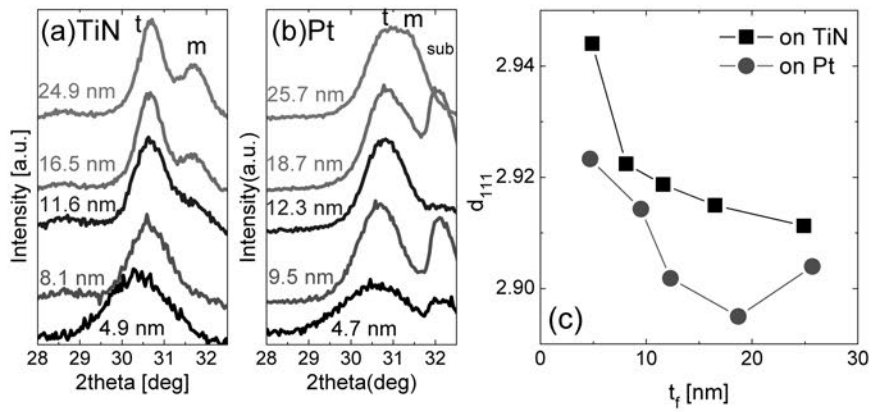


Figure 3.16. (a) Grazing-angle incidence angle X-ray diffraction spectra of the $Hf_{0.5}Zr_{0.5}O_2$ films on the TiN electrode and (b) X-ray diffraction spectra using normal θ-2θ scan of the $Hf_{0.5}Zr_{0.5}O_2$ films on the Pt electrode. (c) Change in the inter-planar distance of the (111) planes of the $Hf_{0.5}Zr_{0.5}O_2$ films on the TiN and Pt electrodes as a function of film thickness.

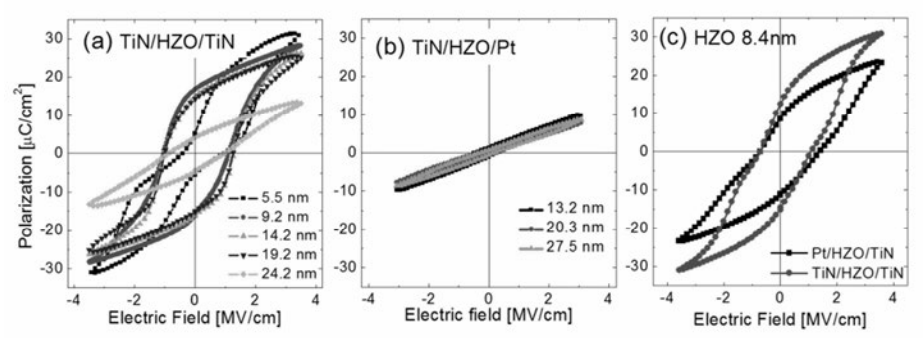


Figure 3.17. (a) P-E characteristics of the $Hf_{0.5}Zr_{0.5}O_2$ capacitors with various film thicknesses on TiN, and (b) those on Pt, respectively. The TE was Pt(60nm)/TiN(20nm) for both cases. (c) P-E characteristics of the 8.4-nm-thick $Hf_{0.5}Zr_{0.5}O_2$ capacitor on TiN with Pt(60nm)/TiN(20nm) and Pt(80nm).

3.3.4.2. Effect of microstructure: comparative study on $Hf_{0.5}Zr_{0.5}O_2$ films on TiN and Ir bottom electrode

HZO films were deposited on TiN or Ir electrode using ALD at a substrate temperature of 280 °C using $Hf[N(C_2H_5)CH_3]_4$, $Zr[N(C_2H_5)CH_3]_4$, and ozone as the Hf-precursor, Zr-precursor, and oxidant, respectively. The 50-nm-thick TiN and 100-nm-thick Ir electrodes were deposited on SiO_2/Si substrates by DC reactive stuttering and sputtering, respectively. The growth per cycle of HfO_2 and ZrO_2 were almost identical (~ 0.12 and ~ 0.16 nm/cycle on TiN and Ir, respectively), so HZO films with an Hf : Zr ratio of 0.5 : 0.5 can be deposited with an HfO_2 : ZrO_2 ALD cycle ratio of 1:1. For the electrical characterization, Pt (60 nm)/TiN (20 nm) TE was deposited using DC sputtering through a shadow mask having a hole whose diameter is 300 μm (TiN contacts the HZO film). After the deposition of TE, post-metallization-annealing was performed for 30 s at 500 °C in an N_2 atmosphere using RTA for the crystallization of the films. The composition and t_f of HZO films were examined using X-ray fluorescence (Quant'X, Thermo SCIENTIFIC) and ellipsometry (L-116d, Gaetner), respectively. For electrical characterization, the polarization-electric field (P-E) characteristics were measured using a ferroelectric tester (TF analyzer 2000, Aixacct systems) at a frequency of 1kHz. The crystal structure of the HZO films was analysed using X-ray diffractometer (X'pert pro, Panalytical) by GAXRD

(incidence angle = 0.5 °) or normal θ-2θ scan.

Figure 3.18a shows the growth behaviour of HZO films on TiN and Ir BE. The growth rate of HZO film on Ir BE was about ~26 % larger than that on TiN BE. It is thought to be due to the orientation of the polycrystalline films or complicated chemical reactions related with BE, but it is not the focus of the present section, and it needs further study to elucidate the origin of the unexpected differencies in the growth behaviour.[39,40] Figure 3.18b and 3.18c show the cross-sectional SEM image of 40-nm-thick HZO films on TiN and Ir BE, respectively. The deposition of uniform and conformal HZO films with clean interface could be confirmed in the SEM images. Figure 3.19a and b shows the polarization-electric field hysteresis curves of HZO films with various t_f on TiN and Ir electrode, respectively, whereas Figure 3.19c shows the change of $2P_r$ values calculated from the P-E hysteresis curves in figure 3.19a and b. It could be firstly confirmed that the excellent ferroelectric properties with large $2P_r$ of >32 $\mu C/cm^2$ could be observed for the case of 12.2-nm-thick HZO films on Ir BE. This is the first report on the ferroelectric HfO_2-based films on noble metal electrode. For the case of HZO capacitors on TiN BE, they could show ferroelectric hysteresis with large $2P_r$ of > 30 $\mu C/cm^2$ with t_f range of 9.2 – 19.2 nm, and $2P_r$ decreased to ~9 $\mu C/cm^2$ abruptly when t_f increases to 24.2 nm. This might be due to the formation of m-phase with increasing t_f and grain size as reported by previous report in HZO.[9] Therefore, the critical thickness (t_{crit})

for the disappearance of ferroelectricity of HZO films on TiN BE is thought to be ~20 nm. For the case of HZO capacitors on Ir BE, on the other hand, $2P_r$ decreased to ~ 20 $\mu C/cm^2$ and ~8 $\mu C/cm^2$ abruptly when t_f increases to 15.3 and 18.3 nm, respectively. Thus, t_{crit} is thought to be ~13 nm on Ir BE, which is ~35 % smaller compared to that on TiN BE. The most probable origin for the unexpected differences of HZO films on TiN and Ir BE is thought to be the difference of the crystal structure of the films. It was already reported that various polymorphs of HZO are competing at the nanoscale on TiN BE. In addition to that, the size effect originated from the surface energy argument is generally accepted both in ZrO_2 and HfO_2, which shows that the microstructure of ZrO_2 and HfO_2 is a key factor which affects their crystal structure significantly. Therefore, the crystal structure and microstructure of HZO films on TiN and Ir BE needed to be examined.

Figure 3.20a and b shows the GAXRD of HZO films with various t_f on TiN and Ir BE, respectively. Due to the small t_f and random orientation of HZO films, the diffraction peaks could be hardly found in XRD spectra using normal θ-2θ scan, and the data is not included in the present dissertation. The diffraction peaks from (111)-, (200)-, and (220)-planes of o-phase HZO could be clearly seen in the GAXRD spectra. With increasing t_f, the intensity of the diffraction peaks from (111)- and (-111)-planes increases both on TiN and Ir BE. Other diffraction peaks of m-phase could be hardly analysed due to the superposition of diffraction peaks from the other set of

planes. The quantitative analyses on the relative portion of m- and o-phase were also tried for the GAXRD spectra with the 2θ range of 27-33°, to which diffraction peaks from (111)- and (-111)-planes of m-phase (m(111) and m(-111) and that from (111)-planes of o-phase (o(111))belong. This range was chosen due to the largest intensity of the diffraction peaks in that range and the absence of the diffraction peaks from the planes with similar inter-planar distance. For the quantitative analysis, the background intensity was subtracted from the original spectra firstly, and then the three diffraction peaks of m(111), o(111), and m(-111) were fitted using Gaussian function. Figure 3.21a shows the calculated relative ratio of the area of o(111) diffraction peaks calculated from the GAXRD spectra. The results of the fitting for the GAXRD spectra of HZO films on Ir and TiN BE can be seen in figure 3.22 and 3.23, respectively. As the next step, the area of the each diffraction peaks were calculated by integrating the area of the diffraction peaks, and the relative ratio of the area of o(111) diffraction peak compared to the summation of area of all the three peaks was calculated finally. The relative ratio of area of o(111) diffraction peak of HZO films on TiN BE was 100 % with t_f of 9.2 nm, and it decreases to ~92, ~76, ~52, and ~36 % when tf increases to 14.2, 19.2, 24.2, and 29.2 nm, respectively. For the case of HZO films on Ir BE, on the other hand, the relative ratio of area of o(111) diffraction peak of HZO films was also 100 % with t_f of 12.2 nm, but it decreases to ~75, ~63, ~58, and ~57 % when t_f increases to 15.3, 18.3, 21.4,

and 24.4 nm, respectively. Compared to the The relative ratio of the area of o(111) diffraction peak of ~76 % is thought to be the minimum limit for the excellent ferroelectric properties with large P_r, and P_r decreases abruptly with the further decrease of the relative ratio of o(111) peak. It can be easily noticed that the abrubt decrease is due to the increase of the portion of m-phase, and it is generally accepted that m-phase is generally formed with relatively large crystallite or grian size compared to metastable t- or o-phase. Therefore, the microstructure of HZO films on TiN and Ir BE needs to be analysed to elucidate the origin of the increase of the portioan of m-phase.

Figure 3.21b shows the change of the average grain size (D_{avg}) of HZO films on TiN and Ir BE as a function of t_f. The D_{avg} was calculated from the plan-view SEM images in figure 3.23. Interestingly, D_{avg} of HZO films on Ir BE was much larger than that on TiN BE with the equivalent t_f, and the result was well-matched with the fact that t_{crit} of HZO films on Ir BE (~13nm) was smaller than that on TiN BE (~20nm). On the other hand, D_{avg} for the HZO films with $t_f = t_{crit}$ on TiN and Ir BE is estimated as ~18 nm from literature.[14,45] Even though the value was slightly larger than the critical grain size calculated from the literature (~18 nm), the critical value can show differences with other different factors such as deposition conditions. Anyway, the differences in t_{crit} of HZO films on TiN and Ir BE could be explained by the grain size effect successfully.

In conclusion, the physical and ferroelectric properties of HZO films

with various t_f on TiN and Ir BE were studies systematically. HZO films can show the excellent ferroelectricity with large P_r of >15 μC/cm^2 both on TiN and Ir BE. Ir was the second electrode on which HZO film can show excellent ferroelectricity, and it was the first report on its ferroelectricity. $2P_r$ of HZO films decreases with increasing t_f with the increase of the portion of m-phase. However t_{crit} for the degradation of the ferroelectricity of HZO films were different for TiN (~20 nm) and Ir BE (~13 nm). From the peak analysis on the GAXRD spectra of HZO films with various t_f, the relative ratio of the intensity of o(111)/{o(111)+m(111)+m(-111)} can be calculated. Interestingly, the relative ratio of HZO films with $t_f = t_{crit}$ both on TiN and Ir BE were all 75-76 %, which might corresponds to the critical relative ratio of o(111) peak. On the other hand, the grain size of HZO films on Ir electrode is relatively larger than the of HZO films with equivalent t_f, and this is the reason for the larger portion of m-phase in HZO films on Ir BE compared with that on TiN BE. Therefore, the difference of t_{crit} on TiN and Ir BE could be explained successfully by the size effect for the m-phase formation.

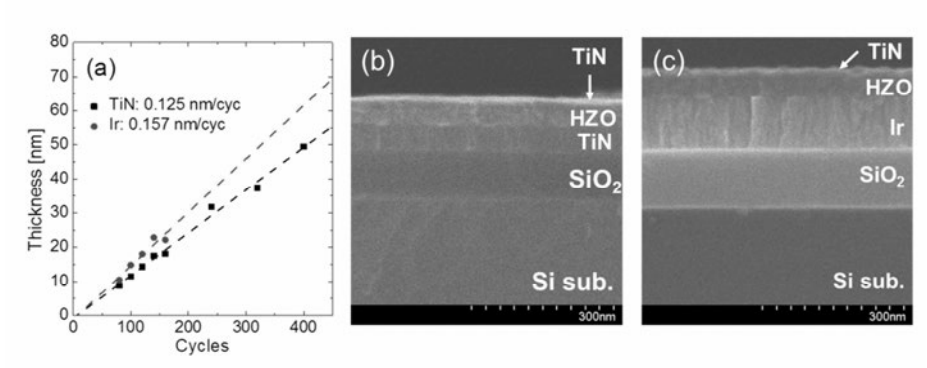


Figure 3.18. (a) The change of thickness of $Hf_{0.5}Zr_{0.5}O_2$ films on TiN and Ir bottom electrode as a function of number of cycles, and cross-sectional scanning electron microscope images of ~40-nm-thick $Hf_{0.5}Zr_{0.5}O_2$ films on (b) TiN and (c) Ir bottom electrode, respectively.

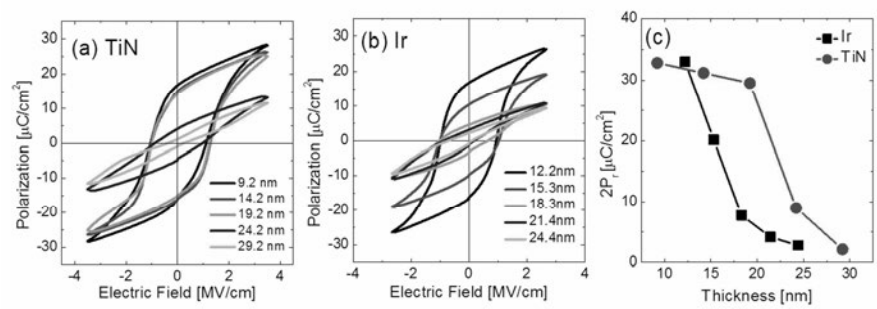


Figure 3.19. The polarization-electric field hysteresis curves of $Hf_{0.5}Zr_{0.5}O_2$ films with various film thickness on (a) TiN and (b) Ir bottom electrode, and (c) the change of double remanent polarization of $Hf_{0.5}Zr_{0.5}O_2$ films on TiN and Ir bottom electrode as a function of film thickness, respectively.

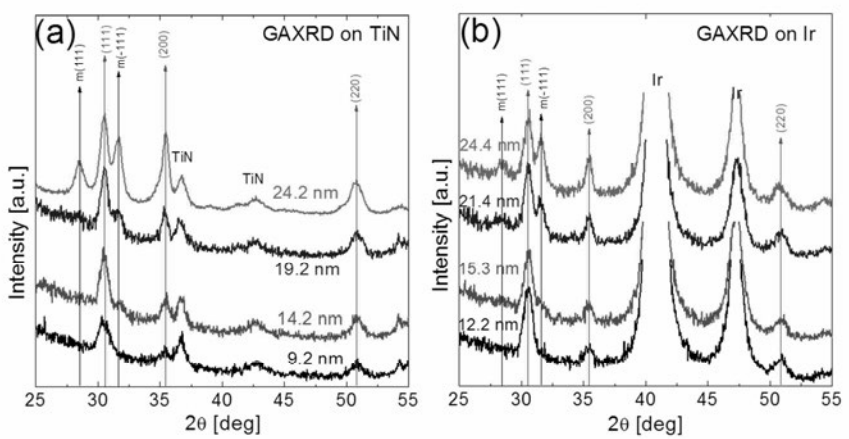


Figure 3.20. The grazing-angle incidence X-ray diffraction spectra of $Hf_{0.5}Zr_{0.5}O_2$ films with various film thickness on (a) TiN and (b) Ir bottom electrode, respectively.

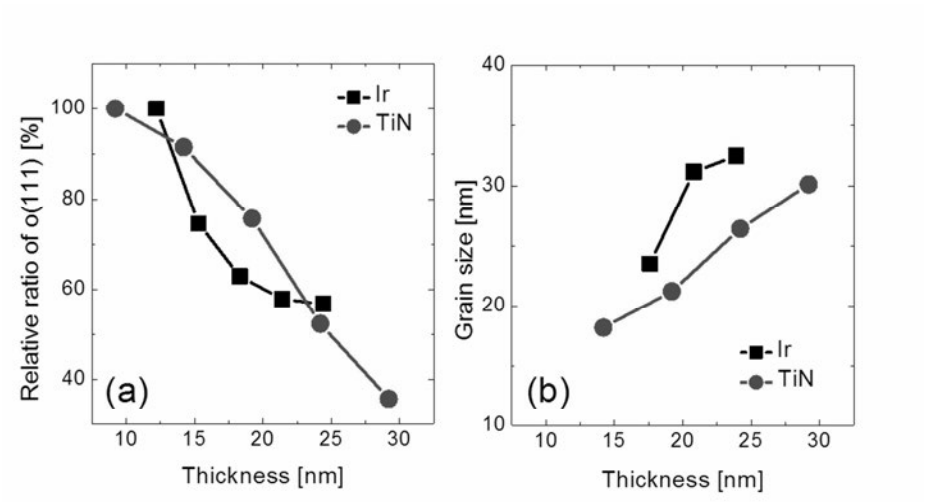


Figure 3.21. (a) The change of the ratio of the intensity of o(111)/{o(111)+m(-111)+m(111)} and (b) that of grain size as functions of film thickness, respectively.

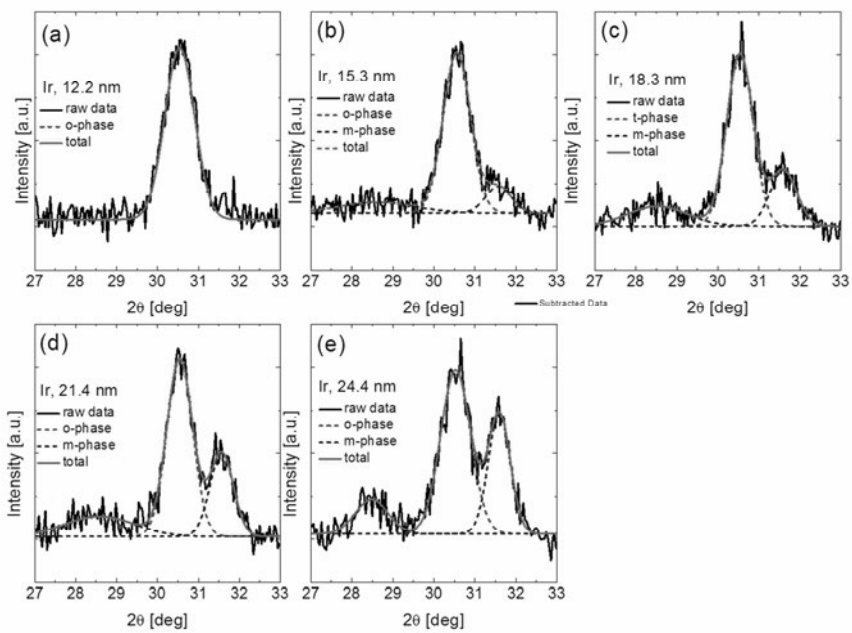


Figure 3.22. The result of peak analysis of grazing-angle incidence X-ray diffraction spectra of $Hf_{0.5}Zr_{0.5}O_2$ films on Ir bottom electrode with film thickness of (a)12.2, (b) 15.3, (c) 18.3, (d) 21.4, and (e) 24.4 nm, respectively.

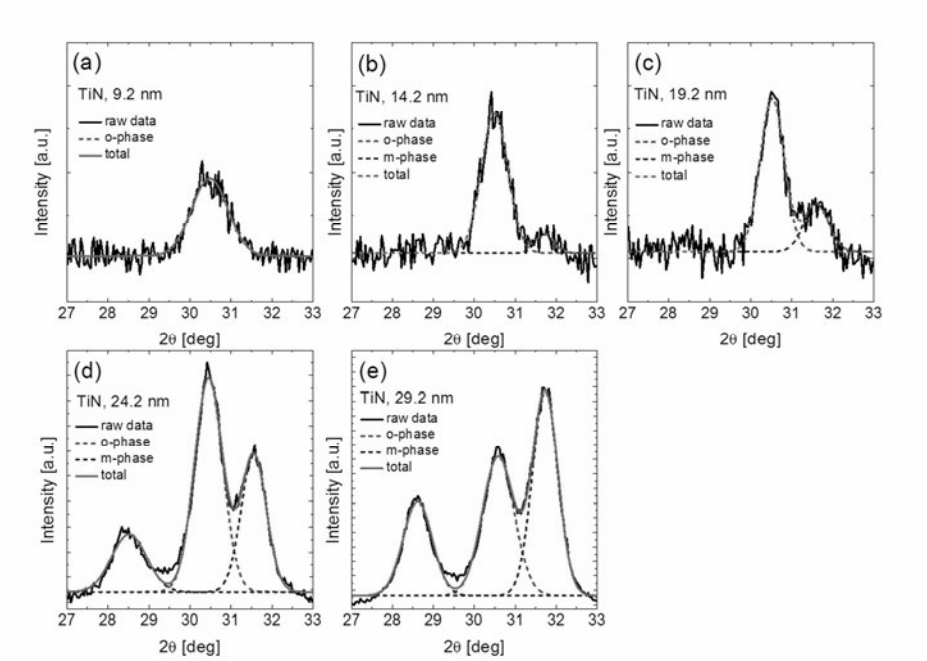


Figure 3.23. The result of peak analysis of grazing-angle incidence X-ray diffraction spectra of $Hf_{0.5}Zr_{0.5}O_2$ films on TiN bottom electrode with film thickness of (a) 9.2, (b) 14.2, (c) 19.2, (d) 24.2, and (e) 29.2 nm, respectively.

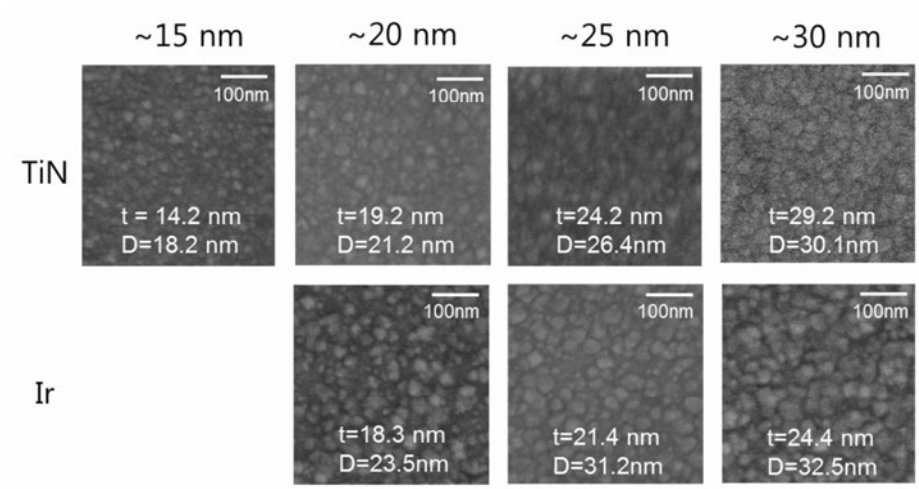


Figure 3.24. The plan-view sccaning electron microscope images of $Hf_{0.5}Zr_{0.5}O_2$ films with various film thickness on Ir and TiN bottom electrode.

3.3.5. Schematic phase diagram

From the experimental results in the previous sections, it can be noted that there are many factors affect the polymorphism in $Hf_{1-x}Zr_xO_2$ films. Grain size is one factor which has been well known for surface energy argument. The critical thickness for the phase boundary of t- and m-phase of HfO_2 and ZrO_2 was ~4 and ~30 nm, respectively. For the case of $Hf_{1-x}Zr_xO_2$ films whose x ~ 0.5, unexpected ferroelectric o-phase could be observed with the thickness range of 7 nm < t_f < 22 nm. The large tensile strain of ~1.5 % and grain size of < 25 nm are thought to be the essential conditions for the formation of ferroelectric o-phase for HZO. At the phse boundary of o- and t- phase, antiferroelectric behaviour could be observed, because the difference of free energy is small enough for the electric field induced phase transformation. On the other hand, the antiferroelectric behaviour cannot be observed at the phase boundary of o- and m-phase. It might be due to that o-phase cannot transform into m-phase directly as pointed by Böscke et al..[47] Figure 3.25 shows a schematic phase diagram of $Hf_{1-x}Zr_xO_2$ films annealed at 500 ^oC with various composition and thickness based on all the results in this chapter.

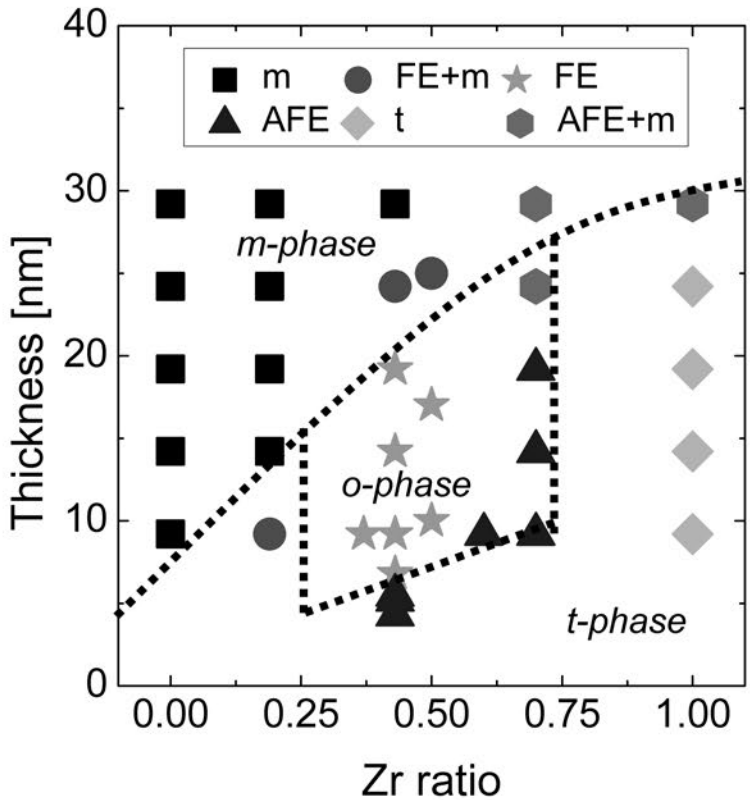


Figure 3.25. Schematic phase diagram of $Hf_{1-x}Zr_xO_2$ films annealed at 500 ^oC with various composition and thickness, where m, t, FE, and AFE correspond to monoclinic, tetragonal, ferroelectric, and antiferroelectric phase, respectively.

3.4. Conclusions

In this chapter, the origin of the ferroelectricity in $Hf_{1-x}Zr_xO_2$ thin films was examined based on their crystallographic structure, micro-structures and resulting in-plane stress. For all the cases of HfO_2, ZrO_2, and $Hf_{1-x}Zr_xO_2$ films, huge in-plane tensile stress could be observed which is thought to be formed during the crystallite coalescence of Volmer-Weber type growth. However, the ferroelectricity could be seen only for the case of $Hf_{1-x}Zr_xO_2$ films thinner than 25 nm. For the case of HfO_2, m-phase was easily formed with small grain size, whereas o-phase cannot be formed due to the large difference (~2%) of crystal structure of t-phase and o-phase. The o-phase can be formed only in HZO films because the formation of m-phase is prevented and ε_{in} of HZO film is large enough (>1.5%) for the formation of o-phase. On the other hand, the ferroelectric behaviors of HZO films on BE other than TiN were also firstly reported. HZO also can show ferroelectricity on Ir or Ru electrode, even though the performance was worse than those on TiN electrode. However, HZO did not show ferroelectricity on Pt electrode with the strongly (111)-prefered onrientation. It might be due to the symmetry of the (111)-oriented grain, and it also supports that the formation of o-phase is strongly related with the in-plane stress. In addition to that, the origin of the huge tensile stress in thin films was also examined, and the tensile stress formed during crystallite coalescence was the only possible origin of the huge tensile stress. Therefore,

it could be concluded that the unexpected ferroelectric phase was formed in near-stoichiometric $Hf_{1-x}Zr_xO_2$ films with appropriate grain size (<25nm) under huge tensile in-plane stress which might be formed during island coalescence process of Volmer-Weber type growth.

3.5. References

[1] J. F. Scott, *Ferroelectric Memories.* (Springer-Verlag Berlin Heidelberg, 2000).

[2] D. S. Jeong, R. Thomas, R. S. Katiyar, J. F. Scott, H. Kohlsted, A. Petraru, and C. S. Hwang, *Rep. Prog. Phys.* **75**, 076502 (2012).

[3] T. S. Böscke, J. Müller, D. Bräuhaus, U. Schröder, and U. Böttger, *Appl. Phys. Lett.* **99**, 102903 (2011).

[4] J. Müller, U. Schröder, T. S. Böscke, I. Müller, U. Böttger, L. Wilde, J. Sundqvist, M. Lemberger, P. Kücher, T. Mikolajick, and L. Frey, *J. Appl. Phys.* **110**, 114113 (2011).

[5] S. Mueller, J. Mueller, A. Singh, S. Riedel, J. Sundqvist, U. Schroeder, T. Mikolajick, *Adv. Funct. Mater.* **22**, 2412 (2012).

[6] J. Müller, T. S. Böscke, U. Schröder, S. Mueller, D. Bräuhaus, U. Böttger, L. Frey, and T. Mikolajick, *Nano Lett.* **12**, 4318 (2012).

[7] S. Mueller, C. Adelmann, A. Singh, S. Van Elshocht, U. Schroeder, and T. Mikolajicka, *ECS J. Solid St. Sci. and Technol.* **1**, N123 (2012).

[8] M. H. Park, H. J. Kim, Y. J. Kim, W. Lee, H. K. Kim, and C. S. Hwang, *Appl. Phys. Lett.* **102**, 112914 (2013).

[9] M. H. Park, H. J. Kim, Y. J. Kim, W. Lee, T. Moon, and C. S. Hwang, *Appl. Phys. Lett.* **102**, 242905 (2013).

[10] O. Ohtaka, H. fukui, T. Kunisada, T. Fujisawa, K. Funakoshi, W. Utsumi, T. Irifune, K. Kuroda, and T. Kikegawa, *J. Am. Ceram. Soc.* **84**,

1369 (2001).

[11] O. Ohtaka, H. fukui, T. Kunisada, T. Fujisawa, K. Funakoshi, W. Utsumi, T. Irifune, K. Kuroda, and T. Kikegawa, *Phys. Rev. B* **63**, 174108 (2001).

[12] J. E. Lowther, J. K. Dewhurst, J. M. Leger, and J. Haines, *Phys. Rev. B* **60**, 14485 (1999).

[13] E. H. Kisi, *J. Am. Ceram.* Soc. **81**, 741 (1998).

[14] M. Shandalov and P. C. Mclntyre, *J. Appl. Phys.* **106**, 084322 (2009).

[15] D. -Y. Cho, H. S. Jung, I. –H. Yu, J. H. Yoon, H. K. Kim, S. Y. Lee, S. H. Jeon, S. Han, J. H. Kim, T. J. Park, B. –G. Park, *Chem. Mater.* **24**, 3534 (2012).

[16] Y. S. Kim, D. H. Kim, J. D. Kim, Y. J. Chang, T. W. Noh, J. H. Kong, K. Char, Y. D. Park, S. D. Bu, J.-G. Yoon, and J.-S. Chung, *Appl. Phys. Lett.* **86**, 102907 (2005).

[17] H. You, *J. Appl. Cryst.* **32,** 614 (1999).

[18] T. Olsen, U. Schröeder, S. Müller, A. Krause, D. Martin, A. Singh, J. Muller, M. Geidel, and T. Mikolajick, *Appl Phys. Lett.* **101**, 082905 (2012).

[19] J. E. Jaffe, R. A. Bachorz, and Gutowski, Phys. Rev. B 72, 144107 (2005).

[20] W. Pabst, G. Tichá, and E. Gregorová, *Ceramics – Silikáty* **48**, 41 (2004).

[21] W. D. Nix and B. M. Clemens, *J. Mater. Res.* **14**, 3467 (1999).

[22] M. L. Green, A. J. Allen , X. Li , J. Wang , J. Ilavsky , A. Delabie , R. L. Puurunen, and B. Brijs, *Appl. Phys. Lett.* **88**, 032907 (2006).

[23] W. F. A. Besling, E. Young, T. Conard, C. Zhao, R. Carter, W. Vandervorst, M. Caymax, S. De Gendt, M. Heyns, J. Maes, M. Tuominen, and S. Haukka, *J. Non-Cryst. Solids* **303**, 123 (2002).

[24] E. P. Gusev, C. Cabral, M. Copel, C. D'Emic, and M. Gribelyuk, *Microelectron. Eng.* **69**, 145 (2003).

[25] E. H. Kisi and C. J. Howard, *J. Am. Ceram. Soc.* **81**, 1682 (1998).

[26] M. W. Pitcher, S. V. Ushakov, A. Navrotsky, B. F. Woodfield, G. Li, and J. Boerio-Goates, *J. Am. Ceram. Soc.* **88**, 160-167 (2005).

[27] E. K. Akdogan, C. J. Rawn, W. D. Porter, E. A. Payzant, and A. Safari, *J. Appl. Phys.* **97**, 084305 (2005).

[28] R. N. Bhowmik, R. Ranganathan, and R. Nagarajan, *Phys. Rev. B* **73**, 144413 (2006).

[29] S. M. Selbach, T. Tybell, M. –A. Einarsrud, and T. Grande, *Chem. Mater.* **19**, 6478 (2007).

[30] L. Lu, L. P. Li, X. J. Wang, and G. S. Li, *J. Phys. Chem. B* **109**, 17151 (2005).

[31] W. M. Tong, L. P. Li, W. B. Hu, T. J. Yan, and G. S. Li, *J. Phys. Chem. C* **114**, 1512 (2010).

[32] M. Okubo, E. Hosono, J. Kim, M. Enomoto, N. Kojima, T. Kudo, H. Zhou, and I. Honma, *J. Am. Chem. Soc.* **129**, 7444 (2007).

[33] L. P. Li, Y. G. Su, and G. S. Li, *Appl. Phys. Lett.* **90**, 054105 (2007).

[34] G. S. Li, J. Boerio-Goates, B. F. Woodfield, and L. P. Li, *Appl. Phys. Lett.* **85**, 2509 (2004).

[35] K. Kamala Bharathi, N. R. Kalidindi, and C. V. Ramana, *J. Appl. Phys.* **108**, 083529 (2010).

[36] D. Harza, S. Datta, M. Mondai, J. Ghatak, P. V. Satyam, and A. K. Gupta, *J. Appl. Phys.* **103**, 103535 (2008).

[37] R. Banerjee , E. A. Sperling , G. B. Thompson , H. L. Fraser , S. Bose and P. Ayyub, *Appl. Phys. Lett.* **82**, 4250 (2003).

[38] M. Seo, S. K. Kim, J. H. Han, and C. S. Hwang, *Chem. Mater.* **22**, 4419 (2010).

[39] S. W. Lee, B. J. Choi, T. Eom, J. H. Han, S. K. Kim, S. J. Song, W. Lee, and C. S. Hwang, *Coord. Chem. Rev.* **257**, 3154 (2013).

[40] S. J. Song, S. W. Lee, G. H. Kim, J. Y. Seok, K. J. Yoon, J. H. Yoon, C. S. Hwang, J. Gatineau, and C. Ko, *Chem. Mater.* **24**, 4675 (2012).

[41] E. H. Kisi and C. J. Howard, *J. Am. Ceram. Soc.* **72**, 1757 (1989).

[42] P. Simoncic amd A. Navrosky, *J. Mater. Res.* **22**, 876 (2007).

[43] M. V. Nevitt, Y. Fang, and S. K. Chan, *J. Am. Ceram. Soc.* **73**, 2502 (1990).

[44] T. Tojo, T. Atake, T. Mori, and H. Yamamura, *J. Chem. Thermodyn.* **31**, 831 (1999).

[45] R. C. Garvie, *J. Phys. Chem.* **69**, 1238-1243 (1965).

[46] R. C. Garvie, *J. Phys. Chem.* **82**, 218-224 (1978).

[47] T. S. Böscke, St. Teichert, D. Bräuhaus, J. Müller, U. Schröeder, U. Böttger, and T. Mikolajick, *Appl. Phys. Lett.* **99**, 112904 (2011).

[48] E. Yurchuk, J. Müller, S. Knebel, J. Sundqvist, A. P. Graham, T. Melde, U. Schröder, and T. Mikolajick, *Thin Solid Films* **533**, 88 (2013).

[49] K. Meinel, A. Eichler, S. Förster, K. –M. Schindler, H. Neddermeyer, and W. Widdra, *Phys. Rev. B* **74**, 235444 (2006).

[50] K. Meinel, K. –M. Schindler, and H. Neddermeyer, *Surf. Sci.* **532**, 420 (2003).

[51] V. Maurice, M. Salmeron, and G. A. Somorjai, *Surf. Sci.* **237**, 116 (1990).

[52] A. Christensen and E. A. Carter, *Phys. Rev. B* **58**, 8050 (1998).

[53] P. M. Oliver, G. W. Watson, and S. C. Parker, *Phys. Rev. B* **52**, 5323 (1995).

Chapter 4. Evolution of phases and ferroelectric properties of thin $Hf_{0.5}Zr_{0.5}O_2$ films according to the thickness and annealing temperature

4.1. Introduction

Recently, it was reported that HfO_2 thin films can be ferroelectric when they are doped with various elements.[1-4] This is highly beneficial in the field of ferroelectric memory, because HfO_2 is compatible with conventional Si technology and appropriate for 3-dimensional capacitors, due to its small film thickness (t_f), highly matured atomic layer deposition (ALD) technique, and strong resistance to the degradation by hydrogen annealing.[1-5] Among the various dopants that have been used, Zr shows great promise, because $Hf_{1-x}Zr_xO_2$ can show robust ferroelectricity in a wider range of composition near the composition of HZO, which makes the material appropriate for mass-production.[4] The ferroelectricity of HfO_2-based films is believed to result from the formation of non-centrosymmetric o-phase. However, the formation of the o-phase in thin HZO film is not trivial, since it is stable only under certain high-pressure (or anisotropic-strain) circumstances,[6-9] while the metastability of t-phase (space group: $P4_2/nmc$) over the stable m-phase (space group: $P2_1/c$) is well known from surface energy arguments.[10-15] There have been several theoretical and experimental works on the possible formation of o-phase in bulk HfO_2 (and ZrO_2) materials.[6,7] Lowther et al. reported that the application of a hydrostatic pressure of 3 - 4 GPa to m-

phase HfO_2 can induce the transition to o-phase using theoretical modelling work.[6] However, thin film systems can hardly experience hydrostatic pressure due to its two-dimensional nature, and thus, the possible transition of the HZO film to the o-phase by the hydrostatic pressure effect can be neglected. In contrast, HZO films can be subjected to a two-dimensional compressive or tensile stress, depending on the process conditions and substrates, due to local lattice and thermal expansion mismatches with the substrate. It has been reported that amorphous-polycrystalline HfO_2 and ZrO_2 films grown by ALD on Si substrates are usually under tensile stress, due to thermal expansion mismatch.[16,17] Kisi reported on the transition of t-phase ZrO_2 grains with lenticular shape embedded in bulk cubic-phase ZrO_2, which was stabilized by MgO doping. The transition from the t-phase to o-phase was facilitated by compressive stress along the a-b plane and tensile stress along the c-axis direction.[7] The necessary stress was only ~760 MPa tensile and ~50 MPa compressive, which can be readily achieved in HZO thin films. Such a phase transition under the anisotropic stress can be easily understood from the structures of the t- and o-phases. The o-phase has the 2c/(a+b) ratio of 1.038 – 1.042,[4-6] depending on the composition, while those of the t-phase of HfO_2 and ZrO_2 are only 1.028[18-20] and 1.015[20,21], respectively.[22] The ferroelectric remanant polarization in the o-phase exists along the a-axis. Therefore, the anisotropic stress facilitates the t- to o-phase transition.

The direct transition between m- and o-phases is usually hindered due to the largely different crystalline structures of the two phases.[23] This may explain the absence of o-phase in pure HfO_2 and ZrO_2.[4] It is also well known that pure polycrystalline HfO_2 films have hardly any t-phase, since the grain size is usually over the critical size for the transition to the t-phase (~7-10 nm),[13] so these films almost always have m-phase. In contrast, polycrystalline ZrO_2 easily shows t-phase, especially on TiN, even without any doping, since its grain size is usually smaller than the critical value (~ 30 nm).[10-12] However, the 2c/(a+b) ratio of t-phase ZrO_2 is too small compared with that of o-phase to induce the transition to o-phase. Therefore, HZO might have an appropriate grain size to induce the t-phase, which could be transformed to the o-phase as the stress evolves with the film growth or heat-treatment, and could also have a 2c/(a+b) ratio close enough to that of the o-phase to induce the phase transition.

In this work, atomic layer deposited HZO films were prepared with different t_f (5.5 – 25 nm) and post-annealing temperatures (T_{anneal}, 400 – 800 ^{o}C). The correlation between the crystallographic structural evolution and ferroelectric properties are examined. The necessity of o-phase for ferroelectricity is confirmed. However, the coexistence of m- and t-phases severely interferes with the overall ferroelectric performance of the HZO films.

Table 4.1. Experimental and theoretical structural parameters and 2c/(a+b) ratio for the HfO_2, ZrO_2, and HZO polymorphs.

	a (Å)	b (Å)	c (Å)	2c/(a+b)	Data type and reference
t-HfO_2	5.150		5.295	1.028	Experiment, Ref. 18
	5.175		5.325	1.029	Experiment, Ref. 19
	5.059		5.200	1.028	Theory, Ref. 20
t-ZrO_2	5.094		5.177	1.016	Experiment, Ref. 21
	5.132		5.207	1.015	Theory, Ref. 20
o-HfO_2	5.11	5.10	5.30	1.038	Theory, Ref. 6
o-ZrO_2	5.07	5.08	5.26	1.036	Theory, Ref. 6
o-HZO	5.01	5.05	5.24	1.042	Experiment, Ref. 4

4.2. Experimental

5.5-, 10-, 17-, and 25-nm-thick HZO films were deposited on sputtered-TiN/Si substrate using thermal ALD at a wafer temperature of 280 °C using $Hf[N(C_2H_5)CH_3]_4$, $Zr[N(C_2H_5)CH_3]_4$, and ozone, as the Hf-precursor, Zr-precursor, and oxygen source, respectively. The growth per cycle of HfO_2 and ZrO_2 were almost identical (~0.12 nm/cycle), so the HZO films with an Hf : Zr ratio of 0.5 : 0.5 could be deposited using HfO_2 : ZrO_2 ALD cycle ratio of 1:1. For the electrical characterization, Pt (60 nm)/TiN (20 nm) TE were deposited using DC sputtering through a shadow mask with a hole diameter of 300 μm (TiN contacts HZO films). After TE deposition, annealing was performed for 30 s at 400-800 °C in an N_2 atmosphere using RTA for the crystallization of the films. The cation composition and t_f were examined using X-ray fluorescence (Quant'X, Thermo SCIENTIFIC) and ellipsometry (L-116d, Gaetner), respectively. The evolution of the crystallographic phase of the films according to t_f and T_{anneal} was examined by GAXRD (Pananalytical X-pert Pro, Cu$k\alpha$ radiation with an X-ray wavelength of 0.15418 nm). For electrical characterization, the polarization-voltage (P-V), capacitance-voltage (C-V), and current-voltage characteristics (I-V) were measured at room temperature using a ferroelectric tester (TF analyzer 2000, Aixacct systems), an impedance analyzer (4194A, HP), and a semiconductor parameter analyzer (4145B, HP), respectively.

4.3. Results and discussions

First, the structural evolution of HZO films according to t_f and T_{anneal} are described. Unambiguous identification of the m-, o-, and t-phases in an HfO_2-ZrO_2 system using a laboratory X-ray system is quite challenging due to the proximity of the diffraction peaks from the different phases. The discrimination of o- and t-phases is especially challenging due to their structural similarity. Nevertheless, the diffraction peaks near a 2θ of 30.5° are very useful to discern these two phases. Peaks ascribed to the m-phase can be identified quite easily, since there are characteristic peaks near 2θ values of 28.5 and 31.6°.

Figures 4.1 (a) – (c) show the detailed GAXRD spectra in the 2θ range of 27 - 33° for 10-, 17-, and 25-nm-thick HZO films, respectively. The GAXRD spectra in the 2θ range of 25 - 65° for 10-, 17-, and 25-nm-thick HZO films can be seen in figure 4.2. For the case of 5.5-nm-thick films, the GAXRD spectra were smeared due to their small t_f. The peaks at ~28.5, ~30.5, and ~31.6° could be assigned as m(-111), o(111)/t(011), and m(111), respectively. The intensity near 30.5° originates from the overlapped o(111) and t(011) peaks, which requires peak simulation to distinguish the two phases. Böscke et al. reported that 2θ value of t(011) peak is slightly larger than that of o(111) peak for the case of Si-doped HfO_2 films.[22] The GAXRD peaks of the 27.5-33° region was simulated using Gaussian functions with fixed peak locations at 28.54, 30.40, 30.80, and 31.64° for m(-

111), o(111), t(011), and m(111), respectively. The assignment of o(111) peak location to 30.40° was based on the lattice parameters of HZO film suggested by Muller et al..[4] However, (011) peak position of t-phase HZO cannot be found from literature. The only data that could be found were on the (011) positions for t-phase HfO_2 (Ref. 14) and t-phase ZrO_2 (Ref. 20). Considering that these two phases form a complete solid solution, and have similar structures, the Vegard's law could be used to determine the (011) peak position of t-phase HZO, and the result was 30.8°. For the case of 10-nm-thick films, the as-deposited film shows no peak suggesting that the film is amorphous. After annealing at 400 and 500°C, a peak at 30.5° can be clearly seen, which indicates that the film first crystallizes into a mixture of o- and t-phase. When the film was annealed at 600 and 700°C, a peak at 28.5° appeared, while the intensity of the peak at 30.5° decreased slightly. This means that further crystallization of the amorphous film by the annealing at higher T_{anneal} results in the formation of m-phase, and a possible transformation of some portion of the o/t-phases into m-phase. For the case of 17- and 25-nm-thick films, the as-deposited films show a strong peak at 30.5° and weak peaks at 28.5 and 31.6°, suggesting that the films were already crystallized with a mixture of m- and o/t- phases. Similarly to the case of 10-nm-thick film, increasing T_{anneal} decreases the intensity of the peak at 30.5°, while the intensities of the peaks at 28.5 and 31.6° increase. Since the peak at 31.6° is also ascribed to the m-phase, this suggests that the

annealing at higher temperature increases the portion of m-phase, while that of the o/t-phase decreases. In addition to the variations in the relative intensities of the peaks, the position of the peak near 30.5° shifted toward the low 2θ region with increasing T_{anneal} for 10- and 17-nm-thick films. However, such a shift was not observed for the peaks near 28.5 and 31.6°. Figure 4.1 (d) shows the variations in the location of the maximum point of the peak near 30.5° as a function of T_{anneal}. Interestingly, the peak near 30.5° of the 25-nm-thick sample did not show such a change, as shown in figure 4.1d.

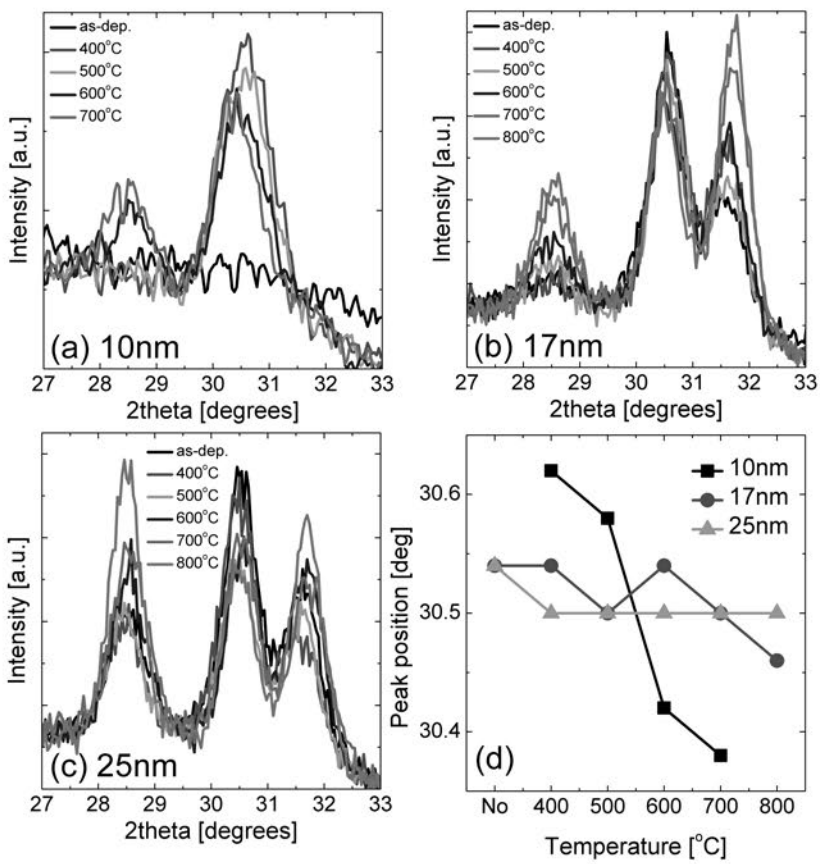


Figure 4.1. Grazing-angle incidence X-ray diffraction spectra with 2θ range of 27-33° of (a) 10-nm-thick, (b) 17-nm-thick, and (c) 25-nm-thick HZO films with annealing temperature of 400-800 °C, respectively. (d) The peak position of superimposed o(111) and t(011) peaks as a function of annealing temperature.

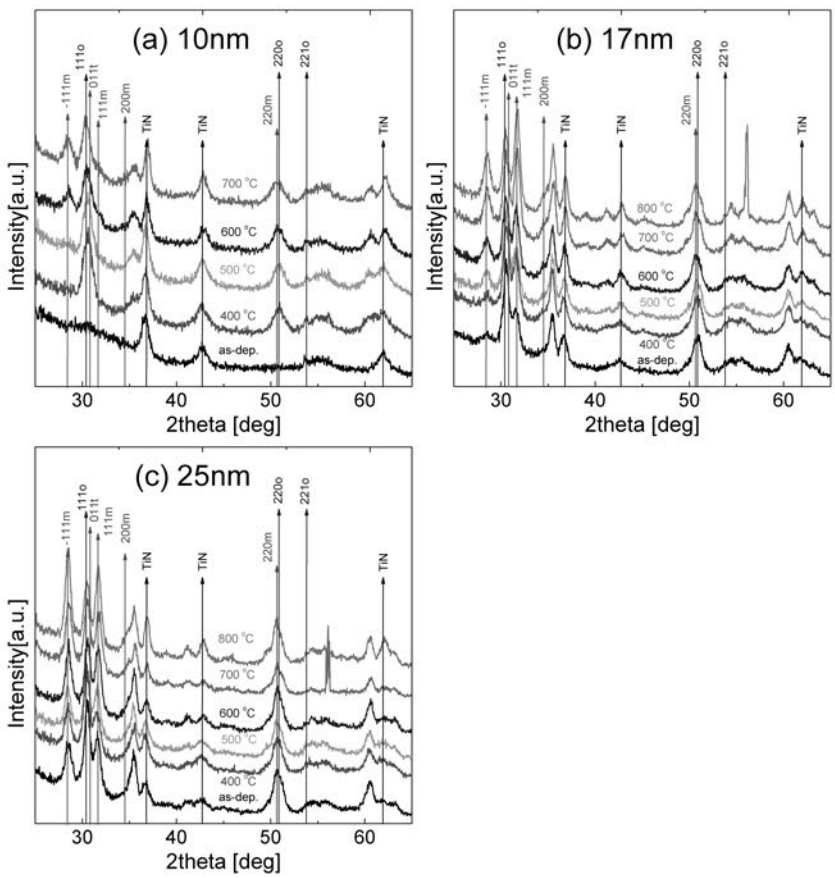


Figure 4.2. Grazing-angle incidence X-ray diffraction spectra of (a) 10-, (b) 17-, and (c) 25-nm-thick HZO films with annealing temperature of 400-800 °C.

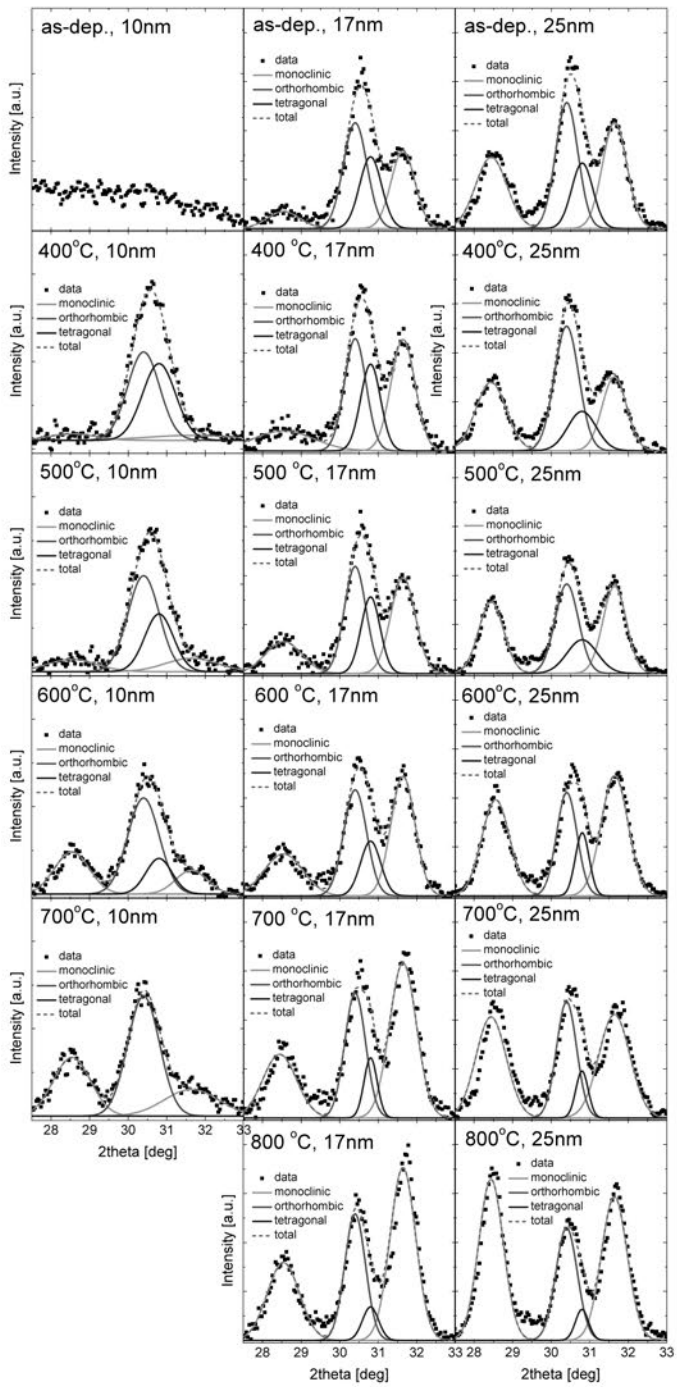


Figure 4.3. Gaussian fitting results of GIXRD spectra with 2θ range of 27.5-33° of 10-, 17-, and 25-nm-thick HZO films with annealing temperature of 400-800°C.

As mentioned above, the locations of the t(011) and o(111) peaks are close to each other, which precludes the direct identification of the two peaks. Therefore, the diffraction peaks near a 2θ of 30.5° were deconvoluted assuming that the peaks are composed of two components with peak locations at 30.4° (o-phase) and 30.8° (t-phase), with Gaussian shapes. In addition, the peaks located at 28.54 and 31.64°, both corresponding to the m-phase, are also simulated using the same Gaussian functions to compare the relative area ratio of the peaks. Figure 4.3 shows the results of the peak simulation of the GAXRD spectra of HZO films with various thickness and t_{anneal}. The variations in the relative ratio of the integrated area of the peaks of each phase to the sum of them are shown in the lower panels of Figs. 4.4 (b) – (d) for the 10-, 17-, and 25-nm-thick films, as a function of T_{anneal}. Post-deposition annealing can influence the film structure by densification and crystallization, which could induce shift in the XRD peak position. However, as can be understood from figure 4.1, the peak positions corresponding to m-phase hardly show any change by the annealing, whereas the peaks near 2θ of 30.5° show substantial change depending on the thickness and annealing temperature. This suggests that the post-annealing and thickness-induced crystallization mainly influence the phase composition not the stress or densification.

Several trends in the phase evolution with the t_f and T_{anneal} can be found in these figures. First, the portion of the o-phase is the highest in the thinner 10-

nm-thick film. Second, the m-phase certainly increases with the increasing t_f and T_{anneal}. Third, the variation in the o-phase with the T_{anneal} is relatively small compared with that in other phases, which is the most obvious for the 10-nm-thick film. Such trends can be well understood from the reported knowledge on the structural correlations between the phases discussed above. The film starts to grow with the amorphous (or even nano-crystalline) structure, and becomes crystallized as its t_f increases (~10 – 15 nm) with the accompanying increase in grain size. Figure 4.5 and Table 4.2 shows the SEM images and the calculated average grain size of HZO films with various t_f and T_{anneal}, respectively. Figures 4.1 (a) and 4 (b) clearly reveal that the first crystallization mostly starts with the formation of the t-phase, some of which then transform into the o-phase, possibly due to the two-dimensional stress effect. As the T_{anneal} or t_f increases, the grain size increases and the portion of m-phase increases, as it is the most stable polymorph in this system. Figure 4.4 (a) reveals that the t- to m-phase transition is mostly responsible for such transition for the 10-nm-thick film. In contrast, the thicker films appear to involve a more complicated o-phase → t-phase → m-phase transition in addition to the t-phase → m-phase transition. The reason for such variation with t_f is not clearly understood yet, but it may have some correlation with the change in the stress state. The almost parallel lines for the t- and o-phases in figure 4.4d explain the invariant peak position of the 25-nm-thick sample in figure 4.1d.

Now, the electrical properties of the films, double the remanant polarization ($2P_r$) and the ε_r (measured at 10 kHz), are compared with the GAXRD data. The P-E, C-E, and J-E curves of each sample are included in figure 4.6, figure 4.7, and figure 4.8, respectively. For the P-V measurement, electric field cycling was performed before the measurement to make the samples free from the wake-up effect in HfO_2-based ferroelectrics.[23] The evolution of P_r with the electric field cycling numbers are included as figure 4.9. The number of cycles needed for the stabilization of P-V hysteresis decreases with increasing T_{anneal}, and the films annealed at ≥600 °C were free from the wake-up effect. The upper panels of Figs. 4.4 (a) – (d) show the variation in $2P_r$ and ε_r of the 5.5-, 10-, 17-, and 25-nm-thick films as a function of T_{anneal}. The variation in ε_r can be understood more easily from the changes in the crystallographic structures than that in $2P_r$. Up to a T_{anneal} of 500 °C, it generally increases due to the overall improvement in the crystallization. In the T_{anneal} region of >500 °C, it generally decreases with increasing T_{anneal}, which can be attributed to the increased portion of m-phase, of which the ε_r is 17 – 20, and the decrease of the t-phase, of which the ε_r is 35 – 40. The small variation in the o-phase may not have a strong impact on such variations, although it has an intermediate ε_r value (~ 30).[4] The ε_r of the as-deposited 5.5- and 10-nm-thick films is only ~17, corroborating the amorphous GAXRD results of these samples. The highest ε_r values of the 5.5-nm-thick film after the annealing at T_{anneal} > 400 °C suggests that the film

is mostly crystallized into the t-phase, but the still rather high $2P_r$ value (~27 $\mu C/cm^2$) suggests that the o-phase formation is not negligible even in this case. The slight increase in $2P_r$ and decrease in ε_r with increasing T_{anneal} suggest that the thinnest film develops more o-phase as the T_{anneal} increases. This is a rather different situation from the other thicker films.

The $2P_r$ value of the thicker films generally shows more complicated variations with T_{anneal}. First, the thicker films generally have lower $2P_r$ values, which can be understood from the higher portion of non-ferroelectric t- and m-phases. Yurchuk et al. also reported that thick Si:HfO_2 film is already crystalized during deposition, which increased the amount of m-phase and accordingly reduced P_r of the layer.[24] This is a critically different aspect of this specific ferroelectric film compared with the conventional perovskite structured ferroelectrics, such as PZT and BTO, which suggests that the HZO films are mixtures of ferroelectric and non-ferroelectric phases. The P_r of a ferroelectric material can be approximately estimated using the ionic displacements in a unit cell.[25] Based on the ionic locations of o-phase reported by Lowther et al. and Kisi et al.,[6,8] the P_r values of o-ZrO_2 and o-HfO_2 are ~51-53 $\mu C/cm^2$. Even though this value is smaller than that of $PbTiO_3$ (~75-85 $\mu C/cm^2$),[25,26] it is still large enough for their application to the ferroelectric memories. This suggests that even the HZO film showing the highest P_r value (~16 $\mu C/cm^2$, T_{anneal} = 600°C for 10-nm-thick film) has a mixed phase, which coincides with the GAXRD result.

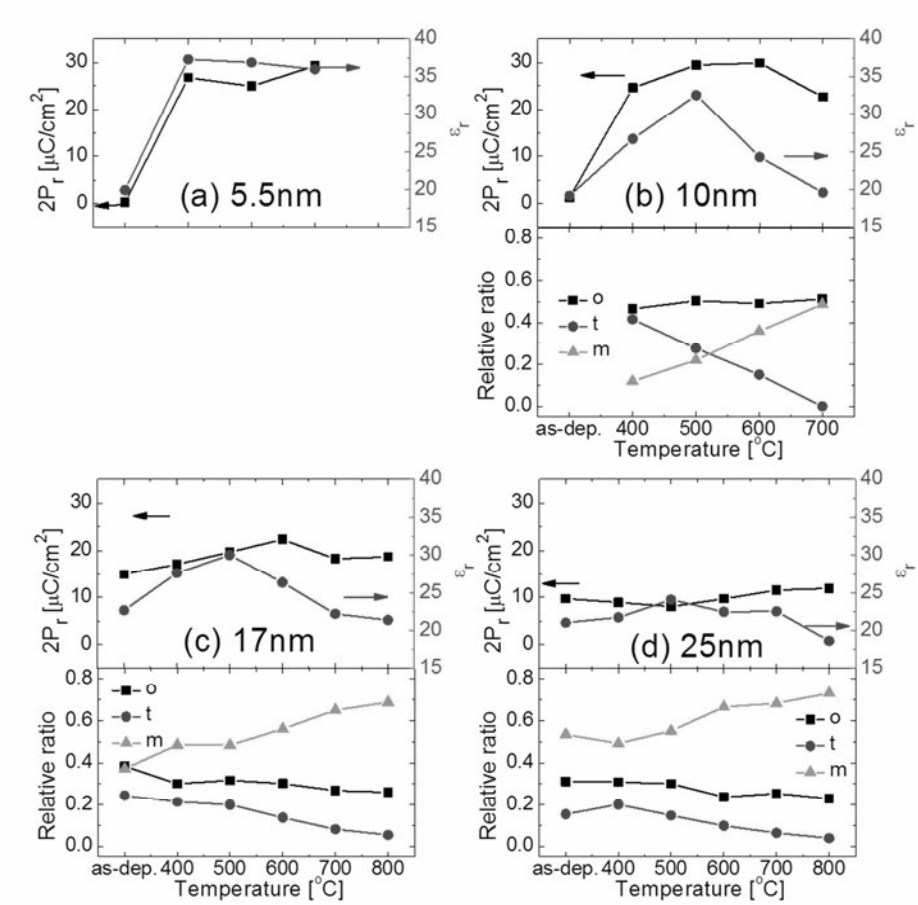


Figure 4.4. The change of $2P_r$ and ε_r (upper panel) and that of the relative ratio of o-, t-, and m-phases (lower panel) as a function of annealing temperature of (a) 5.5-nm-thick, (b) 10-nm-thick, (c) 17-nm-thick, and (d) 25-nm-thick HZO films.

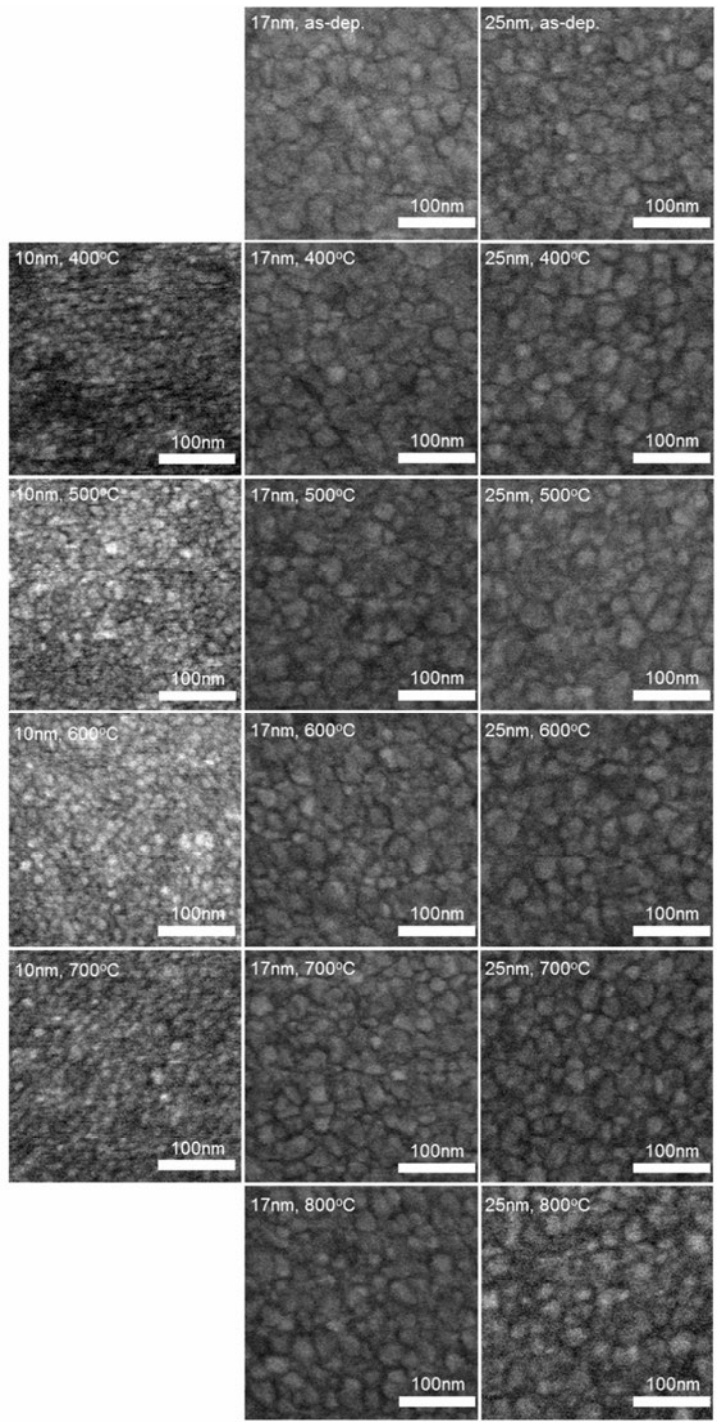


Figure 4.5. SEM images of 10-, 17-, and 25-nm-thick HZO films with annealing temperature of 400-800°C.

Table 4.2. The average grain size of 10-, 17-, and 25-nm-thick HZO films with annealing temperature of 400-800°C calculated from SEM images in figure 4.5.

	10nm	17nm	25nm
as-dep	-	21.0 nm	24.5 nm
400°C	13.5 nm	20.7 nm	27.0 nm
500°C	14.4 nm	23.6 nm	29.4 nm
600°C	15.6 nm	25.0 nm	30.1 nm
700°C	17.4 nm	25.0 nm	30.1 nm
800°C	-	27.0 nm	31.5 nm

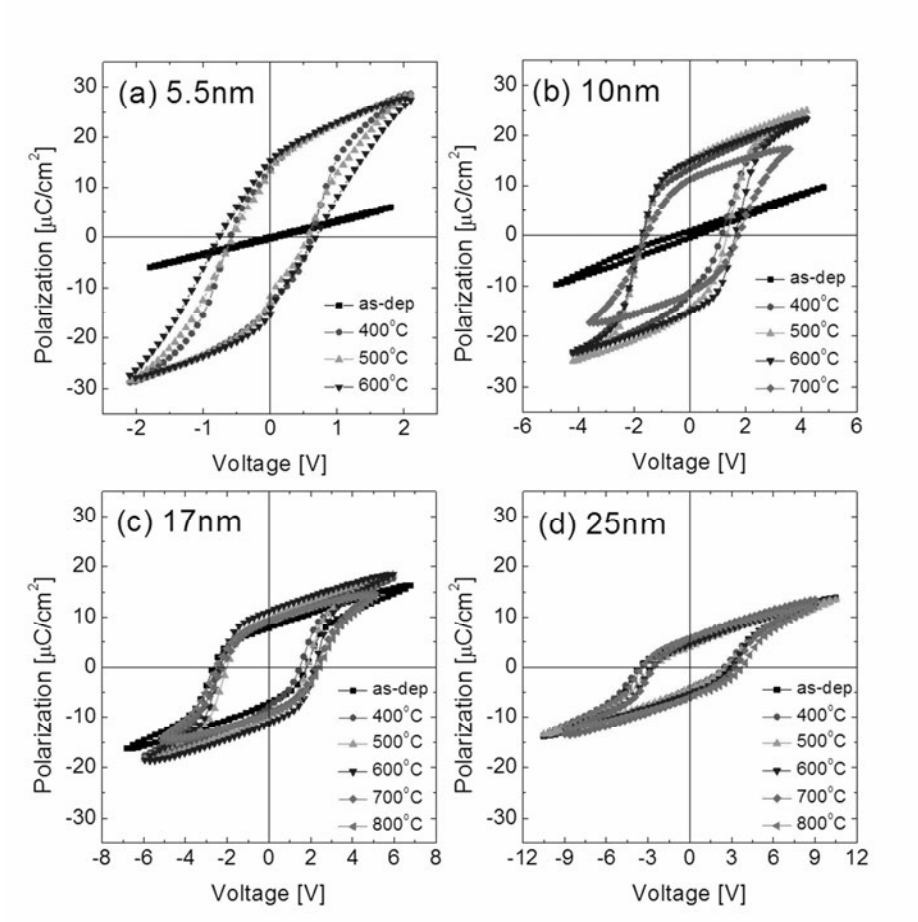


Figure 4.6. Polarization-voltage characteristics of (a) 5.5-nm-thick, (b) 10-nm-thick, (c) 17-nm-thick, and (d) 25-nm-thick HZO films with annealing temperature of 400-800 °C.

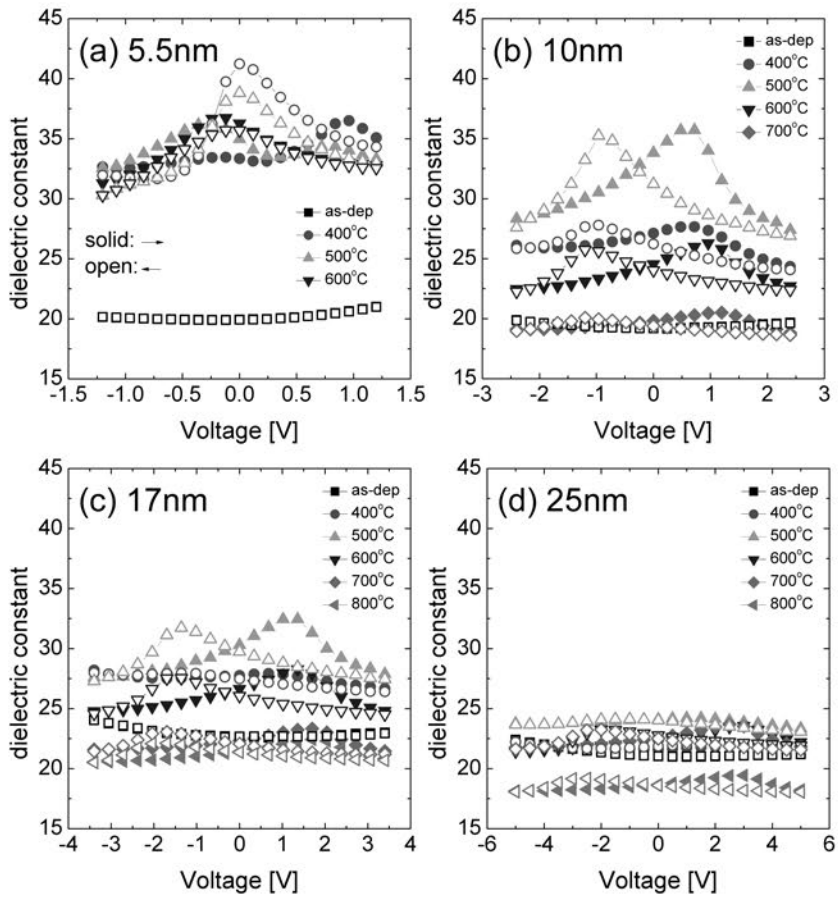


Figure 4.7. Dielectric constant-voltage characteristics of (a) 5.5-, (b) 10-, (c) 17-, and (d) 25-nm-thick HZO films with annealing temperature of 400-800 ^{o}C, respectively.

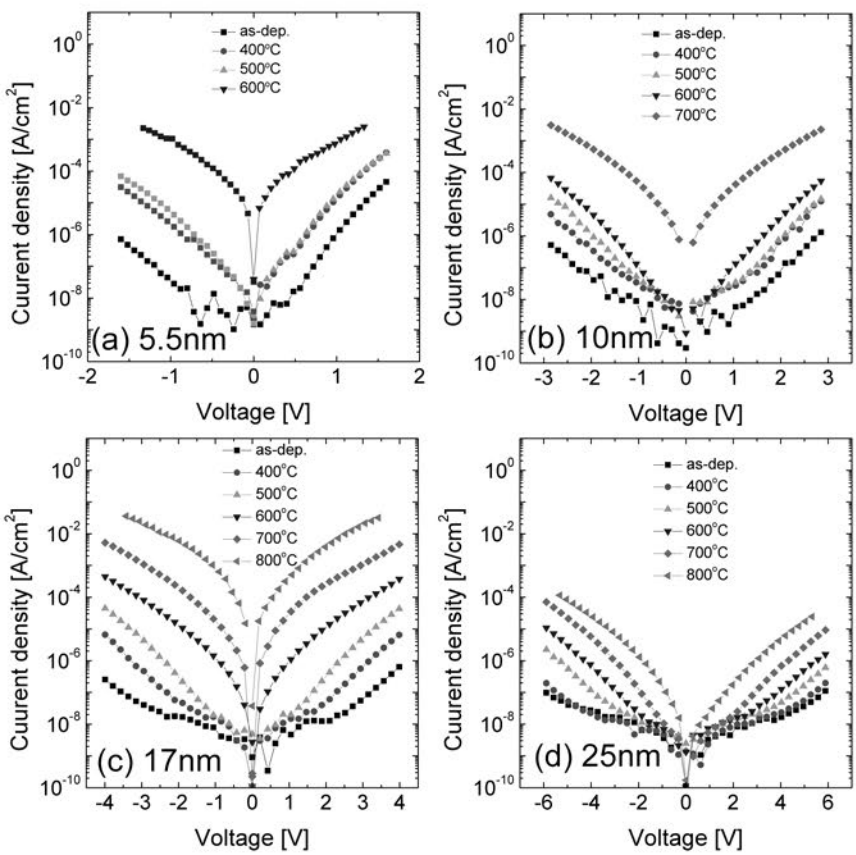


Figure 4.8. Current-voltage characteristics of (a) 5.5-, (b) 10-, (c) 17-, and (d) 25-nm-thick HZO films with annealing temperature of 400-800 °C, respectively.

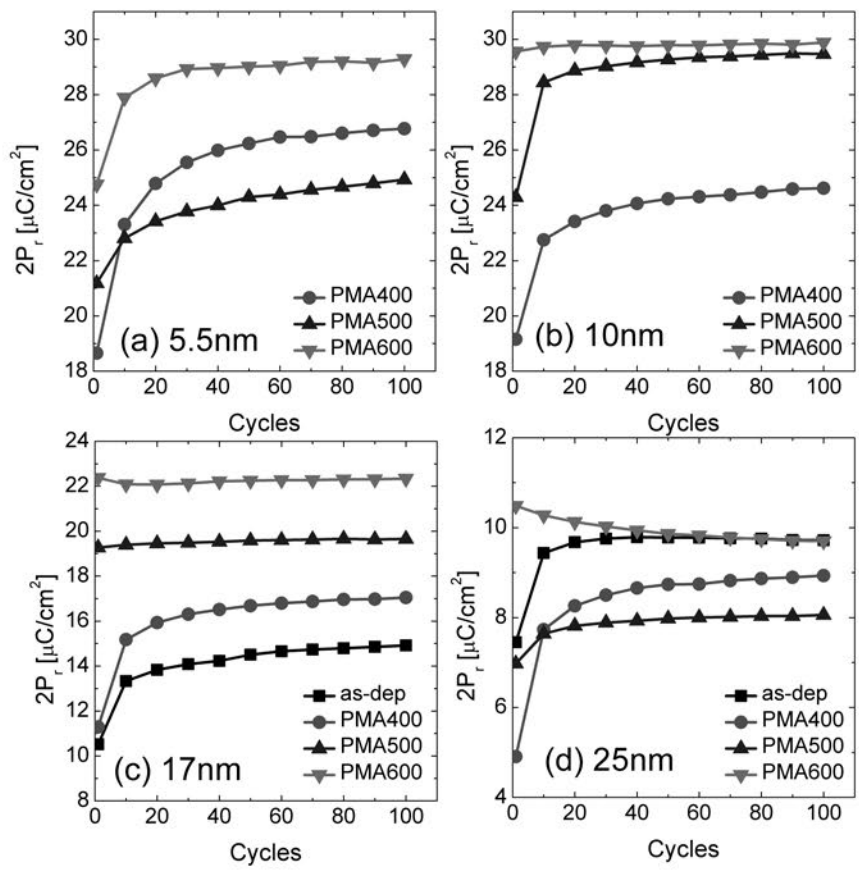


Figure 4.9. The change of $2P_r$ as a function of number of electric field cycling of (a) 5.5-, (b) 10-, (c) 17-, and (d) 25-nm-thick HZO films with annealing temperature of 400-600 ^{o}C, respectively.

The variations in $2P_r$ with T_{anneal} of the 10-, 17-, and 25-nm-thick films compared with the GAXRD suggest the following. The non-linear correlation between the $2P_r$ and relative ratio of o-phase peak intensity reveals that the ferroelectric and non-ferroelectric phases are present with a complicated distribution along the film thickness direction and parallel direction to the film plane. If they were clearly distinguished from each other and were present in parallel along the film plane, the $2P_r$ would have to be proportional to the o-phase intensity, which is certainly not the case. It can be inferred from the generally increasing m-phase portion with the increasing t_f for almost all T_{anneal} values that the m-phase grows on top of the t- and o-phases, which must be a reasonable consequence of increasing grain size with increasing t_f and lower volumetric free energy of m-phase compared with other phases. The highest $2P_r$ of the 10-nm-thick film can be understood from the lower amount of non-ferroelectric m-phase over the o-phase grains. Meanwhile, the 5.5-nm-thick film may suffer from the deleterious interfacial effects with the TiN electrode, such as the dead-layer effect,[27] which eventually decreases $2P_r$ compared with 10-nm-thick film.

With a non-ferroelectric phase on top of the ferroelectric phase, the effective electric field applied to the ferroelectric phase is decreased by the voltage drop over the non-ferroelectric phase. This phenomenon is further aggravated as the ε_r of the non-ferroelectric phase decreases. This can explain the generally decreasing $2P_r$ with the increasing T_{anneal} when it is >

600°C for the 10- and 17-nm thick films, as the m-phase intensity largely increased in that T_{anneal} range. In other words, a certain portion of the t-phase present on top of the o-phase possibly transforms into the m-phase. It has to be noted that the o-phase peak intensities are almost invariant. In contrast, the $2P_r$ values increase with increasing T_{anneal} up to 600 °C, even though the m-phase peak also increases in that region for the 10- and 17-nm-thick films. This must be understood from the improvement of the crystalline quality of the o-phase itself with the increasing T_{anneal}. For the 25-nm-thick film, the dominance of the m-phase peak and generally small $2P_r$ values strongly suggest that the whole area of the film is a double-layer structure composed of o/t-phases at the bottom and m-phase at the top surface region. Therefore, the increasing T_{anneal} for this case does not severely alter the voltage distribution between the ferroelectric and non-ferroelectric phases, while the improvement in the crystalline quality of the o-phase can explain the slight increase in $2P_r$ in the whole range of T_{anneal} with increasing T_{anneal}, although its $2P_r$ values are generally suppressed.

4.4. Conclusion

In conclusion, the effects of T_{anneal} and t_f on the crystal structure and ferroelectric properties of HZO films were examined. From the structural analysis using GAXRD and deconvolution, and from simulation of the diffraction peaks corresponding to the m-, o- and t-phases, the following conclusion can be drawn. The HZO film starts to crystallize at a thickness between 10 and 17 nm, predominantly with t- and o-phases on the TiN electrode. The formation of t-phase can be understood from consideration of the surface energy, while the formation of the o-phase is assumed to be induced by the stress-induced martensitic-type phase transition from the t-phase. As the film thickness increases further, mostly m-phase starts to grow on top of the o/t-phase layer, which mitigates the overall ferroelectric properties of the HZO film. Post-annealing transforms most of the t-phase to m-phase, while its influence on the o-phase was minimal. The variations of the electrical properties, such as $2P_r$ and ε_r, could be well-understood from such crystallographic structural changes with t_f and T_{anneal}. The 10-nm-thick HZO films showed a maximum $2P_r$ of ~32 $\mu C/cm^2$ after annealing at 600 ^oC.

4.5. References

[1] T. S. Böscke, J. Müller, D. Bräuhaus, U. Schröder, and U. Böttger, *Appl. Phys. Lett.* **99**, 102903 (2011).

[2] J. Müller, U. Schröder, T. S. Böscke, I. Müller, U. Böttger, L. Wilde, J. Sundqvist, M. Lemberger, P. Kücher, T. Mikolajick, and L. Frey, *J. Appl. Phys.* **110**, 114113 (2011).

[3] S. Mueller, J. Mueller, A. Singh, S. Riedel, J. Sundqvist, U. Schroeder, T. Mikolajick, *Adv. Funct. Mater.* **22**, 2412 (2012).

[4] J. Müller, T. S. Böscke, U. Schröder, S. Mueller, D. Bräuhaus, U. Böttger, L. Frey, and T. Mikolajick, *Nano Lett.* **12**, 4318 (2012).

[5] M. H. Park, H. J. Kim, Y. J. Kim, W. Lee, H. K. Kim, and C. S. Hwang, *Appl. Phys. Lett.* **102**, 112914 (2013).

[6] J. E. Lowther, J. K. Dewhurst, J. M. Leger, and J. Haines, *Phys. Rev. B* **60**, 14485 (1999).

[7] E. H. Kisi, *J. Am. Ceram.* Soc. **81**, 741 (1998).

[8] E. H. Kisi and C. J. Howard, *J. Am. Ceram. Soc.* **72**, 1757 (1989).

[9] C. J. Howard and E. H. Kisi, *J. Am. Ceram. Soc.* **73**, 2828 (1990).

[10] R. C. Garvie, *J. Phys. Chem.* **69**, 1238 (1965).

[11] R. C. Garvie, *J. Phys. Chem.* **82**, 218 (1978).

[12] M. W. Pitcher, S. V. Ushakov, A. Navrotsky, B. F. Woodfield, G. Li, J. and Boerio-Goates, *J. Am. Ceram. Soc.* **88**, 160 (2005).

[13] M. Shandalov and P. C. Mclntyre, *J. Appl. Phys.* **106**, 084322 (2009).

[14] D. –Y. Cho, H. S. Jung, I. –H. Yu, J. H. Yoon H. K. Kim, S. Y. Lee, S. H. Jeon, S. W. Han, J. H. Kim, T. J. Park, B. -G. Park, and C. S. Hwang, *Chem. Mater.* **24**, 3534 (2012).

[15] S. K. Kim and C. S. Hwang, *Electrochem. Solid St.* **11**, G9 (2008).

[16] T. J. Park, J. H. Kim, J. H. Jang, C. –K. Lee, K. D. Na, S. Y. Lee, H. –S. Jung, M. Kim, S. Han, and C. S. Hwang, *Chem. Mater.* **22**, 4175 (2010).

[17] W. Weinreich, L. Wilde, J. Müller, J. Sundqvist, E. Erben, J. Heitmann, M. Lemberger, and A. J. Bauer, *J. Vac. Sci. Technol.* A **31**, 01A119 (2013).

[18] M. V. Nevitt, Y. Fang, and S. K. Chan, *J. Am. Ceram. Soc.* **73**, 2502 (1990).

[19] T. Tojo, T. Atake, T. Mori, and H. Yamamura, *J. Chem. Thermodyn.* **31**, 831 (1999).

[20] J. E. Jaffe, R. A. Bachorz, and M. Gutowski, *Phys. Rev. B* **72**, 144107 (2005).

[21] P. Simoncic and A. Navrosky, *J. Mater. Res.* **22**, 876 (2007).

[22] T. S. Böscke, St. Teichert, D. Bräuhaus, J. Müller, U. Schröder, U. Böttger, and T. Mikolajick, *Appl. Phys. Lett.* **99**, 112904 (2011).

[23] S. Mueller, J. Müller, U. Schroeder, and T. Mikolajick, *IEEE T. Device Mat. Re.* **13**, 93 (2013).

[24] E. Yurchuk, J. Müller, S. Knebel, J. Sundqvist, A. P. Graham, T. Melde, U. Schröder, and T. Mikolajick, *Thin Solid Films* **533**, 88 (2013).

[25] R. J. Nelmes and W. F. Kuhs, *Solid State Commun.* **54**, 721 (1985).

[26] M. J. Haun, E. Furman, S. J. Jang, and L. E. Cross, *Ferroelectrics* **99**, 63 (1989).

[27] Y. S. Kim, D. H. Kim, J. D. Kim, Y. J. Chang, T. W. Noh, J. H. Kong, K. Char, Y. D. Park, S. D. Bu, J.-G. Yoon, and J.-S. Chung, *Appl. Phys. Lett.* **86**, 102907 (2005).

Chapter 5. Effect of forming gas annealing on the ferroelectric properties of $Hf_{0.5}Zr_{0.5}O_2$ thin films with and without Pt electrodes

5.1. Introduction

Ferroelectric memories, such as FeRAM and FeFET, have been regarded as one of the most promising universal non-volatile memories, because of their reversibly bi-stable polarization states.[1] Most of the previous researches have focused on material systems based on perovskite structure.[1] However, integrating ferroelectric thin films having perovskite structure into conventional Si-based memory technology has been proven rather challenging for many reasons, such as ferroelectric size effect, degradation by thermal budget during crystallization, small E_g, poor interfaces with Si, and degradation due to forming gas annealing (FGA).[1-7] Recently, it was reported that HfO_2 thin films can show ferroelectric properties when they are doped with various elements, such as Si, Y, Al, and Zr.[8-11] This could be a great improvement for ferroelectric memories, because HfO_2 is compatible with conventional Si technology and appropriate for 3-dimensional capacitors, due to its small thickness and highly matured atomic layer deposition (ALD) technique. Among the various dopants that have been used, Zr is believed to be promising, because its chemical properties are almost identical to that of Hf. While HfO_2 thin films with other dopants have shown robust ferroelectricity within only a very narrow range of doping

concentration,[8-10] ZrO_2 and HfO_2 form a solid-solution in the whole composition, and show robust ferroelectricity in a wider range of composition near the composition of Hf : Zr = 0.5 : 0.5 (HZO). This makes the material appropriate for mass-production.[11]

However, the effects of FGA on the ferroelectric properties of HfO_2-based ferroelectrics have not yet been reported. FGA is an inevitable process for any type of Si-based memory devices for achieving appropriate transistor performance. In this study, the effects of FGA on the electrical and physical properties of thin HZO films are reported. The influence of a top Pt electrode on the degree of degradation in the ferroelectric performance was also examined.

5.2. Experimental

10-nm-thick HZO films were deposited on TiN substrate using thermal ALD at a wafer temperature of 280 °C using $Hf[N(C_2H_5)CH_3]_4$, $Zr[N(C_2H_5)CH_3]_4$, and ozone as the Hf-precursor, Zr-precursor, and oxygen source, respectively. The growth per cycle of HfO_2 and ZrO_2 are almost identical (~0.12 nm/cycle), so the HZO films with an Hf : Zr ratio of 0.5 : 0.5 could be deposited using a HfO_2 : ZrO_2 ALD cycle ratio of 1:1. For the electrical characterization, Pt (80 nm) or Pt (60 nm)/TiN (20 nm) TE were deposited using an electron-beam evaporation and a DC sputtering, respectively, through a shadow mask having a hole diameter of 300 m. For the Pt TE, deposition using the e-beam evaporation was chosen due to its better leakage behaviour compared to that using the DC sputtering. After TE deposition, post-metallization-annealing (PMA) was performed for 30 s at 550 °C in an N_2 atmosphere using RTA for the crystallization of the films. Then, FGA (5% H_2+95% N_2) and annealing under N_2 atmosphere (NA) were performed for 2 min at 300-600 °C under a pressure of 400 torr using the RTA process. An RTA time of 2 min was chosen, because the degradation during FGA was saturated when the time was >2min. For X-ray photoelectron spectroscopy (XPS, SIGMA PROBE, ThermoVG), and SEM (S-48000, Hitachi) analyses, ~2-nm-thick Pt films were deposited using electron-beam evaporation on the crystallized HZO films. The composition and the thickness of HZO films were examined using X-ray fluorescence

(Quant'X, Thermo SCIENTIFIC) and ellipsometry (L-116d, Gaetner), respectively. For electrical characterization, the polarization-voltage (P-V) characteristics, and I-V characteristics were measured using a ferroelectric tester (TF analyzer 2000, Aixacct systems) and a semiconductor parameter analyser (4145B, HP), respectively.

5.3. Results and discussions

Figures 5.1a and 1b show the P-V characteristics of the HZO films after various FGA process with Pt and Pt/TiN TE, respectively. The HZO film with the Pt/TiN TE shows ~70 % larger $2P_r$ (~ 34.1 $\mu C/cm^2$) compared with that (~ 20.5$\mu C/cm^2$) of the HZO film with the Pt TE before FGA. The large difference is assumed to be related to the stress by the TiN layer, but clear evidence for this has not yet been obtained.[8] FGA affects the P-V characteristics of the samples, especially for the capacitors with the Pt TE. As shown in figure 5.1a, both $2P_r$ and the slope of P-V loops decreased after FGA at 300-500 ^oC, whereas the initial values were almost recovered after FGA at 600 ^oC. Figure 5.1d shows that $2P_r$ changed to 11.5, 12.5, 14.3, and 19.8 $\mu C/cm^2$ after FGA at 300, 400, 500, and 600 ^oC, respectively, when the FGA was performed on Pt TE sample. However, the degradation is far smaller compared to that of other ferroelectric materials with a Pt TE, such as PZT or SBT.[4-7] The PZT and SBT capacitors lost their ferroelectric properties almost completely after the FGA at a temperature as low as 200 ^oC, and no recovery was reported at higher temperature.[7] For the capacitors with a Pt/TiN TE, the degradation was decreased even further. As shown in figure 5.1d, $2P_r$ changed to 28.4, 30.4, 33.6, and 32.9 $\mu C/cm^2$ after the 2 min of FGA at 300, 400, 500, and 600 ^oC, respectively, for this case. It is believed that the insertion of a 20-nm-thick TiN layer at the Pt/HZO interface largely blocked the degradation by H-diffusion. TiN is well-known

as a barrier layer against hydrogen diffusion.[12,13] It has been reported previously that in PZT and SBT capacitors, Pt works as a catalyst for the chemical reaction between hydrogen and ferroelectric films,[4-7] which is also applicable to HfO_2-based ferroelectrics. Thus, with the insertion of TiN, the degradation effects of FGA are negligible even up to 600 ^{o}C, which is very promising for the fabrication of ferroelectric capacitors using conventional processes. Figure 5.1c shows the P-V characteristics of NA HZO films with the Pt TE. For the HZO films annealed at 600 ^{o}C, P-V measurement with a pulse height of 4 V was impossible, due to the high leakage current. Without introducing H_2 gas during the annealing, no degradation can be observed in the P-V characteristics, summarized again in figure 5.1d, confirming that the degradation was not a result of the thermal budget effect, but of the effect of H_2.

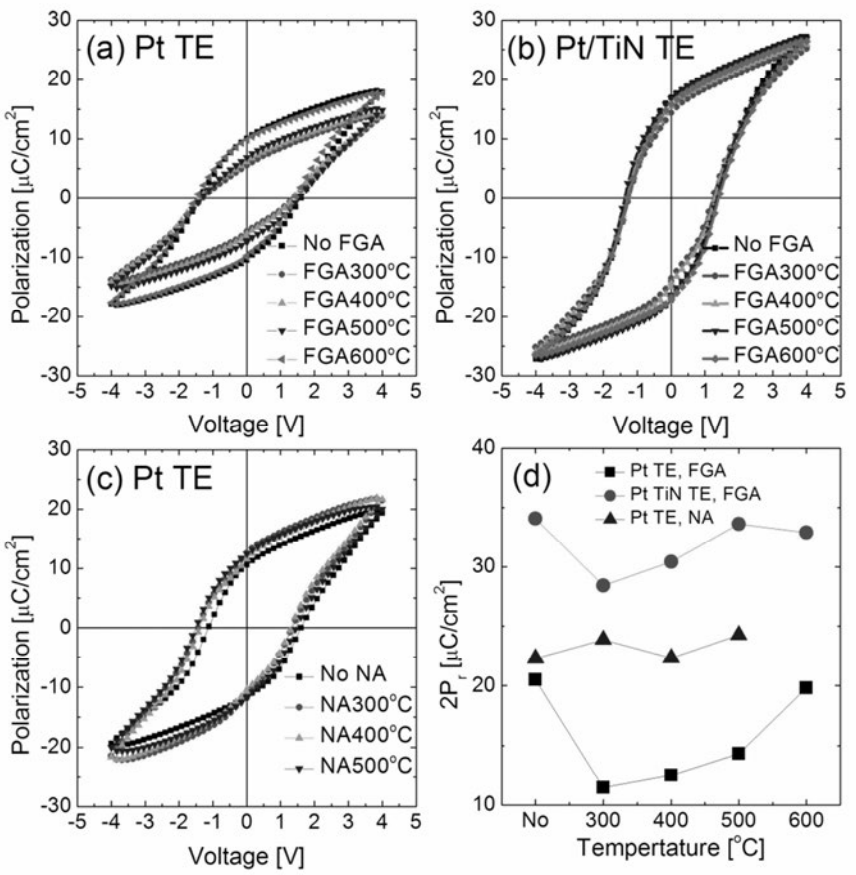


Figure 5.1. Polarization-voltage characteristics of ~10-nm-thick $Hf_{0.5}Zr_{0.5}O_2$ films after (a) FGA with Pt TE, (b) FGA with Pt/TiN TE, and (c) NA with Pt TE. (d) Summary of the changes in $2P_r$ as a function of annealing temperature. (FGA: forming gas annealing, NA: N_2 annealing)

The crystal structures of the HZO films were also examined. Figure 5.2a shows the XRD spectra of HZO films before FGA, and after 2min of FGA at 300, 400, 500, and 600 °C, respectively. Before FGA, the crystal structure appears to be a mixture of m- and o-phase, which is in accordance with the previous reports on the crystal structure of ferroelectric HfO_2 films.[8-11] In fact, it is challenging to distinguish the XRD peaks of o-phase from those of t-phase due to their similar 2θ values. However, t-phase cannot be ferroelectric due to its centrosymmetry.[8] Therefore, the XRD peaks observed at the 2θ values of superimposed orthogonal and t-phase were identified tentatively as orthorhombic peaks, but this does not exclude the possible presence of t-phase. Even though FGA at 300 – 400 °C degrades the ferroelectricity most seriously, no change in the crystal structure can be identified from the XRD. For the case of the sample after FGA at 600 °C, the intensity of the peaks of m-phase increased slightly. However, this does not contribute to the improvement in the ferroelectric performance of the HZO film because the ferroelectricity in this material is believed to originate from the non-centro-symmetric o-phase.

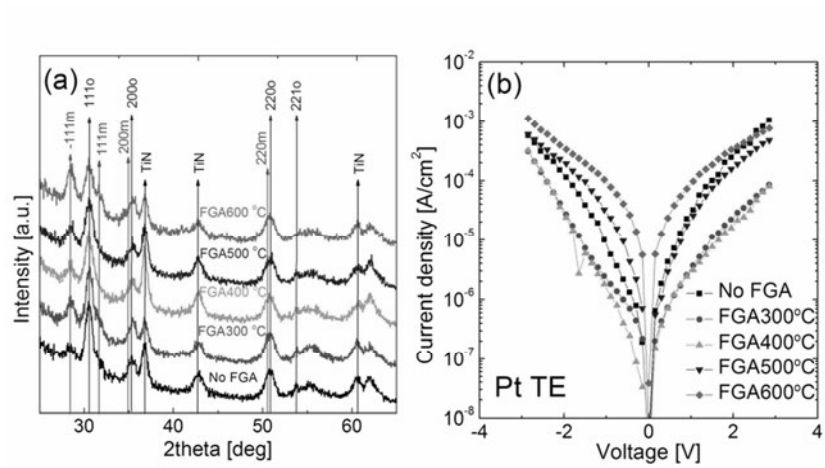


Figure 5.2. (a) X-ray diffraction spectra, and (b) current-voltage characteristics of ~10-nm-thick $Hf_{0.5}Zr_{0.5}O_2$ films with Pt TE before and after the FGA at 300, 400, 500, and 600 °C, respectively. Subscripts m and o in (a) mean monoclinic and orthorhombic phases, respectively.

As the next step, the mechanism for the degradation by FGA was examined. Generally, two mechanisms are suggested for the degradation of ferroelectric performance due to FGA. One is the elimination of O atoms from the films, and the other is the incorporation of H into the films.[4-7] If O atoms are eliminated from the films, the leakage behaviour should also be degraded, since the increase in oxygen vacancies results in an increase of the leakage current. Thus, the I-V characteristics were analysed, and figure 5.2b shows the results. The samples with FGA at 300 and 400 ^{o}C, which showed the largest degradation in $2P_r$, showed the lowest leakage current. In contrast, the sample after the FGA at 600 ^{o}C shows the highest leakage current, suggesting that the oxygen vacancies are formed under these circumstances. However, as shown in figure 5.1a, the P_r recovered its initial value after this FGA. This suggests that the degradation of the ferroelectric properties might not result from O-elimination, but from H-incorporation. This is also consistent with the results shown in figure 5.1c. The decrease in the leakage current after the FGA at 300 and 400 ^{o}C can be understood from the following. Fonseca *et al.* reported that H-incorporation can eliminate the gap state due to oxygen vacancies in HfO_2, which can increase the effective work function of Pt and decrease the leakage current by weakening the pinning by gap states.[14] The same reasoning might be applied to this case. In contrast, the highly reducing environment offered by the FGA at 600 ^{o}C scavenges

some of the oxygen atoms, but this effect is much less severe compared with other ferroelectrics, probably due to the higher bonding energy between Hf (Zr) and O ions in HZO. The different impacts of FGA on HZO and PZT are discussed in more detail at the end of this chapter. Therefore, it can be concluded that H-incorporation occurs at <500°C, while H-desorption occurs at >500 °C, which also matches well with previous reports. Driemeier *et al.* reported that H in $Hf_{0.7}Si_{0.3}O_2$ is eliminated easily by annealing in N_2 and N_2+O_2 atmosphere, and additional FGA at 500 °C did not result in the further incorporation of H.[15] In fact, FGA at 500 °C was even more effective for eliminating H compared to N_2 or N_2+O_2 annealing at 800 °C.[15] Therefore, it is reasonable that H atoms are incorporated during FGA at <500 °C, but not at >500 °C.

To further support the H-incorporation mechanism, the chemical states of the FGA samples were analysed using XPS. Although the presence of H cannot be detected directly by XPS, its presence can be indirectly confirmed by the shift in the binding energy (BE) of metal or oxygen ions.[16] Figures 5.3a and c show the variations in the XPS spectra of Zr 3d and Hf 4f, respectively, of HZO films after the FGA at 300 and 600 °C when the HZO sample was coated with the 2-nm-thick Pt film during FGA. For comparison, the spectra of the samples are also included for before the FGA, and after the FGA at 300 °C, at which the sample showed the most significant degradation, without the 2-nm-thick Pt film. For both spectra, the peaks shift to the high

BE region after FGA at 300 °C, and recover the original value after FGA at 600 °C when the 2-nm-thick Pt film is present. The donation of electrons to H ions further oxidizes Hf and Zr ions, making the BE of core electrons higher.[16] Kang *et al.* reported that the complex of oxygen vacancies and H is energetically most stable among the various models for H incorporation.[17] According to their model, H can passivate the dangling bonds due to oxygen vacancy, so the XPS peaks would shift to the high BE region. The XPS reveals that the degradation in the ferroelectric properties after the FGA at 300 °C is due to the incorporation of H into the HZO film. In contrast, there is almost no shift in the BE of the peaks even after the FGA at 300 °C without the capping Pt. This means that Pt works as a catalyst for H-incorporation during FGA. Figures 3b and d show the XPS spectra of Zr 3d and Hf 4f, respectively, of HZO films after the NA at 300 and 600 °C. There was no discernible shift in BE, in contrast to the FGA case, corroborating the electrical results shown in figure 5.1c. However, the intensity of the XPS signal increased with increasing annealing temperature. This can be understood from the results shown in figure 5.4.

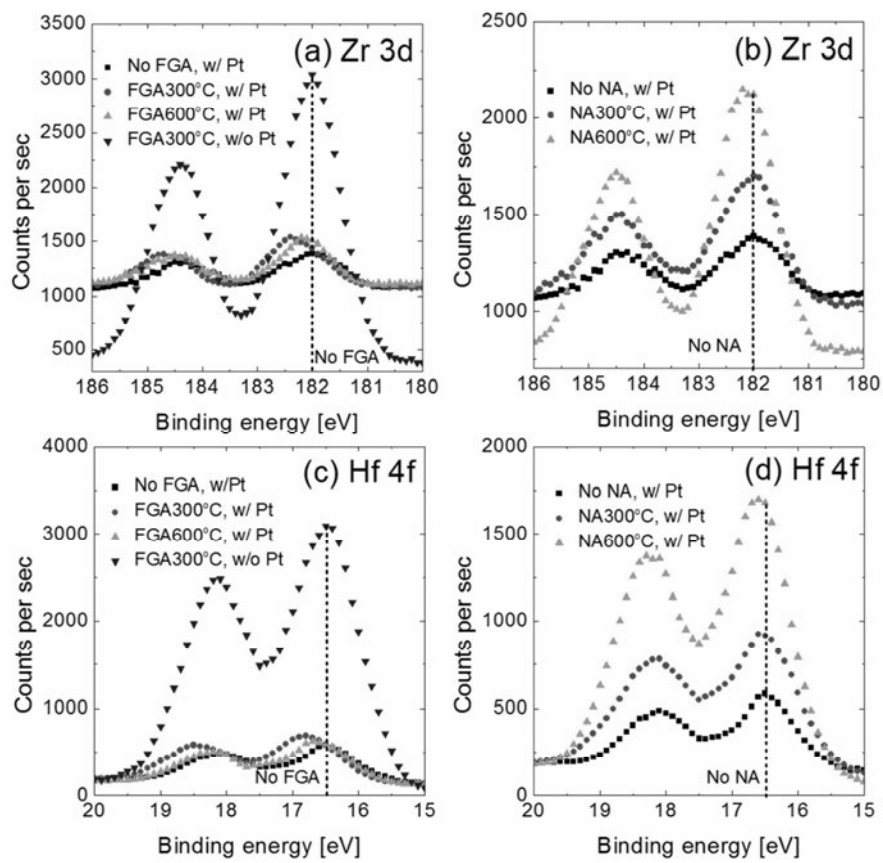


Figure 5.3. (a) Zr 3d and (c) Hf 4f XPS spectra of HZO films before and after the FGA with 2-nm-thick Pt TE at 300 and 600 °C, and after the FGA without the TE at 300 °C. (b) and (d) show the same XPS spectra for the NA samples with the 2-nm-thick Pt TE.

Figures 5.4a and b show the SEM images of 2-nm-thick Pt/HZO films after the FGA at 300 and 600 °C, respectively, and Figs. 5.4c and d do the same after the NA. The inset figure of figure 5.4a is the SEM image of Pt/HZO film before FGA. It can be understood that the NA induced agglomeration of the Pt film into clusters, which is very evident after the NA at 600 °C. In contrast, the agglomeration was quite suppressed after the FGA. Such a difference in the degree of Pt agglomeration is believed to result from the difference of adhesion of the thin Pt film onto HZO films. Driemeier and Baumvol reported that the bulk region of HfO_2 films contain a smaller amount of deuterium compared to the surface region by about one order of magnitude when an HfO_2 film is exposed under D_2O atmosphere at room temperature.[18] The abundant H ions on the surface of HZO or the interface region between the HZO and Pt appear to mediate the stronger chemical bonding between the HZO and Pt. Furthermore, this may make it relatively difficult for hydrogen to penetrate into the bulk of HfO_2 films. For the case of PZT films, on the other hand, Pb-O bonding is easily affected by H-incorporation. Koo *et al.* reported that XPS peaks of Pb 4f are largely distorted by FGA, whereas those of Zr 3d and Ti 2p show no change in their research on FGA of PZT films.[19] They ascribed the phenomenon to the lower free energy change during oxidation of Pb (-129 kJ/mol) compared with those of Zr (-926 kJ/mol) and Ti (-780 kJ/mol).[19,20] The free energy change due to oxidation of Hf is -1088 kJ/mol, which is much more negative

compared to that of Pb.[21] Therefore, it can be concluded that Hf-O and Zr-O bondings are much more robust compared with Pb-O bonding, making HfO_2 more resistant to the degradation by FGA compared to PZT.

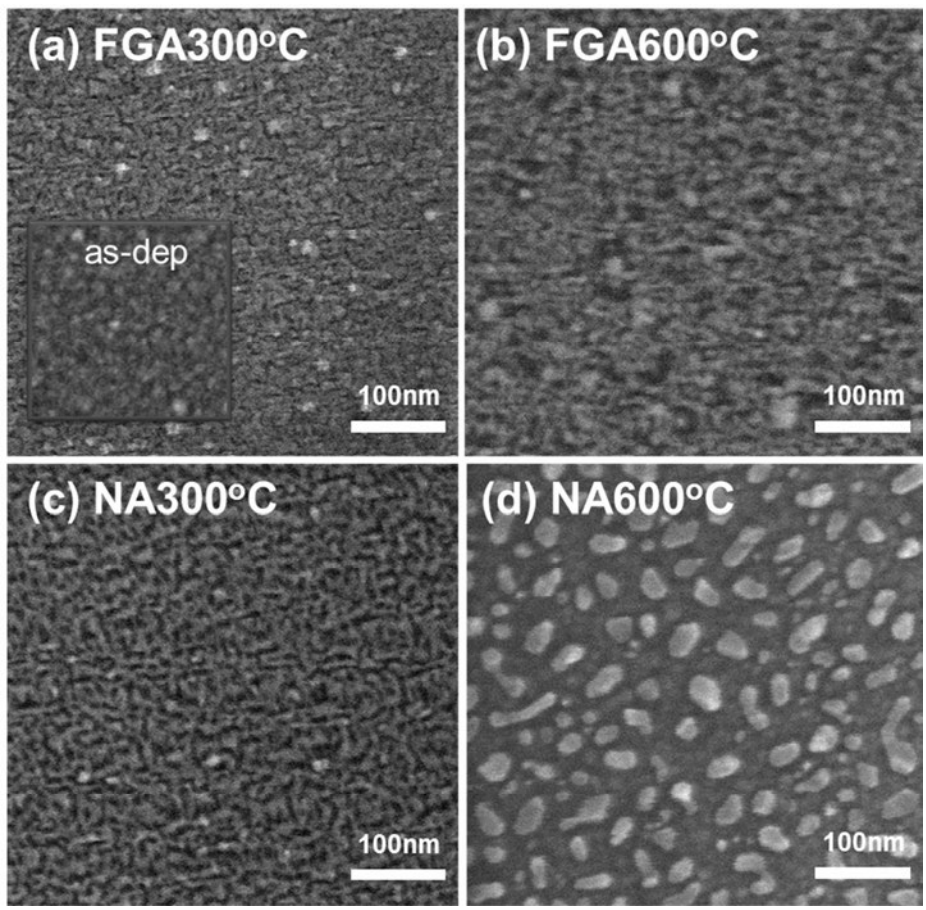


Figure 5.4. SEM images of 2-nm-thick Pt/10-nm-thick HZO film after FGA at (a) 300 and (b) 600 °C, and those after NA at (c) 300 and (d) 600 °C. The inset figure in figure (a) shows the SEM images of 2-nm-thick Pt/HZO film before FGA.

5.4. Conclusions

In summary, the effects of FGA on the electrical and physical properties of HZO films were examined. It was confirmed that H-incorporation during FGA degrades the ferroelectric properties of HZO films, but the degree was much smaller compared to the conventional perovskite-structured ferroelectrics. Pt works as a catalyst for H-incorporation, and a maximum $2P_r$ loss of ~40% occurs after the FGA at 300 °C. However, the insertion of a ~20-nm-thick TiN layer between Pt and HZO decreased the degradation to ~12%. In contrast, the degradation was almost completely recovered after the FGA at 600 °C due to desorption of H atoms at that temperature. The annealing under the N_2 atmosphere had little effect on the ferroelectric properties of the HZO films. The I-V characteristics and core-energy XPS revealed that the degradation and recovery have almost no relationship with the oxygen vacancy formation. The results show that HZO is much more resistant to the ferroelectric degradation by FGA compared to conventional ferroelectrics, such as PZT, which is believed to be due to the larger energy of Hf-O and Zr-O bondings compared to that of Pb-O bonding. These results are very promising for the use of HZO ferroelectric films in the fabrication of integrated memory devices.

5.5. References

[1] J. F. Scott, *Ferroelectric Memories.* (Springer-Verlag Berlin Heidelberg, 2000)

[2] T. P. Ma, *Electr. Dev. Lett.* **23**, 386 (2012)

[3] D. S. Jeong, , R. Thomas, R. S. Katiyar, J. F. Scott, H. Kohlsted, A. Petraru, C. S. Hwang, *Rep. Prog. Phys.* **75**, 076502 (2012).

[4] S. Aggarwal, S. R. Perusse, C. W. Tipton, R. Ramesh, H. D. Drew, T. Venkatesan, D. B. Romero, V. B. Podobedov, and A. Weber, *Appl. Phys. Lett.* **73**, 1973 (1998).

[5] Y. Shimamoto, K. Kushida-Abdelghafar, H. Miki, and Y. Fujisaki. *Appl. Phys. Lett.* **70**, 3096 (1997).

[6] K. Kushida-Abdelghafar, H. Miki, K. Torii, and Y. Fujisaki, *Appl. Phys. Lett.* **69**, 3188 (1996)

[7] J. -P. Han, and T. P. Ma, *Appl. Phys. Lett.* **71**, 1267 (1997).

[8] T. S. Böscke, J. Müller, D. Bräuhaus, U. Schröder, and U. Böttger, *Appl. Phys. Lett.* **99**, 102903 (2011).

[9] J. Müller, U. Schröder, T. S. Böscke, I. Müller, U. Böttger, L. Wilde, J. Sundqvist, M. Lemberger, P. Kücher, T. Mikolajick, and L. Frey, *J. Appl. Phys.* **110**, 114113 (2011).

[10] S. Mueller, J. Mueller, A. Singh, S. Riedel, J. Sundqvist, U. Schroeder, T. Mikolajick, *Adv. Funct. Mater.* **22**, 2412 (2012).

[11] J. Müller, T. S. Böscke, U. Schröder, S. Mueller, D. Bräuhaus, U.

Böttger, L. Frey, and T. Mikolajick, *Nano Lett.* **12**, 4318 (2012).

[12] Y. Sugizaki, T. Furuya, and H. Satoh, *Nucl. Instrum. Methods Phys. Res.* **B59/60**, 722 (1991).

[13] T. Nishikiori, T. Nohira, and Y. Ito, *J. Electrochem. Soc.* **148**, E52 (2001)

[14] L. R. C. Fonseca, A. L. Xavier, Jr., M. Ribeiro, Jr., C. Driemeier, and I. J. R. Baumvo, *J. Appl. Phys.* **102**, 044108 (2007).

[15] C. Driemeier, J. J. Chambers, L. Colombo, and I. J. R. Baumvol, *Appl. Phys. Lett.* **89**, 051921 (2006).

[16] S. J. Kerber, J. J. Brucker, K. Wozniak, S. Seal, S. Hardcastle, and T. L. Barr, *J. Vac. Sci. Technol. A* **14**, 1314 (1996).

[17] J. Kang, E. –C. Lee, Y. –G. Jin, and K. J. Chang, *Appl. Phys. Lett.* **84**, 3894 (2004).

[18] C. Driemeier and I. J. R. Baumvol, *Phys. Stat. Sol.* **204**, 945 (2007).

[19] J. –M. Koo, N. –H. Park, J. Park, W. H. Lee, J. -G. Lee,, and J. Kim, *J. Korean Phys. Soc.* **40**, 729 (2002).

[20] T. Kim, J. Koo, H. Min, I. Lee, and J. Kim, *Korean J. Mater. Res.* **10**, 684 (2000).

[21] M. M. Frank, G. D. Wilk, D. Starodub, T. Gustafsson, E. Garfunkel, Y. J. Chabel, J. Grazul, and D. A. Muller, *Appl. Phys. Lett.* **86**, 152904 (2005).

Chapter 6. The ferroelectric properties and switching endurance of $Hf_{0.5}Zr_{0.5}O_2$ films on TiN bottom and TiN or RuO_2 top electrodes

6.1. Introduction

The ferroelectric/electrode interface is one of the most important factors that affect the ferroelectric properties and endurance of ferroelectric devices [1]. For the conventional materials such as PZT, it suffered from the insufficient switching endurance for working memory application with the Pt electrode [2]. The origin of the degradation during electric field cycling is generally known to be related with the accumulation and possible ordering of oxygen vacancies in the region near the noble metal electrodes, such as Pt [3,4]. Therefore, adopting the oxide electrode, such as IrO_2, is a promising method of enhancing the ferroelectric properties and endurance of ferroelectric capacitors [2-5]. The oxide electrode can work as an oxygen vacancy sink, allowing the endurance properties of ferroelectric capacitors to be improved significantly [3-4]. For the HfO_2-based materials, in contrast, the effect of the electrode on the ferroelectric and endurance properties has been rarely reported since the first report by Böscke et al. [6]. Park et al. reported that the remnant polarization (P_r) of TiN/HZO/TiN capacitors was ~30% larger than that of the Pt/HZO/TiN capacitor, which means that the

TiN/HZO interface was beneficial in achieving better ferroelectric performance compared with the Pt/HZO interface [7]. The reason for such aspect of the TiN electrode, however, has not been clearly elucidated. Meanwhile, TiN is a reactive metal that could be relatively easily oxidized into TiO_xN_y or TiO_2, which is not expected to be appropriate for achieving the optimum properties [8]. Changing the BE, however, is a very challenging task given the fact that the HZO film showed the best ferroelectric properties when they were grown on TiN BE [9]. It was also noted that the formation energy of the oxide electrode, such as RuO_2, is relatively smaller than that of TiO_2 [10, 11]. This means that the severe loss of oxygen from RuO_2 could be induced when it is adopted as the TE in TiN BE through the thin HZO layer. This indicates that adopting RuO_2 as the TE material may not result in the optimum endurance performance. Therefore, it is an important task to examine the interactions of oxide TE and TiN BE with the HZO ferroelectric thin films with a thickness of only ~10 nm. In addition, the E_c of HfO_2-based thin films is larger than that of thin PZT films by about one order of magnitude [7]. Such a large electric field is known to change the resistance state of oxide films through the motion of the defects, such as oxygen vacancy, which can also make a difference in terms of endurance compared to PZT [12]. In this study, the ferroelectric properties and endurance of the TiN/HZO/TiN and RuO_2/HZO/TiN capacitors were compared, and their

differences were explained via structural and chemical analysis, which has not yet been reported in detail.

6.2. Experiments

HZO films were deposited on a sputtered 50-nm-thick TiN/Ti/SiO_2/Si substrate via thermal ALD at a 280°C wafer temperature, using $Hf[N(C_2H_5)CH_3]_4$, $Zr[N(C_2H_5)CH_3]_4$, and ozone as the Hf precursor, Zr precursor, and oxygen source, respectively. As the growth per cycle of HfO_2 and ZrO_2 were almost identical (~0.12 nm/cycle), the HZO films with a 0.5:0.5 Hf:Zr ratio could be deposited using a 1:1 HfO_2:ZrO_2 ALD cycle ratio. For the electrical characterization, Pt(60nm)/TiN(20nm) and Pt(60nm)/RuO_2(20nm) TEs were deposited via DC (reactive for RuO_2 and TiN) sputtering through a shadow mask with a 300 m hole diameter (TiN and RuO_2 contacts HZO films). The TiN TE samples were annealed at 500°C for 30 s in a N_2 atmosphere after TE deposition (TiN/PMA). The details of the optimized RuO_2 deposition condition were reported elsewhere [13]. For the RuO_2 TE samples, on the other hand, the following three annealing conditions were adopted: (1) post-metallization-annealing (RuO/PMA) - annealing at 500°C for 30 s in a N_2 atmosphere after TE deposition; (2) post-deposition-annealing (RuO/PDA) - annealing at 500°C for 30 s in a N_2 atmosphere before TE deposition; and (3) PDA+curing (RuO/curing) - annealing the PDA samples at 400°C for 30 min in an air atmosphere after TE deposition. The cation composition and film thickness were examined via X-ray fluorescence (Quant'X, Thermo Scientific) and

ellipsometry (L-116d, Gaetner), respectively. For the structural analysis, Pt(10nm)/TiN(20nm) and Pt(10nm)/RuO_2(20nm) layers were deposited on HZO films with no patterning. The crystallographic phase of the films was examined through a normal θ-2θ scan and via GAXRD using an X-ray diffractometer (Pananalytical X-pert Pro, Cu Kα radiation with a 0.15418 nm X-ray wavelength). Depth profiling was performed via Auger electron spectroscopy (AES, Perkin-Elmer, 660). For electrical characterization, the polarization electric field (P-E) and capacitance-field (C-E) were measured at room temperature using a ferroelectric tester (TF Analyzer 2000, Aixacct Systems) with a 1 kHz frequency and an impedance analyzer (4194A, HP) with a 10 kHz AC frequency. An endurance test was performed using a ferroelectric tester (TF Analyzer 2000, Aixacct Systems) with a 100 kHz electrical cycling frequency.

6.3. Results and Discussions

Figure 6.1a shows the P-E hysteresis curves for the capacitors with 10.5-nm-thick HZO films with various TE and annealing conditions. The P-E loops of the capacitors with different film thickness (t_f) values can be seen in figure 6.2. The $2P_r$ values of TiN/PMA and RuO/PMA were ~34 and ~24 $\mu C/cm^2$, respectively, and the P-E loop of TiN/PMA was almost symmetric whereas that of RuO/PMA was shifted to the positive bias direction by ~0.48 MV/cm. This means that the RuO_2 TE degraded the ferroelectric properties of the HZO capacitor, which is quite different from the reports on the PZT capacitors [4, 5]. To elucidate this unexpected result, the crystal structure of RuO/PMA was analysed using GAXRD spectra, as can be seen in Figure 6.1b. To confirm the deposition of the fully oxidized RuO_2 TE, the Pt/RuO_2 TE was also deposited on a 100-nm-thick thermal SiO_2/Si substrate, and no RuO_2 reduction was observed, as can be seen in Figure 6.1b. For RuO/PMA, however, no diffraction peak was seen from both RuO_2 and Ru. This means that there might be chemical reactions related with the RuO_2 layer. Figures 6.3a-c show the AES depth profile results. In Figure 6.3b, it can be easily noticed that RuO_2 was significantly reduced to Ru, and that the Ru atoms diffused into the Pt layer due to the RuO/PMA. Figure 6.3a shows, on the other hand, that the Pt/TiN TE kept the structure intact even after the TiN/PMA. To address the problem related with the reduction of RuO_2, the

HZO film was crystallized before the deposition of RuO_2 TE (RuO/PDA). The sample, however, showed an even more distorted P-E loop, which might have resulted from the space charge layer at the RuO_2/HZO interface. In fact, the process of TE sputtering is well known as a source of interfacial defects [13]. It is surprising to note that an Ru peak can be observed even for the GAXRD spectra of RuO/PDA, meaning that RuO_2 is partly reduced during the sputtering process of RuO_2 even without any thermal treatment. Therefore, the RuO/PDA capacitor was annealed in an air atmosphere to supplement the oxidation of the partly reduced RuO_2. The P-E curve of the RuO/curing capacitor, however, shifted to the positive bias region even more. It can be understood that the oxidation of TiN BE as well as the reduction of RuO_2 TE occurred during the curing process from the decrease of the intensity of the TiN(111) peak and the increase of the Ru(101) peak in the GAXRD spectrum of the sample.

Figure 6.3d shows the change in the equivalent oxide thickness (t_{ox}), which shows the thickness of the SiO_2 film with the equivalent capacitance, from the C-E characteristics of various capacitors as a function of t_f. The C-E curves of the various samples can be seen in figure 6.4. The t_{ox} values were extracted from the capacitance value measured at -2 V (-2MV/cm) to exclude the effect of ferroelectric switching. Generally, the thickness of the interfacial low-k layer (t_i) can be extracted from the y-axis intercept of the linear fitting of the t_{ox}-t_f plot. Park et al. reported, however, that a change in

the value of t_f will affect the competition of the polymorphs of HZO [14]. In their report, the portion of the polymorphs of HZO changed with the changing t_f. Therefore, t_i cannot be directly extracted from the y-axis intercept, but the obviously different y-axis intercept indicated that there were significant changes in the interfacial state depending on the TE material as well as the annealing conditions. As expected from the P-E characteristics, the adverse contribution from the interface of RuO/curing was the largest, whereas that in TiN/PMA was the smallest among the samples. The t_{ox} values of RuO/PMA, RuO/PDA, and RuO/curing were larger than that of TiN/PMA by ~0.2, ~0.4, and ~1.1 nm. Such an increase in t_{ox} could be attributed to the oxidation of the TiN electrode. Assuming that the ε_r of TiO_2 is ~40, 1.1 nm t_{ox} corresponds to ~11 nm [15]. The significant oxidation of TiN BE to TiO_2 (or TiO_{2-x} or TiO_xN_y) could be observed in the AES spectra in Figure 6.3c. For RuO/PMA, in contrast, the mixing of the reduced Ru and Pt could be observed, which interferes with the crystallization of RuO_2 and Ru, as shown in Figure 6.1b. This means that the TE of the RuO/PMA sample was the mixture of Pt and Ru, which is not favourable for the optimal ferroelectric properties of the HZO film. The formation enthalpy of RuO_2 was much smaller (~ -280 kJ/mole at 773 K) [10] than that of TiO_2 (~ -907 kJ/mole at 773 K) [11], which is the fundamental driving force that induces such a significant reaction. It is also interesting to note that oxygen atoms could be observed in the TiN TE and BE. It is generally known that the

electrode with oxygen can work as an oxygen vacancy sink, which is known as the degradation due to electric field cycling. Therefore, the TiN electrodes are also expected to work as oxygen vacancy sinks and are expected to show promising endurance properties, although they are not oxide electrodes.

Figure 6.5a and b show the switching endurance properties of TiN/PMA and RuO/PMA, respectively. TiN/PMA shows robust P-E characteristics up to 10^9 cycles, with a large P_r (>15 $\mu C/cm^2$) when the switching field was 2.5 MV/cm, which is much higher than the usual switching field for the endurance test for PZT. Another notable feature from this endurance test was that the HZO film usually broke down after endurance failure, which is usually not the case for PZT. The large E_c of ~1 MV/cm and the small t_f of ~10 nm might be the reasons for such hard breakdown with the formation of a permanent leakage path through the films. The number of cycles for the breakdown decreased with increasing electric field, and the number of electric cycling was ~10^7 and ~10^6 for 3 and 3.5 MV/cm electric fields, respectively. These levels of endurance properties of HZO were as good as those of the Si-doped HfO_2 films reported by Müller et al. [16]. In the case of RuO/PMA, however, its endurance was worse than that of TiN/PMA. Even for the case of electric cycling with a 2.5 MV/cm electric field, the hard breakdown with significant leakage current degradation could be observed before the switching cycle number of 10^7. This degradation might have resulted from the RuO_2 reduction and from the mixing of the reduced

Ru and the Pt TE, as already observed in Figure 6.3b, which could enhance the roughening and the formation of local current paths. The endurance properties of the RuO_2 TE samples with other annealing conditions could not be tested because their P-E curves were overly imprinted in the positive bias direction. As a result, TiN/PMA showed the best endurance among the samples.

Next, the effect of the annealing temperature (T_{anneal}) and t_f on the endurance properties were examined to optimize the endurance properties of the TiN/PMA samples. Figure 6.6a shows the endurance test results of the TiN/PMA samples with 10-nm-thick HZO films whose T_{anneal} values were 400, 500, and 600°C, respectively. The physical and ferroelectric properties of the samples were reported elsewhere [14]. With an electric field for cycling of 3MV/cm, the initial P_r of the sample annealed at 500°C was the largest, whereas that of the sample annealed at 400°C was the smallest. It is believed that T_{anneal} affects the crystalline quality of the ferroelectric film, and that a 400°C T_{anneal} is too low to produce a high-quality film with a low density of defects. In addition, the interface between the ferroelectric film and the electrode could also be affected by T_{anneal}. Meanwhile, an increase in T_{anneal} can result in the formation of the partial m-phase, which can also affect the ferroelectric and endurance properties. Especially, a double-layered structure with an upper m-phase and a lower ferroelectric o-phase can be formed partly with the increasing T_{anneal} or t_f of the HZO films [14].

The effect of the m-phase formation can be observed more clearly in Figure 6.6b. TiN/PMA, whose t_f is 17 nm, contains more m-phase than thinner films, which is consistent with the previous report [11]. The m-phase can work as a dead layer in ferroelectrics and would thus degrade both the ferroelectric properties [14] and the endurance of the HZO capacitors. For the endurance, the problem can be even worse because the loss of the switching electric field across the m-phase with a low ε_r must be more severe, and an even higher voltage is necessary to induce sufficient electrical switching. The concentred electric field across the low-ε_r region can more easily result in a hard breakdown. As can be seen in figure 6.6b, the TiN/PMA sample, whose t_f was 17 nm, was broken down at an electric cycling of only 10^6, whereas the samples whose t_f values were 10 and 5.5 nm showed robust ferroelectric characteristics up to ~10^8 and ~10^9 cycles, respectively. Even though the 5.5-nm-thick TiN/PMA could switch to a cycle number more than 10-nm-thick one, its P_r was much smaller than that of the 10-nm-thick one. This might have been due to the increase of the portion of non-ferroelectric t-phase or the increase of the low-dielectric interfacial layer. Therefore, the ~10 nm t_f was found to be the best thickness for the optimum ferroelectric properties and endurance.

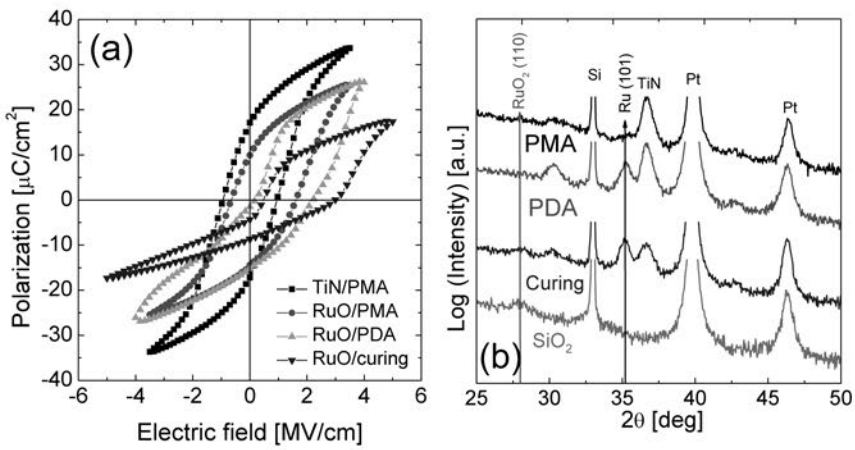


Figure 6.1. (a) P-E hysteresis of 10.5-nm-thick $Hf_{0.5}Zr_{0.5}O_2$ capacitors with a TiN and RuO_2 top electrode with various annealing conditions. (b) Grazing-angle incidence angle X-ray diffraction spectra of the $Hf_{0.5}Zr_{0.5}O_2$ and SiO_2 films with an RuO_2 top layer with various annealing conditions.

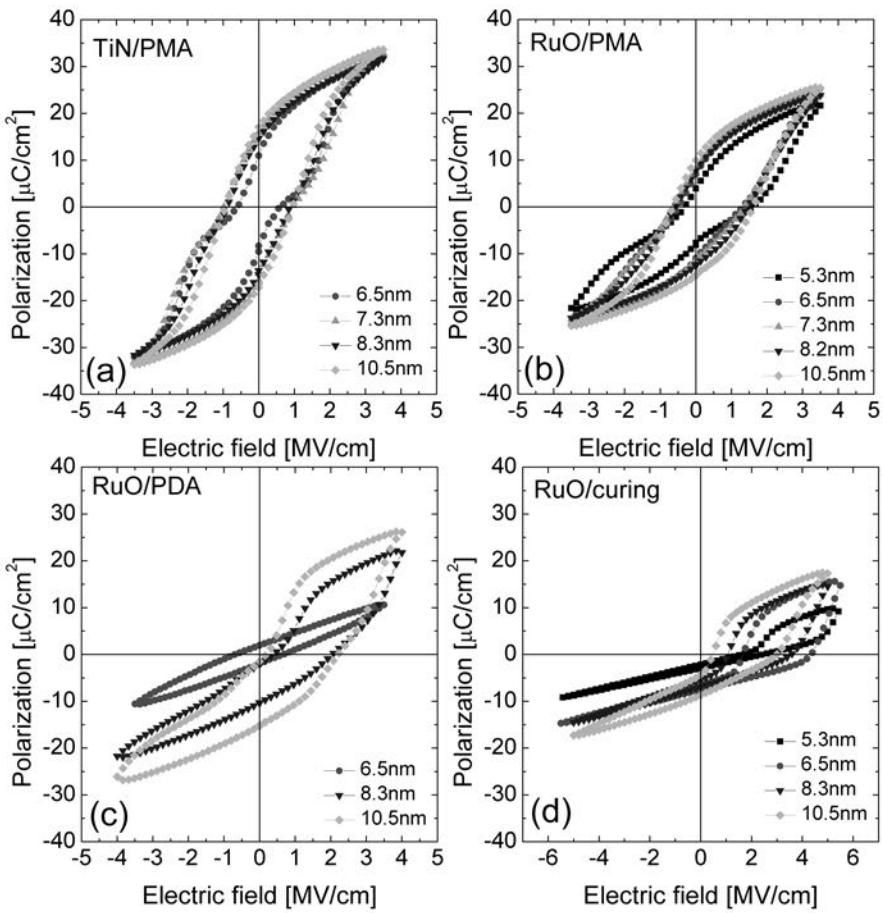


Figure 6.2. The polarization-electric field characteristics of (a) TiN/PMA, (b) RuO/PMA, (c) RuO/PDA, and (d) RuO/curing with various film thickness, respectively.

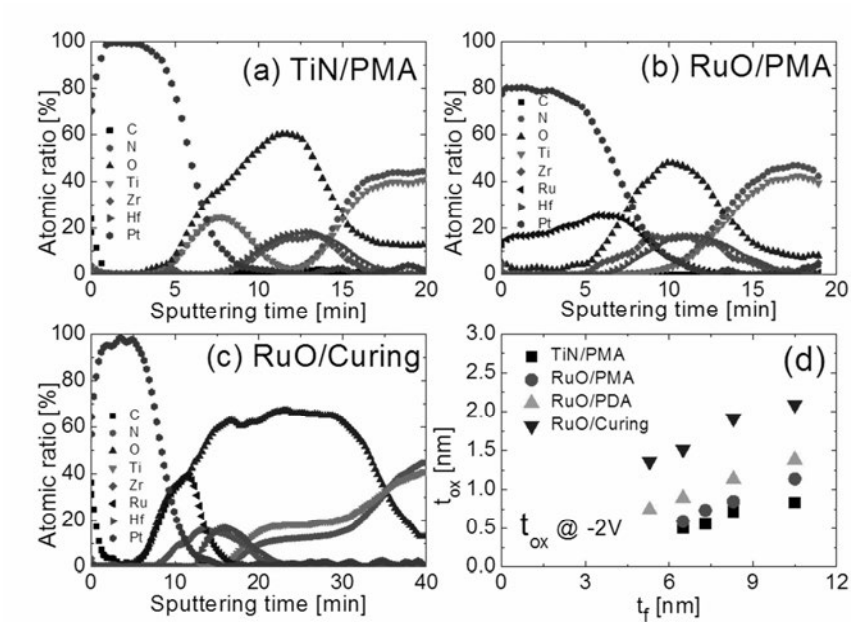


Figure 6.3. Auger electron spectroscopy spectra of (a) TiN/PMA, (b) RuO/PMA, and (c) PDA/curing. (d) The change of the equivalent oxide thickness from the C-E characteristics of various capacitors as a function of film thickness.

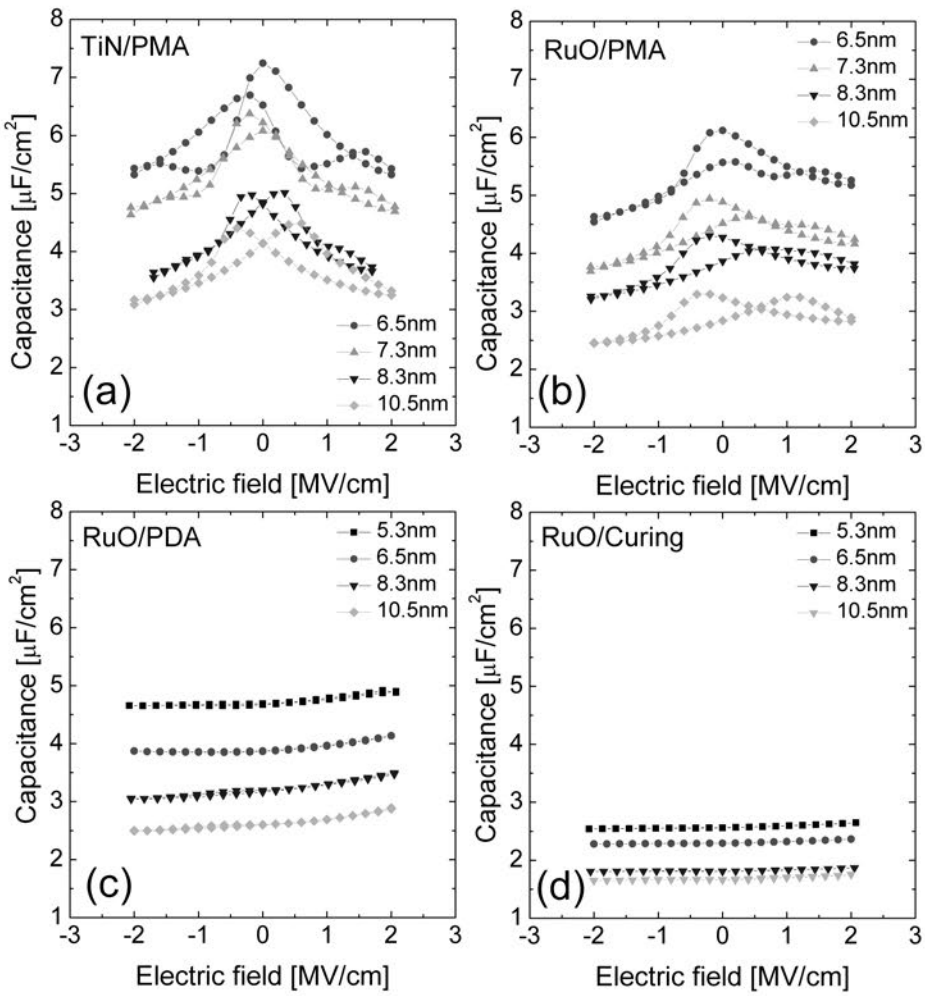


Figure 6.4. The capacitance-electric field characteristics of (a) TiN/PMA, (b) RuO/PMA, (c) RuO/PDA, and (d) RuO/curing with various film thickness, respectively.

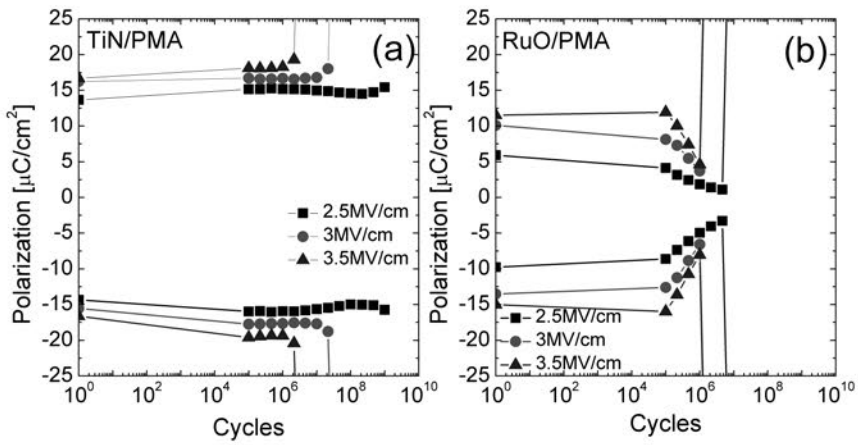


Figure 6.5. Endurance properties of (a) TiN/PMA and (b) RuO/PMA with 2.5, 3, and 3.5 MV/cm electric field cycling, respectively.

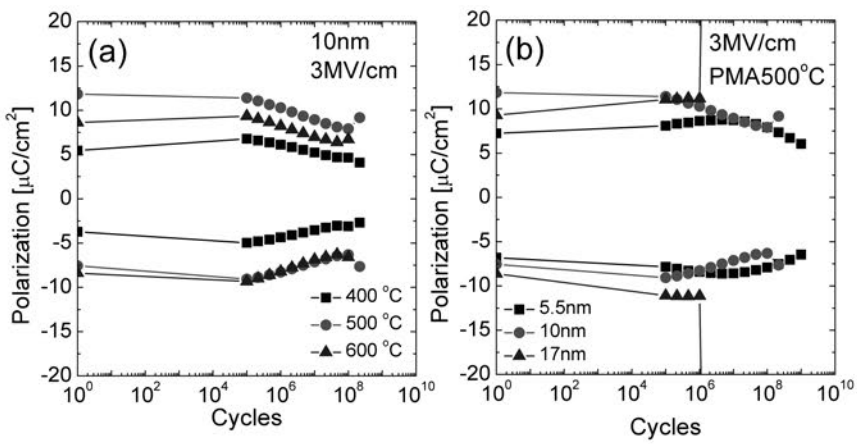


Figure 6.6. Endurance properties of (a) TiN/PMA with a 10 nm film thickness and annealed at 400, 500, and 600°C, and (b) TiN/PMA with 5.5, 10, and 17 nm film thicknesses and a 500°C annealing temperature, respectively.

6.4. Conclusions

In conclusion, unlike the conventional ferroelectrics, such as PZT with a noble metal BE, the RuO_2 electrode could not improve the ferroelectric properties and endurance of the HZO capacitors with the TiN BE. The reason for this was the reduction of the RuO_2 TE by the chemical reaction with the reactive TiN BE. TiN appears to be the best and only BE material that is known to work well with ferroelectric HfO_2-based films, and as such, it seems unlikely that TiN BE will be replaced with another electrode material. Meanwhile, the TiN electrode contained a significant amount of oxygen atoms, which may decrease the oxygen vacancy concentration in the HZO layer during the repeated switching, which in turn can improve the endurance of the ferroelectric capacitors. The TiN/PMA sample showed robust ferroelectric properties even after electric cycling for 10^9 times with a switching field of 2.5 MV/cm. The effect of T_{anneal} and t_f were also examined. With a 3 MV/cm electric field for cycling, the 500°C T_{anneal} showed the best endurance, which can be ascribed to the minimized m-phase formation and the improved crystalline quality of the HZO film.

6.5. References

[1] T. M. Shaw, S. Trolier-McKinstry, and P. C. McIntyre, *Annu. Rev. Mater. Sci.* **30**, 263 (2000).

[2] C. B. Eom, R. B. Van Dover, J. M. Phillips, J. H. Marshall, C. H. Chen, R. J. Cava, and R. M. Fleming, *Appl. Phys. Lett.* **63**, 2570 (1993).

[3] J. F. Scott and M. Dawber, *Appl Phys. Lett.* **76**, 3801 (2000).

[4] I. K. Yoo and S. B. Desu, *Phys. Status Solidi A* **133**, 565 (1992).

[5] J. J. Lee, C. L. Thio, and S. B. Desu, *J. Appl. Phys.* **78**, 5073 (1995).

[6] T. S. Böscke, J. Müller, D. Bräuhaus, U. Schröder, and U. Böttger, *Appl. Phys. Lett.* **99**, 102903 (2011).

[7] M. H. Park, H. J. Kim, Y. J. Kim, W. Lee, H. K. Kim, and C. S. Hwang, *Appl. Phys. Lett.* **102**, 112914 (2013).

[8] H. –Y. Chen and F. –H. Lu, *J. Vac. Sci. Technol. A* **23**, 1006 (2005).

[9] S. W. Lee, B. J. Choi, T. Eom, J. H. Han, S. K. Kim, S. J. Song, W. Lee, and C. S. Hwang, *Coord. Chem. Rev.* 257, 3154 (2013).

[10] E. H. P. Cordfunke and R. J. M. Konings, *thermochimica Acta* **129**, 63 (1988).

[11] M.W. Chase Jr., J. Phys. *Chem. Ref. Data*, *Monograph* **9**, 1 (1998).

[12] D. –H. Kwon, K. M. Kim, J. H. Jang, J. M. Jeon, M. H. Lee, G. H. Kim, X. –S. Li, G. –S. Park, B. Lee, S. Han, M. Kim, and C. S. Hwang, *Nat. Nanotechnol.* **5**, 148 (2010).

[13] H. K. Kim, I. –H. Yoo, J. H. Lee, and C. S. Hwang, *ACS Appl. Mater. Interfaces* **5**, 1327-1332, 2013

[14] M. H. Park, H. J. Kim, Y. J. Kim, W. Lee, T. Moon, and C. S. Hwang, *Appl. Phys. Lett.* **102**, 242905 (2013).

[15] S. K. Kim, G. –J. Choi, S. Y. Lee, M. Seo, S. W. Lee, J. H. Han, H. –S. Ahn, S. Han, and C. S. Hwang, *Adv. Mater.* **20**, 1429 (2008).

[16] S. Müller, J. Müller, U. Schröder, and T. Mikolajick, *IEEE T. Device Mater. Re.* **13**, 93 (2013).

Chapter 7. Novel ferroelectric device: tri-states memory using ferroelectric-insulator-semiconductor hetero-junction

7.1. Introduction

Charge based FeRAM has a long history of being the most promising candidate for nonvolatile memory due to its potential for high speed, low power consumption, complementary metal-oxide-semiconductor (CMOS) compatibility, and nonvolatility of the stored data. On the other hand, its future as a mass-productive memory appears elusive and studies on it tend to be retarded, particularly due to the difficulties in scaling down its feature size. Because of its inappropriate reliability originating from the depolarization field and leakage current, there has been no great success in reducing the feature size of the ferroelectric memory compared to other nonvolatile memories, such as phase-change RAM. [1-3] Despite some impressive reports on overcoming the size effect, improving the low retention property of nano-scale ferroelectric devices still remains a tough challenge. [4-6]

If scaling down of the feature size of the conventional ferroelectric memory is difficult, the increase in the number of memory states per ferroelectric memory cell could be a viable solution for the scaling problem. There have been many reports on the design and fabrication of multi-level or

even analog type ferroelectric memories but no breakthrough has been reported yet. [7-9] Most efforts were concentrated on using a depolarized state as the third memory state in addition to the two spontaneously polarized states with opposite signs. Raiter reported the possibility of using three data signal levels to increase the array storage density from 1 bit per cell to 1.5 bits per cell using three-level FeRAM. [10] When each cell of the FeRAM has three polarization states (named L, M, and H), nine states (LL, LM, LH, ML, MM, MH, HL, HM, and HH) can be memorized into two FeRAM cells. Therefore, if eight among nine possible states are used, two cells of the FeRAM can work as three cells of a traditional binary memory with the aid of peripheral circuitry. As a result, 50% increase in data can be memorized in the same area compared to conventional FeRAM with binary memory states. They suggested that three levels are possible if the depolarized state as well as two polarization states of the ferroelectric material can be used. On the other hand, this approach has a fundamental problem of low reliability and narrow sensing margin for the general charge (or voltage) sense circuitry. Depolarizing a polarized ferroelectric state in FeRAM circuit is not a trivial task. The use of unsaturated ferroelectric polarization can be a possible solution but this also has several problems; the ferroelectric layer with unsaturated polarization is not in a thermodynamically stable state. As a result, the memory state using unsaturated polarization may not be reliable. In addition, the unsaturated

polarization state can be achieved more readily from the non-square-like polarization – voltage (P-V) hysteresis loop, but this P-V loop actually decreases the signal margin for the two basic (saturation) polarization states. The other approach was focused on the circuitry or programming sequence, which can result in a highly improved reliability. [9] Such a radical change in the circuit structure is quite burdensome to the design and may not be compatible with the conventional CMOS technology. Therefore, a novel approach is needed to realize a ferroelectric memory cell with three or even more memory states. In this work, a ferroelectric capacitor with three memory states by dividing the compensating charges for the ferroelectric bound charges into two different layers is reported.

In the conventional metal-ferroelectric-metal (MFM) capacitor structure, the compensating charges are stored in the metal layer, particularly at the F/M interface. Recently, Jiang and Lee reported interesting results on that inserting a thin Al_2O_3 layer between PZT and Pt electrode resulted in unexpected improvement of the ferroelectric properties of the metal-ferroelectric-insulator-metal (MFIM) structure. [11-13] They showed that the thin Al_2O_3 layer works as a tunnel switch meaning that it is open during polarization switching whereas it is closed during non-switching or after switching is complete. This closed tunnel switch improves the retention of compensating charge for the ferroelectric bound charge. The compensation charges are located at the PZT/Al_2O_3 interface due to the presence of the

interface states. Step-by-step polarization switching would be possible if a number of tunneling barriers with a different tunneling threshold voltage are used, and finally, the ferroelectric capacitors with multiple memory states can be achieved. To achieve this goal, in this study, metal-ferroelectric-insulator-semiconductor-metal (MFISM) structures were fabricated using PZT, thin Al_2O_3 and ZnO films as the ferroelectric, insulator and semiconductor layers, respectively. (See section 7.2.) The PZT/Al_2O_3 and Al_2O_3/ZnO interfaces work as the two interfaces where the compensating charges can be stored. Other dielectric layers, such as TiO_2, might also work as a second dielectric layer, but the ZnO layer was chosen in this study because the carrier accumulation/depletion property of the semiconducting ZnO layer can be used to better understand the electrical response of such a complicated system. The combination of the ferroelectric and the semiconducting materials often results in interesting properties for memory device applications. [14] Pt was used as the metal layer as it has minimal effect on the chemistry of the oxide layers. In this experiment, three MFISM structures with different ZnO layer thicknesses were fabricated and their electrical characteristics were examined to confirm the effect of the ZnO layer and show the feasibility of this structure as a ferroelectric memory element with tri-memory states. One of the problems with this MFISM structure is the difficulty in the precise understanding of electrical responses due to its complicated energy band structure. The last part of this chapter

(Figure 7.13) discusses the variation of the energy band structure according to the applied bias in detail, which would contribute to the better understanding of the memory operation using this complicated material system.

7.2. Experiment

A 150-nm-thick $Pb(Zr_{0.3},Ti_{0.7})O_3$ film was formed on a platinized Si substrate using a sol-gel method. A 4.0- or 5.5-nm-thick Al_2O_3 tunnel barrier layer was deposited on the PZT film using plasma enhanced atomic layer deposition with tri-methyl aluminum as the Al precursor and O_2 – plasma as the oxygen source. 5-, 10-, and 20-nm-thick ZnO thin films were deposited on the Al_2O_3 layer by RF magnetron sputtering at room temperature. A platinum TE was formed by electron-beam evaporation. The ZnO layer was etched selectively using a 10 vol% HCl solution with a Pt TE as a hard mask.

The film thickness was measured by ellipsometry (L-116d, Gaertner). The microstructure of the films was examined by XRD (X'pert PRO, Panalytical), SEM (S-4800, Hitachi) and cross-section high-resolution transmission electron microscopy (HRTEM, JEM 3000F, JEOL). P-V characteristics were measured using a TF Analyzer 2000 (Aixacct systems, Germany) at the frequency of 1000 Hz. The C-V characteristics were measured using a HP 4194A with the AC voltage input combined with a DC bias sweep. The amplitude of the AC voltage was 0.05V and the frequency was 100 kHz. All the electrical measurements were carried out by the driving voltage on the top Pt electrode while the bottom Pt electrode was grounded.

Figure 7.1 shows a schematic diagram (left panel) of the setup for the pulse-switching experiment, where the pulse generator, sample and oscilloscope were connected serially. The upper right panel shows a

schematic diagram of the pulse application (writing and read pulses separated by a 5 μs time span. The lower right graph shows the typical current density-time response of the sample. The $2P_r$ value can be estimated by integrating the current response over time up to 5 μs, as shown by the equation in the figure.

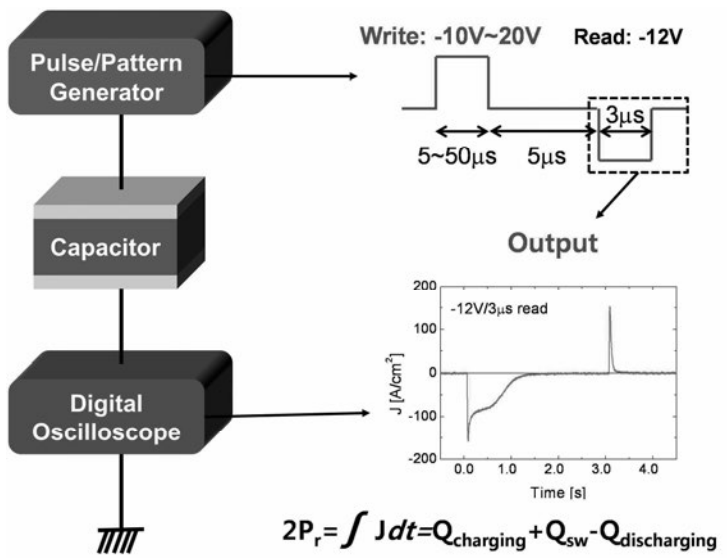


Figure 7.1. Schematic diagram of the measurement system using a pulse generator and digital oscilloscope (left panel), shape of the input pulse by the pulse generator (right upper panel), and switching current density as a function of time read by a digital oscilloscope (right lower panel).

7.3. Results and Discussions

Figure 7.2 shows the structure of the fabricated MFISM structure and its schematic energy band structure with two interfaces containing trapped charges. Here, the trapped charges are electrons, indicating that the polarization in the PZT layer is pointing from the left hand side to the right hand side in Fig. 7.2 (b), and are assumed to be separately present at the two interfaces. ZnO is an intriguing semiconductor material of which the electric conductivity can be controlled by the polarization state of the contacting ferroelectric materials. Kato et al. reported that a two dimensional electron gas is formed at the PZT/ZnO interface and can be controlled by the polarization direction of the PZT. [15] Yoon et al. reported research on an organic ferroelectric thin film transistor using Al_2O_3 as an insulating layer and ZnO as a channel layer.[16]

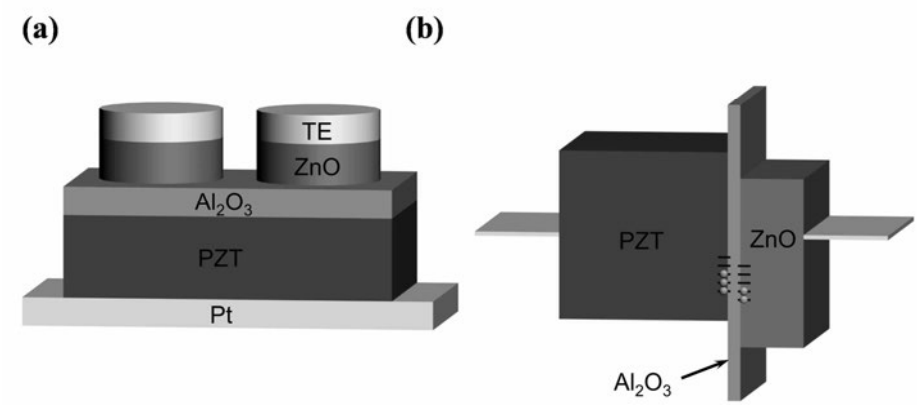


Figure 7.2. (a) Structure of the fabricated MFISM capacitor with a ZnO semiconducting layer between the Al_2O_3 and top electrode, (b) schematic diagram of the ferroelectric capacitor with two interfaces with charge trap states

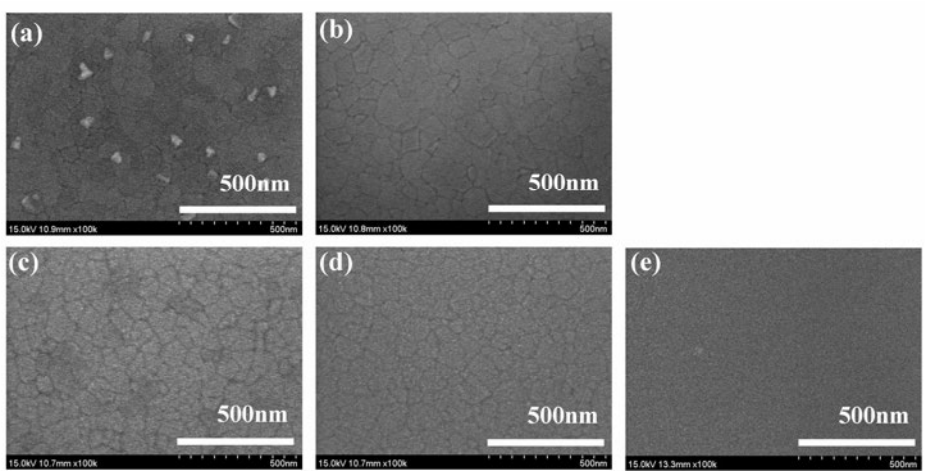


Figure 7.3. The SEM image of (a) 150-nm-thick PZT film on Pt electrode, (b) 5.5-nm-thick Al_2O_3 film on 150-nm-thick PZT film, (c) 5-nm-thick ZnO film on 5.5-nm-thick Al_2O_3/150-nm-thick PZT film, (d) 10-nm-thick ZnO film on 5.5-nm-thick Al_2O_3/150-nm-thick PZT film, and (e) 20-nm-thick ZnO film on 5.5-nm-thick Al_2O_3/150-nm-thick PZT film.

Figures 7.3 (a)-(e) shows SEM (S-4800, Hitachi, Japan) images of the surface of (a)150-nm-thick PZT film on Pt electrode, (b) 5.5-nm-thick Al_2O_3 film on 150-nm-thick PZT film, (c) 5-nm-thick ZnO film on 5.5-nm-thick Al_2O_3/150-nm-thick PZT film, (d) 10-nm-thick ZnO film on 5.5-nm-thick Al_2O_3/150-nm-thick PZT film, and (e) 20-nm-thick ZnO film on 5.5-nm-thick Al_2O_3/150-nm-thick PZT film. As shown in figure 7.3 (a), there are some particles on the grain boundary edges. These could be PbO particles considering that the PZT film contains a 10% excess Pb. No PbO particles could be found after depositing a 5.5nm-thick-Al_2O_3 layer, as shown in figure 7.3 (b). The grains of the Al_2O_3 and ZnO were barely found from the SEM images because the thickness of the Al_2O_3 and ZnO was too thin to form grains large enough to be observed by SEM. The grain-like images in Figs. 7.3 (b) and (c) are due to the PZT layer. The Al_2O_3 layer exists in an amorphous form, which would be observed below in the HRTEM (JEM-3000F, JEOL, Japan) image.

Figure 7.4 shows XRD patterns of 150-nm-thick PZT film on Pt electrode, 5.5-nm-thick Al_2O_3 film on 150-nm-thick PZT film, 5-nm-thick ZnO film on 5.5-nm-thick Al_2O_3/150-nm-thick PZT film, 10-nm-thick ZnO film on 5.5-nm-thick Al_2O_3/150-nm-thick PZT film, and 20-nm-thick ZnO film on 5.5-nm-thick Al_2O_3/150-nm-thick PZT film. The peaks were assigned to the perovskite-structure PZT. Peaks due to the Al_2O_3 could not be found because

it is amorphous. On the other hand, the (104) peak of α- Al_2O_3 was observed, even for the PZT film, because Al_2O_3 was used as an adhesion layer for the Pt electrode. For the case of the ZnO film, the (002) peak was observed, meaning that the ZnO layer had crystallized.

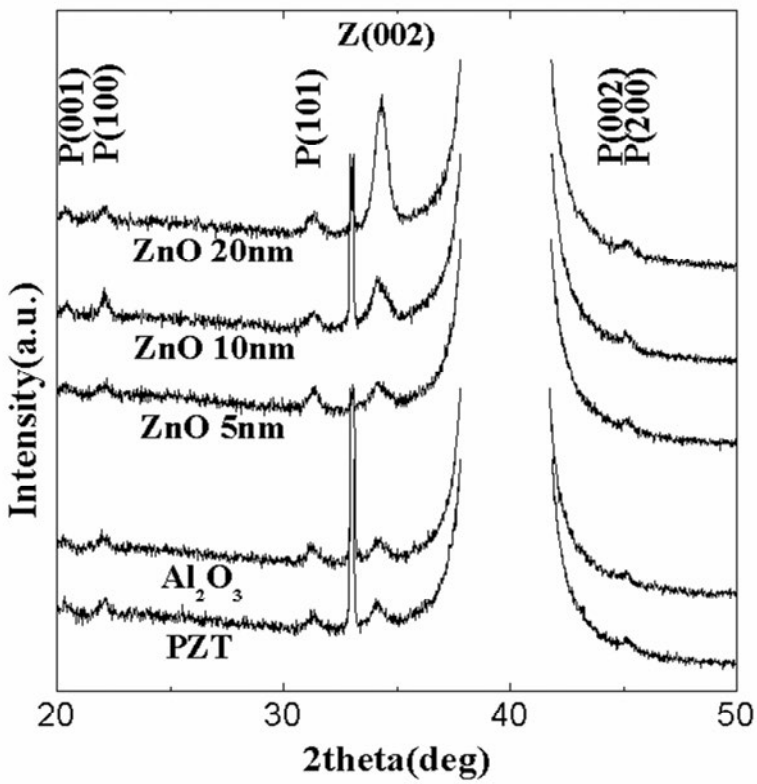


Figure 7.4. The X-ray diffraction patterns of a 150-nm-thick PZT film on Pt electrode, 5.5-nm-thick Al_2O_3 film on 150-nm-thick PZT film, 5-nm-thick ZnO film on 5.5-nm-thick Al_2O_3/150-nm-thick PZT film, 10-nm-thick ZnO film on 5.5-nm-thick Al_2O_3/150-nm-thick PZT film, and 20-nm-thick ZnO film on 5.5-nm-thick Al_2O_3/150-nm-thick PZT film, respectively. P: Perovskite, Z: ZnO

Figure 7.5 (a) shows the low magnification cross-section HRTEM image of the Pt TE/20-nm-thick ZnO/5.5-nm-thick Al_2O_3/150-nm thick PZT on Pt substrate. As shown in the figure, ZnO is crystalline and Al_2O_3 is amorphous. PZT and Pt are well crystallized. This is consistent with the XRD patterns shown in figure 7.4. The interface between each layer appears clear and smooth. The thin amorphous Al_2O_3 layer was not deformed during the ZnO sputtering and post-deposition-annealing processes. The interface quality was good enough for the discussions in this study. This was further confirmed by the high resolution image shown in (b).

Figure 7.6 shows the P-V hysteretic (upper panel) and switching current (I_{sw}) response curves (lower panel) of the MFISM structures measured using a standard ferroelectric tester in virtual ground mode (TF 2000, Aixacct Systems, Germany). In this figure, the thickness of the ZnO layer was (a) 5 nm, (b) 10 nm, and (c) 20 nm, whereas the PZT and Al_2O_3 layer thickness was fixed at 150 nm and 5.5 nm, respectively. The P-V loops generally show a rather distorted shape due to the involvement of a semiconducting ZnO layer, and a large coercive voltage (V_c) due to the adoption of a Al_2O_3 tunnel switch layer [11]. A further notable finding is that the P-V loops in the positive V region shows a hump, whereas those in the negative region do not. This can be seen even more clearly from the I_{sw} versus voltage curves. The split of the I_{sw} peak under a positive bias could be observed in all samples. For convenience, the peak centered at ~ 9V was named peak A, and the

other peak at a higher positive voltage was named peak B. Although the position of peak A was almost fixed, that of peak B increased with increasing ZnO thickness. The position of the I_{sw} peak under a negative bias was almost voltage independent (- 7.5 ~ - 8.0 V). The split of the I_{SW} peak means that the charges compensating for the polarization bound charges of the ferroelectric were divided into two groups; each flowing under different bias conditions. Peak splitting would not be observed if all the compensating charges were located at the metal electrode or PZT/Al_2O_3 interface. Therefore, it was assumed that the compensating charges were separated and stored on the PZT/Al_2O_3 and Al_2O_3/ZnO interfaces, where the threshold voltages of the charges of the two interfaces to flow are different. As shown in Fig. 7.6, the difference between peaks A and B increased with increasing ZnO layer thickness. Another set of samples with a thinner Al_2O_3 layer (4 nm) were also fabricated, and the same electrical tests were performed. Fig. 7.8 shows the P-V test results of these samples. Owing to the thinner thickness of the Al_2O_3 layer, the operation voltage was decreased and even clearer current peaks and their separation were observed.

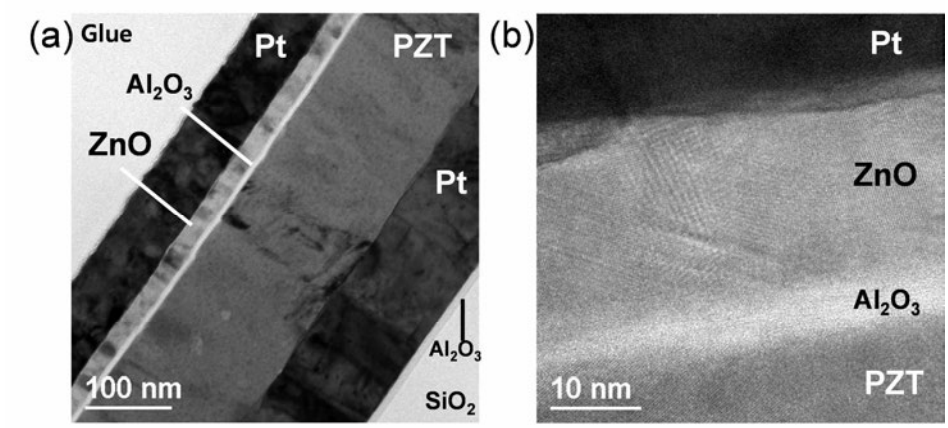


Figure 7.5. (a) low magnification and (b) high resolution transmission electron microscopy of the Pt/20-nm ZnO/5.5-nm Al_2O_3/150-nm PZT/Pt stack capacitor.

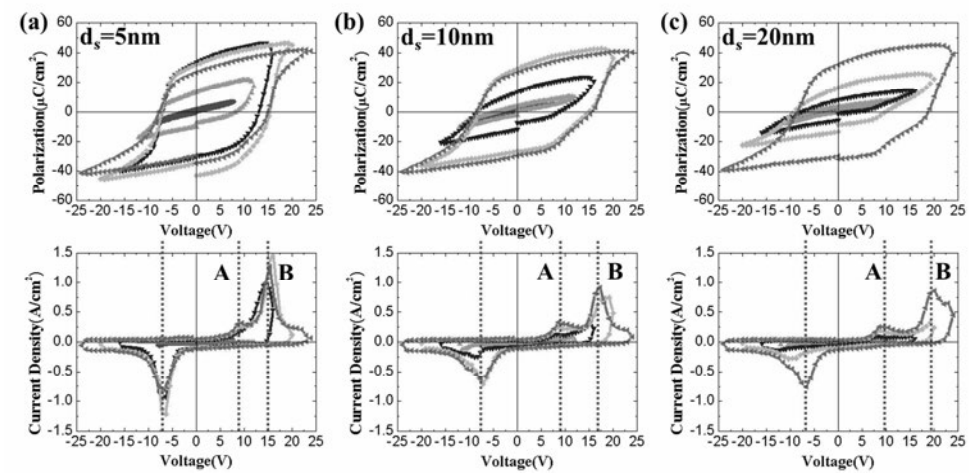


Figure 7.6. P-V hysteresis (upper panel) and current response (lower panel) curves measured using a TF analyzer 2000 with a 1000Hz triangular pulse with an amplitude of 4, 8, 12, 16, 20, 24 V of MFISM capacitors using Pt top electrode with (a) 5-nm-thick ZnO, (b) 10-nm-thick ZnO, and (c) 20-nm-thick ZnO. Al_2O_3 thickness was 5.5 nm.

The different P-V hysteresis behavior under a positive and negative bias (to the top Pt electrode while the bottom Pt electrode was grounded) must have originated from the depletion (positive bias) and accumulation (negative bias) of the ZnO layer. When a negative bias was applied, the electrons may flow into the ZnO layer first so that the ZnO layer works as a part of the electrode, and the P-V loop resembles that of the PZT/Al_2O_3 capacitor. More detailed discussions on the carrier depletion in the ZnO layer will be shown later. The negative V_c and integrated charges are similar to those from the PZT/Al_2O_3 capacitor [11]. For the sufficiently low negative bias, compensating carriers (electrons) are injected onto the Al_2O_3/ZnO and finally onto the PZT/Al_2O_3 interfaces by tunneling through the thin Al_2O_3 layer [11] and compensate for the polarization bound charges. On the other hand, under a positive bias, the ZnO layer could be carrier depleted and should work as an insulating layer. The correct understanding of the charge transport behavior under a positive bias requires a quantitative simulation of the electric field distribution, which is shown in Fig. 7.13 and the related discussions. Therefore, the possible operation of the tri-state memory of this structure is discussed first using the pulse-switching experiment.

Figures 7.7 (a), (b), and (c) show the switching current density-time curves (for write voltages of -10, -5, 5, 10, 15, and 20V) of the MFISM capacitors with 5-nm, 10-nm and 20-nm thick ZnO layers, respectively. In this case, 4-nm-thick Al_2O_3 layer was used. Figure 7.8 shows the P-V hysteresis (upper

panel) and switching current density-time curve (lower panel) of the MFISM capacitors with an Al_2O_3 layer thickness of 4 nm, and a ZnO layer thickness of (a) 5, (b) 10, (c) 20 nm. Plateaus in the positive bias region of the P-V hysteresis and the two switching current peaks in the positive bias region were observed. The P_r values of the samples were ~35-40 $\mu C/cm^2$, which was coincident with the switching charges measured using the pulse measurement. Although the V_c of the samples was smaller than those of the MFISM capacitors with the 5.5-nm thick Al_2O_3 layer, 20V was still not enough for the sample with the 20-nm-thick ZnO layer. The operation of the tri-level MFISM capacitor was reconfirmed for the sample with the Al_2O_3 layer with different thicknesses. Here, the write pulse time was 5, to 20 and 50 μs for the 5-nm, 10-nm and 20-nm thick ZnO layers, respectively. The switching charges could be calculated by integrating the switching current density-time curves in Fig. 7.7 (a), (b), and (c) and being multiplied by -1 for sake of convenience. Figures 7.7 (d), (e) and (f) show the change in switching charge as a function of the write pulse voltage of the MFISM capacitors with 5-nm, 10-nm and 20-nm thick ZnO layers, respectively. Here, the write pulse time of 5, to 20 and 50 μs was adopted for each case.

As expected, almost no switching charge was detected when the writing voltage was negative. A positive write voltage, ~ 6 V, was necessary to induce significant switching due to the increased V_c of the PZT/Al_2O_3 stack layer [11]. The switching charge increased with increasing write voltage > 6

V. The increase in switching charge occurs in two steps for Figs. 7.7 (e) and (f). The switching charges increase suddenly up to ~ 10-15 μC/cm^2 and remain at that value up to ~ 12 V and ~ 17 V in Figs. 7.7 (e) and (f), respectively. This charge is believed to corresponds to double the stored charges at the Al_2O_3/ZnO interface. The first saturation region for the sample with a 5-nm thick ZnO layer was so narrow that it could barely be found (Fig. 7.7 (d)). With further increases in the write voltage, the switching charge increased to the saturation switching charge, but this value was not reached even with 20 V, which is the maximum voltage of the present set-up, for the case of the sample with a 20-nm thick ZnO layer, due to the large thickness of depleted ZnO in Fig. 7.7 (f). The saturated remanant polarization ($2P_r$) of this specific PZT film was ~ 70 μC/cm^2 from the P-V loop or pulse switching results of the MFIM sample.(Fig. 7.8) Therefore, the measured charge of ~ 70 μC/cm^2 corresponds to the full switching charge of the PZT layer.

In MFM or MFIM structures [11], a sudden increase in the switching charge in the pulse switching set-up corresponds to polarization reversal, so that the voltage where the sudden increase in switching charge occurs approximately coincides with the V_c of the P-V measurement. In this MFISM structure, the P-V loops showed two V_c values (two peaks in the I_{sw} – voltage diagram) that coincide well with the pulse switching results. The occurrence of a plateau with the switching charge of ~ 10-15 μC/cm^2

suggests that polarization switching occurs partially within this voltage range. Partial switching can also occur if the ferroelectric quality is not optimal (slanted P-V loop). On the other hand, in this case, the switching charge – write pulse curve would show a gradual increase not the step-wise variation shown in Figs. 7.7 (e) and (f). Therefore, the data strongly suggests that the compensating charges are stored separately in the structure at different interfaces, and have different threshold voltages. The wide voltage region of the plateau show that the tri-state memory has a very large voltage margin for stable operation.

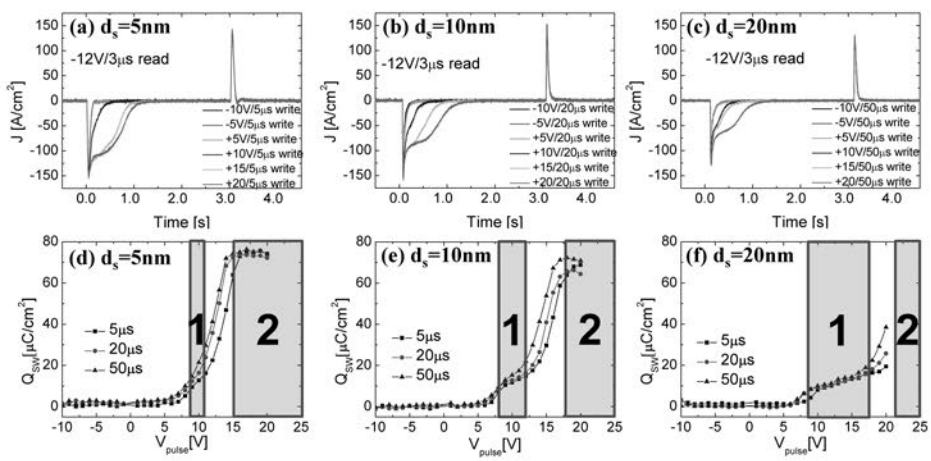


Figure 7.7 Switching current as a function of time (Upper panel) and switching charge integrated from the measurement as a function of V_{pulse} (Bottom panel) for the case of the samples (Al_2O_3 thickness =4.0 nm) with (a) 5-nm-thick ZnO film, (b) 10-nm-thick ZnO film and (c) 20-nm-thick ZnO film, respectively.

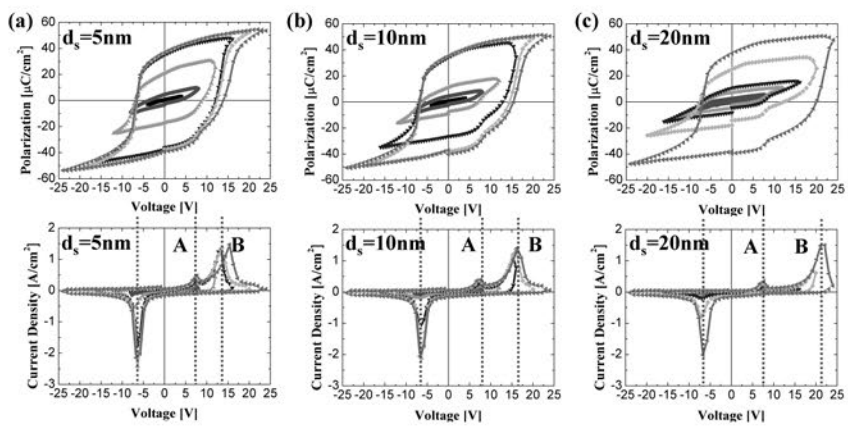


Figure 7.8. the P-V hysteresis(Upper panel) and the switching current density-time curve(Bottom panel) of the MFISM capacitors(d_i = 4nm) with (a) 5-nm, (b) 10-nm, (c) 20-nm thick, which were used for the pulse measurement.

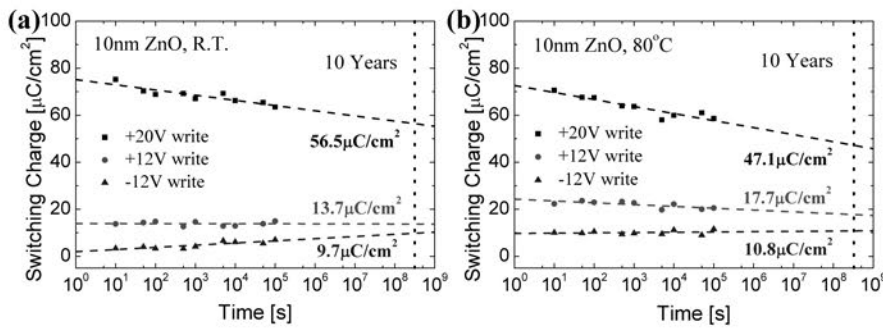


Figure 7.9. Retention properties of the three memory states of the MFISM capacitor with 4-nm Al_2O_3 and 10-nm ZnO (a) at room temperature and (b) at 80°C.

Because the compensating charges are divided into two layers, the retention properties could be the most serious reliability concern of the memory. The retention property of the MFISM capacitor was also examined. Figures 7.9 (a) and (b) show the retention properties of the samples with 4-nm-thick Al_2O_3 and 10-nm-thick ZnO layers at room temperature and 80°C, respectively. The data was written by 5 μs pulse with the amplitude of -12V, +12V, and +20V for the state 0, 1, and 2, respectively, and read by 5 μs pulse with the amplitude of -12V. The measurement was performed for the retention time from 10 to 10^5s. The points in the graph showed the measured data, and the dashed line shows the extrapolation based on the data measured. At room temperature, the data 0, 1, and 2 remained after 10 years are expected to be 9.7, 13.7, and 56.5 μC/cm^2, respectively. The read margin between data 1 and 2 was as large as 32.8 μC/cm^2, but that between data 0 and 1 was only 4.0 μC/cm^2. At 80°C, the read margin of data 1 and 2 decreased to 29.3 μC/cm^2, but that of data 0 and 1 increased to 6.9 μC/cm^2. Although the clarification of the retention degradation mechanism requires further study, the present retention property appears to be quite promising for the 10 years lifetime of nonvolatile memories.

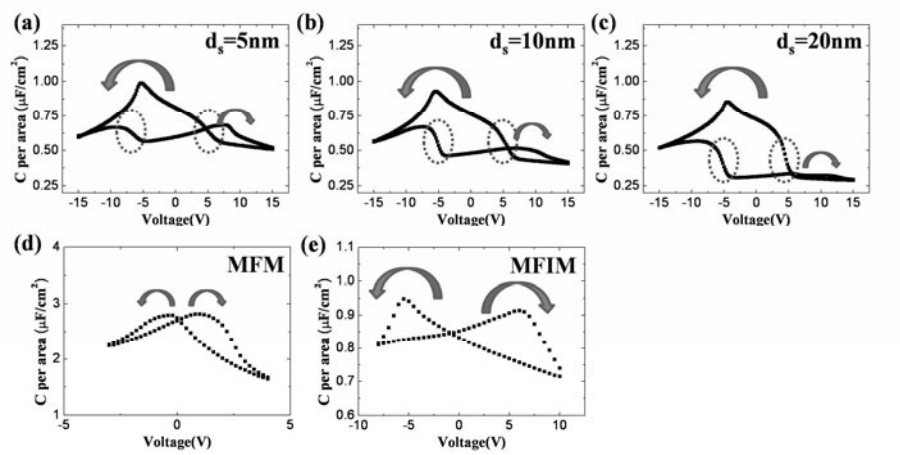


Figure 7.10. Measured C-V characteristics using a 100kHz AC voltage input with an amplitude of 0.05V combined with the DC voltage sweep of MFISM capacitors using a Pt top electrode with (a)5-nm-thick ZnO, (b)10-nm-thick ZnO, (c)20-nm-thick ZnO, of (d)MFM capacitor, and of (e)MFIM capacitor, respectively. Al_2O_3 thickness was 5.5 nm.

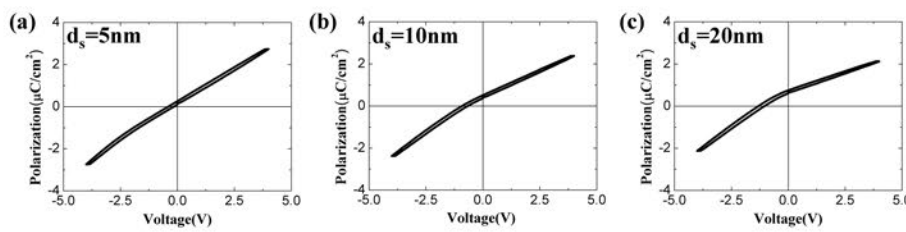


Figure 7.11. P-V hysteresis using a triangular voltage pulse with a height of 4V for the MFISM capacitors with (a) 5-nm-thick ZnO, (b) 10-nm-thick ZnO, and (c) 20-nm-thick ZnO

The mechanism for two step polarization reversal is discussed. For that, the function of the ZnO layer as a semiconductor layer within the structure was confirmed first. For this purpose, the small signal capacitance – voltage (C-V) characteristics of the MFISM capacitors were examined in the larger voltage region where polarization switching can occur. Figures 7.10 (a), (b) and (c) show the C-V characteristics of the MFISM structures with a ZnO layer thickness of 5nm, 10nm and 20nm, respectively. Those for the MFM, and MFIM stacks, are also shown in (d) and (e), respectively, for comparison. Owing to the presence of defects and their asymmetric distribution, the C-V curves of the MFM and MFIM samples are not symmetrical with respect to the bias polarity. On the other hand, the MFISM capacitors show very distinctive C-V curve shapes. When the ZnO layer thickness was small (5 nm), the C-V curve is somewhat similar to that of MFIM, whereas it more resembles that of the defective (hysteretic) C-V curve of metal oxide semiconductor (MOS) capacitor when the ZnO film was thicker (20 nm). This might appear reasonable but it was actually not the case, as can be understood from the abnormal direction of hysteretic C-V curves. The more MOS-like C-V curve in Fig. 7.10 (c) does not represent the defective C-V of MOS either because the MOS capacitors with traps always have clockwise hysteresis, which is in the opposite direction to that shown in Fig. 7.10 (c). In fact, the quantitative analysis of the role of depletion involves not only the semiconductor (ZnO in this case), but that of the ferroelectric. [18,19]

However, only the depletion of ZnO is considered in this study, because the role of semiconducting ZnO is much more dominant than that of PZT. The transition of ZnO may occur independently from ferroelectric switching. To justify the assumption, the P-V hysteretic curves of the MFISM capacitors without ferroelectric switching (when the applied voltage is smaller than V_c) were examined. Figure 7.11 shows the P-V curves of non-poled MFISM capacitors measured using a triangular pulse with a voltage lower than the V_c. The slopes of these almost linear curves correspond to the capacitance of the entire structure as the ferroelectric remains in the non-poled state. Owing to the non-uniform internal charge distribution, the flat band voltage might not be 0 V. ZnO is depleted and accumulated with the carriers in the positive and negative side of voltages, as can be understood from the small and large slopes. This means that the transition of the ZnO layer occurs independently of ferroelectric switching, as expected in C-V curves.

Interesting but complicated properties of the MFISM capacitors were obtained from the P-V, pulse-switching and C-V measurements. To understand such complicated behavior, the energy band structure of the samples and its variation with the bias voltage were calculated using the Gauss's equation under the assumption that the charges are trapped on the two interfaces (PZT/Al_2O_3, Al_2O_3/ZnO). Scott showed how interface match-up energies (electrode work function and ferroelectric electron affinity) determined transport characteristics of FeRAMs. [20] Then, the

band structure can be compared with the characteristic charge responses, C-V and P-V loops. To do this, several assumptions were made. First, a change in carrier density of the ZnO layer occurs abruptly at a certain bias voltage from the sharp change in capacitance noted in the C-V curves of the MFISM capacitors shown in figure 7.10. Therefore, the capacitor was considered to be a MFI_1I_2M(I_1=Insulator1, I_2=Insulator2) structure when the ZnO layer is depleted, and a MFIM capacitor when it is accumulated with carriers (electrons). The ZnO layer is barely inverted due to the large band gap and possible Fermi level pinning.[21] Second, the PZT and Al_2O_3 layers were assumed to be defect-free insulators. Charges can move through the Al_2O_3 layer only under biases greater than the tunneling threshold.[11] The tunneling threshold voltage is related with the onset of Fowler-Nordheim tunneling mechanism. [11] Therefore, the leakage current due to thermionic emission or defect-related mechanisms were neglected. Third, the charges in the ZnO layer (~0.03 $\mu C/cm^2$) can be ignored, which was only ~1% of remanant polarization of PZT even when the defect density of ZnO was as high as $10^{17}/cm^3$. Fourth, the ferroelectric polarization of PZT and the charges at the PZT/Al_2O_3 interface were considered to be constant, and they change only at V_c. Fifth, the ferroelectric layer was considered to be a combination of the ideal ferroelectric capacitor with rectangular hysteresis and a linear capacitor. Sixth, the amount of charges estimated from the switching current density-time curves (lower panel of figure 7.6 (b)) were

assumed to coincide with the trapped charges at the two interfaces.

Table 7.1 summarizes the parameters used for the band structure simulations, where the charge density at each interface was estimated from pulse switching measurements.

Table 7.1. Band gap, relative permittivity, electron affinity, and Schottky barrier with Pt for PZT, Al_2O_3, and ZnO, respectively.

	PZT	Al_2O_3	ZnO
Bandgap (eV)	3.4[a]	8.8[a]	3.44[b]
Relative Permittivity	300[c]	8[c]	10[c]
Electron Affinity (eV)	3.5[a]	1[a]	4.5[b]
Electron Schottky barrier with Pt (eV)	1.45[d]	No need	0.7[e]

[a] See reference 22; [b] See reference 23; [c] From C-V measurement in this experiment; [d] See reference 24; [e] See reference 17.

Equations (7.1) and (7.2) shows the two basic equations for MFIM capacitors when the ZnO layer is in the accumulated state. Equation (7.1) was formulated from Gauss's law applied to the rectangular closed surface enveloping PZT/Al_2O_3 interface and equation (7.2) was formulated from the voltage distribution over a series of PZT capacitors and Al_2O_3 capacitors.

$$\varepsilon_0\varepsilon_i E_i - \varepsilon_0\varepsilon_f E_f = sign(P_d)(P_d - Q_{fi}) \tag{7.1}$$

$$-d_i E_i - d_f E_f = V_{appl} \tag{7.2}$$

Sign(P_d) is"+1" when the polarization of the ferroelectric layer has a positive value and "-1" when it has a negative value. Q_{fi} represents the quantity of charges at the PZT/Al_2O_3 interface, and P_d represents the ferroelectric polarization of PZT, which means that the linear polarization of PZT was subtracted from the total polarization of PZT. ε_i (d_i) and ε_f (d_f) represent the relative permittivity (thickness) of the insulator, and linear permittivity of the ferroelectric, respectively. E_i and E_f represents the electric field across the insulating layer and ferroelectric layer, respectively. Q_{fi}, P_d, and ε_i can be calculated from the electrical characteristics of the capacitors. E_i and E_f could be formulated from the following two equations. Equations (7.3) and (7.4) show the formula for E_i and E_f, respectively.

$$E_i = \frac{-V_{appl} + sign(P_d)(P_d - Q_{fi})(\frac{d_f}{\varepsilon_0 \varepsilon_f})}{d_i + d_f \frac{\varepsilon_i}{\varepsilon_f}} \quad (7.3)$$

$$E_f = \frac{-V_{appl} - sign(P_d)(P_d - Q_{fi})(\frac{d_i}{\varepsilon_0 \varepsilon_i})}{d_i \frac{\varepsilon_f}{\varepsilon_i} + d_f} \quad (7.4)$$

Equations (7.3) and (7.4) indicate that E_i and E_f can be divided into two parts. One is the electric field by applied voltage distributed across each layer, and the other is the electric field originating from the discrepancy of the ferroelectric dipolar polarization and the interfacial charges at PZT/Al_2O_3 interface.

The electric field across the each layer of the MFISM capacitors when ZnO was depleted can also be calculated. E_f, E_i, and E_s (E_s is the electric field across the ZnO layer) should be calculated, and three equations are needed. Equations (7.5), (7.6), (7.7) show the three equations for the MFISM capacitors with a depleted ZnO layer. Equation (7.5) and equation (7.7) were formulated from Gauss's law applied to the closed rectangular surface enveloping the PZT/Al_2O_3 interface and that enveloping the Al_2O_3/ZnO interface. The space charges from defects in the depleted ZnO layer was neglected due to the relatively low defect concentration and thin ZnO layer.

The total space charges of the 20-nm thick ZnO layer were only ~0.032 μC/cm^2 with an assumed defect density of 10^{17} /cm^3. Equation (7.7) was formulated from the voltage distribution over a series of PZT, Al_2O_3 and ZnO layers.

$$\varepsilon_0\varepsilon_i E_i - \varepsilon_0\varepsilon_f E_f = \text{sign}(P_d)(P_d - Q_{int}) \tag{7.5}$$

$$\varepsilon_0\varepsilon_i E_i - \varepsilon_0\varepsilon_s E_s = -\text{sign}(P_d)\, Q_{is} \tag{7.6}$$

$$-d_i E_i - d_f E_f - d_s E_s = V_{appl} \tag{7.7}$$

Q_{is} is the interfacial charge at the Al_2O_3/ZnO interface. E_i, E_f, and E_s could be formulated from three equations (7.5), (7.6) and (7.7). Equations (7.8), (7.9) and (7.10) show the formula for E_i, E_f and E_s, respectively.

$$E_i = \frac{-V_{appl} + sign(P_d)\{(P_d - Q_{fi})(\frac{d_f}{\varepsilon_0\varepsilon_f}) + Q_{is}(\frac{d_s}{\varepsilon_0\varepsilon_s})\}}{d_i + d_f\frac{\varepsilon_i}{\varepsilon_f} + d_s\frac{\varepsilon_i}{\varepsilon_s}} \tag{7.8}$$

$$E_f = \frac{-V_{appl} - sign(P_d)(P_d - Q_{fi})\{(\frac{d_i}{\varepsilon_0\varepsilon_i} + \frac{d_s}{\varepsilon_0\varepsilon_s}) + Q_{is}(\frac{d_s}{\varepsilon_0\varepsilon_s})\}}{d_i\frac{\varepsilon_f}{\varepsilon_i} + d_f + d_s\frac{\varepsilon_f}{\varepsilon_s}} \tag{7.9}$$

$$E_s = \frac{-V_{appl} + sign(P_d)\{(P_d - Q_{fi})(\frac{d_f}{\varepsilon_0 \varepsilon_f}) - Q_{is}(\frac{d_i}{\varepsilon_0 \varepsilon_i} + \frac{d_f}{\varepsilon_0 \varepsilon_f})\}}{d_i \frac{\varepsilon_s}{\varepsilon_i} + d_f \frac{\varepsilon_s}{\varepsilon_f} + d_s}$$

(7.10)

From equations (7.8) and (7.10), E_i and E_s could have a negative value due to the existence of a Q_{is} term. This was the origin of the abnormal electrical properties of the MFISM capacitors, as shown below. The existence of Q_{fi} reduces the magnitude of E_i, E_f, and E_s significantly by decreasing the total charges at the PZT/Al_2O_3 interface from P_d to (P_d – Q_{fi}). In particular, the decrease in depolarization field (E_f) should improve the retention property of the ferroelectric capacitor. If there were no Q_{fi}, they would have an approximately one order of magnitude stronger electric field. Therefore, the depolarization field across the PZT layer should be decreased significantly when the thin alumina tunnel barrier was on during switching.

Based on the formulation of E_f, E_i, E_s, the potential distribution and resulting band structure of the MFISM capacitor with a 10-nm thick ZnO layer can be determined (semi-) quantitatively, as show in Fig. 7.11 and Fig. 7.12, respectively.

Figure 7.12 shows the change in electrical potential distribution of the PZT (V_f), Al_2O_3 (V_i) and ZnO (V_s) when the V_{appl} varies (a) from negative to positive and (b) from positive to negative direction, when the Al_2O_3 and ZnO

layer was 5.5- and 10-nm-thick, respectively. For the calculations the measured parameters, such as dipolar polarization and ε_r, and the reported parameters from the literature, such as E_g, electron affinity, and Schottky barrier with Pt were used. Table 7.1 shows the parameters used for each layer. In Fig. 7.12 (a), under -5V during negative-to-positive sweep, V_s changed its sign naturally, and it had an opposite sign from that of V_i. In addition, under +9V during the negative-to-positive sweep, sharp band bending, which is large enough for carriers to tunnel through the depleted ZnO layer could be found. After that, V_s decreased and V_i increased abruptly. Finally, under +17.5V during the negative-to-positive sweep, V_i and V_s reached a voltage high enough for tunneling.

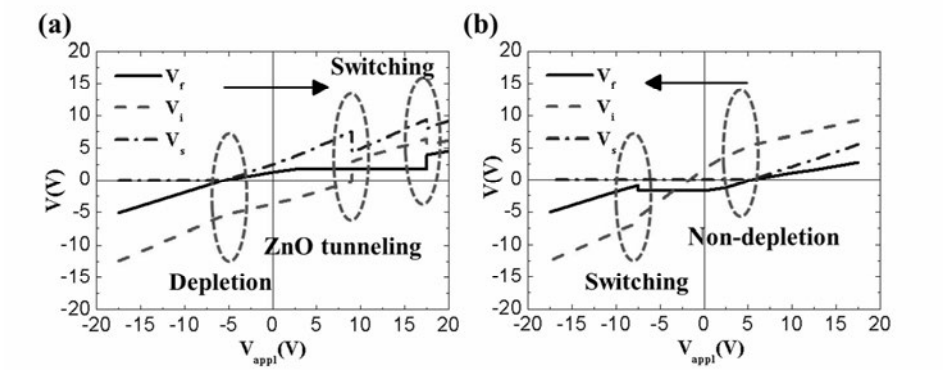


Figure 7.12. Calculated voltage across each layer (a) for the case of a negative-to-positive sweep, (b) for the case of a positive-to-negative sweep, respectively.

In Fig. 7.12 (b), under +5V, the depleted ZnO layer changed into a non-depleted state, and no bias was applied across the ZnO layer. V_s varies smoothly compared to the case in Fig. 7.12 (a), which corresponds to the results shown in Fig. 7.6. Under -7.5V, V_i has a sufficiently high value for the carriers to tunnel through the Al_2O_3 layer. The voltage across each layer is redistributed after polarization switching, and a discontinuous point could be observed, as shown in figure 7.12(b).

Figure 7.13 shows schematic band diagrams at several characteristic applied voltages (V_{appl}) when the V_{appl} increases from a low enough negative bias voltage to a high enough positive bias and decreases to a low negative bias again. The ZnO and Al_2O_3 thickness thickness was 10 and 5.5 nm, respectively. For easy comparison, the I_{sw} vs. voltage during the P-V sweep (Fig. 7.13 (m)) and C-V curve (Fig. 7.13 (n)) were reproduced from Figs. 7.6 and 7.10, respectively.

Figure 7.13(a) shows the electrical band structure and trapped charge distribution when the V_{appl} = -17.5 V, which is low enough to saturate the polarization in the PZT and trapped charges. ZnO accumulates and no voltage was applied to that layer. Therefore, the bias was applied to the PZT and Al_2O_3 layer, where the electric field applied to the Al_2O_3 layer was as high as ~ 12 MV/cm. This is a large enough field for the Al_2O_3 tunnel switch to open [~ 10 - 15 MV/cm, Ref. 11] so that the compensating charges are safely trapped at the PZT/Al_2O_3 interface. The trapped charge density (Q_{fi})

was ~ 21 $\mu C/cm^2$, as discussed above, which was actually the value that was used to simulated this band profile. As the saturation polarization (P_s) of PZT is larger than this value (~28 $\mu C/cm^2$), some of the compensating charges (Q_{is}) are trapped at the Al_2O_3/ZnO interface, of which density was assumed to be ~ 7 $\mu C/cm^2$. (Figure 7.6) With increasing negative bias up to -5V, no substantial change occurs in the band structure except for the decrease in applied voltage over each layer. On the other hand, at -5V, the ZnO layer changed from the non-depleted state to the depleted state as the energy band tilted toward the TE direction (Figs. 7.13 (b) and (c)). This can explain the sudden decrease in the C-V curve around this V_{appl} (point (2) in Fig. 7.13 (n)), whereas the gradual increase of C in the lower V_{appl} region was attributed to the increase in the ε_r of PZT with increasing negative bias voltage. The charge density at the PZT/Al_2O_3 (Q_{fi}) and charge density at the Al_2O_3/ZnO (Q_{is}) remained unchanged at this bias. Owing to the existence of Q_{is}, the electric field in the Al_2O_3 layer (E_i) and that in the ZnO layer (E_s) could have different polarity, which cannot be considered using the simple voltage distribution over a series of insulating layers. Therefore, the ZnO layer can be depleted, even with the negative value of V_{appl}. The charge in the ZnO layer, which is calculated to be ~ 0.03 $\mu C/cm^2$ assuming a carrier density of 10^{17} cm^3, is negligible compared to the ferroelectric compensating charges so that there is barely any signal in the I_{sw} – voltage curve at this voltage (Fig. 7.13 (m)). No substantial change occurs with further increases in V_{appl} up to

~ 9V, except for the gradual increase in the capacitance of PZT as its polarization decreases. At 9 V, most of the V_{appl} applied to the depleted ZnO layer, as can be understood from Fig. 7.13 (d), which results in the detrapping of Q_{is} and hole injection to the Al_2O_3/ZnO interface probably by a tunneling mechanism. This charge exchange corresponds to the partial switching of the ferroelectric polarization (~ 14 $\mu C/cm^2$) in Fig. 7.6 (b), and also corresponds to the I_{sw} peak at ~ 9V (point (3) in Fig. 7.13 (m)). This relatively large change in switching charge might induce a local peak in capacitance but this capacitance is masked by the depleted ZnO capacitance. Therefore, only a broad peak is observed in the C-V curve (Fig. 7.13 (n), marked as (3)). Once the discharging of Q_{is} and hole trapping occurs, a large portion of V_{appl} applied to the Al_2O_3 layer, as shown in Fig. 7.13 (e). This might induce the partial compensation of Q_{fi} by another tunneling mechanism (Fig. 7.13 (e), red arrows), and result in a situation like Figure 7.13 (f). This partial compensation does not contribute to the detected charge in external circuitry, making the charge detected almost constant near this voltage. Therefore, once this takes place, the ferroelectric polarization is decreased before complete polarization reversal occurs at a much higher V_{appl}. Figure 7.13 (g) shows the situation when V_{appl} = 17.5 V, which is the voltage where peak B was observed, was applied. Owing to the dissipation of positive trapped charges shown in Fig. 7.13 (e), both Al_2O_3 and ZnO layers underwent a high electric field, so that the positive charges tunneled

through both layers and the previously remaining negative charges dissipate fully, meaning that complete ferroelectric switching occurs. The dissipated Q_{fi} can be smaller than the originally stored charges due to the partial compensation shown in Fig. 7.13 (d), but the overall estimated switching charge at this moment still amounts to ~ 42 $\mu C/cm^2$ because of the larger hole current, part of which would be trapped at the Al_2O_3/ZnO interface. The band structure and charge distribution might be observed once this switching has been completed, as shown in Fig. 7.13 (h). This shows that the polarization vector of PZT is reversed and the compensating charges (with positive sign now) of the reversed ferroelectric bound charges distribute on both the PZT/Al_2O_3 and Al_2O_3/ZnO interfaces. An accurate charge density at each interface might not necessarily be the same as that of electrons for the opposite polarization state. This cannot be discriminated because these charges discharge simultaneously at the moment of subsequent polarization switching, as shown in Figs. 7.13 (g)-(h). This complete switching at V_{appl} = ~ 17 – 18 V (point (4) in Fig. 7.13 (m) might induce another sharp peak in the C-V curves near this voltage. However, the small signal C-V set-up did not allow an increase in the dc bias voltage to such a value; the samples were easily broken down, so the C-V curves were measured from -15 V to 15 V.

As the V_{appl} decreases to 5V after complete switching at ~ 17 – 18 V, the voltage applied to the ZnO layer decreases quite fast while maintaining the voltage across the Al_2O_3 almost unchanged (Fig. 7.13 (i)). At 5V, the ZnO

layer changes from a depleted state (Fig. 7.13 (i)) to a non-depleted one (Fig. 7.13 (j)), which is reflected in the C-V curve as an abrupt increase in the capacitance at this voltage (point (6) in Fig. 7.13 (n)). With further decreases in the V_{appl} down to -7.5 V, the trapped charges remained constant, and only the overall increase in capacitance was observed due to the relaxation of ferroelectric polarization. At V_{appl} = -7.5 V, it appears that the discharging of Q_{is} and Q_{fi} occurs almost simultaneously due to the low electron injection barrier at the ZnO/Pt interface, and large enough electric field over the Al_2O_3 layer (~12 MV/cm) at this point. As the electrons are injected to the Al_2O_3/ZnO interface, the electrons trapped at that interface increase largely with the electric field across the Al_2O_3 layer, which triggers the dissipation of Q_{fi}. Therefore, the switching back of ferroelectric polarization in this case occurs in a single step, as opposed to the case with the opposite direction explained above (two-step). There could be slight mismatch between the electron injections to the PZT/Al_2O_3 and Al_2O_3/ZnO interfaces, which could be the reason for the slight hump near -10 V in the I_{sw} vs. voltage curve in Fig. 7.13 (m). This is in a stark contrast to the previously explained ferroelectric switching charge migration shown in Fig. 7.13 (d) - (h). Figure 7.13 (l) shows the situation where ferroelectric switching back to the original direction was completed at -15 V. A further decrease in V_{appl} to -17.5 V returns the system back to the starting position of the sequence shown in Fig. 7.13 (a). The peak in the C-V curve at ~ -6 V corresponds to this polarization

switching back to the original direction (figure 7.13 (n)).

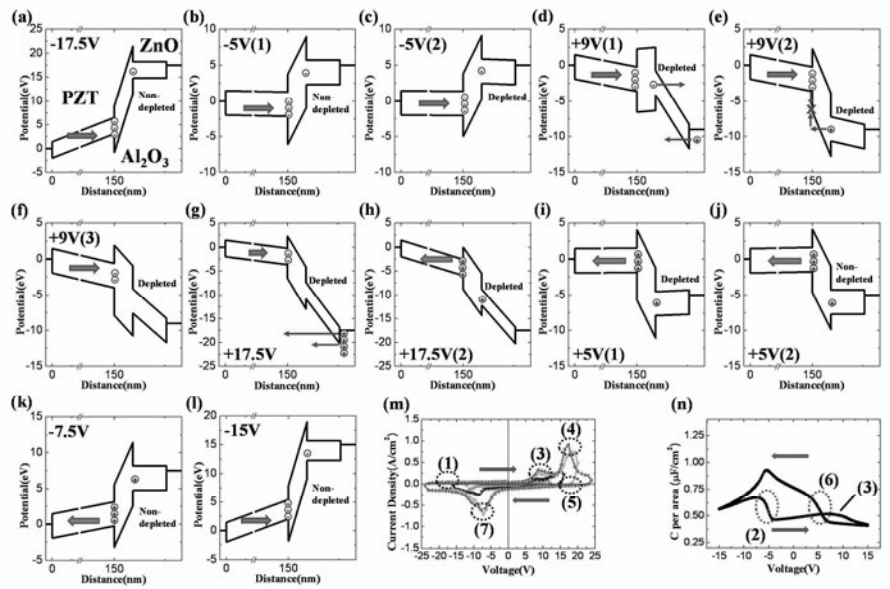


Figure 7.13. Electrical band structure calculated based on the model of the MFISM capacitors under certain bias conditions: (a) -17.5V with positive polarization, (b) -5V before depletion of the ZnO layer, (c) -5V after depletion of the ZnO layer, (d) +9V with partial polarization switching due to the flow of Q_{is}, (e) +9V with the recombination of electrons at the FI interface and holes at IS interface due to tunneling , (f) -9V after partial polarization, (g)+17.5V tunneling of carriers at PZT/Al_2O_3 interface , (h) +17.5V after the polarization switching due to Q_{fi}, (i) +5V before the transition of ZnO from the depleted state to the non-depleted state, (j) +5V after the transition of ZnO from the depleted state to the non-depleted state, (k) -7.5V with the polarization switching, (l) -15V with the positive polarization; (m) The switching current density-voltage curve, and (n) small signal C-V curve of the MFISM capacitor with d_s=10nm. Al_2O_3 thickness was 5.5 nm.

These calculations can be regarded as semi-quantitative as the ε_r of the PZT layer was taken as a constant value (300, which is approximately the average between the high and low values), otherwise the calculation becomes too complicated to be handled analytically. On the other hand, the primary features of the P-V, C-V and tri-state memory operation can be explained well by this simplified model. For the operation of the novel tri-states memory, the large difference of ε_r of the ferroelectric and tunneling dielectric layers is essential. The low-ε_r $Hf_{1-x}Zr_xO_2$ fim was also tested as a candidate for replacing PZT layer in the present experiment, but it did not work well with Al_2O_3 tunneling layer. It should be noted that the electric field should be concentraded across thin tunneling layer for the tunneling and trapping of electrons at the ferroelectric/dielectric interface.

7.4. Conclusions

In summary, a feasible structure and actual operation of tri-state memory function for high density FeRAM are presented based on the MFISM material, where the PZT, Al_2O_3, and ZnO layers were the ferroelectric, insulator and semiconductor layers, respectively. The separated trapping of the compensating charges at the interfaces between the PZT and Al_2O_3, and Al_2O_3 and ZnO layers appears to result in the discrete dissipation of trapped charges, which results in a two-step-like voltage signal in the pulse switching experiment. The retention property of the tri-level memory is also robust enough for the nonvolatile memory application. This can comprise a tri-state ferroelectric memory with singular ferroelectric switching in the opposite bias polarity. This new mechanism can increase the memory density by 50% compared to the conventional FeRAM at a given cell size.

7.5. References

[1] J. F. Scott, C. A. Araujo, *Science* **246**, 1400 (1989).

[2] J. F. Scott, L. Kammerdiner, M. Parris, S. Traynor, V. Ottenbacher, A. Shawabkeh, and W. F. Oliver, *J. Appl. Phys.* **64**, 787 (1988).

[3] J. F. Scott, H. M. Duiker, P. D. Beale, B. Pouligny, K. Dimmler, M. Parris, D. Butler and S. Eaton, *PhysicaB/C* **150**, 160 (1988).

[4] D. D. Fong, G. B. Stephenson, S. K. Streiffer, J. A. Eastman, O. Auciello, P. H. Fuoss, and C. Thompson, *Science* **304**, 1650 (2004).

[5] M. Stengel, D. Vanderbilt and N. A. Spaldin, *Nature Materials* ***8***, 2429 (2009).

[6] C. Lichtensteiger, and J. –M. Triscone, *Phys. Rev. Lett.* **94**, 047603 (2005).

[7] T. C. MacLeod, T. A. Phillips, and F. D. Ho, *Integr. Ferroelectr.* **89**, 12 (2007).

[8] Y. –H. Xie, Y. –Y. Lin, T. -A. Tang, *Integr. Ferroelectr.* **67**, 263 (2010).

[9] D. Ricinschi, and M. Okuyama, *J. Phys. D: Appl. Phys.* **42**, 085410 (2009).

[10] K. R. Raiter, and B. F. Cockburn, Proceedings of the 2005 IEEE International Workshop on Memory Technology, Design, and Testing (MTDT'05) (2005**)**.

[11] A. –Q. Jiang, H. J. Lee, G. H. Kim, and C. S. Hwang, *Adv. Mater.* **21**, 2870 (2009).

[12] A. –Q. Jiang, H. J. Lee, C. S. Hwang, and T. –A. Tang, *Phys. Rev. B.* **80**, 024119 (2009).

[13] H. J. Lee, G. H. Kim, M. H. Park, A. –Q. Jiang, and C. S. Hwang, *Appl. Phys. Lett.* **96**, 212902 (2010).

[14] R. Thomas, J. F. Scott, D. N. Bose and R. S. Katiyar, *J. Phys.: Condens. Matter* **22**, 423201 (2010).

[15] Y. Kato, Y. Kaneko, H. Tanaka, and Y. Shimada, *Jpn. J. Appl.Phys.* **47**, 2719 (2008).

[16] S. M. Yoon, S. H. Yang, S. H. K. Park, S. W. Jung, D. H. Cho, C. W. Byun, S. Y. Kang, C. S. Hwang, and B. G. Yu, *J. Phys. D: Appl. Phys.* **45**, 245101 (2009).

[17] S. Adachi, "Handbook on Physical Properties of Semiconductors, Kluwer Academic Publishers", Norsell, Massachusetts, USA (2004**)**.

[18] P. Zubko, D. J. Jung, and J. F. Scott, *J. Appl. Phys.* **100**, 114113 (2006).

[19] P. Zubko, D. J. Jung, and J. F. Scott, *J. Appl. Phys.* **100**, 114112 (2006).

[20] J. F. Scott, Ferroelectric Memories (Springer, Heidelberg, 2000).

[21] S. B. Zhang, S. H. Wei, and A. Zunger, *Phys. Rev. B*, **63**, 075205 (2007).

[22] P. W. Peacock, and J. Robertson, *J. Appl. Phys.* **92**, 4712 (2002).

[23] A. Janotti, and C. G. V. Walle, *Rep. Prog. Phys.* **72**, 126501 (2009).

[24] J. Robertson, and C. W. Chen, *Appl. Phys. Lett.* **74**, 1168 (1999).

[25] G. V. Samsonov, The Oxide Handbook Second Edition, Metallurgiya Press, Moscow, Russia (1978**).**

[26] K. Natori, D. Otani, N. Sano, *Appl. Phys. Lett.*, **73**, 632 (1998).

Chapter 8. Conclusions

In this dissertation, the origin of the ferroelectricity in $Hf_{1-x}Zr_xO_2$ thin films was examined based on their crystallographic structure, micro-structures and resulting in-plane stress. For all the cases of HfO_2, ZrO_2, and $Hf_{1-x}Zr_xO_2$ films, huge in-plane tensile stress could be observed which is thought to be formed during the crystallite coalescence of Volmer-Weber type growth. However, the ferroelectricity could be seen only for the case of $Hf_{1-x}Zr_xO_2$ films thinner than 20 nm. For the case of HfO_2, m-phase was easily formed with small grain size, whereas o-phase cannot be formed due to the large difference of crystal structure of t-phase and o-phase. The o-phase can be formed only in $Hf_{1-x}Zr_xO_2$ films because the formation of m-phase is prevented and the difference of the cryatal structure of t-phase and o-phase is small. On the other hand, the origin of the huge tensile stress in thin films was also examined, and the tensile stress formed during crystallite coalescence was the only possible origin of the huge tensile stress. Therefore, it could concluded that the unexpected phase was formed under huge tensile in-plane stress with might be formed during island coalescence process of Volmer-Weber type growth.

In addition to that, the effects of FGA on the electrical and physical properties of HZO films were examined. It was confirmed that H-incorporation during FGA degrades the ferroelectric properties of HZO films,

but the degree was much smaller compared to the conventional perovskite-structured ferroelectrics. Pt works as a catalyst for H-incorporation, and a maximum $2P_r$ loss of ~40% occurs after the FGA at 300 °C. However, the insertion of a ~20-nm-thick TiN layer between Pt and HZO decreased the degradation to ~12%. In contrast, the degradation was almost completely recovered after the FGA at 600 °C due to desorption of H atoms at that temperature. The annealing under the N_2 atmosphere had little effect on the ferroelectric properties of the HZO films. The I-V characteristics and core-energy XPS revealed that the degradation and recovery have almost no relationship with the oxygen vacancy formation. The results show that HZO is much more resistant to the ferroelectric degradation by FGA compared to conventional ferroelectrics, such as PZT, which is believed to be due to the larger energy of Hf-O and Zr-O bondings compared to that of Pb-O bonding. These results are very promising for the use of HZO ferroelectric films in the fabrication of integrated memory devices.

As the next step, the effects of FGA on the ferroelectric properties of HZO films were examined. Although the H-incorporation during FGA degrades the ferroelectric properties of HZO films, the degree of degradation was much lower compared with other ferroelectrics, such as PZT. Pt worked as a catalyst for H-incorporation, and maximum $2P_r$ loss of ~40% occurred. However, the insertion of a ~20-nm-thick TiN layer between Pt and HZO decreased the degradation to ~12%. HZO is more resistant to degradation by

FGA compared with the conventional ferroelectrics, which is a highly promising result for next-generation ferroelectric memory.

In addition to that, the effect of the TE on the ferroelectric properties and switching endurance of thin HZO films was examined. The TiN/ HZO /TiN capacitor can endure up to 10^9 times the electric cycling, which is promising for the next-generation memory. RuO_2 TE was reduced during annealing due to the reactive TiN BE, resulting in the degradation of the ferroelectric properties and endurance. In addition, the endurance of the TiN/ HZO /TiN capacitors was optimized by changing the film thickness and the post-annealing temperature.

Finally, a feasible structure and actual operation of tri-state memory function for high density FeRAM are presented based on the metal-ferroelectric-metal-insulator-metal structure, where the PZT, Al_2O_3, and ZnO layers were the ferroelectric, insulator and semiconductor layers, respectively. The separated trapping of the compensating charges at the interfaces between the PZT and Al_2O_3, and Al_2O_3 and ZnO layers appears to result in the discrete dissipation of trapped charges, which results in a two-step-like voltage signal in the pulse switching experiment. The retention property of the tri-level memory is also robust enough for the nonvolatile memory application. This can comprise a tri-state ferroelectric memory with singular ferroelectric switching in the opposite bias polarity. This new mechanism can increase the memory density by 50% compared to the

conventional FeRAM at a given cell size.

This thesis presents new pathways for the next-generation ferroelectric memory by exploring the new material system of $Hf_{1-x}Zr_xO_2$ films and by suggesting the new structure and operation of ferroelectric capacitor with novel ferroelectric-insulator-semiconductor heterojunction. Even though the ferroelectric memory is still far from the adoption as a universal memory, the results in this thesis could shed light on this field by suggesting new pathways different from the conventional approach.

Curriculum Vitae

Min Hyuk Park

Department of Materials Science and Engineering

College of Engineering, Seoul National University

San 56-1 Silim-dong, Gwanak-gu, Seoul, 151-742, Korea

Tel: +82-02-880-8923

E-mail: nowhere0328@gmail.com

EXECUTIVE SUMMARY

Min Hyuk Park received the B. S. degree in 2008 (*summa cum laude*), and will receive Ph. D. degree in 2014 from Seoul National University. He is an expert in the field of ferroelectric thin films with various techniques for deposition and characterization of various materials for various hot topics. Especially, he is one of the young leading scientist in the field of ferroelectric HfO_2-based films which was initiated in 2011 by Namlab in Germany. Even though his research on this topic started in May of 2012, two papers were already published, and two more are in preparation. He firstly reported the effect of hydrogen annealing on ferroelectric properties of HZO films, whose degradation was much mitigated compared with that of conventional ferroelectrics such as PZT due to the absence of weak metal-oxide bonding such as Pb-O. He also examined the competition of the

polymorphs of HZO with the change of film thickness and annealing temperature using the peak simulation of the GAXRD spectra. In his first paper in preparation and Ph.D dissertation, he firstly suggested that the large tensile stress formed during the coalescence process of Volmer-Weber type growth is the reason for the formation. His assumption is well-matched with all the reports on this topic, and is the most reasonable one until now. In addition to that, he also conducted research on conventional ferroelectrics such as PZT. His creative idea of dividing compensating charges into two interfacial layers made it possible to increase the number of memory states of ferroelectric capacitor into three. This can make 9 states using two cells, and they can work as three cells of bi-states memory with the help of the simple external circuit. Therefore, the novel tri-states memory can be increased the information storage up to 50%. In addition, he was awarded a prize due to the excellence of achievement of the research. In his paper on PZT in preparation, he fabricated self-rectifying ferroelectric resistive memory with $I_{on}/I_{off} \sim 10^5$ and $I_{forward}/I_{reverse} \sim 10^5$, which are the best properties reported in the field of ferroelectric resistive memory using the novel multi-layered structure. He was also awarded a prize due to the excellence of achievement of the research on the novel self-rectifying ferroelectric resistive memory. In addition to that, he was awarded a prize due to the excellence of achievement of the research on ferroelectric films during a governmental project of Korea. In addition to that, he also took part in

important researches of his coworkers with various materials, such as $(Ba,Sr)TiO_3$, $PbTiO_3$, $Pb(Zr,Ti)O_3$, and $BiFeO_3$. Recently, he is also taking part in on-going researches on hot topics in the field of ferroelectricity, such as negative capacitance and huge dielectric constant based on domain dynamics.

EDUCATION

M.S. & Ph. D. course, Department of Materials Science and Engineering

Seoul National University, Seoul, Korea
2008.09 – 2013.02

B.S., Department of Materials Science and Engineering

Seoul National University, Seoul, Korea
2001.03 – 2008.09

RESEARCH AREAS

1. Multi-functional HfO_2-based films

- The effect of substrate on the orientation of thin HfO_2-based films and its influence on electrical characteristics.
- The structural analysis on the polycrystalline HfO_2-based films at Pohang accelerator laboratory.
- The degradation mechanism of thin HfO_2-based films due to hydrogen annealing.
- The competition of polymorphs in thin HfO_2-based films with the change of film thickness and annealing conditions.
- The change of the microstructure of thin HfO_2-based films and its effect on the electrical properties.
- Thin antiferroelectric HfO_2-based films as a candidate for high energy density capacitor.
- The improvement of endurance properties of ferroelectric films by

changing electrode materials and annealing conditions.

2. Science behind the novel devices using ferroelectrics

- Examination on the negative capacitance in ferroelectrics for low power electronics.
- Tri-state memory using ferroelectric-insulator-semiconductor heterojunction for 50 % increased data storage.
- The observation of huge dielectric constant based on domain dynamics.
- Novel self-rectifying resistive memory using ferroelectric films.
- The role of ultra-thin dielectric layer in ferroelectric/dielectric bilayer capacitor

TECHNICAL SKILLS

1. Deposition method

- ALD for fabrication of high-k material (TiO_2, Al_2O_3, HfO_2, and ZrO_2)
: by termal ALD (using travelling wave type), PEALD, and liquid-injection ALD
- Chemical solution Deposition using spin coater for fabricating the ferroelectric oxide $Pb(Zr,Ti)O_3$
- RF magnetron sputtering for fabricating dielectric($SrTiO_3$, $(Ba,Sr)TiO_3$) and ferroelectric materials($Pb(Zr,Ti)O_3$, $BiFeO_3$)
- E-beam evaporation and DC sputtering for metal electrode

2. Analysis method

- TF 2000 analyzer (aixacct) for ferroelectric characterization
- Pulse pattern generator (Agilent, 81110A) and digital oscilloscope for pulse switching measurement of ferroelectric materials
- Atomic Force Microscopy (AFM, JEOL, JSPM-5200) for topography
- HP4194A for C-V and impedance measurement of capacitors
- HP4145B and HP4155A for I-V measurement of capacitors
- X-ray Fluorescence (XRF) for the analysis of areal density and cation

composition of the films

- Ellipsometer for film thickness measurement
- Spectroscopic Ellipsometry for the optical characterization of films
- Characterizing thin films by XPS, AES, and SIMS

3. Furnace and Rapid Thermal Process (RTP) for ambient and vacuum annealing

List of publications

1. Journals (SCI)

1.1 International

13. **Min Hyuk Park**, Han Joon Kim, Yu Jin Kim, Taehwan Moon, Woojin Jeon, and Cheol Seong Hwang, "The ferroelectric properties and switching endurance of $Hf_{0.5}Zr_{0.5}O_2$ films on TiN bottom and TiN or RuO_2 top electrodes", submitted to SCI journal.
12. **Min Hyuk Park**, Han Joon Kim, Yu Jin Kim, Taehwan Moon, and Cheol Seong Hwang, "The factors that determine the ferroelectricity in thin $Hf_{0.5}Zr_{0.5}O_2$ films", submitted to SCI journal.
11. Yu Jin Kim, **Min Hyuk Park**, Han Joon Kim, Doo Seok Jeong, and Cheol Seong Hwang, "Negative Capacitance Achieved at Room Temperature from Switching Regions of Ferroelectric Thin Films", in preparation
10. An Quan Jiang, Xiang Jian Meng, David Wei Zhang, **Min Hyuk Park**, Sijung Yoo, Yu Jin Kim, James F. Scott, and Cheol Seong Hwang, "Giant Dielectric Permittivity in Ferroelectric Thin Films: Domain Wall Ping-Pong", submitted to SCI journal.

9. **Min Hyuk Park**, Han Joon Kim, Yu Jin Kim, Woongkyu Lee, Taehwan Moon and Cheol Seong Hwang, "Evolution of phases and ferroelectric properties of thin $Hf_{0.5}Zr_{0.5}O_2$ films according to the thickness and annealing temperature", Appl. Phys. Lett. 102, 242905 (2013).

8. **Min Hyuk Park**, Han Joon Kim, Yu Jin Kim, Woongkyu Lee, Hyo Kyeom Kim, and Cheol Seong Hwang, "Effect of forming gas annealing on the ferroelectric properties of $Hf_{0.5}Zr_{0.5}O_2$ thin films with and without Pt electrodes", Appl. Phys. Lett. 102, 112914 (2013).

7. Woo Young Park, **Min Hyuk Park**, Jong Ho Lee, Jung Ho Yoon, Jeong Hwan Han, Jung-Hae Choi and Cheol Seong Hwang, "Strain evolution of each type of grains in poly-crystalline $(Ba,Sr)TiO_3$ thin films grown by sputtering", Scientific Reports, 2, 939 (2012).

6. Hyun Ju Lee, **Min Hyuk Park**, Yu Jin Kim, Cheol Seong Hwang, Jeong Hwan Kim, Hiroshi Funakubo, and Hiroshi Ishiwara, "Improved ferroelectric property of very thin Mn-doped $BiFeO_3$ films by an inlaid Al_2O_3 tunnel switch", J. Appl. Phys. 110, 074111 (2011).

5. **Min Hyuk Park**, Hyun Ju Lee, Gun Hwan Kim, Yu Jin Kim, Jeong Hwan Kim, Jong Ho Lee, and Cheol Seong Hwang, "Tristate Memory Using Ferroelectric–Insulator–Semiconductor Heterojunctions for 50% Increased Data Storage", Adv. Funct. Mater. 21, 4305-4313 (2011).

4. Hyun Ju Lee, **Min Hyuk Park**, Gun Hwan Kim, Jun Yeong Seok, Yu Jin Kim, Cheol Seong Hwang, and An Quan Jiang, "Polarization switching and discharging behaviors in serially connected ferroelectric Pt/$Pb(Zr,Ti)O_3$/Pt and paraelectric capacitors" J. Appl. Phys. **109**, 114113 (2011).

3. Hyun Ju Lee, **Min Hyuk Park**, Yo-Sep Min, Guylhaine Clavel, Nicola Pinna,

and Cheol Seong Hwang, "Unusual Growth Behavior of Atomic Layer Deposited $PbTiO_3$ Thin Films Using Water and Ozone As Oxygen Sources and Their Combination", J. Phys. Chem. C **114**, 12736 (2010).

2. Hyun Ju Lee, Gun Hwan Kim, **Min Hyuk Park**, An-Quan Jiang, and Cheol Seong Hwang, "Polarization reversal behavior in the Pt/Pb(Zr,Ti)O_3/Pt and Pt/Al_2O_3/Pb(Zr,Ti)O_3/Pt capacitors for different reversal directions", Appl. Phys. Lett. **96**, 212902 (2010).

1. Gun Hwan Kim, Hyun Ju Lee, An Quan Jiang, **Min Hyuk Park**, and Cheol Seong Hwang. "An analysis of imprinted hysteresis loops for a ferroelectric Pb(Zr,Ti)O_3 thin film capacitor using the switching transient current measurements", J. Appl. Phys. **105**, 044106 (2009).

2. Proceedings

2. **Min Hyuk Park**, Hyun Ju Lee, Gun Hwan Kim, and Cheol Seong Hwang, "The Effect of Periodic Relaxation on the Growth Behavior and Electrical Properties of Atomic Layer Deposited $PbTiO_3$ Thin Film", ECS Trans. 19(2), 815 (2009).

1. Hyun Ju Lee, **Min Hyuk Park**, and Cheol Seong Hwang, "The Effects of Oxidants on the Growth Behavior of $PbTiO_3$ Thin Film by Atomic Layer Deposition", ECS Trans. 19(2), 829 (2009).

3. Conferences

2.1 International

23. Han Joon Kim, **Min Hyuk Park**, Yu Jin Kim, Hyo Kyeom Kim, Il-Hyuk Yu, and Cheol Seong Hwang, "Investigation on ferroelectric properties of Hf_xZr_{1-}

$_xO_2$ thin film with various compositions", The 8th Asian Meeting on Ferroelectrics(AMF-8), Dec 9-14, Pattaya, Thailand, Dec 12, 2012 - Poster.

22. Yu Jin Kim, **Min Hyuk Park**, Hyung-Suk Jung, Han Joon Kim, and Cheol Seong Hwang, "Direct Observation of Transient Negative Capacitance in Switching Domains of Ferroelectric/Dielectric Bi-layer Structure", The 8th Asian Meeting on Ferroelectrics(AMF-8), Dec 9-14, Pattaya, Thailand, Dec 12, 2012 - Oral.
21. **Min Hyuk Park**, Han Joon Kim, Yu Jin Kim, Woonkyu Lee, Hyo Kyeom Kim, Il-Hyuk Yoo and Cheol Seong Hwang, "Examination on the ferroelectricity of $Hf_xZr_{1-x}O_2$ thin film on various substrates", The 8th Asian Meeting on Ferroelectrics(AMF-8), Dec 9-14, Pattaya, Thailand, Dec 13, 2012 - Oral.
20. Yu Jin Kim, **Min Hyuk Park**, Han Joon Kim, and Cheol Seong Hwang*, "Transient Negative Capacitance in switching domain of ferroelectric thin films", The 8th Asian Meeting on Ferroelectrics(AMF-8), Dec 9-14, Pattaya, Thailand, Dec 11, 2012 - Plenary talk.
19. Han Joon Kim, **Min Hyuk Park**, Yu Jin Kim, Hyo Kyeom Kim, Il-Hyuk Yu, and Cheol Seong Hwang, "Effect of Composition on the ferroelectric properties of $Hf_xZr_{1-x}O_2$ thin film", KJC-FE09, Ulsan, Korea, August(07-10), August 8th (2012) - Poster.
18. Yu Jin Kim, **Min Hyuk Park**, Han Joon Kim, Doo Seok Jeong, Anquan Jiang, and Cheol Seong Hwang, "Transient Negative Capacitance in Domain Wall of Ferroelectric Thin Films", KJC-FE09, Ulsan, Korea, August(07-10), August 8th (2012) - Poster.
17. **Min Hyuk Park**, Han Joon Kim, Yu Jin Kim, Hyo Kyeom Kim, Il-Hyuk Yu,

and Cheol Seong Hwang, "Examination on the ferroelectricity in $Hf_xZr_{1-x}O_2$ thin film", KJC-FE09, Ulsan, Korea, August(07-10), August 8th (2012) - Contributed Talk.

16. Yu Jin Kim, **Min Hyuk Park**, Han Joon Kim, Doo Seok Jeong, Anquan Jiang and Cheol Seong Hwang, "Direct observation of transient negative capacitance in domain wall of ferroelectric thin films", Nature Conference 2012, Aachen, Germany, June(17-20), June 19th (2012)-poster.
15. **Min Hyuk Park**, Hyun Ju Lee, Yu Jin Kim, Jong Ho Lee, Woongkyu Lee, Han Joon Kim, and Cheol Seong Hwang, "Diode-Embedded Resistive Memory Using Stacked Ferroelectric/Dielectric Layer", WoDiM 2012, Dresden, Germany, 25th~27th June, 25th June (2012)-poster.
14. **Min Hyuk Park**, Hyun Ju Lee, Gun Hwan Kim, Yu Jin Kim, Jeong Hwan Kim, Jong Ho Lee, and Cheol Seong Hwang, "Novel tri-states memory using ferroelectric-insulator-semiconductor hetero-junctions for fifty percent increased data storage", WoDiM 2012, Dresden, Germany, 25th~27th June, 27th June (2012).
13. Yu Jin Kim, Hyun Ju Lee, **Min Hyuk Park**, An Quan Jiang, and Cheol Seong Hwang, "The tunnel switching behavior in SiO_2/Pb(Zr,Ti)O_3 Bi-layer Capacitors" ISAF-PFM-2011 July 24-27, Vancouver, Canada (2011) - poster.
12. **Min Hyuk Park**, Hyun Ju Lee, Yu Jin Kim, and Cheol Seong Hwang, "Novel Diode-Embedded Ferroelectric Resistive Memory for Crossbar Array Application", ISAF-PFM-2011, July 24-27, Vancouver, Canada (2011) - poster.
11. Invited, Cheol Seong Hwang, Hyun Ju Lee, An Quan Jiang, Gun Hwan Kim, and **Min Hyuk Park**, "Understanding of ferroelectric switching of the ultra-

thin Pb(Zr,Ti)O3 thin films using the inlaid Al_2O_3 tunnel switch layer", JKC-FE08, Himeji, Japan, August 4 (2010).

10. **Min Hyuk Park**, Hyun Ju Lee, Yu Jin Kim, and Cheol Seong Hwang, "Ferroelectric Properties of Pt/Pb(Zr, Ti)O_3/Al_2O_3/ZnO/Pt Stack Capacitors for Nonvolatile Memory Applications", The 7th AMF-AMEC 2010, Jeju, Korea, June 28-July 1 (2010).
9. Hyun Ju Lee, Gun Hwan Kim, **Min Hyuk Park**, Yu Jin Kim, and Cheol Seong Hwang, "Study on the charge injection for the polarization reversal in the Pt/Pb(Zr,Ti)O_3/Pt and Pt/Al_2O_3/Pb(Zr,Ti)O_3/Pt ferroelectric capacitors", The 7th AMF-AMEC 2010, Jeju, Korea, June 28-July1 (2010).
8. **Min Hyuk Park**, Hyun Ju Lee and Cheol Seong Hwang, "Ferroelectric Properties of Pt/Pb(Zr, Ti)O_3/Al_2O_3/ZnO/Pt Stack Capacitors for Nonvolatile Memory Applications.", MRS spring meeting 2010 (oral), San Francisco Marriott, April 8, (2010).
7. Hyun Ju Lee, Gun Hwan Kim, **Min Hyuk Park** and Cheol Seong Hwang, "Polarization Reversal in the Pt/Pb(Zr,Ti)O3/Pt and Pt/Al_2O_3/Pb(Zr,Ti)O_3/Pt Ferroelectric Capacitors.", MRS spring meeting 2010 (oral), San Francisco Marriott, April 7, (2010).
6. An Quan Jiang, Hyun Ju Lee, Gun Hwan Kim, **Min Hyuk Park** and Cheol Seong Hwang, "Inlaid Al2O3 Tunnel Switch Layer for Improving the Ferroelectric Performance of the Ultra-thin Pb(Zr,Ti)O_3 Thin Films.", MRS spring meeting 2010 (oral), San Francisco Marriott, April 7, (2010).
5. An Quan Jiang, Hyun Ju Lee, Gun Hwan Kim, **Min Hyuk Park** and Cheol Seong Hwang, "Unusual improvement in the functionality of ferroelectric films by using the inlaid Al_2O_3 tunnel switch layer", (Invited) IMF-ISAF

2009, Xi'an, China, Aug. 23-26 (2009).

4. **Min Hyuk Park**, Hyun Ju Lee, Gun Hwan Kim, and Cheol Seong Hwang, "The effect of periodic relaxation on the growth behavior and electrical properties of atomic layer deposited $PbTiO_3$ thin film", (oral) IMF-ISAF 2009, Xi'an, China, Aug 23-26 (2009).
3. Hyun Ju Lee, **Min Hyuk Park**, and Cheol Seong Hwang, "The effect of oxidants on the growth behavior of $PbTiO_3$ thin film by atomic layer deposition", (oral) IMF-ISAF 2009, Xi'an, China, Aug. 23-26 (2009).
2. Hyun Ju Lee, **Min Hyuk Park** and Cheol Seong Hwang, "The Effects of Oxidants on the Growth Behavior of $PbTiO_3$ Thin Film by Atomic Layer Deposition", (poster) 215th ECS meeting, San Francisco, CA, May 24-29. (2009).
1. **Min Hyuk Park**, Hyun Ju Lee, Gun Hwan Kim and Cheol Seong Hwang, "The Effect of Periodic Relaxation on the Growth Behavior and Electrical Properties of Atomic Layer Deposited $PbTiO_3$ Thin film", (poster) 215th ECS meeting, San Francisco, CA, May 24-29. (2009).

2.2 Domestic

15. **Min Hyuk Park**, Han Joon Kim, Yu Jin Kim, Hyo Kyeom Kim, Woongkyu Lee, Il-Hyuk Yu, and Cheol Seong Hwang, "The effects of grain size on the electrical properties of ferroelectric $Hf_{1-x}Zr_xO_2$ thin films", Feb. 4-6, 성우리조트, 제 20회 한국 반도체 학술대회, 2013 - oral.
14. 김유진, **박민혁**, 정형석, 김한준, 황철성 "The observation of Negative Capacitance at Room Temperature from Switching Domains of Ferroelectric Thin Films" Feb. 4-6, 성우리조트, 제 20회 한국 반도체 학술대회,

2013 - oral.

13. Han Joon Kim, **Min Hyuk Park**, Yu Jin Kim, Hyo Kyeom Kim, Il-Hyuk Yu, and Cheol Seong Hwang, "Examination on the ferroelectric properties and reliability of $Hf_xZr_{1-x}O_2$ films on Ir substrates", Feb. 4-6, 성우리조트, 제 20회 한국 반도체 학술대회, 2013 - poster.

12. Yu Jin Kim, **Min Hyuk Park**, Hyun Ju Lee, Hyung-Suk Jung, Han Joon Kim and Cheol Seong Hwang, "Polarization switching in ferroelectric thin films with interposed interfacial layer", 제8차 강유전체 연합 심포지엄, 무주 2.12-2.14 (2012)_Poster.

11. **Min Hyuk Park**, Hyun Ju Lee, Gun Hwan Kim, Yu Jin Kim, Jeong Hwan Kim, Jong Ho Lee, Han Joon Kim and Cheol Seong Hwang, "Novel tri-states memory using ferroelectric-insulator-semiconductor hetero-junctions for fifty percent increased data storage", 제8차 강유전체 연합 심포지엄, 무주, 2.12-2.14 (2012)_Poster.

10. **Min Hyuk Park**, Yu Jin Kim, and Cheol Seong Hwang, "Is there a negative capacitance?" 제8차 강유전체 연합 심포지엄, 무주, 2.12-2.14 (2012)_Invited .

9. **Min Hyuk Park**, Hyun Ju Lee, Gun Hwan Kim, Yu Jin Kim, Jeong Hwan Kim, Jong Ho Lee, and Cheol Seong Hwang, "Tri-states memory using ferroelectric-insulator-semiconductor hetero-junctionsfor fifty percent increased data storage", 제19회 반도체학술대회, 고려대학교 2/15~2/17, Feb 17th (2012)-oral.

8. **Min Hyuk Park**, Hyun Ju Lee, Yu Jin Kim, and Cheol Seong Hwang, "Novel Diode-Embedded Ferroelectric Resistive Memory Using $Pt/Pb(Zr,Ti)O_3/Al_2O_3/TiOx/Pt$ stack capacitor", 제 7차 강유전체

연합심포지엄, February 13-15 (2011) -Poster.

7. 이현주, **박민혁**, 김유진, 김건환, 석준영, Anquan Jiang, 황철성, "Polarization switching and discharging behaviors in serially connected ferroelectric Pt/Pb(Zr, Ti)O_3/Pt and paraelectric capacitors", 제 18회 한국 반도체 학술대회, February 16-18 (2011) -Poster.

6. **Min Hyuk Park**, Hyun Ju Lee, and Cheol Seong Hwang, "Ferroelectric properties of Pt/Pb(Zr,Ti)O_3/Al_2O_3/ZnO/Pt stack capacitors for nonvolatile memory application", 제 17회 한국 반도체 학술대회, 호텔 인터불고 엑스코,(poster) 2. 24~26 (2010).

5. Hyun Ju Lee, Gun Hwan Kim, **Min Hyuk Park**, and Cheol Seong Hwang, "Polarization reversal in the Pt/Pb(Zr,Ti)O_3/Pt and Pt/Al_2O_3/Pb(Zr,Ti)O_3/Pt ferroelectric capacitors", 제 17회 한국 반도체 학술대회, 호텔 인터불고 엑스코, (oral) 2. 24~26 (2010).

4. Hyun Ju Lee, An Quan Jiang, Gun Hwan Kim, **Min Hyuk Park**, and Cheol Seong Hwang, "Unusual improvement in the functionality of ferroelectric films by using the inlaid Al_2O_3 tunnel switch layer"(oral), 제 16회 한국반도체학술대회, 대전컨벤션센터, Feb. 18~20, 2009.

3. Hyun Ju Lee, **Min Hyuk Park**, Cheol Seong Hwang, "The effects of oxidants on the growth behavior of $PbTiO_3$ thin film by atomic layer deposition", 제 5차 강유전체 연합 심포지엄, 무주리조트, Feb. 8-10, 2009..

2. **Min Hyuk Park**, Hyun Ju Lee, Gun Hwan Kim, and Cheol Seong Hwang , "The effect of periodic relaxation on the growth behavior and electrical properties of atomic layer deposited $PbTiO_3$ thin film", 제 5차 강유전체 연합 심포지엄, 무주리조트, Feb. 8-10, 2009.

1. Gun Hwan Kim, Hyun Ju Lee, **Min Hyuk Park**, C. S. Hwang, and An Quan

Jiang, "A new analysis of imprinted hysteresis loops for ferroelectric Pb(Zr, Ti)O_3 thin film capacitor using the switching transient current measurements", 제 5차 강유전체 연합 심포지엄, 무주리조트, Feb. 8-10, 2009.

3. Academic Honors

1. Excellent poster awards second prize, The 7th AMF-AMEC-2010, 2010/7/1.
2. 최우수 발표상, 제 7차 강유전체 연합심포지움, 2011/2/14.
3. 우수연구원상, 나노기반 정보·에너지 사업본부, 2011/9/22.
4. SK-Hynix Award, The 23th Korean Conference on Semiconductors, 2014/2/25.

Abstract (in Korean)

Ferroelectric random access memory (FeRAM)은 차세대 메모리의 유망한 후보로 오랜 기간 주목받았다. 하지만, 메모리의 cell size의 scaling이 어려운 문제로 인해서 고집적 FeRAM을 만드는 것이 불가능했던 것이 현실이다. 만약, size scaling이 강유전체 물질의 복잡한 결정구조와 증착 공정에 의해서 불가능하다면, 새로운 강유전체 물질에 대한 연구는 그에 대한 가장 좋은 해결책이 될 것이다. 그 밖에도 한 개의 cell이 3가지 이상의 상태를 저장할 수 있다면, 물질을 바꾸지 않고서도 같은 면적으로 더 많은 정보를 저장할 수 있을 것이다.

이 학위 논문에서는 새로운 강유전체 물질인 $Hf_{1-x}Zr_xO_2$ 박막의 강유전성의 원인에 대한 연구를 결정구조, 미세구조, 박막 내의 응력 분석을 바탕으로 진행하였다. 그 동안의 연구 결과로부터 non-centrosymmetric한 orthorhombic phase ($Pbc2_1$)의 형성이 강유전성 발현의 원인인 것은 명확해 보이나, 이러한 결정상의 형성의 원인은 밝혀지지 않았다. 다양한 두께와 조성의 $Hf_{1-x}Zr_xO_2$ 박막을 분석한 결과 강유전성은 x=0.5 부근의 조성 범위와 특정 두께 범위 이내에서 나타나는 것을 확인할 수 있었다. 이 영역은 기존 연구에 따르면 tetragonal phase가 형성되어야 할 부분이지만, 기존 결과와는 다르게 orthorhombic phase가 형성되었다. 이 원인을 찾기 위해 기판의 곡률 변화로부터 추정되는 응력의 변화와 X-선 회절 분석법으로 구한 면간 거리의 변화 및 strain을 분석하였고, 이를 통해서 예

상치 못한 orthorhombic phase의 생성은 monoclinic phase의 생성이 억제되는 grain size 하에서 일정 크기 이상의 tensile strain과 함께 발생하는 것을 확인할 수 있었다. 이와 같은 큰 tensile strain의 원인은 Volmer-Weber type의 박막 성장의 island coalescence에 의해서 발생하는 큰 in-plane tensile stress와 관련된 것으로 결론지을 수 있었다. 또한, 다양한 하부 전극 위에서 $Hf_{1-x}Zr_xO_2$ 박막의 특성을 분석한 결과, Pt 하부 전극 위에서는 (111) 방향의 우선배향성을 가지고 자라며 tetragonal phase가 형성되고 강유전성이 거의 나타나지 않는 것을 볼 수 있었다. 한편, X-선 회절 분석으로 얻은 in-plane strain은 TiN 하부 전극과 비슷한 값을 보이며, o-phase의 형성에 충분한 크기였다. 하지만, (111) 배향성의 경우에 박막의 a-, b-, c-축이 거의 같은 stress를 받는 조건이기 때문에 비대칭적인 stress하에서 생성되는 o-phase의 생성조건에는 맞지 않았다. 이와 같은 기판에서의 거동 역시 tensile strain에 의해서 잘 설명될 수 있었다.

이 밖에도, 열처리 온도와 박막의 두께에 따른 결정 구조 변화와 그에 따른 강유전성의 변화를 분석하였다. $Hf_{0.5}Zr_{0.5}O_2$ 박막 내에는 tetragonal, orthorhombic, monoclinic 상이 혼재하고 있다. 강유전성과 직접적인 관계사 있는 orthorhombic 상의 양은 열처리 온도와는 거의 무관하였지만, 박막의 두께가 증가할 때는 감소하였다. 반면에, 열처리 온도와 박막 두께의 증가는 monoclinic 상의 증가와 tetragonal 상의 감소로 나타났고, 이는 유전상수의 변화와도 잘 맞았다. 결과로부터, 잔류분극의 크기는 orthorhombic 상의 양과 다른

상과의 공간 상의 배치로부터 영향을 받는다는 것을 알 수 있었다.

다음 단계로, $Hf_{0.5}Zr_{0.5}O_2$ 박막의 강유전성에 대한 forming gas 열처리의 영향을 분석하였다. 비록 forming gas 열처리 중의 수소 삽입에 의하여 강유전성이 열화되지만, 기존의 $Pb(Zr,Ti)O_3$와 같은 강유전체에 비해서는 열화되는 정도가 매우 작았다. Pt 상부전극의 경우에 수소 삽입의 촉매 역할을 하였으며, 잔류분극이 40%까지 감소하는 것을 볼 수 있었다. 하지만, TiN층을 $Hf_{0.5}Zr_{0.5}O_2$ 박막과 Pt 상부 전극 사이에 삽입한 경우에는 잔류 분극의 열화 정도가 12% 까지 감소하였다. 이를 통해, $Hf_{0.5}Zr_{0.5}O_2$ 박막이 forming gas 열처리에 더 강한 것을 확인할 수 있으며, 이는 차세대 강유전체 메모리 물질로써 우수한 특성이다.

다음으로, $Hf_{0.5}Zr_{0.5}O_2$ 박막의 강유전성과 switching endurance에 대한 상부전극의 영향을 연구하였다. TiN / $Hf_{0.5}Zr_{0.5}O_2$ / TiN 구조의 TiN 상하부 전극을 가진 커패시터는 2.5 MV/cm의 전계 하에서 10^9번까지 스위칭이 가능한 우수한 endurance 특성을 보였는데, 이는 차세대 강유전체 메모리로써 유망한 특성이라 할 수 있다. 기존의 PZT와 같은 강유전체와 noble metal로 이루어진 커패시터와는 다르게 $Hf_{0.5}Zr_{0.5}O_2$ 박막과 TiN 하부전극으로 이루어진 커패시터는 RuO_2 상부전극과의 조합이 강유전성을 열화시켰고, 이것은 TiN 전극이 산화되며 RuO_2 전극이 환원되는 현상에 의한 것임을 밝혔다. 또한, 다양한 두께와 열처리 온도에서 $Hf_{0.5}Zr_{0.5}O_2$ 박막의 endurance 특성을 최적화시키는 데 성공하였다.

끝으로, 이 학위 논문에서는 강유전체인 $Pb(Zr,Ti)O_3$/부도체인 Al_2O_3/반도체인 ZnO 등을 적층하고 상하부 전극으로 Pt를 사용한 구조에서 세가지 상태를 가지는 메모리의 구조와 동작에 대해 보고하였다. 이 적층 구조에서는 복잡한 전기적 특성으로부터 $Pb(Zr,Ti)O_3/Al_2O_3$와 Al_2O_3/ZnO의 계면층에 compensating charge가 분산되어 저장되는 것을 확인할 수 있었다. 이 새로운 구조를 기반으로 한 강유전체 커패시터를 사용하면 같은 면적에 저장되는 정보의 양을 50%까지 증가시킬 수 있다.

Keywords : Ferroelectric, HfO_2, $(Hf,Zr)O_2$, ZrO_2, $Pb(Zr,Ti)O_3$, $Pbc2_1$, In-plane stress, microstructure, Tri-state memory, FeRAM, Capacitor, Nonvolatile memory, Atomic Layer Deposition

Student ID : 2008-22846

Min Hyuk Park

Acknowledgement (감사의 글)

이제야 뒤를 돌아볼 여유가 생겨 멈춰서 생각해보니, 제 힘으로 된 것이 하나도 없습니다. 태초부터 제 삶을 계획하시고 항상 신실하게 이끌어주신 하나님께 감사드립니다.

만 5년 10개월의 세월을 대학원에 와서 유전박막실험실에서 보냈고, 2001년 3월부터 2014년 2월까지 군휴학 기간을 제외하고는 모두 서울대학교에서 보냈습니다. 좋은 일이 많았고, 간혹 나쁜 일도 있었지만, 모든 일에서 배울 것들이 있었습니다. 서울대학교는 제가 가장 긴 시간을 보낸 특별한 곳입니다. 부족하고 무지한 제가 여기까지 오게 된 것은 전적으로 그 과정에서 만난 많은 분들의 도움과 가르침 덕분입니다.

2008년 4월에 시작한 학부생 인턴 생활부터 만 5년 10개월의 기간동안 저를 지도해 주신 황철성 교수님께 감사드립니다. 교수님께서는 연구에 대한 학문적 지도 뿐만 아니라 연구에 임하는 자세, 학문에 대한 열정, 나아가 인생을 살아가는 데 있어서 중요한 가르침을 많이 주셨습니다. 또한, 교수님께서 구축하신 최고의 연구 환경을 가진 유전박막실험에서 학위 기간동안 연구할 수 있었던 것 자체가 제게는 너무나 큰 행운이었습니다. 세미나 때마다 많은 조언과 가르침을 주셨고, 심사위원장을 맡아주신 김형준 교수님께도 큰 감사를 드립니다. 또한, 제 논문 심사를 위해서 바쁘신 일정에도 시간을 내어주시고 많은 조언을 해 주신 한승우, 윤성민 교수님과 김성근 박사님께도 감사드립니다.

실험실에서 함께 생활하면서 대학원생으로서 모범을 보여주신 여러 선배님, 후배님들께 감사를 드립니다. 가장 먼저 제 사수였던 현주누나께 감사드립니다. 제가 신입생으로 들어왔을 때, 따뜻하게 맞아주시고, 연구 뿐만 아니라 실험실 생활 전반에서 늘 제게 많은 것을 가르쳐 주시고 이끌어 주셔서 감사합니다. 건환이형과 늘 행복하시고, 앞으로 좋은 일이 두 분께 더 많을 거라고 확신합니다. 짧은 시간 함께 했지만 지금은 중국에서 교수님이 되신 금석이형, 독실한 크리스천으로 제가 하는 실험실 생활에 길을 닦아 주셨던 준섭이형, 항상 분위기를 밝게 만드시고 지금은 행복한 가정의 가장이신 근이형, 모두 감사드리고 앞으로 하시는 일이 더욱 잘 되시길 바랍니다. 또, 같은 팀에서

동고동락했던 FRAM 팀의 후배들에게도 감사의 말을 전합니다. 실험실에서 가장 명석한 후배로 어려운 연구 주제도 잘 소화했던 유진이, 함께 같은 주제를 연구하면서 늘 성실하게 연구했던 꼼꼼하고 착한 의리의 한화팬 한준이, 그리고 흠 잡을 데가 없어 보이는 미남 태환이에게 감사합니다. 내가 참 후배 복이 많았던 것 같아. 다들 앞으로 좋은 성과를 내고 바라는 길을 갈 수 있을 거야. 제가 신입생 때 실험실에서 포닥 생활을 하시면서 연구자로서 모범을 보여주시고 이제는 교수님이 되신 태주형, 제가 닮았다는 말을 들은 유일한 선배이자 타고난 학자이신 것 같은 성근이형, 무섭다는 얘기도 들었지만 유쾌하고 재미있는 모습을 보여주셨던 재원이형, 지금도 포항가속기 연구소에서 종종 함께 실험을 하면서 많은 가르침을 주시는 맑은 목소리의 덕용이형, 항상 묵묵하게 자신의 일을 해내시며 함께 재기모 생활을 했던 우영이형, 제가 아는 사람 중 유일하게 미국에서 교수가 되신 민환이형, 항상 밝은 모습을 보여주시고 TEM을 잘 찍으시던 재혁이형, 모두 감사 드리고, 형들과 가족들에게 늘 좋은 일이 가득 하시길 바랍니다. 항상 분위기를 밝게 만들고 예의가 바르고 배려심이 깊으신 정환이형, 형 옆에서 배운 것들이 참 많은 것 같습니다. 졸업 후에도 실험실에 종종 오셔서 후배들을 잘 챙겨 주셔서 더 감사합니다. 곧 미국으로 출국하시고 포닥생활을 시작하실 RRAM의 대가 경민이형, 농구를 제일 잘 하는 교수님이 아닐까 싶은 미남 상운이형, 항상 진중해 보이시고 실험실 최다 피인용 논문의 저자이신 병준이형, 항상 저를 따뜻하게 대해 주시고 모두에게 자상하셨던 상영 누나 모두 정말 감사드립니다. 동기분들이 정말 보기 좋았고, 앞으로는 더욱 그러하실 것 같습니다. 앞으로도 저한테 많은 가르침 부탁드립니다. 다른 팀이지만 제게는 늘 같은 팀 같았던 반공연 공정의 대가 건환이형, 형한테 고마운 일들이 유독 많았습니다. 앞으로 현주 누나와 더욱 행복한 가정 꾸려가시길 바랍니다. TEM을 찍을 때마다 도움을 받았던 종호형, 타지 생활에 힘드시겠지만 힘내시고 더 행복하세요. 자동차와 바이크를 모두 잘 다루셨던 설이형, KIST에 계셨지만 늘 유쾌하셨던 성가대원 광덕이형, 어딜 가도 최단 시간 주행을 곧잘 하시던 민하 누나, MIT에서 계속 뛰어난 연구를 하고 계실 용철이형,

지금은 MIT에 계시지만 실험실 초기 생활을 함께 했던 훤칠하신 규원이형 모두 감사드립니다. 앞으로 각자의 자리에서 더 빛이 나리라 확신합니다. 술을 정말 잘 드시고 좋은 얘기를 많이 해 주신 형석이형, 꼼꼼하시고 실험실에서 가장 몸이 좋으셨던 효겸이형, 기발하시고 공정으로 고생을 많이 하셨던 상호형, 지금은 아기 엄마로 행복하게 지내시는 지심 누나, 같이 ALD 5호기를 쓰면서 고생하셨던 화목한 가정의 재호형, 긴 시간을 같이 하지는 못했지만 성격 좋고 남자다운신 경엽이형 모두 감사드리고 형, 누나들을 통해 많은 것을 배웠습니다. 앞으로 무엇을 하시든 다 잘 되시길 바랄게요. 실험실 생활 도중 불의의 사고로 먼저 하늘 나라로 가신 병견이형께도 감사합니다. 지금도 형과 같이 있었던 자리에 가면 문득 생각날 때가 있습니다, 먼저 하늘 나라에 가셨지만 편히 쉬세요. 실험실에서 유일하게 서로 말을 편하게 했던 친구 정환이에게도 감사합니다, 네가 있어서 실험실 생활이 더 즐거웠던 것 같아. 보기와 다르게 성실하고 항상 다른 사람을 잘 챙기는 웅규, 놀랄 정도로 명석하고 컴퓨터의 대가인 준영이, 착실하게 연구를 잘 하고 예의가 참 바른 우진이, ALD 5호기를 같이 쓰면서 고생도 참 많았던 같은 KIA팬 일혁이, 예의 바르고 착하고 연구도 잘했던 모범생 규진이, 이제는 새 신랑이 된 근성의 주휘, 모두 고맙고 앞으로도 무얼 하든 다 잘 되길 바래. 같이 졸업하면서 많이 의지가 되었고 세련미 속에 인간미가 있는 훈남 태용아, 네 덕분에 졸업할 때 의지도 많이 되고 더 마음 편하게 준비할 수 있던 것 같아. 미리 결혼도 축하해. 신입생 역할을 같이 하면서 의지가 되었던 힘찬이, 뛰어난 패션감각을 가지고 뭐든지 열심히 하는 승준이, 모두 감사드립니다. 누구보다 열정적이고 RRAM팀장으로 팀을 잘 이끌고 있는 슬지, 사투리가 매력적이고 만능 스포츠맨인 TFT팀 팀장 언기, 이제 곧 졸업일텐데 모두 마무리 잘 하고 좋은 결과 얻길 바래. 야구를 정말 좋아하고 항상 유쾌하던 형광이, 예의 바르고 새로운 도전에 용감한 것 같은 은석이, 예술가의 자질이 있는 것 같은 베이시스트 윤수, 자신감 넘치고 속도를 즐기던 소라도 모두 고맙습니다. 석사 졸업생이면서 박사과정 이상의 성과를 냈던 능력자 윤장이, 자신의 일에 열심이고 꾸준하게 좋은 성과를 내는 정호, 항상 밝은 모습으로 주변을

밝게 만드는 경진이, 같이 정부과제를 담당하면서 고생을 많이 한 태홍이 다들 앞으로 좋은 결과를 내는 자랑스러운 후배들이 될 거라 확신합니다. 매력적인 사투리를 쓰는 군필 상남자 시정이, 의정부에서 고등학교를 나와 반쯤 고향 후배 같은 연우, 믿음직하고 겁이 없어 보이는 대은이, 섬세하고 주관이 뚜렷한 것 같은 태형이, 허술해 보이지만 똑똑한 준식이, 바로 KIST로 가 많은 시간 함께 하지 못했지만 왠지 믿음이 가는 재홍이에게도 모두 고맙습니다.

박막 실험실의 모든 선배님, 후배님들께도 감사를 전합니다. 일일이 이름을 언급하고 감사드려야 마땅하지만 그러지 못하는 점은 양해해 주십시오. 연구를 하면서 박막 실험실의 여러 선후배님들께 큰 도움을 많이 받았습니다. e-beam evaporator 등의 여러 장비를 사용할 때 받은 도움들이 제 실험에 큰 도움이 되었고, 랩세미나 때에도 좋은 발표와 질문들로 제 연구에 도움을 주신 것들 감사합니다. 앞으로 모든 분들의 앞에 좋은 일들만 가득하길 기원합니다. 그 밖에도 바쁜 일정에도 제 졸업을 위한 실험을 많은 시간을 투자하며 도와주셨던 주영창 교수님 실험실의 조주영 박사과정 학생에게 특별히 감사드립니다. 덕분에 박막 응력 측정을 잘 진행할 수 있었습니다. 분명 성가신 일이실 텐데도 늘 친절하고 정확한 측정을 해 주신 것 감사드리며, 앞으로 더 좋은 일들이 많으실 것을 확신합니다. 아직까지 이해를 다 못하는 부분도 있지만 앞으로 같이 잘 해결해 나갔으면 합니다. 또한, ALD 장비가 고장났을 때 늘 빠른 도움을 주셨던 CN1의 최재호 이사님을 비롯한 모든 직원분들, SNTEK의 여러 직원분들께 감사를 드립니다.

군 제대 후 저에게 많은 가르침을 주셨던 김재민 목사님과 박영순 사모님께 감사드립니다. 그리고 시민교회의 하늘비젼 공동체의 모든 지체들에게 고맙습니다. 분명하게 시민교회는 제 인생에 전환점이 된 곳이고 제 마음의 고향과 같은 곳입니다. 사랑하는 교회의 박미래 목사님과 부족한 저를 챙기느라 고생하신 모든 목자님들과 셀원분들께도 감사합니다. 재기모에서 함께 시간을 보내면 좋은 가르침을 주셨던 모든 교수님들과 학생들에게도 깊은 감사를 전합니다. 고등학교 생활을 같이 하며 좋은 추억을 만들었고, 지금도 기쁠 때 어려울 때 힘이 되어주는

사랑하는 내 친구들, 규성, 기환, 필동, 재선, 민섭, 찬규, 충훈, 우람, 한얼에게도 너무 고맙다. 앞으로도 서로 도우면서 다들 행복하게 살자. 대학생활을 함께 했던 대학동기들도 이름을 다 나열하지는 못했지만 모두 고마워. 다들 각자의 자리에서 행복하길 바랄게. 외고, 의여고 – 서울대 동문회의 여러 선후배님들께도 감사를 드립니다. 지금까지 각자의 자리에서 건승하셨듯이 앞으로도 더욱 좋은 일이 많기를 기원합니다.

혹시, 제가 미처 감사를 표한 분이 있더라도 너그럽게 용서해 주시기 바랍니다, 제가 말씀드린 분들 외에도 감사해야 할 분들이 너무 많습니다.

마지막으로 제가 이 자리까지 오기까지 항상 뒤에서 저를 뒷받침해주셨던 제 가족들에게 감사드립니다. 지금은 하늘 나라에 계시지만 항상 저를 아껴주시고 칭찬해주셨던 할아버지께 감사합니다. 아직도 제게 칭찬해 주시던 할아버지의 모습이 눈에 선합니다. 어렸을 때부터 제게 맛있는 음식도 많이 해 주시고 가까이에서 늘 돌봐주시며, 늘 기도해주신 할머니께 감사드립니다. 오래오래 건강하시고, 앞으로 저희가 살아가는 모습 지켜봐 주세요. 가족들에게 늘 든든한 버팀목이 되어주셨던 아버지께도 감사합니다. 자상한 아버지께 좋은 것들을 많이 물려받았습니다. 항상 가족들을 위해서 사랑으로 희생하셨던 제가 세상에서 가장 존경하는 어머니께 진심으로 감사합니다. 앞으로 더 어머니를 닮은 삶을 살고 싶습니다. 지금은 떨어져 있지만 늘 저를 사랑하고 기도해 주시는 둘째 아버지, 어머니께도 감사드립니다. 또, 본가에 갈 때마다 반갑게 저를 맞아주시고 응원해 주셨던 셋째 아버지, 어머니와 고모, 고모부께도 감사드립니다. 제가 어릴 적부터 어른들께 많은 사랑을 받았기 때문에 건강하고 밝게 자랄 수 있었습니다. 멀리 봉화에 계시지만 항상 저를 사랑해 주시는 외할아버지, 외할머니, 외삼촌들, 외숙모들께도 진심으로 감사드립니다. 항상 건강하시고 앞으로도 오래오래 저희 가족이 사는 모습 지켜봐 주세요. 그리고, 부족한 형, 오빠 밑에서 잘 자라준 쌍둥이 동생 민철이, 민정이도 정말 고맙다. 이제 다 가정을 꾸렸는데, 더욱 행복하고 늘 우애 좋은 형제자매로 서로 아끼며 살자. 또, 어렸을 때부터 좋은 추억을 늘 함께 했던 우리 사촌들

(삼열, 우미, 지예, 민선, 형용, 애리) 모두 고마워. 모두 행복한 가정을 꾸리고 앞으로도 좋은 일로 많이 보자. 가까이 계신데도 자주 찾아뵙지 못해 늘 죄송한데도, 늘 저와 나리를 사랑으로 도와주시는 처외할머니께 감사드립니다. 항상 건강하시고 오래도록 저희가 행복한 것을 지켜봐 주세요. 부족한 사위를 항상 사랑해 주시고, 제가 졸업 준비를 하는 동안 항상 기도해 주시고, 사랑으로 재인이를 돌봐주시며, 물심양면으로 도와주신 장인어른, 장모님께 정말 감사드립니다. 앞으로 더욱 믿음직한 사위가 되도록 노력하겠습니다. 또 형부를 위해서 항상 기도해 준 처제도 너무 고마워요. 좋은 사람을 만나고 행복한 가정을 꾸리길 기도합니다. 마지막으로, 항상 내 편이 되어주고 나를 믿어주는 사랑하는 아내, 나리에게 진심으로 감사합니다. 그 동안 나를 믿고 기다려준 것 정말 고마워. 이제 사랑하는 우리 아들 재인이까지, 우리 세 식구 더 행복하게 살자. 진심으로 사랑하고 매일 어제보다 더 나은 남편이 될 수 있도록 최선을 다 할게. 사랑하는 우리 아들 재인이도 너무 고맙다. 네가 태어난 일은 내 인생에서 가장 기쁜 일 중 하나란다. 늘 건강하게 하나님 은혜 가운데 자라렴. 너에게 좋은 아버지가 될 수 있도록 아빠도 최선을 다 할게.

2014년 1월 관악에서
박 민 혁